Plastic Deformation of Flash Butt Welds in High Strength Rail Steels in Heavy Haul Railway Systems

Hang SU

Bachelor of Engineering (Honours)
Mechanical and Aerospace Engineering

Submitted in fulfilment of the requirements for the award of
Doctor of Philosophy

Department of Mechanical and Aerospace Engineering
Monash University, Clayton, Australia
2020

Copyright Notices

Notice 1

Notice 2

Abstract

The application of premium high strength rail steels has been evidenced to improve the overall performance of heavy haul operations by controlling or reducing rail degradation such as wear and rolling contact fatigue (RCF). However, these benefits can be offset by the potential of localised degradation in rail flash butt welds, which is mainly caused by the inherent variability of microstructure and the induced difference in mechanical properties between the heat-affected zones and parent rails. It has been found that plastic ratcheting plays an essential role in causing rail degradation. In order to fulfil the demanding conditions imposed by rail transport of mining products and maintain a safe heavy haul environment simultaneously, the main objective of this doctoral study is to investigate the ratcheting behaviour and quantify cyclic plasticity of new flash butt welds in a heat-treated hypereutectoid rail steel (R400HT) currently used in Australian heavy haul railways.

Experimental study consisting of both uniaxial and biaxial stress-controlled cyclic tests was performed to investigate the ratcheting behaviour of new R400HT rail flash butt welds. The results show that the ratcheting strain distribution can be correlated to the longitudinal hardness profile of the weld. Moreover, the softened zone with a significant hardness drop is more sensitive to plastic deformation and results in higher ratcheting strain than the region around the bond line. Compared with the parent rail, the softened zone shows much worse ratcheting resistance, while the region around the bond line demonstrates slightly better ratcheting resistance. Metallographic analysis indicates that the microstructure and resulting ratcheting resistance of the weld vary with the longitudinal position. Severe ratcheting strain in the softened zone is mainly attributed to the existence of the spheroidised microstructure with a

high amount of ferrite.

To quantify the ratcheting of new R400HT rail flash butt welds, a developed cyclic plasticity constitutive model for high strength rail steels was updated for the welds. The experimental results were used to calibrate the material parameters for the constitutive model and then the simulated results were validated with the experimental data. The comparison between the simulated results and the experimental data indicates that the updated constitutive model is capable of describing the ratcheting behaviour of the welds with reasonable accuracy. Furthermore, the updated constitutive model can be applied to simulate the ratcheting performance of rail welds in practice.

The ratcheting performance of new R400HT rail flash butt welds was numerically evaluated under a typical heavy haul in-service condition by finite element simulations with the application of the developed constitutive model. A dynamic simulation of wheel–rail weld rolling contact was first carried out to obtain the total vertical contact force, followed by multiple quasi-static wheel–rail weld contact simulations to determine the non-Hertzian contact pressure distribution. Finally, a cyclic loading simulation was conducted by repeatedly translating the normal contact pressure and estimated longitudinal tangential traction distributions on the running surface. The ratcheting performance of the rail weld was then evaluated in terms of the RCF initiation life. The results reveal that the subzone with the lowest hardness in the softened zone is predicted to have the shortest RCF initiation life among the weld region, followed by the region around the bond line. The parent rail presents the longest RCF initiation life and therefore has the best resistance to RCF development. Additionally, the existence of the softened zone can shorten the RCF initiation life of the parent rail and the bond line section, particularly the regions located

adjacent to the softened zone.

The possible location of RCF initiation in the softened zone of the rail head can reach to a depth of 4 mm from the running surface and extend up to 3 mm away from the initial wheel–rail contact point towards either side in the transverse direction. For the parent rail and the region around the bond line, possible location of RCF initiation can reach to a depth of 2 mm beneath from the running surface and extend up to 1 mm transversely from the initial wheel–rail contact point. According to these phenomena, more frequent attention should be employed at the softened zone, particularly the region with lower hardness, after the welds are subject to in-service loading conditions.

The ratcheting performance of high strength rail steels installed in curved tracks under different heavy haul in-service conditions was numerically evaluated, which is the additional work during this doctoral study. The wheel–high rail cyclic rolling contact was simulated by repeatedly translating the normal contact pressure and the estimated longitudinal tangential traction distributions on the running surface of high rail. The results indicate that the RCF initiation life of all three considered rail steel grades decreases with the increase in normalised tangential traction coefficient, friction coefficient, ratio of lateral/vertical load, and axle load. Under the same loading condition, the ratcheting performance of the rails in curved tracks is worse than that in tangent tracks. The hypereutectoid rail steel with a lower carbon content always shows the best RCF resistance and is likely to be the most reliable choice for high rails in curved tracks. Moreover, RCF is predicted to initiate around 1 mm beneath from the wheel–rail initial contact point under low traction conditions. As the traction conditions become more severe, the location of RCF initiation may shift from the subsurface to the running surface.

The outcomes of this study can assist researchers to further understand the ratcheting performance of rail welds and parent rails in terms of RCF initiation, and potentially provide useful information for the railway operators to develop more reliable and cost-effective maintenance strategies for rails, i.e. grinding, to control the RCF development more efficiently. Therefore, a more efficient and safer heavy haul environment can be expected to meet the continuously increasing demand for freight transportation.

Declaration

I, Hang SU, hereby declare that all the work presented in this thesis is solely my own work and to the best of my knowledge is original except those cited by references. No part of this work has been submitted for any degree.

Hang SU

Date: 31/12/2020

Acknowledgements

This doctoral research is a collaborative project between Monash University in Australia and Southwest Jiaotong University in China, which is funded by Australian Research Council (ARC) through the ARC Industry Transformation Research Hub (ITRH) Project (IH150100006) and Pangang Group Vanadium Titanium and Resources Co. Ltd in China. The financial support from the Rail Manufacturing Cooperative Research Centre (funded jointly by participating rail organisations and the Australian Federal Government's Business Cooperative Research Centres Program) through Project R2.7.6 - Optimisation of rail welding process parameters to mitigate rolling contact damage is also acknowledged.

All the experiments were carried out in Southwest Jiaotong University, which were supported by the Projects of Traction Power State Key Laboratory (TPL1606) in China. The rail weld samples were provided by BHP Ltd in Australia and Pangang Group Vanadium Titanium and Resources Co. Ltd. The metallographic analysis was conducted by using the facilities within the Monash Centre for Electron Microscopy in Monash University. The numerical simulations were undertaken with the assistance of resources and services from the National Computational Infrastructure (NCI) in Australian National University, which is supported by the Australian Commonwealth Government.

I am extremely grateful to my main supervisor Assoc. Prof. Wenyi Yan (Department of Mechanical and Aerospace Engineering, Monash University) for his profound help and guidance throughout this study. I must also express my deepest appreciation to my associate supervisors, Mr. Peter Mutton and Dr. Chung Lun Jerome Pun (Institute of Railway Technology, Monash University)

for their constructive advice and valuable support on the completion of this project.

I would like to extend my sincere thanks to Prof. Qianhua Kan (School of Applied Mechanics and Engineering, Southwest Jiaotong University) for providing technical support and helpful advice on the completion of the experiments. Thanks must also go to Mr. Jian Li (School of Applied Mechanics and Engineering, Southwest Jiaotong University) and Dr. Quan Lai (Institute of Railway Technology, Monash University) for providing the extensive knowledge on the completion of the experiments.

I cannot begin to express my thanks to my family for their relentless support throughout my study, particularly my parents. I would not be where I am today without their love and support.

Publications

Journal Papers

1. Su, H., Pun, C. L., Mutton, P., Kan, Q. & Yan, W. (2019). Numerical study on the ratcheting performance of heavy haul rails in curved tracks. *Wear* 436, 203026.

2. Su, H., Li, J., Lai, Q., Pun, C. L., Mutton, P., Kan, Q., Kang, G. & Yan, W. (2020). Ratcheting behaviour of flash butt welds in heat-treated hypereutectoid steel rails under uniaxial and biaxial cyclic loadings. *International Journal of Mechanical Sciences* 176, 1055.

3. Mojumder, S., Su, H., Qiu, C., Mutton, P., Singh, A. & Yan, W. (2020). The role of bending stress on the initiation of reverse transverse defects. In: *Proceedings of the Institution of Mechanical Engineers, Part F: Journal of Rail and Rapid Transit*, 0954409720904329.[1]

4. Su, H., Pun, C. L., Mutton, P., Kan, Q. & Yan, W. (2021). Numerical study on the ratcheting performance of rail flash butt welds in heavy haul operations. *International Journal of Mechanical Sciences* (under review).

Conference Papers

1. Su, H., Pun, C. L., Mutton, P., Kan, Q. & Yan, W. (2018). Numerical study on the ratcheting performance of heavy haul rails in curved tracks. In: *Proceedings of the 11th International Conference on Contact Mechanics and Wear of Rail/Wheel Systems (CM2018)*, pp. 938-947, Delft, The Netherlands.

[1]This paper is not part of the PhD study. In this research, I contributed in developing the finite element models and discussing the results.

Table of Contents

List of Figures

List of Tables

Nomenclature

Abbreviations

2D/3D	Two/Three-dimensional
AAR	Association of American Railroads
A-F	Armstrong-Frederick model
ALE	Arbitrary Lagrangian Eulerian
AOA	Angle of Attack
AREMA	American Railway Engineering and Maintenance-of-Way Association
AS60	Australian Standard 60 kg/m rail profile
ATW	Aluminothermic Welding
BL	Bond Line
C	Carbon
Cr	Chromium
Cu	Copper
DIC	Digital Image Correlation

ELKP	Elastic-Linear-Kinematic-Hardening-Plastic material
EPP	Elastic-Perfectly Plastic material
FBW	Flash Butt Welding
FE	Finite Element
Fe_3C	Cementite
Fe-C TTT	Iron-Carbon Time-Temperature-Transformation diagram
GDP	Gross Domestic Product
HAZ	Heat-Affected Zone
HCT	Hertz Contact Theory
HE	Hypereutectoid steel grade
HSW	Horizontal Split Web
HV	Vickers Pyramid Number for hardness test
IHHA	International Heavy Haul Association
LAHT	Low Alloy Heat-Treated steel grade
MBDS	Multi-Body Dynamics Simulations
MGT	Million Gross Tonnes

MTS	MTS Systems Corporation
MWR	Magic Wear Rate
Mg	Magnesium
Mn	Manganese
Mo	Molybdenum
Ni	Nickel
O-W model	Ohno-Wang model
P	Phosphorus
PR	Parent Rail
PWHT	Post-Weld Heat Treatment
Typical steel types (For rail use)	9Cr-1Mo, 10Ni5CrMoV, 25CDV4.11, 316FR, 316L, 42CrMo, SS304, SUS301L (R260, R350HT, R370HT, U20Mn, U71Mn, U75V)
R400HT	Hypereutectoid Heat-Treated steel grade with a head hardness of roughly 400 HV (**Current work focus**)
RCF	Rolling Contact Fatigue
SEM	Scanning Electron Microscopy
Si	Silicon

SZ	Softened Zone
SZ1B, SZRest, etc.	Subzones in the softened zone
Ti	Titanium
TOR–FM	Top-of-Rail Friction Management
V	Vanadium
WEL	White Etching Layer

Symbols

a_i	Semi-width of a strip in the contact patch
a_i'	Semi-width of the stick zone in a strip with in the contact patch
a_0	Major semi-width of the contact patch
a_0'	Major semi-width of the stick zone in the contact patch
b_0	Minor semi-width of the contact patch measured along the lateral direction
b_0'	Semi-width of the stick zone measured along the lateral direction in the contact patch
$\boldsymbol{\alpha}$	Tensor of deviatoric components of backstress
$\boldsymbol{\alpha_i}$	Tensor of backstress components (deviatoric parts)
$\dot{\boldsymbol{\alpha}}_{\boldsymbol{i}}$	Tensor of evolution of backstress components (deviatoric parts)
$\boldsymbol{D}$	Fourth order tensor of elasticity
D	Ductility
d	Rolling distance

$d\varepsilon_r/dN$	Axial ratcheting strain rate (ratcheting strain rate in Chapters 5 & 6)
$(d\varepsilon_r/dN)_{max}$	Maximum ratcheting strain rate
$(d\varepsilon_r/dN)_{max,sta}$	Stabilised maximum ratcheting strain rate
$d\gamma_r/dN$	Shear ratcheting strain rate
δ	Elongation at the specimen fracture
E	Young's Modulus
$\boldsymbol{\varepsilon^e}$	Tensor of elastic strain
$\boldsymbol{\varepsilon^p}$	Tensor of plastic strain
$\dot{\boldsymbol{\varepsilon}}^{\boldsymbol{p}}$	Tensor of plastic strain rate
$\boldsymbol{\varepsilon^T}$	Tensor of total strain
ε	Axial strain
ε_a	Axial strain amplitude
ε_{eff}^p	Effective plastic strain
$(\varepsilon_{eff}^p)_{max}$	Maximum effective plastic strain
ε_{min}, ε_{max}	Minimum and maximum axial strains
ε_p	Axial plastic strain

ε_r	Axial ratcheting strain (ratcheting strain in Chapters 5 & 6)
$\varepsilon_{r,max}$	Maximum ratcheting strain
η	Ratio of lateral/vertical load
F_t	Tangential traction force
F_y	Von Mises yield function
F_2	Total dynamic vertical contact force
$F_{2,max}$	Maximum total dynamic vertical contact force
f	Friction coefficient
f_i	Critical surfaces for the dynamic recovery in the kinematic hardening rule
g	Gravity
γ	Shear strain
γ_m	Material parameter to control the evolution rate of isotropic deformation resistance
$\gamma_{min}, \gamma_{max}$	Minimum and maximum shear strains
γ_r	Shear ratcheting strain
H	Heaviside function

$\boldsymbol{I}$	Unit tensor
K	Ratio of major semi-width of the stick zone in the contact patch to major semi-width of the contact patch
L	Axle load
$\dot{\lambda}$	Rate of plastic multiplier
μ (μ_i)	Ratcheting parameter
N	Number of loading cycle
N_i	Crack (RCF) initiation life
ω	Angular velocity
$p(x,z)$	Normal contact pressure
$\dot{p}$	Effective plastic strain rate
Q	Isotropic deformation resistance
Q_{sa}	Saturated isotropic deformation resistance
Q_0	Initial isotropic deformation resistance
ν	Poisson's ratio
R	Reduction of area
ρ	Density

r_i	Material constants to describe the evolution of the backstress
$\boldsymbol{s}$	Tensor of deviatoric components of stress
$\boldsymbol{\sigma}$	Tensor of stress
σ	Axial stress
σ_a	Axial stress amplitude
σ_{eq}	Equivalent stress
σ_m	Axial mean stress
σ_{min}, σ_{max}	Minimum and maximum axial stresses
σ_{ult}	Ultimate tensile strength
$\sigma_{0.2}$	Yield strength
τ	Shear stress
$\tau_z(x,z)$	Longitudinal tangential traction
v	Translational speed
ξ	Normalised tangential traction coefficient
ζ_i	Material constants to describe the evolution of the backstress

X, Y, Z	Lateral, vertical, and longitudinal (rolling) directions

Chapter 1

Introduction

The thesis is to report the doctoral study on plastic deformation of flash butt rail welds in Australian heavy haul railway systems. In this chapter, a general introduction of this research study, which consists of the background and motivations, is presented. The main objectives of this research study are also provided and specified into multiple aims in accordance with different sub-studies. Finally, the structure of the thesis is presented.

1.1 Background & Motivations

Mining in Australia has been a primary industry and an essential contributor to the growth of the Australian economy. According to the recent report on resources and energy (BREE, 2020), the mining sector accounted for roughly 28% of Australian GDP growth in 2019. As one of the major producers of iron ore and coal within the globe, Australia has mainly exported these minerals to Asian countries, i.e. China, Japan, India and South Korea. In the financial year of 2018-19, the total exported volume of these mineral products was approximately 819 million tonnes of iron ore, 184 million tonnes of metallurgical coal and 210 million tonnes of thermal coal. In addition, it is predicted that the export volume of all these minerals will continue to increase as demonstrated in Fig. 1-1 even though the COVID-19 outbreak has slowed the global economic growth to some extent.

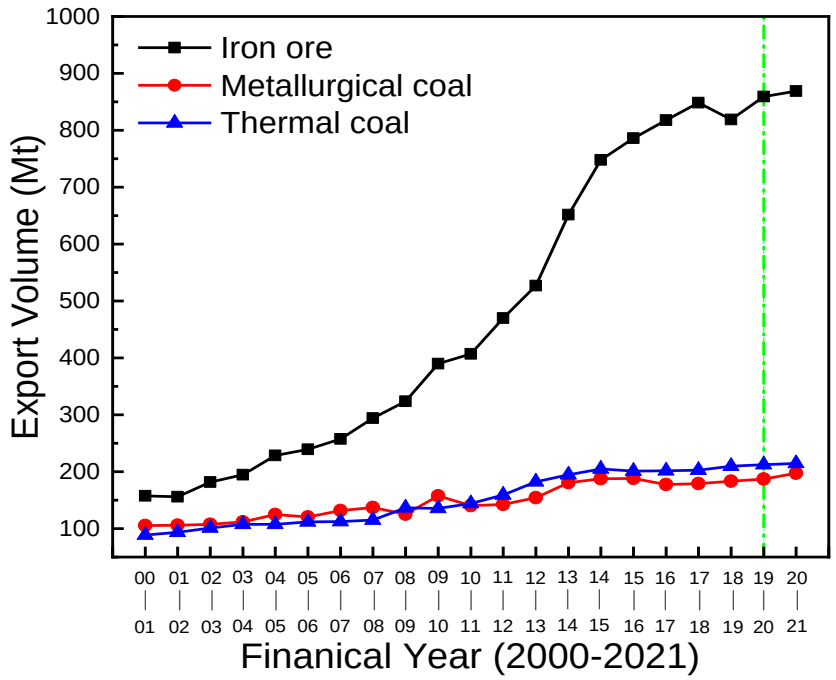

Figure 1-1: Export volume of major minerals between 2000 and 2021 in Australia (BREE, 2020).

In order to transport these mineral products from mines to ports efficiently, mining companies mainly rely on the freight transportation through heavy haul railway systems, and thus it is vital to guarantee the safety and reliability of the

railway network. However, the continuously demanding conditions imposed by a combination of higher axle loads, higher train speeds and increasing annual haulage rates, lead to more frequent occurrences of rail deterioration, which present a number of significant challenges in maintaining a safe heavy haul environment.

Since 1990s, premium high strength rail steels have gradually substituted traditional as-rolled ones applied in existing heavy haul railway systems. Such high strength rail steels with a hardness level of 400 HV and above, have effectively improved the overall rail performance and the reliability of railway operations by controlling or mitigating rail degradation such as wear and rolling contact fatigue (RCF). Additionally, the application of these steels can extend the interval of grinding maintenance as rail grinding is the common method to control the development of rail degradation (Marich, 2009). However, these benefits can be offset by the potential of localised degradation in rail welds, particularly in heat-affected zones (HAZ) that are generated by the uneven thermal input along the rail from welding and the shrinkage due to further cooling process. The increasing potential for damage in such welds is mainly caused by the inherent variability of microstructure and the induced difference in mechanical properties between HAZs and parent rails (PR). Although continuous welded rail segments have been widely used to provide more robust joints and more continuous running surface, the presence of HAZs that exhibit lower longitudinal hardness levels than PRs, is more likely to cause severe localised plastic deformation under high wheel–rail contact loads, and hence result in higher sensitivity to RCF. Generally, RCF is the dominant deterioration mode in the case of high strength rail steels used in heavy haul operations. Furthermore, RCF damage in HAZs may propagate to greater depths than that identified in PRs, and therefore is relatively more difficult to be cleaned-up by rail grinding. If such damage in HAZs is not attended at an early stage, it can gradually facilitate the development of transverse defects as shown in Fig. 1-2b, and increase the risk of complete rail failures when combined with higher dynamic loading which usually occurs at rail welds (Steenbergen & Van Bezooijen, 2009).

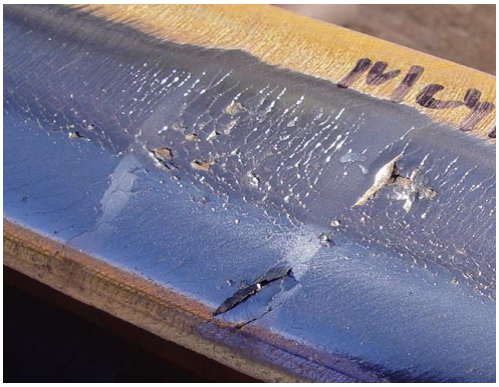

(a)

(b)

Figure 1-2: (a) Localised RCF damage and (b) transverse defect developed from RCF damage at a flash butt weld in a hypereutectoid rail (Wessels et al., 2015).

Aluminothermic welding (ATW) and flash butt welding (FBW) are two major welding techniques used in Australia as presented in Fig. 1-3. ATW is a cast welding method whereby two rail ends are bonded by the aluminothermic welded metal, while FBW is a resistance welding process that consists of preheating and forging (upsetting) at two rail ends (Skyttebol et al., 2005). Owing to the nature of both welding processes, the HAZs in aluminothermic welds are usually much wider than those in flash butt welds, resulting in increased sensitivity to localised RCF damage. To eliminate the concern with aluminothermic welds, the use of such welds has been limited by the increased application of flash butt welds in heavy haul operations. Nevertheless, various localised RCF damage, such as spalling (Fig. 1-2a) and squats, has been found in the HAZs of flash butt welds, particularly located at the gauge corner of high rails in curved tracks (Mutton et al., 2016). For the purpose of reducing the sensitivity to such damage and further improving the quality of rail flash butt welds, it is considered necessary to understand the mechanical response and

quantify the cyclic plasticity in such welds under practical wheel–rail contact situations.

(a)

(b)

Figure 1-3: (a) ATW (From "PANDROL", https://www.pandrol.com/product/aluminothermic-welding-kit/. Copyright by Henderson); (b) FBW (http://www.railsystem.net/flash-butt-welding/).

In wheel–rail interface, the rail is subjected to cyclic rolling and sliding conditions with higher contact stresses. It has been found that if the rail stress level exceeds the plastic shakedown limit, new plastic deformation will generate and accumulate in each loading cycle, which is known as plastic ratcheting mechanism (Fig. 1-4d). The increment of plastic deformation in one cycle may be very small, but it can accumulate to large values after many loading cycles (Kapoor, 1997). When the ratcheting strain reaches the limiting ductility of the rail material, rail degradation will initiate at the local material point. Such information indicates that ratcheting plays an essential role in causing RCF (Su & Clayton, 1997; Tyfour et al., 1996). Since the yield strength of steels is roughly three times of the corresponding Vickers hardness value (Pavlina & Van Tyne, 2008), the region with lower yield strength in HAZ will suffer more severe plastic deformation under the wheel–rail contact, which may increase the

potential of damage initiation in rail welds.

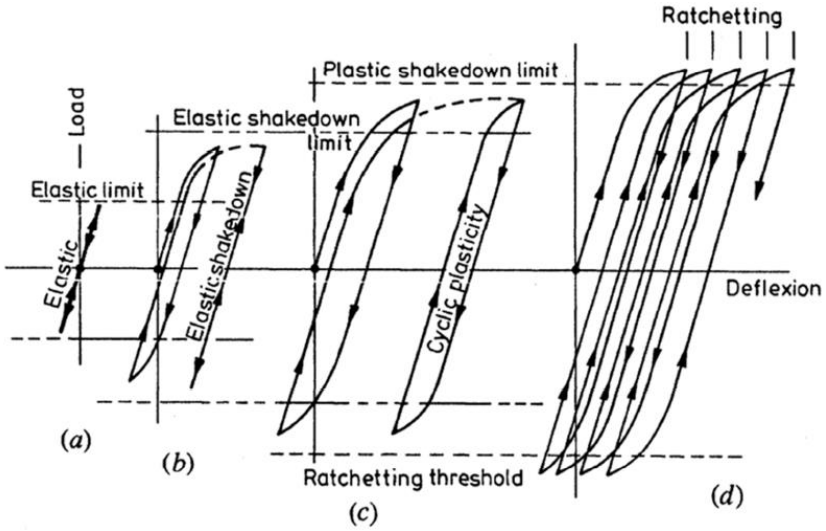

Figure 1-4: Mechanical response of a material subjected to cyclic loading: (a) elastic; (b) elastic shakedown; (c) plastic shakedown; (d) ratcheting (Kapoor & Johnson, 1994).

Fig. 1-5 shows an example of longitudinal hardness distribution measured at 5 mm below the top rail surface in a new low alloy heat-treated (LAHT) rail flash butt weld. A significant hardness decrease can be identified between approximately 6 mm to 30 mm from the welding centre line, also known as the bond line (BL), which can offset the overall strength of the welded joint. Additionally, yield strength is not the only material parameter affecting the ratcheting behaviour of rail materials. Work hardening behaviour, which varies with different materials, can also have significant influence on the evolution of ratcheting. So far, most of the studies on ratcheting behaviour have focused on PR or other types of steel which can be treated as homogeneous materials (further discussion is provided in Chapter 2.4), and no similar research has been conducted on rail welds to investigate the effect of the inhomogeneity present in each weld and the inconsistency among different welds in the same steel grade on the ratcheting behaviour.

With the widespread use of flash butt welds in high strength rail steels, it is essential to investigate the ratcheting behaviour of such welds under in-service heavy haul loading conditions. The outcomes should provide valuable information about understanding the cyclic deformation behaviour of these

welds and evaluate their ratcheting performance in terms of RCF initiation life. Furthermore, cost-effective rail maintenance strategies can be potentially developed for the purposes of fulfilling the demanding conditions and maintaining a safe heavy haul environment simultaneously.

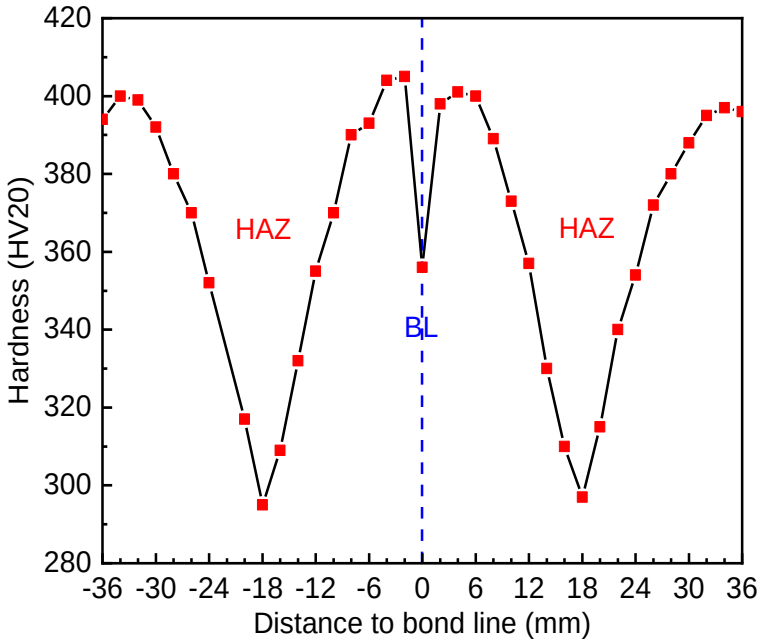

Figure 1-5: Longitudinal hardness distribution at 5 mm below the top rail surface in a new LAHT rail flash butt weld.

1.2 Research Aims

The main aim of this doctoral research is to systematically investigate the ratcheting behaviour of flash butt welds in high strength rail steels which are currently used in Australian heavy haul railway systems. The materials considered in the present study are new flash butt welds in R400HT (hypereutectoid heat-treated steel grade with a minimum head hardness of 400 HV) rail steel grade with a carbon content of 0.88%. To achieve the main aim, this research on such welds has three major objectives:

(a) To investigate the ratcheting behaviour by undertaking experimental studies which consists of monotonic tensile tests and cyclic loading tests.

(b) To establish a cyclic plasticity constitutive model which can describe the ratcheting behaviour with reasonable accuracy.

(c) To quantify the ratcheting performance in terms of RCF initiation life in the rail head under practical heavy haul loading conditions by utilising finite element simulations.

For each major objective, several specific aims are listed as follows:

For objective (a):

- To obtain basic material parameters, i.e. Young's Modulus, yield strength, ultimate tensile strength, and ductility, of the rail weld from monotonic tensile tests.

- To compare with the basic material parameters of parent rail obtained from a monotonic tensile test.

- To design the appropriate stress level to be used in the uniaxial and biaxial stress-controlled cyclic loading tests in accordance with the experimental results from monotonic tensile tests.

- To investigate the ratcheting behaviour under asymmetrical uniaxial stress-controlled cyclic loading tests.

- To investigate the ratcheting behaviour under non-proportional biaxial compression-torsion stress-controlled cyclic loading tests.

- To compare with the ratcheting behaviour of parent rail under similar uniaxial and biaxial stress-controlled cyclic loading tests.

- To investigate the influence of microstructure on the ratcheting behaviour by metallographic analysis on the weld specimens before

and after the cyclic loading tests.

For objective (b):

- To calibrate the material parameters required for the cyclic plasticity constitutive model of weld region and parent rail based on the experimental results.

- To establish the cyclic plasticity constitutive model that can describe the deformation characteristics and the ratcheting behaviour simultaneously based on the previously developed constitutive model for high strength rail steels.

- To verify the updated cyclic plasticity constitutive model by comparing the simulated results with the corresponding experimental data.

For objective (c):

- To develop a three-dimensional finite element model with the application of the established cyclic plasticity constitutive model to simulate the practical wheel–rail weld cyclic rolling contact conditions in heavy haul operations.

- To evaluate the ratcheting performance in terms of RCF initiation life based on the ratcheting strain rates and the ductility.

- To compare with the ratcheting performance of parent rail.

1.3 Structure of the Thesis

The thesis is to report the doctoral research on investigating the ratcheting behaviour of new flash butt welds in R400HT high strength rail steel grade which is currently used in Australian heavy haul railway systems. The structure

of this thesis is demonstrated as follows:

In Chapter 1, a brief introduction of this research is provided, including the background information, research motivations and research aims.

Chapter 2 gives a comprehensive review of relevant literature related to this study. Basic knowledge of rail flash butt welds is firstly introduced. After that, the common theories and methods to analyse wheel–rail contact problems are reviewed, followed by a brief overview of rail materials and associated degradation, typically wear and RCF. The investigation on ratcheting behaviour of materials and the development of constitutive cyclic plasticity material models are also presented. Finally, selected literature regarding the simulations on wheel–rail weld rolling contact are reviewed.

Chapter 3 reports the experimental results on the ratcheting behaviour of new rail flash butt welds in R400HT rail steel grade. The basic mechanical properties of these welds are obtained from the monotonic tensile tests while the ratcheting behaviour are investigated under the uniaxial and bi-axial compression–torsion stress-controlled cyclic loading tests. These results are also compared with those obtained from the similar tests on R400HT PR. Additionally, metallographic analysis was conducted on the original specimens and the specimens after the cyclic loading tests. Based on these results, the influence of microstructure characteristics on the ratcheting behaviour of both weld region and PR is demonstrated.

Chapter 4 presents the established cyclic plasticity constitutive model which can describe the ratcheting behaviour of new R400HT rail flash butt welds and PR based on the previously developed constitutive model for high strength rail steels. The approach to calibrate the material parameters from the experimental study for the cyclic plasticity constitutive model is proposed, and then the model is verified by comparing the simulated results with the corresponding experimental data.

Chapter 5 reports the evaluation of the ratcheting performance of new R400HT

rail flash butt welds under an actual heavy haul loading condition by performing three-dimensional (3D) finite element (FE) wheel–rail weld cyclic loading simulations with the application of the developed cyclic plasticity constitutive model. The ratcheting performance is evaluated in terms of the RCF initiation life which is estimated based on the stabilised ratcheting strain rate and the ductility of the rail materials. The influence of weld region on the ratcheting performance of PR is also investigated. Furthermore, the most possible location of RCF initiation in both weld region and PR is identified based on the ratcheting results.

Chapter 6 reports the numerical study on the ratcheting performance of three high strength rail steels (LAHT and two types of HE with different carbon content) in curved tracks under different heavy haul loading conditions, which is an additional work during the doctoral research. The RCF initiation life of each steel grade in high rails under different in-service loading cases is also predicted based on the corresponding stabilised ratcheting strain rate and the ductility of these rail steels. This study is also the extension of work from Pun et al. (2015), which investigated the ratcheting performance of the same steel grades in tangent tracks under heavy haul operations.

Summaries and conclusions of the significant research outcomes are provided in Chapter 7. The recommendations for future research work on rail welds are also given.

Chapter 2

Literature Review

In this chapter, a comprehensive review of relevant literature related to this doctoral study is provided. Basic knowledge of rail flash butt welds is firstly introduced. After that, the common theories and methods to analyse wheel–rail contact problems are reviewed, followed by a brief overview of rail materials and associated degradation, typically wear and rolling contact fatigue. The investigation on ratcheting behaviour of materials and the development of constitutive cyclic plasticity material models are also presented. Finally, selected literature regarding the simulations on wheel–rail weld rolling contact are reviewed.

2.1 Flash Butt Welding

2.1.1 What is Flash Butt Welding?

FBW, as a continuous welding method, has widely replaced traditional fish-bolted rail joints that produce the discontinuity of track running surface. Such discontinuity can cause high dynamic impact loads on wheel–rail interface, and this leads to great stresses on ballast and subgrade, which can ultimately accelerate rail failure. The introduction of FBW has vastly improved the smoothness of running surface and consequently the geometric stability of track structures (Zaayman, 2007). Generally, there are two types of FBW: stationary (or fixed plant) FBW and mobile FBW. Stationary welding is mainly used in large welding plants for joining short rail segments to long ones. Furthermore, components for switch construction can be welded. With the help of mobile welding, continuous welded rail segments can be directly produced in-track. Mobile welding is also often used for welding rails in heavy haul operations.

In Fig. 2-1, the entire process of FBW and a typical recorded thermal cycle are illustrated. At first, two rail ends are rapidly heated by the current flow and the free rail end is moved forward at a low speed. When two rail ends contact each other, flashing or arcing will occur across the interface by the resistance heating with high amperage and low voltage. The flashing process involves several main stages: (i) flashing even to ensure contact over the full rail cross-section; (ii) preheating; (iii) final flashing. Flashing during preheating can be either continuous or pulsed/interrupted, depending on the type of welding machine and how it is configured. The rail end is oxidised during flashing, so prior to upset the flashing rate is increased to ensure that the end surfaces are sufficiently free of oxide to form a sound bond. Finally, both rail ends are pushed and compressed together under a high pressure to expel all impurities, which is known as upsetting (Fujii, 2015). After the welding, a hydraulic shearing device is used to remove the welding upset followed by surface grinding in order to obtain a good geometry (Saita et al., 2013). Finally, cooling should be controlled to avoid the formation of martensite based on the Fe-C TTT diagram, particularly for special alloy and head-hardened rail steels while for steels with

lower hardenability, increased (forced air) cooling of the head region may be necessary to ensure that the hardness in the re-austenitised region matches as closely as possible the hardness of the PR (Steenbergen & Van Bezooijen, 2009). In many cases of flash butt welds, post-weld heat treatment (PWHT) is performed to obtain required mechanical properties and alleviate the residual stress level.

Generally, the strength of the welded joint is almost the same as or even exceeds that of the PR. Unlike ATW, FBW does not require any additional material, and hence, the produced rail weld is almost flawless (i.e. negligible fusion defects). Additionally, flash butt welds have a better fatigue resistance than aluminothermic welds (Wimmer et al., 2002), and hence the use of aluminothermic welds has been limited in many railway systems. According to the Australian standard (AS1085.20, 2020), there are several tests to assess the quality of welds, such as hardness measurements, slow bend tests and fatigue tests.

2.1.2 'Discontinuities'

The presence of welds induces three major 'discontinuities' along the longitudinal direction of the rail owing to the nature of FBW process. Specifically, they are geometry irregularities, material inhomogeneities and residual stress, which lead rail flash butt welds to be more susceptible to damage compare with PRs.

The geometry irregularity can be caused by multiple factors, including mismatch of rail end positioning, unstraightened rail ends, poor grinding of the rail surface and inhomogeneous material shrinkage after cooling combined with early grinding. The geometry irregularity can affect the smoothness of running surface at welds, consequently giving rise to high dynamic loads in the wheel–rail interface. Generally, the length of such irregularity is less than 1 m (Steenbergen & Van Bezooijen, 2009).

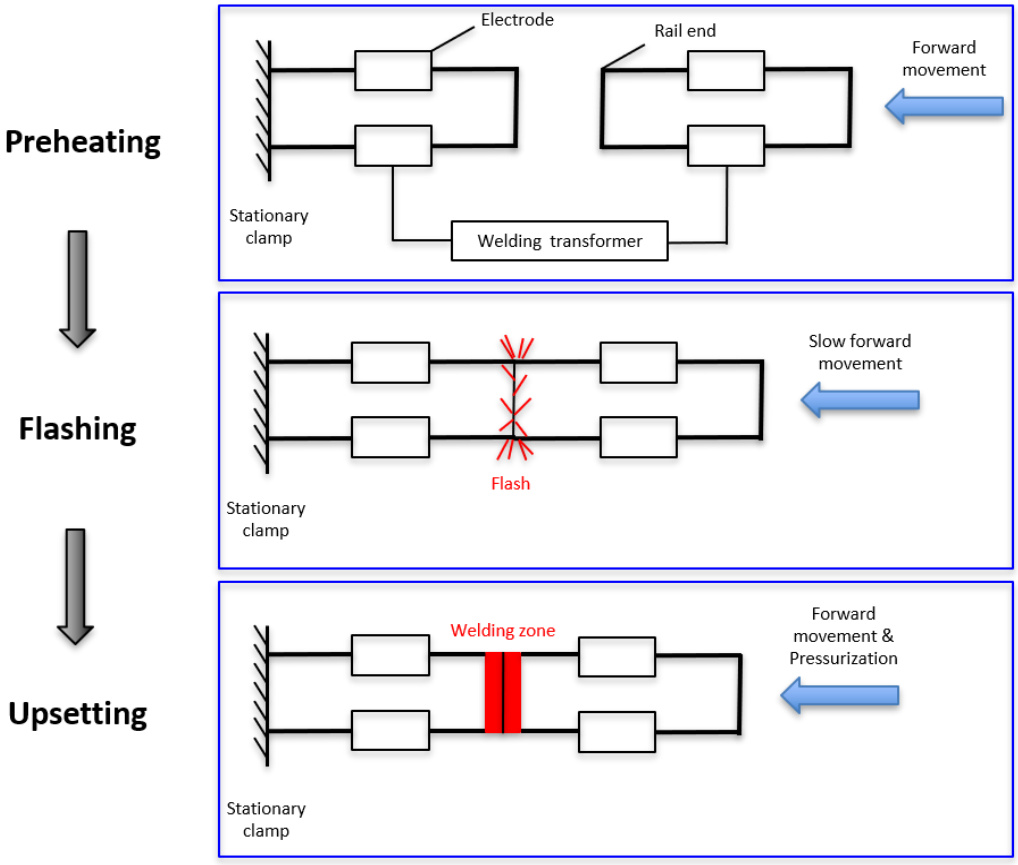

(a)

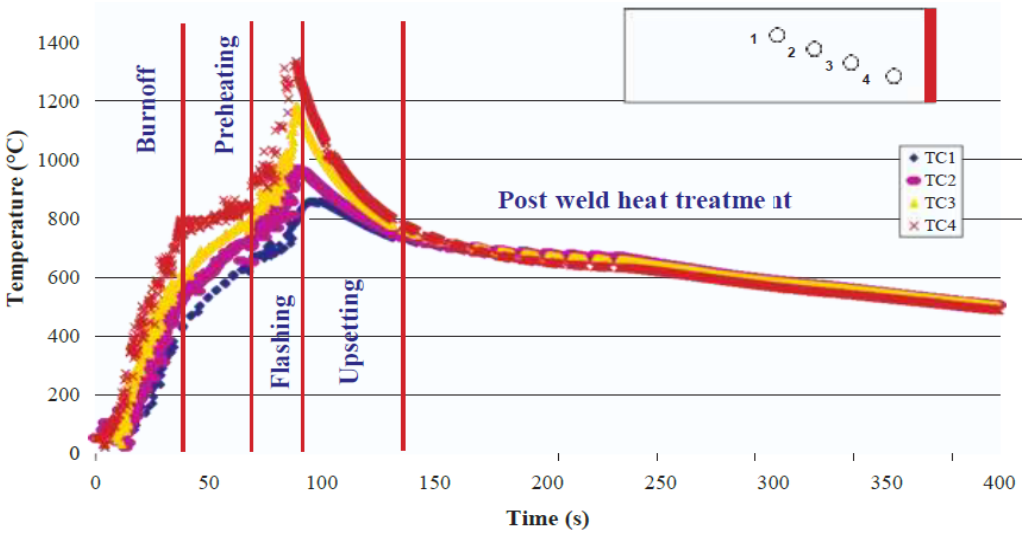

(b)

Figure 2-1: (a) FBW process (Wöhnhart & Wenty, 2002); (b) A recorded thermal cycle during FBW (Demofonti et al., 2007).

Due to the uneven thermal input from preheating and welding along the longitudinal direction of rail segments, the induced variabilities of

microstructure and mechanical properties between softened HAZ and PR represent another 'discontinuity' adjacent to the welded joint. A number of works have been carried out to investigate such 'discontinuity'. Mansouri & Monshi (2004) described the structural variations from the FBW of a pearlitic rail. From the location of BL to the end of HAZ along the longitudinal direction of the rail weld, the microstructure consisted of grain growth region, recrystallised region with fine grain and partially transformed region. Similar microstructures were observed by Micenko & Li (2013) and Porcaro et al. (2019), and both studies reported that the hardness and corresponding yield strength decreased at the grain refined and partially transformed regions due to the partial Fe_3C spheroidisation. Xi et al. (2016) also reported the similar microstructure from a flash butt weld in high strength wheel steel and the strength of the welded joint was slightly higher than that of the base metal.

Mutton et al. (2016) examined the microstructure of new and ex-service flash butt welds in hypereutectoid rail steels. The authors classified the microstructure in HAZ with more detailed illustrations: a region adjacent to the BL line where almost no grain boundary Fe_3C existed, a region that grain boundaries were concentrated by continuous cementite network, a region with the co-existence of grain boundary Fe_3C and spheroidised microstructure, and a fully spheroidised region. From the longitudinal hardness distribution of a new rail flash butt weld and typical SEM images captured at different locations to the BL as presented in Fig. 2-2, the microstructure changed from re-austenitised region (finer pearlite) to spheroidised region and finally returned to fine pearlite (PR). The longitudinal hardness decreased rapidly from the start of HAZ to the fully spheroidised region and reached to a minimum at the position that the carbide was extensively spheroidised. Such phenomenon revealed that a narrower transition from re-austenitised region to fully spheroidised region was expected to minimise the formation of grain boundary Fe_3C and therefore the region with steep hardness reduction. However, no strong relation could be established between grain boundary carbides and crack initiation at surface. It was also difficult to establish if such carbide contributed to crack propagation. The main reason for the crack initiation and propagation was more likely the incremental plastic flow (ratcheting) associated with the lower yield strength in

the softened region of HAZ.

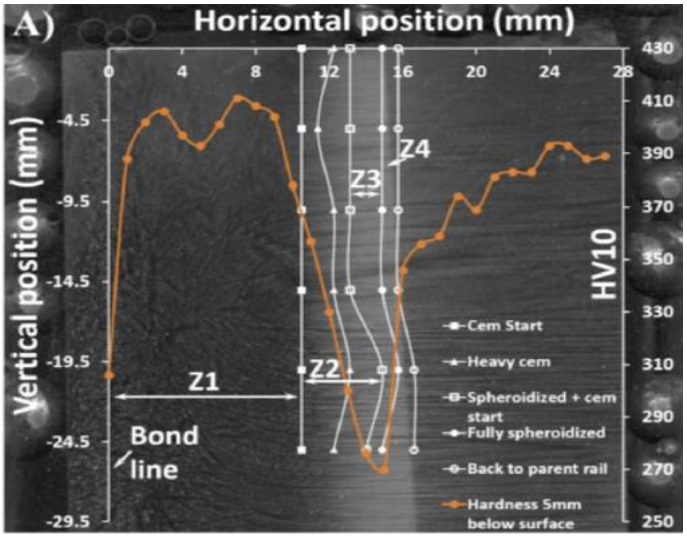

(a) longitudinal hardness distribution.

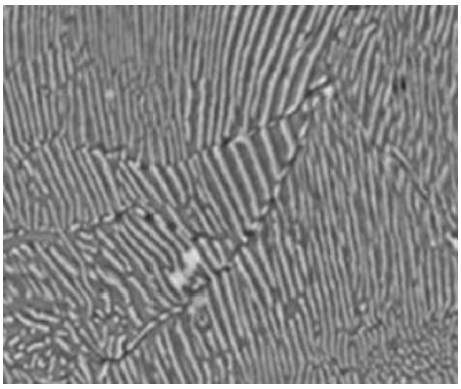

(b) re-austenitised region, 5 mm to BL.

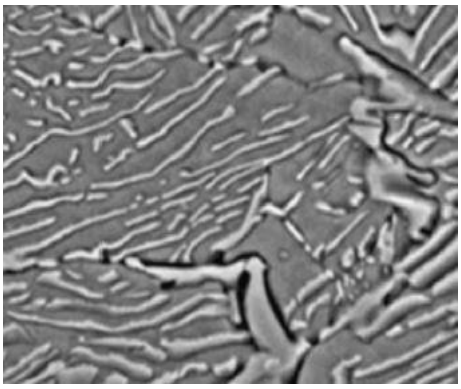

(c) partially-spheroidised region, 7 mm to BL.

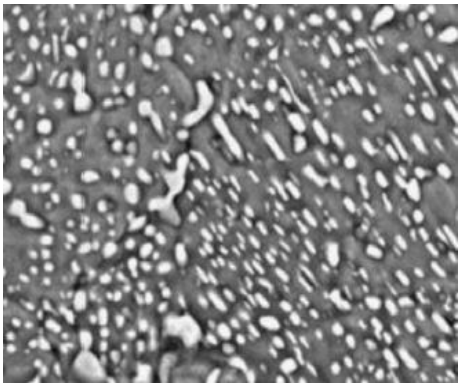

(d) spheroidised region, 12 mm to BL.

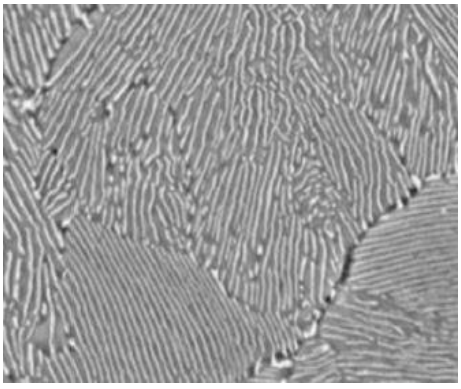

(e) PR, 20 mm to BL.

Figure 2-2: The longitudinal hardness distribution of a new rail flash butt weld and typical SEM images captured at different locations to the BL (Mutton et al. 2016).

Based on the literature review above, HAZs are caused by the spheroidisation of pearlite into conglomerates of Fe_3C as the Fe_3C tends to form a more stable

configuration which is driven by the reduction of grain boundary Fe_3C (smaller surface area of spheres than that of lamellae). Such diffusion creates greater area of pure ferrite, which is soft and weak. In other words, the temperature in HAZs is not high enough for re-austenitisation and the spheroidisation of pearlite forms more continuous soft ferrite phase, which limits the hardness and strength of welds (Gutscher et al., 2014). As the extent of spheroidisation depends on the carbon diffusion, the pearlitic microstructure with larger interlamellar spacing and lamellar thickness usually has a slower spheroidisation rate. Furthermore, the kinetics of spheroidisation can be inhibited by the presence of elements such as Cr, Si and Mo (Parker, 2002).

Another significant discontinuity at welds is the residual stress that is unavoidable in the welding process. Residual stress plays an important role in the service life of welds as it may facilitate the growth of fatigue damage in welds when combined with the higher dynamic loading in wheel–rail interface. During the FBW process, the current density that passes through the web cross-section surface and therefore the heat generated in the web region are higher than those in the head and foot regions since the web has a higher ratio of cross-section area to volume. Consequently, the amount of contraction that occurs in the web is higher during the cooling process, which leads that high tensile residual stress develops in the web, while the base and head regions exhibit compressive residual stress (Mansouri & Monshi, 2004).

A number of studies have been carried out to measure the residual stress distribution in rail welds by experimental and numerical methods. Tawfik et al. (2006) utilised the neutron diffraction technique to measure the residual stress across an AS60 rail flash butt weld from a mobile welder with the normal cooling operation. As illustrated in Fig. 2-3, tensile residual stresses in the longitudinal and vertical directions were mainly concentrated in the mid web of the weld, while the head and foot mainly exhibited compressive longitudinal stress. Transverse residual stress along the weld was close to zero. Similar findings were also reported by Yan et al. (2011), which measured the residual stress in a U71Mn rail flash butt weld from a stationary welder. Tawfik et al. (2005 & 2008) suggested that the tensile residual stress can be alleviated by

localised rapid PWHT without affecting the microstructural characteristics. Deng et al. (2013) clarified that phase transformation induced plasticity can affect the residual stress by simulating the welding process of a low temperature transformation steel by an in-house FE programme. Ma et al. (2015) applied the hole-drilling method to measure the residual stress in a U71Mn rail flash butt weld. Meanwhile, an in-house FE programme was developed to simulate the welding process. The results showed that solid-state transformation can affect the residual stress distribution, particularly in the HAZ and re-austenitised zone in which steep stress gradients were found. Such phenomenon revealed that the hole-drilling method might not be suitable for the residual stress measurement due to its low resolution.

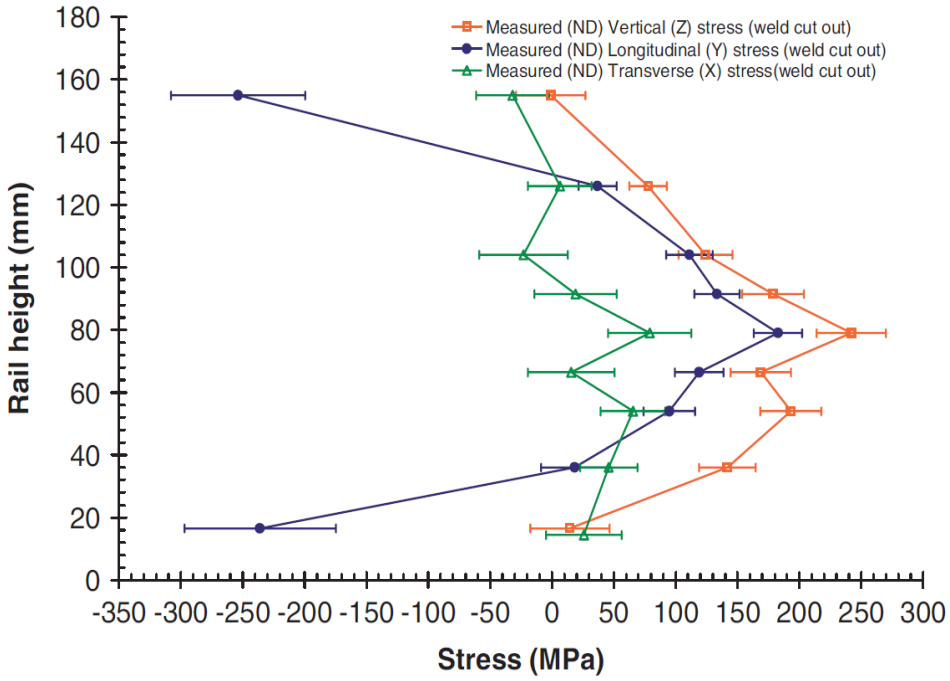

Figure 2-3: Vertical (Z), longitudinal (Y) and transverse (X) residual stress distributions along the BL of an AS60 rail flash butt weld (Tawfik et al. 2006).

2.1.3 Damage at Rail Flash Butt Welds

Generally, rail flash butt welds are more susceptible to damage, such as squats and corrugation, compared with PRs due to two main reasons (Li et al., 2006). The first reason is the presence of material inhomogeneities along the longitudinal direction of welds, which consist of non-constant longitudinal

hardness distribution and various microstructural characteristics. The other reason is that the presence of welds represents a geometrical irregularity along the longitudinal direction of the rail, resulting in higher dynamic loads at the wheel–rail interface. This can increase both normal and tangential stresses in the rail when combined with residual stress. It is worth noted that both mechanisms interact with each other and accelerate the propagation of existing damage (Steenbergen & Van Bezooijen, 2009).

The most common damage mode in rail flash butt welds is RCF, which will initiate when the accumulated plastic deformation (ratcheting) caused by high repeated normal and tangential stresses reaches the ductility of local material with lower yield strength in HAZ as mentioned in Chapter 1.1. RCF can be presented in different forms, depending on the location of initiation. If RCF initiates at or very close to the rail surface, squats and head checks as shown in Fig. 2-4, are more likely to occur at top running surface and high rail gauge corner (also called gauge corner checking), respectively. Due to the softer microstructure in HAZ, such RCF cracks will grow deeper as the service continues. Squats usually occur randomly, but multiple squats within the length of several sleeper spans are usually associated with rail corrugation and should be treated with more care (Li, 2009). A recent work by Deng et al. (2019) hypothesised the formation process of squats at welds based on a five-year field observation. Initially, a roughly V-shaped surface irregularity appears in HAZ at each side due to varied surface deformation across the HAZ under cyclic loading. Then such a V-shaped irregularity excites a high dynamic contact force which further enhances the difference in surface deformation so that the V-shaped irregularity develops into a W-shaped pattern. The continuous development of the W-shaped pattern increases the dynamic force and the resulting deformation at the same location, leading to a positive-feedback growth loop of the irregularities and eventually the formation of typical squats.

Spalling is a specific result of surface cracking, which initiates at the trailing side of the spheroidised regions and propagates inwardly at a shallow angle, leading to a small section spalling away (dipped weld). With the increase in the service period, other RCF cracks will join the existing spalled region and

enlarge the dip (Mutton et al., 2016). Fig. 2-5 explains the propagation of surface cracking mentioned above in flash butt welds. The subsurface-initiated RCF is known as shelling (Fig. 2-6) and such damage will be eventually progressed to the surface, resulting in material breaking out of the rail head. If the damage forementioned originates at the gauge corner and is not addressed early, it will increase the possibility of transverse crack development under cyclic loading condition as presented in Fig. 1-2b, and consequently, this may lead to a broken rail and increase the potential of derailment (IHHA, 2015). Therefore, routine rail grinding is conducted frequently to ensure track safety.

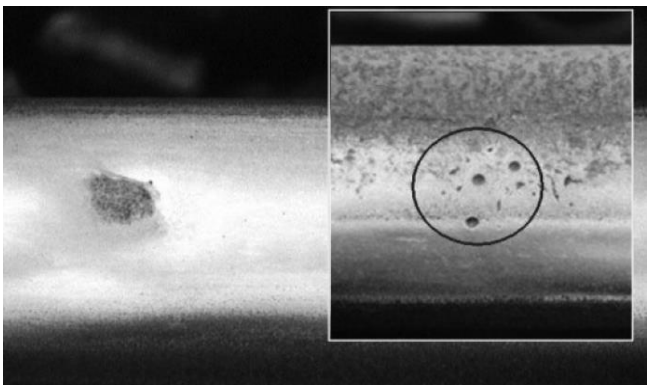

(a)

(b)

Figure 2-4: Surface-initiated RCF damage: (a) squats (IHHA, 2015); (b) head checks at gauge corner (Mutton et al., 2015).

Rail corrugation, so-called “wavelength-fixing mechanism”, is also due to the gross plastic flow as a consequence of excessive contact stresses induced by the high dynamic force from the unsprung mass of vehicles bouncing on the track support with loaded stiffness, particularly in heavy haul operations (Grassie, 2009b). Such a phenomenon is exacerbated by discrete irregularities, such as

the geometry irregularities after welding mentioned in Chapter 2.1.2, dipped welds and surface defects due to RCF. In addition, previous work found the linear relationship between the maximum dynamic wheel–rail contact force and the train speed with the consideration of rail weld geometry irregularity (Steenbergen, 2006 & 2008). According to this, rail corrugation will become more severe in the lines operating with higher axle loads and train speed.

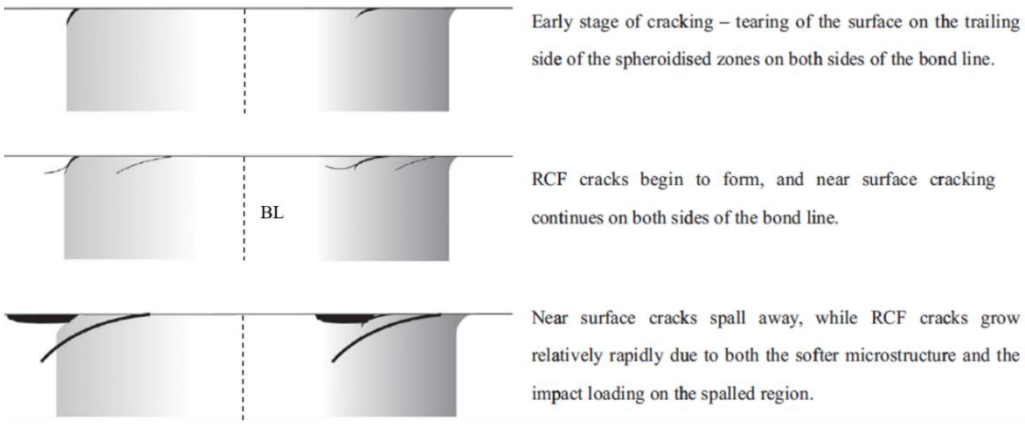

Figure 2-5: Schematic of the surface crack propagation (Mutton et al. 2016).

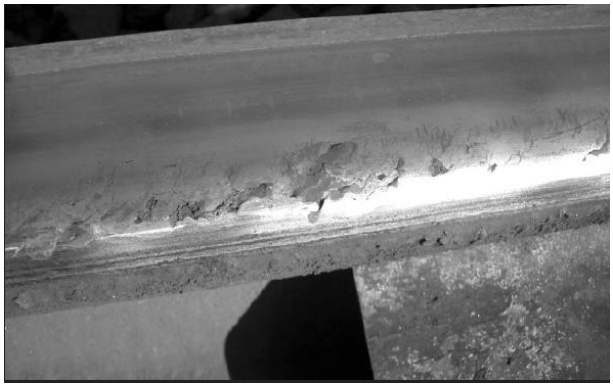

Figure 2-6: Subsurface-initiated RCF damage: shelling (IHHA, 2015).

Another predominant failure mode in rail flash butt welds under heavy haul conditions is the horizontal split web (HSW) (Fig. 2-7), which originates from the fatigue cracks with a relatively small size in the web region due to a combination of tensile residual stress from welding and cyclic bending stresses (Mutton & Jeffs, 1992, Beretta et al., 2005, Mutton et al., 2011 & Ozakgul et al., 2015). Godefroid et al. (2015) investigated the failure mechanism of the web region in a hypereutectoid rail flash butt weld used in Brazilian railways. Firstly, fatigue cracks initiated and grew steadily in the internal parts of web, where

multiple stress concentrators were observed. Secondly, such fatigue cracks gradually reached a critical size and the rest of section was unable to support more repeated loading. Finally, the cracks grew unstably until the occurrence of catastrophic failure. Furthermore, detection of these small cracks prior to the unstable growth by routine ultrasonic inspection is difficult and therefore, the most effective way is to prevent such cracks from initiating.

Figure 2-7: HSW failure (Mutton et al., 2011).

2.1.4 Strategies on Improving the Quality of Flash Butt Welds

It has been found that regardless of the extent of property variation within the HAZs, the long-term rail degradation can be minimised by limiting the length over which the variation occurs (Sichani & Bezin, 2018). Since most of the damage identified at rail flash butt welds is linked with the softened region in HAZ, particularly RCF, minimising the influence of HAZ and therefore improving the quality of rail weld have become an attractive research field in recent years. Minimising the width of HAZ by optimising the conventional FBW conditions is considered as one of the effective methods. Although the width of HAZ width was not minimised in some studies and no specific relationship has been established between the width of HAZ and the quality of weld, the overall mechanical properties and therefore the reliability of welds were still enhanced to some extent.

Saita et al. (2017) successfully reduced the width of HAZ in Japanese standard rail flash butt welds by increasing the flashing velocity and distance. Ichiyama

et al. (2006) mentioned that large amount of flash may increase the chance of defects at welds, but special upsetting conditions can remove the oxides formed during the flashing process and the inclusions. Yu et al. (2015) investigated the fatigue fracture mechanism of a U71Mn rail flash butt weld in Chinese railways and recommended that optimising upsetting parameters should be considered to ensure the welding quality. Zhao et al. (2015) conducted the similar work on U75V rail flash butt welds and concluded that the fatigue performance of the weld can be improved by increasing the upset pressure, which allows the oxides to be squeezed out during the upsetting process. Other work also highlighted that a suitable combination of flashing and upsetting parameters can improve the mechanical properties of flash butt welds, even though they focused on traditional steels instead of ones for railways (Çetinkaya et al., 2006, Lu et al., 2017 & Ziemian et al., 2012).

As illustrated in Chapter 2.1.2, the softened region in HAZ is due to the reconfiguration of Fe_3C from the perspective of microstructure. In another word, the width of HAZ can be shortened if the migration of carbon can be minimised. Demofonti et al. (2007) increased the hardness of European rail flash butt welds by reducing the heat input, especially during the preheating, and cooling rapidly. Kuchuk-Yatsenko et al. (2016) applied the pulsating welding technique on R260 and R350HT rail steels to reduce the energy input and obtained the corresponding welds with finer microstructure. Similarly, previous work on traditional steels successfully improved the weld quality by controlling the thermal input and increasing the cooling rate (Kuroda et al., 2006 & Xi et al., 2016). Additionally, Zhang et al. (2017) applied such strategies to U20Mn bainitic rail flash butt welds.

Besides optimisation of the FBW parameters, there are other approaches to enhance the quality of welds. As outlined in Chapters 2.1.2 and 2.1.3, residual stress may cause the fatigue damage at welds. Therefore, PWHT has been widely utilised after welding to minimise the effect of residual stress and further to improve the resistance to fatigue damage, particularly HSW (Demofonti et al., 2007, Saita et al., 2017 & Tawfik et al., 2008). Fan et al. (2016) used ultrasonic peening treatment, which is an effective method of surface treatment

by a severe plastic deformation process, to extend the fatigue of U75V flash butt welds. To avoid premature failure of flash butt welds in Fortescue mainline, Australia, phased array ultrasonic testing was applied to detect relatively smaller defects (Eddy et al., 2015). This method can also be used to monitor the width of HAZs of finished welds and further to identify a decline in the welder performance (Cookson & Mutton, 2016). Addition of alloying elements (Cr, Mn, Si, etc.) can limit the formation of spheroidised microstructure. However, these elements may affect the weldability by FBW and some steel grades have been found to be more problematic in this regard than others (Eddy et al., 2015).

2.1.5 Summary

Basic knowledge of rail flash butt welds has been introduced, including manufacturing process, variability in material characteristics and associated RCF damage. To summarise, the presence of these welds has increased the sensitivity to localised RCF damage and significantly affected the performance of rails. Whilst some applicable and useful strategies, i.e. shortening the widths of HAZs by optimising the welding parameters, have been implemented to improve the quality of rail flash butt welds, further investigations are still required to gain a betting understanding of RCF at these welds and develop more effective strategies for enhancing the resistance to such damage.

2.2 Basic of Wheel–rail Interface

2.2.1 Introduction

For successful railway transportations, good performance of the wheel–rail interface plays the most important role and therefore, research on wheel–rail contact has been carried out for decades. The major phenomena treated are contact stresses, friction and deterioration mechanisms which are related to cost, energy consumption, maintenance, safety and environment. The wheel–rail interface is extremely complex since it is a part of the whole train-track system, which means that reliable work in this field should be conducted on a system level (Lundén & Paulsson, 2009).

When a wheel is rolling on a rail, the contact mechanism depends on many factors such as axle load, material properties, creepages, train speed, wheel/rail profiles, track curvature and track foundation (Vo et al., 2014). Thus, analysis on wheel–rail interface is very complex and challenging. Generally, wheel–rail interface research can be classified into two main fields: contact mechanics or tribology and vehicle dynamics (Busquet et al., 2006). The major aim of both fields is to investigate the wheel–rail contact behaviour, which can be further applied to analyse the mechanical response and deterioration of wheel/rail materials. In the past few decades, multiple analytical models and numerical solutions were developed, and laid the foundation for simulating the practical wheel–rail cyclic rolling contact conditions. The following content in this sub-chapter briefly introduces these existing methods and their applications for the wheel–rail weld simulations will be reviewed in Chapter 2.5.

2.2.2 Analytical Models

The main goal of developing the analytical models for contact problems is to calculate the magnitude of stresses and deformation at the contact interface and in the interior of bodies. The size and shape of the contact patch may also be of interest (Iwnicki et al., 2009). Therefore, these analytical models constitute the basic theories of contact mechanisms.

The classic theory of contact was developed by Hertz (1882) and has been widely used to solve many contact problems even today. Hertz Contact Theory (HCT) proved that the contact patch would be elliptical when two non-conformal bodies are pressed together. It also established an analytical solution of normal contact pressure distribution and the size of the contact patch. To further determine the stresses and deformation, the contact theory developed by Johnson (1985) can be applied. HCT is strictly restricted to smooth contact surface, linear elastic materials, frictionless condition, half-space assumption and small displacement. However, it can still provide reasonable results for most contact problems that can satisfy these restrictions. This can be highlighted by

Yan & Fischer (2000) which compared the results from FE simulations with the analytical solutions from HCT for elastic wheel–rail contact problems.

The limitations employed in HCT can cause discrepancies in the contact pressure between the analytical solutions and actual situations, i.e. considering the plastic deformation (Chen, 2003; Yan & Fischer, 2000). In addition, HCT may not be applied to the contact problems for the bodies violating the half-space assumption, i.e. the radius of wheel/rail profile is changing sharply or is small compared with the size of contact patch, resulting a non-elliptical contact shape. This usually happens at the contact between the wheel flange and rail head or the wheel and rail gauge corner. Telliskivi & Olofsson (2004) found significant deviations in contact patch and maximum contact stress when studied the wheel flange–rail gauge corner contact. An alternative method is to split the contact patch into multiple strips with Hertz contact being calculated for each strip, so-called Multi-Hertzian method, which was first used by Pascal & Sauvage (1991). Other methods based on the concept of virtual penetration which is simply neglecting the calculation of surface deformation, such as Ayasse & Chollet (2005), Knothe & Le The (1984), Kik & Piotrowski (1996) and Linder (1997), provided semi-elliptical normal pressure solutions when the geometry of contact bodies may not rigorously satisfy the assumption of HCT.

The start of the research on rolling contact was carried out by Carter (1926), which estimated the tangential traction based on the HCT for the case of contact between a cylinder and a plane when the creepage (stick and slip zones) of the contact was confirmed. However, the main limitation of Carter's theory is that it is only suitable for mono-dimensional (rolling or longitudinal direction) problems and unable to capture the tangential traction in practical wheel–rail rolling contact conditions. Due to this restriction, Johnson (1958a & 1958b) and Vermeulen & Johnson (1964) expanded Carter's theory to 3D rolling contact with the consideration of longitudinal creepage (relative velocity of wheel and rail divided by the velocity of vehicle), lateral creepage (function of the angle of attack (AOA)) and spin (function of contact angle and yaw velocity). Haines & Ollerton (1963) divided the contact area into multiple strips to obtain more accurate tangential traction for the case of pure longitudinal creepage, so-called

the strip theory. This theory was extended to its application to a more general case by Kalker (1967), but it is much less accurate for the problems of circular contact, contact patches elongated in the rolling direction and high spin. In the early 1970s, the more sophisticated line contact theory was developed by Kalker (1972). Years later, Kalker (1979a) proposed a linear relationship between creepages and creep forces based on the strip theory. However, this linear theory is limited to small creepages as well as the difference in contact shape.

A complete theory of rolling contact for elastic bodies under the half-space assumption was developed to solve the general contact problems with the consideration of all creepages and spin for contact bodies with arbitrary profiles (Kalker, 1979b). After that, this theory was implemented into a code called CONTACT (Kalker, 1990), but its computational cost was very high. Therefore, a simplified theory (Kalker, 1982) was further published based on the assumption that the deformation at each point on the contact surface is the linear function of only the corresponding stress at that point and the application of Kalker's linear theory. According to the simplified theory, the FASTSIM algorithm was developed and it is widely used in multi-body dynamics simulation (MBDS) package today, even though Kalker (2001) later mentioned that the error margins of tangential traction from FASTSIM is within 5-20%. All these theories developed by Kalker was also named as Kalker theory (Kalker, 1990). Polach (1999) proposed a simplified version of FASTSIM, which is faster than FASTSIM but neglects the moment effects of creepages.

The simplified theory by Kalker is very popular since the non-Hertzian methods based on virtual penetration, which are mentioned previously, also used this theory (with some modifications of parameters) to calculate the tangential traction (Piotrowski & Chollet, 2005; Piotrowski & Kik, 2008). Furthermore, Spiryagin et al. (2013) introduced a slip-velocity-dependent friction coefficient in FASTSIM to calculate the creep forces under large creepages. Sichani et al. (2016) combined the strip theory and the FASTSIM approach to improve the accuracy of estimating the tangential traction, which was called as FaStrip. The authors also developed a code called ANALYN based on the method of approximate surface deformation, which can solve the rolling contact problems

without the restriction of the half-space assumption and reduce the computational cost compared with CONTACT. Despite this, significant deviation can still be found when high plastic deformation takes place around the contact region as these theories and algorithms are limited by linear-elastic materials. More details regarding their limitations were reviewed by Meymand et al. (2016) recently.

2.2.3 Finite Element Method

Due to the limitations of the analytical models outlined in Chapter 2.2.2, the applications of these models are likely to generate remarkable discrepancies between the analytical solutions and practical situations. The FE method has been demonstrated to be a more flexible tool for modelling wheel–rail contact problems since this method is not restricted by the half-space assumption and can deal with both elastic, elastic-plastic and even more complex material behaviour. However, FE simulations also have drawbacks. A large number of elements and non-linear problems can significantly increase the computational costs (Sladkowski & Sitarz, 2005). In general, two different ways are used for simulating wheel–rail contact problems. One is quasi-static analysis while the other one is dynamic transient analysis.

The idea of quasi-static analysis assumes that wheel–rail contact models have quasi-static contact state and the contact loads can be applied independently (Sladkowski & Sitarz, 2005). As the inertia of wheel and rail is not considered in the model, this method is unable to capture any dynamic effect related to the contact. In reality, the rolling motion between wheel and rail will be transient initially when the wheel starts to roll from stationary under the influence of traction at contact. Within the transient period, the traction will develop into the distribution that exists in the steady state for steady-state rolling. In order to investigate the transient state of wheel–rail rolling contact, transient FE analysis, which can capture the dynamic response related to the contact, can be applied. This kind of analysis is an explicit time-dependent process which applies the classical Lagrangian formulation to solve the rolling contact problems (Yang et

al., 2019).

During the transient analysis, each element in the FE model will undergo a repeated history of stress and deformation. According to this, a fine mesh region may be required on the complete circumference of both wheel and rail. Moreover, a certain length of rolling distance from the initial position of wheel to a quasi-steady state is necessary to damp the oscillations generated by the kinematic and potential energy from breaking the static state of wheel–rail contact (Deng et al., 2015). A relatively small size of time step has to be selected to guarantee the stability of the explicit integration (Wu & Gu, 2012). Such information revealed that the transient analysis is computationally expensive due to a large number of degrees of freedom and a small size of time step.

A relatively new approach developed by Nackenhorst (2004), called Arbitrary Lagrangian Eulerian (ALE) formulation, can be used in the FE method to solve the steady state of wheel–rail rolling contact problems. The principle of the ALE formulation is to decompose the total deformation of a rolling wheel into a rigid body motion and material deformation, which is described by the Eulerian method and the Lagrangian method, respectively (Chang et al., 2010). This indicates that although the rotating wheel does not undergo the large rigid body motion, the dynamics of the rotating wheel during rolling contact can still be captured. Therefore, wheel–rail rolling contact problems can be simulated without the explicit time-dependence. The ALE method can effectively solve the problem of frictional rolling with large deformation, but it has problem in treating frictional rolling with small deformation. This has to do with the non-differentiability of the Coulomb friction law at zero slip in relation to the stick-slip areas in the contact area (Wriggers, 2006).

2.2.4 Summary

In conclusion, wheel–rail contact solutions by the analytical models can lead to significant discrepancies with practical situations mainly because those models are limited by linear elastic materials and the half-space assumption. The FE

method is limited neither of these and can provide more realistic solutions. However, one of the most concerned drawbacks is the high computational cost by dynamic transient analysis, and hence a combination of the analytical models and FE simulations has been considered more efficient to solve wheel–rail rolling contact problems with an acceptable accuracy.

2.3 Rail Materials

2.3.1 Introduction

From the history, railway systems have been developed with rails as a beam support for trains. With the development of freight transportation, the advent of trains with higher axle loads has resulted in remarkable challenges for metallurgists, engineers, and railway operators on the performance of rails and safe operations. Moreover, the economic value of installed rails is usually the costliest asset in the financial account of any rail operation. Therefore, research has been widely performed on improving the quality of rails for many decades. In this sub-chapter, typical types of rail steels currently in use are introduced, followed by the studies on rail degradation and common maintenance strategies.

2.3.2 Rail Steel Types

Since the early 1900s, the majority of rails were produced essentially from carbon-manganese steels (IHHA, 2015), and generally, pearlitic rail and bainitic rail are two main types of rail steels used in global railway networks. The normal microstructure of pearlitic rails is pearlite, which consists of relatively soft ferrite and much harder but brittle Fe_3C. Due to the 'sandwich-like' configuration (parallel lamellae) of the pearlite within each pearlitic cell and its various orientation between cells, pearlitic steels can exhibit an excellent combination of the mechanical properties required for railways, including high strength and reasonable ductility. The microstructure of bainitic rails is bainite. It is nominally a two-phase microstructure which is formed by austenite transformation between the temperature ranges at which pearlite and martensite form (Krauss, 1992). In order to obtain bainitic microstructure, continuous

cooling is limited and additional alloying is introduced during the manufacturing process. This can prevent the formation of Fe_3C and results in finer austenite films intervening between ferrite plates. Therefore, bainitic microstructure is no longer a configuration of parallel lamellae (Garnham & Davis, 2009). Some carbide-free bainitic rail steels have been developed with some mechanical properties superior to pearlitic ones.

Many efforts have been made in the past to produce high-durability rail steels with improved mechanical properties, particularly the pearlitic ones. The main concept is to achieve the microstructural refinement of the austenite prior to transformation, the elimination of grain boundary pro-eutectoid Fe_3C during cooling and the formation of fully pearlitic microstructure with finer interlamellar spacing (Hernandez et al., 2008). Two representative methods were mainly used: heat treatment and additional alloying (Ueda et al., 2011). The former includes special heat treatment on hardening the ferrite and controlling the cooling rate to form finer pearlitic microstructure while the latter uses alloying elements, such as Cr, Mn and Mo, to refine the pearlite content. An alternative method is work-hardening by loading to increase the proportion of pearlite (Pickering, 1992).

In the past few decades, heat-treated (head-hardened) pearlitic rail steels with a carbon content of 0.5% (medium grade) to 0.8% (eutectoid grade), have been widely applied in heavy haul operations due to ease of manufacture, improved overall mechanical properties and reduced costs. However, the market requirements for increased reliability and extended rail life to fulfil the demanding conditions of higher axle loads and increased traffic (i.e. annual haulage), have driven the research on developing rail steels with more refined pearlitic structures. A more recent improvement to the primary pearlitic rail steels, has been the introduction of hypereutectoid rail steels with a carbon content of around 0.8% up to 1% by Nippon Steel (Uchino et al., 1998). The goal of these steels is to improve the resistance to wear in heavy haul systems by increasing the thickness and density of carbide lamella without a significant increase in hardness compared with standard high-grade rail steels; i.e. to facilitate the compaction of carbide lamella cells at and near the running surface.

Elwazri et al. (2005) further investigated the influence of microstructural characteristics of pearlite on the mechanical properties of hypereutectoid steel and found that decreasing the temperatures of austenitisation and transformation may improve the formability of such rail steel grade. In addition, although it is well known that some material properties, such as hardness, are altered as a result of wheel–rail contact, there is perhaps a lack of complete scientific understanding of the changes in material properties, as suggested by Pointner (2008).

2.3.3 Rail Degradation: Wear and Rolling Contact Fatigue

Wear and RCF are two dominant modes of rail degradation, depending crucially on the nature of wheel–rail contact behaviour and the number of loading cycles. The mechanism of both failure modes, particularly RCF, is driven by ratcheting, which is referred to as surface fatigue by the accumulation of cycle plastic deformation (further discussed in Chapter 2.4). Surface fatigue mechanism involves the initiation and propagation of cracks under repeated stresses, including normal contact, shear and bending stresses, which ultimately leads to the loss of particles from the rail surface. The crack growth at rails can be divided into three main phases and each can be characterised by a dominant mechanism, as illustrated in Fig. 2-8 (Fletcher et al., 2009).

Wear is the loss or displacement of material from the contact surface and can lead to many issues such as track gauge widening, loss of profiles leading to high wheel–rail dynamic forces and, in extreme cases, loss of rail cross-section resulting in the deterioration of rail rigidity and load-bearing ability. However, a small degree of wear can be beneficial in removing small cracks and slowing the growth rate of relatively larger cracks. RCF, which has already become one of the critical issues in many railway systems (Zerbst et al., 2009), is a competitive mode of rail degradation to wear (Donzella et al., 2005) and it is characterised by dense surface or subsurface cracks at rails. RCF damage has multiple forms such as head checks, squats, shelling and spalling, which is briefly illustrated in Chapter 2.1.3 (RCF at rail flash butt welds). Zerbst et al.

(2005) found that RCF damage at rails is usually originated from either a small surface crack or a sub-surface crack within 5 mm depth from the running surface. Similarly, Ekberg and Kabo (2014) reported that the majority of RCF cracks can extend from the surface to a depth of 4-5 mm. At this depth, some cracks show evidence of branching, with subsequent growth approximately parallel to the surface, or turning downwards, and ultimately developing into transverse defects. Several transverse defects may be present in close proximity, increasing the probability of rail failure. Ekberg et al. (2014) mentioned that subsurface initiated RCF cracks are relatively rare but can also potentially lead to dangerous transverse defects. Furthermore, RCF can also interact with wear to cause the complete failure of rails (Lewis & Olofsson, 2009).

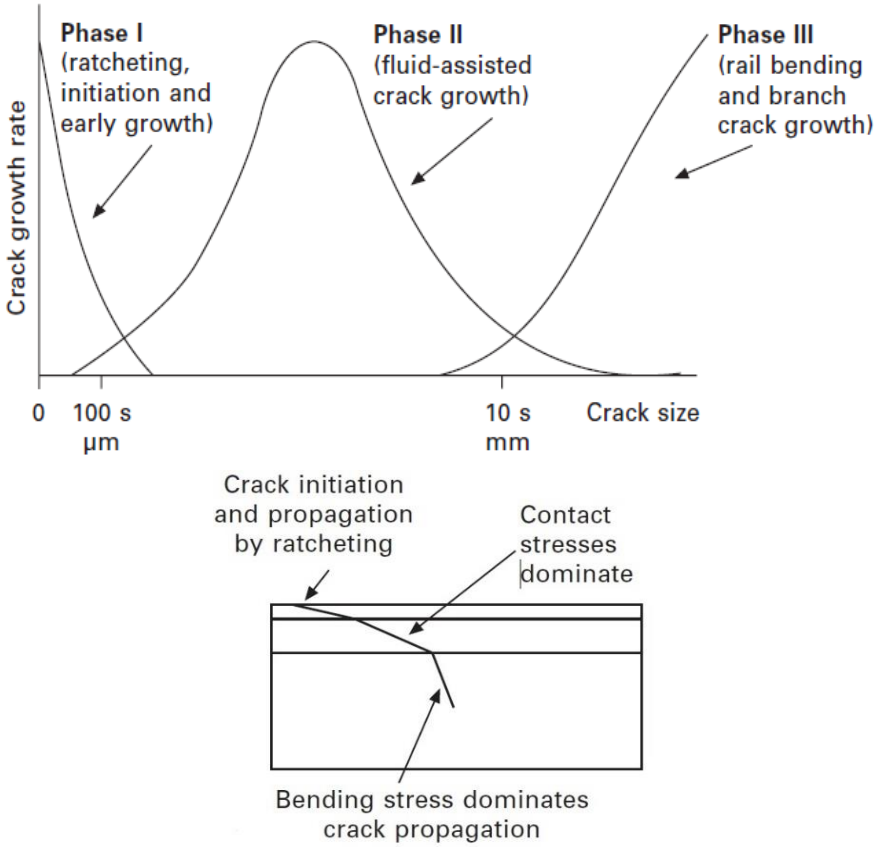

Figure 2-8: Three phrases of crack growth at rails. (Kapoor et al., 2003).

Over the years, many analytical models and experimental studies have been conducted to investigate wear and RCF behaviour of rails. The analytical models are mainly used to predict damage and further to develop damage criteria. These models can also be incorporated with MBDS to predict wear of

wheel/rail profiles (Tao et al., 2016) and to study rail corrugation. Regarding experimental methods, the most commonly used ones are small-scale pin-on-disc tribometers (Fig. 2-9c) and twin-disc machines (Fig. 2-9b) due to their availability, low cost and easy operation. However, both methods are very limited in their ability to reproduce environmental conditions that exist in practice. Scaled test rigs, full-scale experiments (Fig. 2-9a) and field trials are also feasible but expensive and hard to carry out. Therefore, a good strategy would be a combination of multiple methods based on the available budget and time (Lewis et al., 2017 & Zhu et al., 2019). Typical analytical models followed by experimental studies are briefly reviewed in the next content.

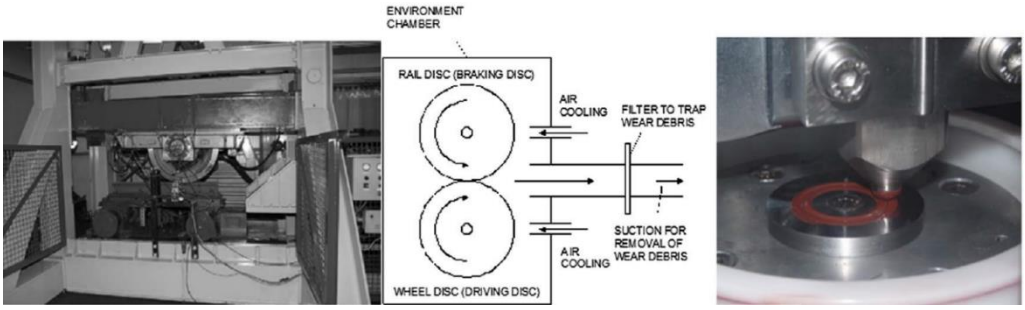

(a) (b) (c)

Figure 2-9: Laboratory based test methods: (a) full-scale (Stock & Pippan, 2011); (b) twin-disc machine (Lewis & Dwyer-Joyce, 2004); (c) pin-on-disc machine (Lewis et al., 2013).

The most common model for wear is the Archard equation, which proposed that wear volume is proportional to load and sliding distance on the contact surface, but inversely proportional to surface hardness (Archard, 1953). This model is also used to calculate wear coefficients based on the data from pin-on-disc and twin-disc tests. RCF initiation is usually predicted by the shakedown method based on Hertzian contact. Specifically, crack initiation strongly depends on friction coefficient and ratio of Hertzian pressure to yield stress in shear of the material as demonstrated in the shakedown map (Fig. 2-10a), which was derived under the assumption of full slip. However, the shakedown model is unable to predict fatigue life and does not account for the effects of wear (Ponter et al., 1985). An empirical model, which can predict both wear and RCF fatigue life, is the $T\gamma$ approach based on frictional energy dissipated in the contact (Fig. 2-10b), where $T\gamma$ is the product of traction and creepage across the contact patch.

Combined with data of wear rate from twin-disc tests, three wear regimes can be defined as mild, severe and catastrophic (Bolton & Clayton, 1984). Due to its basic empirical structure, it can be applied by any railway operations in possession of reliable performance data (Burstow et al., 2003). A very recent work presented by (Hiensch & Steenbergen, 2018) still used the $T\gamma$ method to establish the RCF damage functions for the conventional R260 and the premium R370HT rail steels.

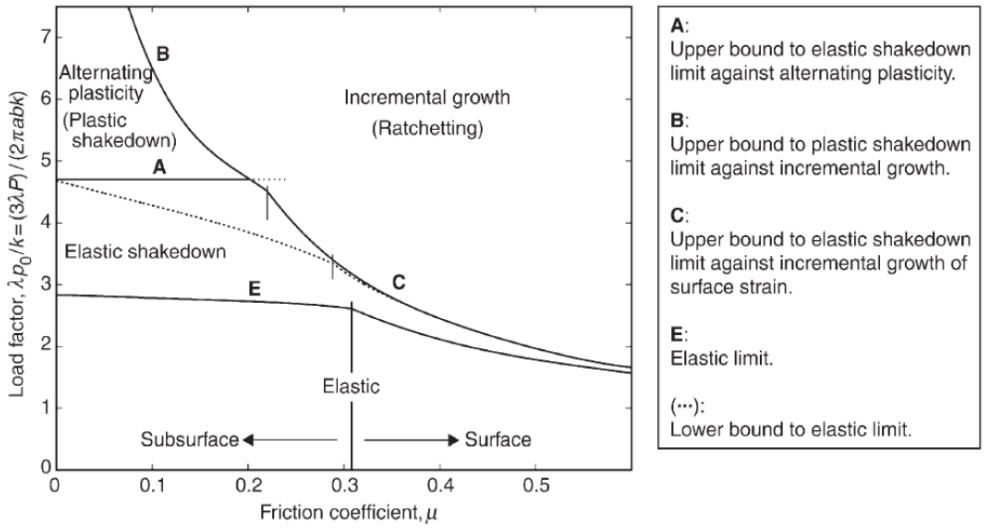

(a)

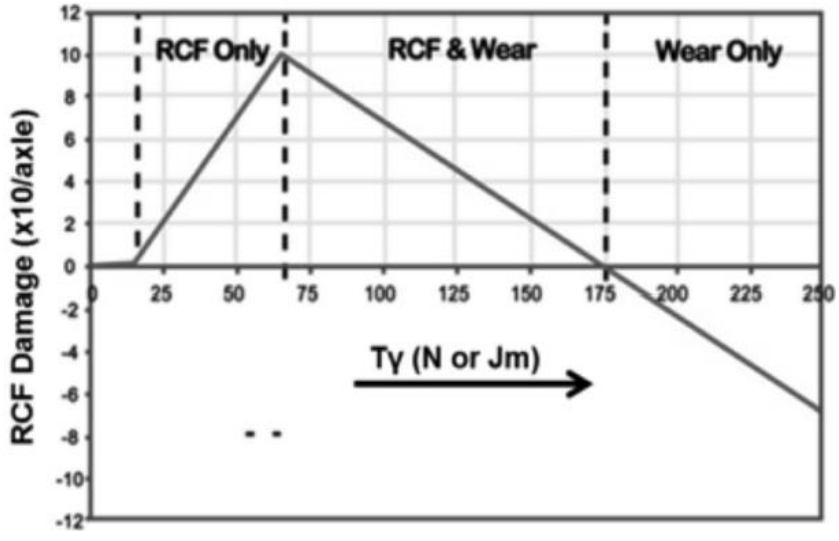

(b)

Figure 2-10: (a) Shakedown map (Ponter et al., 1985); (b) $T\gamma$ relationship. (Burstow et al., 2003).

In addition, several multiaxial damage models and criteria have been widely

applied to predict RCF damage in railways. Dang et al. (1989) proposed a multiaxial stress-based fatigue damage criterion for high cycle fatigue damage, namely Dang Van criterion. The concept of this criterion is related to the elastic shakedown limit and hydrostatic stress components play an important role in this criterion. Classical Crossland (Crossland, 1956) and Papadopoulos fatigue criteria (Papadopoulos et al., 1997) are also multiaxial stress-based, in which equivalent stress dominates. However, Ciavarella & Monno (2010) suggested that the Dang Van criterion provides over optimistic RCF limits, while both Crossland and Papadopoulos criteria are less sensitive to the exact geometrical shape of contact or the material constant. The authors also mentioned that the formation of most RCF damage is due to high cycle fatigue and ratcheting. Other than stress-based criteria, plenty of theoretical models have been developed to investigate RCF damage, i.e. equivalent strain approaches, critical plane models, energy-based models, energy density-based models and combined energy density-based and critical plane models. A representative energy density-based model is the Smith-Watson-Topper method proposed by Smith et al. (1970), which assumes that cracks will initiate and grow in the direction of the maximum energy density value. A combination of energy density-based and critical plane models is able to predict the RCF initiation life due to plastic shakedown and ratcheting (Ringsberg, 2001). A typical example of such models was proposed by Jiang & Sehitoglu (1999). If RCF crack initiation is due to ratcheting only, an empirical model proposed by Kapoor (1994) can be applied.

Experimental studies on wear of rail materials have been conducted since last century. Tyfour et al. (1995) conducted twin-disc tests to study the onset of steady state wear behaviour of pearlitic rail steel under dry rolling–sliding contact conditions. The results showed that wear rate increases initially with the number of loading and gradually becomes stabilised after the ratcheting threshold is reached. Lewis & Olofsson (2004) used mapping methods to obtain wear regimes and transitions, which were defined in terms of slip, contact pressure and $T\gamma$, from twin-disc and pin-on-disc tests on several European rail steels. The results indicated that wear becomes severe with an increase in slip and contact pressure. Moreover, the wear regime under different wheel–rail

contact situations can be predicted by combining the wear maps and MBDS package. Similar wear mapping work on various rail steels was also performed by Olofsson & Telliskivi (2003), Zhu et al. (2013), Ding et al. (2016), Ma et al. (2016), Wang et al. (2016), Cuervo et al. (2018), Christoforou et al. (2019) and Lewis et al. (2019).

According to Mutton et al. (2009b), over 10 mm depth of rail material was removed from the top surface due to wear in a heavy haul line after a traffic of approximately 300 million gross tonnes (MGT). The further study by Mutton et al. (2009a) indicated that with the increase in carbon content and hardness, the major damage mode of rail steels may shift from wear to RCF. Zhou et al. (2014) suggested that RCF, i.e. in the form of head checks, and wear can mutually affect the development of each other. Zhong et al. (2011b) performed the rolling tests to simulate the wheel–rail rolling contact situations for both heavy haul and high-speed railways. Their results concluded that wear is the dominant damage mode in heavy haul railways due to higher axle loads, while RCF is the major damage mode in high-speed railways. The authors also suggested that higher hardness can improve the wear resistance of rail materials but may increase the sensitivity to RCF.

Many previous works have also applied the experimental methods forementioned to study the influence of environmental factors, i.e. water (Nilsson, 2005 & Hardwick et al., 2014), humidity (Lyu et al., 2015), temperature (Ma et al., 2018), leaves (Cann, 2006 & Zhu et al., 2014), and iron oxides (Lyu et al., 2015 & Zhu et al., 2015), on wear characteristics of rail materials. A detailed review regarding the effects of contaminants on wear and even RCF behaviour was summarized by Lewis & Dwyer-Joyce (2009).

Meanwhile, investigation on RCF behaviour of rail materials under laboratory conditions has also been performed for many years. Garnham & Beynon (1991) updated a rolling–sliding wear machine with an eddy current technique to detect the initiation of RCF cracks. Such technique was applied in the twin-disc tests by Beynon et al. (1996) to study the RCF behaviour of three pearlitic rail steels and the outcome showed that the one with higher strength has better resistance

to RCF. Shur et al. (2005) mentioned that the sensitivity to RCF depends not only on the purity and hardness of rail steels but also their microstructure, such as grain size, carbide content, etc. The relationship between the RCF and microstructure of rail steels was also investigated by many researchers. Carroll & Beynon (2006) found that decarburisation has almost no influence on RCF by performing the twin-disc tests and microstructure analysis on British Grade 220 rail steel. Wetscher et al. (2007) illustrated that shear deformation can change the alignment of cementite lamellae and further affect the orientation of RCF crack growth. Franklin et al. (2008) carried out similar work on three pearlitic rail steels and suggested that RCF initiation life can be extended by reducing pro-eutectoid ferrite fraction. The same conclusion was also highlighted by Garnham & Davis (2008) and they further suggested that RCF cracks of pearlitic rail steels are linked to the crack initiation and propagation at the boundaries of singular, strain-deformed, prior austenite grains at the surface, especially where pro-eutectoid ferrite exists (Garnham & Davis, 2011 & Olivares et al., 2011). Olivares et al. (2011) also demonstrated that the presence of inclusions can aid the development of secondary cracks. Zhong et al. (2011a) conducted the cyclic loading tests on U71Mn and U75V rail steels and highlighted that RCF crack growth can be inter-granular and trans-granular, depending on steel grades. Stock & Pippan (2011) investigated the wear and RCF behaviour of several pearlitic and bainitic rail steels with the same hardness level on a full-scale test rig and also in several track tests. They found that the bainitic rail steels present reduced wear resistance but improved RCF resistance compared with the pearlitic ones. Szablewski & LoPresti (2014) mentioned that a higher amount of cementite tends to result in earlier and more severe development of RCF, but no direct relationship can be found. Ding et al. (2015) found that the morphology of RCF in rails can be turned from peeling to spalling with the rolling speed increasing by rolling–sliding wear tests. Ueda & Matsuda (2020) indicated that pearlitic rail steels with relatively high carbon content tend to have a large RCF crack inclination angle from the surface.

Other than the influence of the microstructure and composition of rail steels, environmental factors, i.e. water, oxygen and temperature, can also affect the RCF behaviour (Cookson & Mutton, 2011, Wang et al., 2017a & Ma et al.,

2018). Additionally, rolling contact may induce the formation of brittle white etching layers (WEL) on rail surface, which are composed predominately of martensite, some retained austenite and undissolved carbide (Steenbergen, 2015, Al-Juboori et al., 2017, Pan et al., 2017 & Wu et al., 2018). Such WELs can further result in crack initiation and squat formation (Al-Juboori et al., 2019), which have become a popular research area in wheel–rail interface recently.

According to the literature reviewed in this sub-chapter, many experimental studies have been carried out to investigate the wear and RCF behaviour of rail materials. Meanwhile, analytical models have been developed to quantify wear and predict RCF initiation. Despite this, rail degradation, particularly RCF, is still a long-term issue in wheel–rail interface due to its complex characteristics related to microstructure, loading history and environmental conditions. Therefore, it is expected that more thorough investigations on RCF mechanisms will be continuously conducted.

2.3.4 Strategies on Improving Resistance to Rail Degradation

In order to optimise the life of rail materials and further improve the overall performance of railway systems, various techniques and approaches were developed and implemented by rail operators to prevent and mitigate rail degradation. As illustrated in Chapters 2.3.2 & 2.3.3, refining the pearlitic microstructure to produce high strength rail steels is able to enhance the resistance to wear and RCF. However, rail degradation in reality is not so simple to be completely avoided by such 'preventative' strategy. To achieve well-maintained railway systems, 'corrective' and combined strategies are also widely applied. In this sub-chapter, two fundamental methods, control of friction and rail grinding, are briefly reviewed.

Friction is the resistance to relative motion between two bodies in contact and an appropriate friction level is essential to the performance of wheel–rail interface. Specifically, if the friction coefficient is too low, it will limit tractive and braking capacities of a train (particularly under high creepages) and

similarly limit the tangential force that can be developed in curving because the maximum level of tangential force depends on the friction coefficient and normal load, as shown in Fig. 2-11. However, if the friction coefficient is high, rail degradation will occur more readily due to high tangential forces (Grassie, 2009a). Therefore, optimisation of friction levels depends on contact situations and is classified into two main interfaces according to IHHA (2015): wheel flange–rail gauge corner (high rails in intermediate and sharp curves) contact and wheel tread–rail top (tangent tracks and curves) contact, also called gauge face lubrication and top-of-rail friction management (TOR–FM), respectively. Generally, low friction modifiers (lubricants) applied in the former can almost eliminate wear resulting from high creepages by separating the wheel flange and rail gauge corner effectively, while high friction modifiers or friction enhancers are used in the latter to increase adhesion for both traction and braking (Magel, 2017). When the TOR–FM is applied, a so-called "positive friction" at the wheel–rail interface can be created, meaning that the shape of the traction creepage curve (Fig. 2-11) is modified to provide continuously increasing traction with increasing creepage (Spiryagin et al., 2014). In addition, reducing the wheel tread–rail top friction in a controllable way from dry conditions can reduce the lateral forces induced by the AOA at high rails (Tomeoka et al., 2002, Aldajah et al., 2003 & Eadie et al., 2003). A dry and thin film of friction modifier usually does not accelerate the growth of existing cracks (Stock et al., 2011). The Canadian Pacific Railway implemented a 100% effective friction management to improve the overall rail performance and reduce the cost successfully (Sroba et al., 2005).

The proper choice of lubricant is essential as both the type and amount of lubrication can affect the performance of rails dramatically (Hardwick et al., 2017 & Wang et al., 2017b). An intermittent lubrication at high rail gauge corners may accelerate the growth of RCF cracks (Fletcher & Beynon, 2000) or cause a more drastic wear rate than no lubrication (Lewis et al., 2014). High viscosity lubricants are recommended if continuous lubrication cannot be assured (Ekberg et al., 2014). An over-lubrication may lead migration of lubricant onto the rail top, causing loss of adhesion. Additionally, over-lubrication is also likely to result in rapid RCF crack growth due to hydraulic

pressure within the cracks. One of the best ways to control the application of lubricant to the rails is to use vehicle-mounted systems (Dwight & Jiang, 2006). TOR–FM will be ideal if a friction modifier can provide an intermediate friction range, usually 0.3–0.4 according to the American Railway Engineering and Maintenance-of-Way Association guidelines (AREMA, 2013), which is sufficient to reduce wear, noise and fuel consumption but not impede traction and braking (Spiryagin et al., 2014). Some high friction modifiers for heavy haul operations can even provide a friction range of 0.4 – 0.6, depending on the service requirements. However, the wear rate of rail materials can be increased substantially (Lewis & Dwyer-Joyce, 2006). In addition, atmospheric conditions, i.e. humidity, temperature and railhead contamination, can affect the performance of friction modifiers (Lewis et al., 2013 & Magel, 2017). Due to this, friction management has historically found to be not cost-effective in some heavy haul operations, especially those located remotely (Welsby et al., 2014).

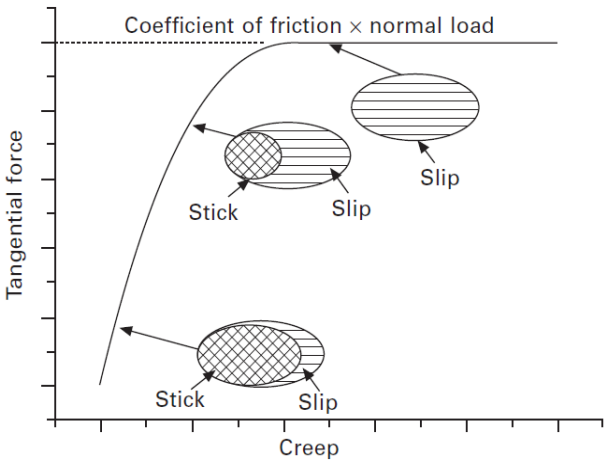

Figure 2-11: Relationship between the tangential force and creep (Olofsson, 2009).

Rail grinding has become a standard rail maintenance strategy in global railway systems, although its original objective was to eliminate rail corrugations. Nowadays, routine rail grinding has become an important remedy for not only correcting or controlling rail degradation, particularly RCF, but also rectify the rail profiles to ensure desirable wheel–rail contact condition. It should be clarified that an optimum grinding strategy is developed in accordance with the characteristics of railway systems, such as axle loads, curve radius, friction management and rail steel, in order to simultaneously maximise the efficiency

and minimise the cost of grinding. Generally, rail grinding can be classified into three categories: corrective grinding, preventive grinding and preventive-gradual grinding (Fröhling, 2007). Corrective grinding refers to the implementation of grinding on rails that present visible and severe RCF damage. Such grinding is inefficient since the removal of significant cracks requires multiple grinding passes, which are often unable to be completed in one occupation window. Furthermore, corrective grinding usually removes the work-hardened layer of rails and this can further accelerate rail degradation. Therefore, corrective grinding has been substituted by more frequent and efficient preventive grinding in most of railway systems (Stanford et al., 2001).

Preventive grinding is designed to remove an optimal amount (usually a thin layer) of rail material to prevent both surface-initiated and subsurface-initiated RCF crack cracks entering the stage of rapid growth. The rate of material ground is so-called the 'magic wear rate (MWR)' (Kalousek & Magel, 1997). The MWR represents the optimum level of wear where RCF damage can be predictable and controlled to extend the rail life. As illustrated in Fig. 2-12a, natural wear (no grinding) leads to a low rail life due to RCF, while corrective grinding causes a high wear rate and poor performance of the rail. In the case of preventive grinding, the rail life will be maximised if the MWR is achieved successfully. In Fig. 2-12b, the procedure of preventive grinding on the MWR is detailed. An innovative grinding method is preventive-gradual grinding, which involves conventional frequent one-pass grinding but with additional material removed at each pass. This will gradually meet the requirements of running surface condition and targeted profiles. To conduct reliable preventive grinding, detecting RCF cracks and measuring the rates of these cracks accurately should be assured.

Except for eliminating cracks, grinding has now been widely applied to implement modified rail profiles (Wheel profiles are usually turned to restore profiles or implement revised profiles, except in the case of single-wear wheels). Specifically, profiles are usually designed as their naturally worn shape to improve the wheel–rail interaction characteristics and further train stability as well as curving performance. Suitable contact situations can balance contact

stresses, avoid trains hunting in tangent tracks and enhance the steering behaviour of wheelsets in curved tracks. Fig. 2-13 shows the general modified wheel and rail profiles for most categories. For low rails in curved tracks and tangent rails (or shallow curves), profiles are ground to establish a broader contact zone that can reduce the contact stresses, and hence extend the initiation of rail degradation. Similarly, profiles for high rails in heavy haul operations with less steering capability but higher potential for gauge corner damage are ground to establish a conformal or near-conformal contact. As for passenger lines with light axle loads, particularly high rails in sharp curves, a narrower contact zone at gauge corners is ideal to increase steering capability. Therefore, rail and wheel profiling must be system-specific with the consideration of traffic conditions, track geometries, major deterioration mode, etc (Marich, 2009). A detailed review of profiling in Australian railway systems can be found in Kerr & Marich (2001).

Although rail grinding has made significant contributions to optimise the performance and maintain the safety, there are still some potential challenges and improvements towards more cost-effective grinding strategies. Surface finish is likely to be a critical issue after grinding even if RCF can be easily dealt with (Satoh & Iwafuchi, 2008). In heavy haul operations, the margin for error in profiling has reduced with the increasing application of harder rail materials. If anomalies are not carefully minimised, it will be difficult for such rails to be ground to the designed shape (Welsby et al., 2014). As mentioned in Chapter 1.1, RCF cracks associated with HAZs in welds are deeper and more difficult to mitigate by grinding. Previous research revealed that grinding specifications should be reconsidered for the damaged rails with the formation of WELs (Steenbergen, 2016). In the future, research on grinding will focus on solving these challenges for best practice grinding. Moreover, developing rail grinders with high metal removal capabilities and establishing a high-quality grinding program with specific pre-grinding plans and post-grinding quality measurements are also considered important.

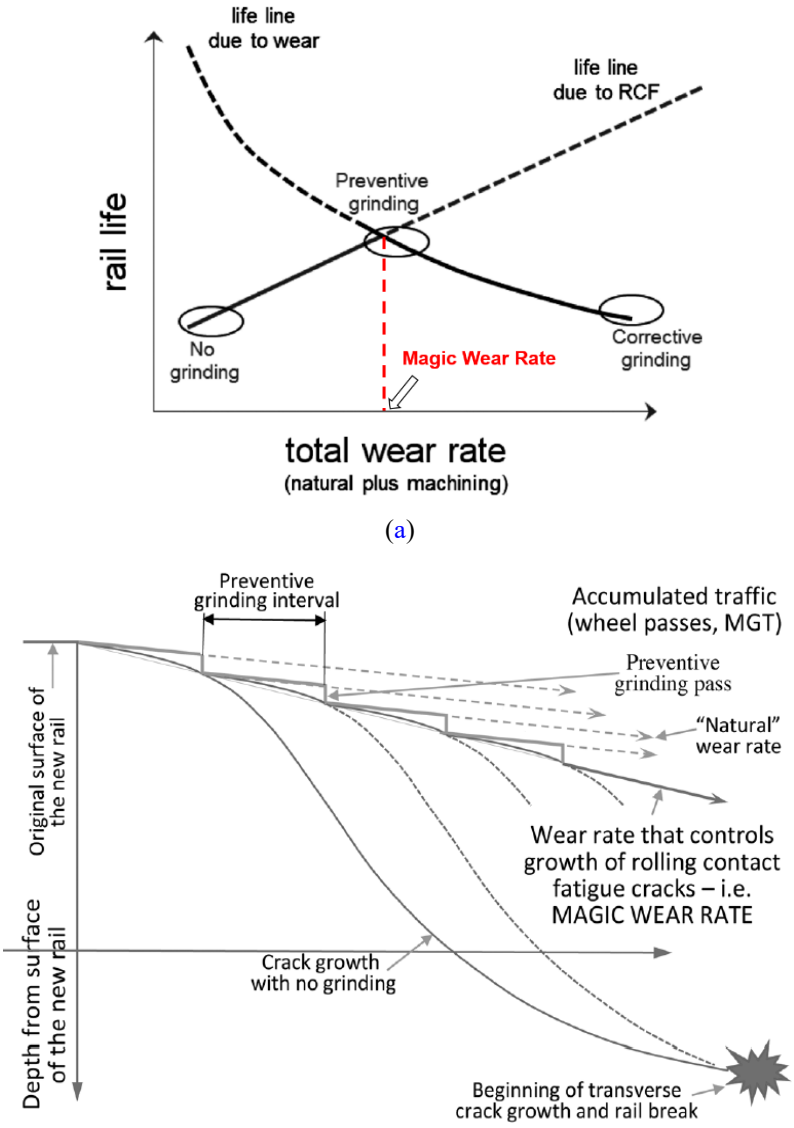

Figure 2-12: (a) Different rail grinding practices; (b) Preventive grinding on the MWR (IHHA, 2015).

According to the strategies reviewed above, each of them can provide benefits for improving the resistance to rail degradation. However, it is necessary to combine all the strategies together in order to maximise the benefits and cost reductions. A holistic approach should involve selecting suitable rail materials, optimising wheel and rail profiles to reduce contact stresses, introducing effective friction management and applying preventive grinding. In recent years, laser cladding is considered as another technique to combat rail degradation, which uses laser energy to melt the powders of atomised metal and metallurgically bond it to the surface of a substrate (Clare et al., 2012, Lewis et

al., 2015 & Hernández et al., 2016). However, similar to FBW process, the microstructure and corresponding mechanical properties of claddings and HAZs can affect the final performance of laser-cladded rails significantly (Lai et al., 2018). Therefore, the availability of laser cladding technologies for rails has not to date resulted in such technologies being widely applied even if many researchers found that laser-cladded rails have comparable or better performance than the uncladded ones by testing various cladding materials and combinations of cladding parameters (Clare et al., 2013, Fu et al., 2015, Roy et al., 2018 & Lai et al., 2019).

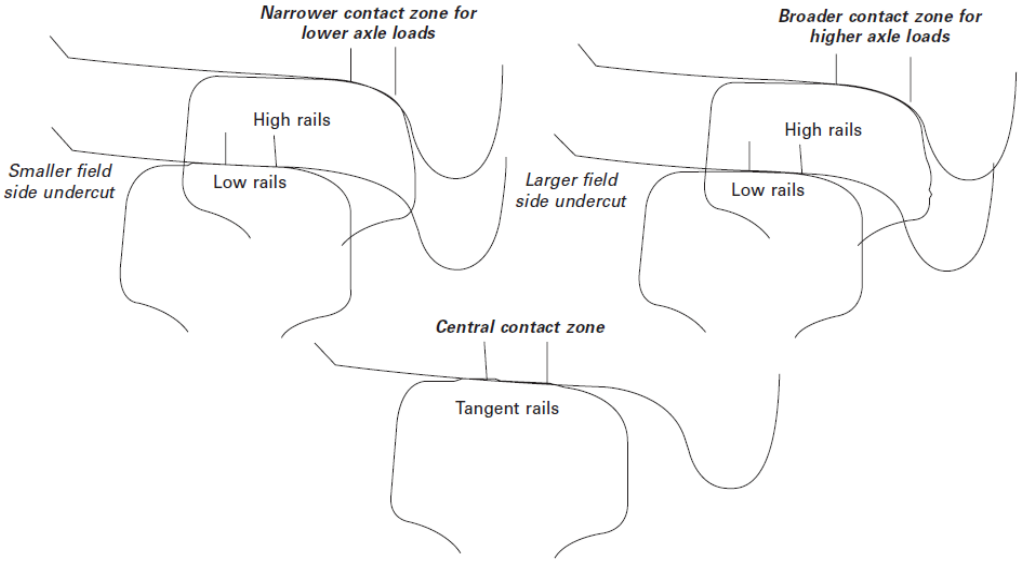

Figure 2-13: Illustration of general wheel–rail contact with modified profiles (Marich, 2009).

2.3.5 Summary

Despite the fact that rail degradation can be effectively mitigated and prevented to some extent by the application of high strength rail steels, friction management and grinding, RCF is still a dominant problem in railway transport due to its complex characteristics induced by various in-service and environmental conditions. Therefore, continuous adjustments to altered operational conditions based on identification of damage are required. Furthermore, more RCF damage associated with rail flash butt welds has been identified in heavy haul operations (Mutton et al., 2016). Meanwhile, to meet the requirements for rails with better durability, more thorough investigations

on RCF mechanisms and potential cost-effective solutions should be carried out in the future. It is also suggested that these strategies should be periodically reviewed, consolidated, and implemented with the aim of avoiding or at least minimising the duplication of research activities.

2.4 Ratcheting Behaviour of Materials

2.4.1 General Review

Ratcheting behaviour has been one of the attractive research fields in the study of fatigue of metal materials for the last few decades. As illustrated in Fig. 1-4, if the materials are subjected to a cyclic stress level above the plastic shakedown limit (or ratcheting threshold), non-zero plastic deformation will generate and accumulate in each loading cycle. Such phenomenon is known as ratcheting (Bower & Johnson, 1991, Kapoor & Johnson, 1994, Tyfour et al., 1996 & Kapoor, 1997). Generally, stress-controlled cyclic tests are used to investigate the ratcheting behaviour of materials. Extensive studies also used strain-controlled cyclic tests to investigate the cyclic deformation characteristics of materials, i.e. cyclic hardening, cyclic softening or cyclic stabilised. Both types of tests can be uniaxial and multiaxial, and it should be noted that monotonic tensile tests are usually conducted firstly to determine the loading range for cyclic loading tests, which should exceed the yield point of materials but should not be too close to the failure point at which materials may fracture.

Under asymmetrical stress-controlled cyclic loading tests, the hysteresis stress–strain loops never close due to ratcheting. The ratcheting behaviour of a material can be quantified by the ratcheting strain and corresponding ratcheting strain rate. In each loading cycle, the maximum and minimum axial strains (ε_{max} & ε_{min}) can be collected from the experimental data. Similarly, the maximum and minimum shear strains are represented as γ_{max} and γ_{min}, respectively. The axial ratcheting strain ε_r and the shear ratcheting strain γ_r in each cycle are defined as,

$$\varepsilon_r = \frac{1}{2}(\varepsilon_{max} + \varepsilon_{min}) \qquad (2-1)$$

$$\gamma_r = \frac{1}{2}(\gamma_{max} + \gamma_{min}) \qquad (2-2)$$

The ratcheting strain rate is the increment of ratcheting strain per cycle, which is defined as $d\varepsilon_r/dN$ and $d\gamma_r/dN$ (N: loading cycle number). There are three types of ratcheting behaviour when a material is subjected to stress-controlled cyclic loading, as demonstrated in Fig. 2-14. The first type is that the decreasing ratcheting strain rate leads to elastic/plastic shakedown, which means that no ratcheting occurs after a certain number of loading cycles. The second type is ratcheting with a constant rate. The ratcheting strain rate decreases at first and gradually becomes cyclically stabilised with the increase in the number of loading cycles. The third type is ratcheting with an unstable rate and can result in high ratcheting strain, which may lead to plastic instability. Materials that experience such type of ratcheting behaviour can fail within a very low number of cycles, and such phenomenon is known as very low cycle fatigue (Satyadevi et al., 2007). From stress-controlled cyclic loading tests, the cyclic deformation characteristics of a material can also be obtained by analysing the relationship between the strain amplitude ε_a (defined by Eq. 2-3) in each cycle and the number of loading cycles N. If the strain amplitude decreases with the increase in the number of loading cycles, the material will harden and vice versa. The strain amplitude ε_a is determined as,

$$\varepsilon_a = \frac{1}{2}(\varepsilon_{max} - \varepsilon_{min}) \qquad (2-3)$$

Under strain-controlled cyclic loading tests, the maximum and minimum stresses (σ_{max} & σ_{min}) in each loading cycle can be obtained and so the stress amplitude σ_a can be defined as,

$$\sigma_a = \frac{1}{2}(\sigma_{max} - \sigma_{min}) \qquad (2-4)$$

If the stress amplitude increases with the number of loading cycles, the material

will harden and vice versa. Previous research (Stephens et al., 2001) mentioned that the tendency for cyclic hardening/softening of a material is affected by its microstructure, particularly the configuration of dislocation structure. Sunwoo et al. (1982) suggested that when an initially soft material (with coarse interlamellar spacing) is subjected to plastic deformation, more dislocations will be generated and constrained to form dislocation cells with the existing dislocations. In other words, the dislocation mobility is reduced and such phenomenon can enhance dislocation-dislocation interactions and lead to cyclic hardening of the material. In contrast, cyclic softening occurs more readily in hardened or initially hard materials (with fine interlamellar spacing) under cyclic loading since the existing dislocations tend to rearrange into a configuration with greater mobility. In addition, the extent of change in dislocation configuration is also strongly influenced by the cyclic stress level which determines the amount of imposed plastic deformation. Strain-controlled cyclic loading tests usually result in mean stress (defined by Eq. 2-5) which may relax partially or fully due to the occurrence of plastic deformation. Therefore, the extent of mean stress relaxation depends on the plastic strain amplitude and there is more relaxation at larger plastic strain amplitudes. It should be noted that mean stress relaxation is different from cyclic softening and even can occur in a cyclically stabilised material (Hassan & Kyriakides, 1992a & 1994a).

$$\sigma_m = \frac{1}{2}(\sigma_{max} + \sigma_{min}) \qquad (2-5)$$

As ratcheting plays an essential role in the failure mechanism of materials, experimental studies have conducted using cyclic loading tests to investigate the uniaxial and multiaxial ratcheting behaviour of different materials. Meanwhile, cyclic deformation characteristics of these materials were also evaluated under different testing conditions. Typical studies include: 10Ni5CrMoV high strength steel (Wang & Liu, 2017), 1020 and 1026 carbon steels (Hassan & Kyriakides, 1992a & 1992b), 1045 carbon steel (Jiang, 2001, Zhang & Jiang, 2005), 1070 carbon steel (Jiang & Huseyin, 1994a & 1994b), 25CDV4.11 steel (Kang et al., 2005b & Kang & Kan, 2009), 42CrMo medium carbon and low alloy steel (Kang & Liu, 2008, Kang et al., 2008 & Kang et al.,

2009), SS304 stainless steel (Ruggles & Krempl, 1990, Hassan & Kyriakides, 1994a & 1994b, Kang et al., 2002a, Kang et al., 2004, Kang et al., 2005a & 2005b, Kang et al., 2006a & 2006b), 316FR steel (Portier et al., 2000, Mizuno et al., 2000 & Date et al., 2008), 316L stainless steel (Kang et al., 2001), modified 9Cr-1Mo martensitic steel (Yaguchi & Takahashi, 2005), as-rolled rail steel (Bower, 1989 & McDowell, 1995), heat-treated rail steel (McDowell, 1995) and U71Mn rail steel (Kang & Gao, 2002 & Kang et al., 2002b). More recent works on high strength rail steels used in heavy haul operations were also performed by Khoddam et al. (2014), Pun et al. (2014b) and Athukorala et al. (2016). There are also plenty of works on other metals and their alloys, i.e. copper (Bower, 1989, Lim et al., 2009 & Kim et al., 2010), magnesium (Xiong et al., 2014) and NiTi alloy (Kang et al., 2012). These experimental studies indicated that the ratcheting behaviour and cyclic deformation characteristics of materials are directly influenced by stress levels (mean stress and stress amplitude), loading path and loading history. Furthermore, the ratcheting behaviour of materials in these studies was mostly investigated under uniaxial or multi-axial tension–torsion cyclic loading tests. In the case of rail materials, Pun et al. (2014b) suggested that biaxial compression–torsion cyclic loading tests are one of the most suitable methods to simulate the loading from the wheel–rail rolling contact.

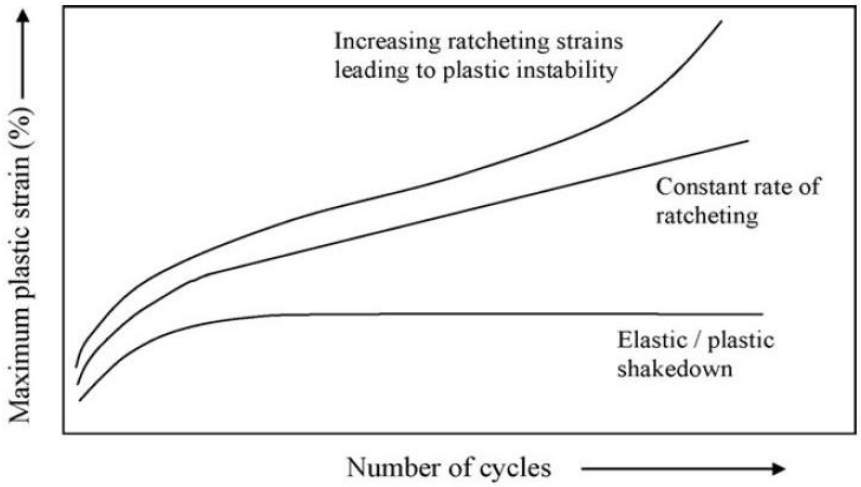

Figure 2-14: Ratcheting behaviour of a material subjected to stress-controlled cyclic loading (Satyadevi et al., 2007).

Although numbers of studies have been performed to study the ratcheting

behaviour of various metal materials, very limited similar research has been conducted on welds and other inhomogeneous materials, and the key reason is that the conventional method for strain measurements—using an extensometer, is unable to investigate the heterogeneous ratcheting behaviour induced by the varied properties across the welds. To date, the work carried out by Luo et al. (2017 & 2020) is the only related research, which investigated the heterogeneous ratcheting behaviour of SUS301L stainless steel butt welded joint under uniaxial cyclic loading. The digital image correlation (DIC) method was applied to measure the strain field and its evolution at every point on the gauge surface of specimens during the tests. However, there are no studies conducted on the ratcheting behaviour of flash butt welds in high strength rail steels to date, which have been identified as a hazardous region, suffering more severe plastic deformation and therefore resulting in higher sensitivity to RCF than PRs in heavy haul operations. Since different materials exhibit different ratcheting behaviour and cyclic deformation characteristics, it is considered necessary and urgent to investigate the ratcheting behaviour of flash butt welds in high strength rail steels.

2.4.2 Constitutive Cyclic Plasticity Models for Ratcheting

The establishment of constitutive cyclic plasticity models is mainly used to quantify the ratcheting behaviour of different materials from experimental studies and further to be applied in FE simulations. In general, the plastic behaviour of materials subjected to cyclic loading can be described by two types of hardening rules: isotropic hardening and kinematic hardening. As shown in Fig. 2-15, isotropic hardening is where the shape of yield surface remains constant but expands with the increase in stress, while for kinematic hardening, both the yield surface shifts in space but its shape and size keep unchanged, i.e. the increase in the yield stress in the tensile direction of a material and plastic deformation causes the decrease in the yield stress in its compressive direction, which is termed as Bauschinger effect (Asaro & Lubarda, 2006). Therefore, an isotropic hardening model cannot capture the Bauschinger effect as the yield stresses in both directions of the material are always equal. In the following

content, typical constitutive cyclic plasticity models developed in the last few decades are briefly reviewed.

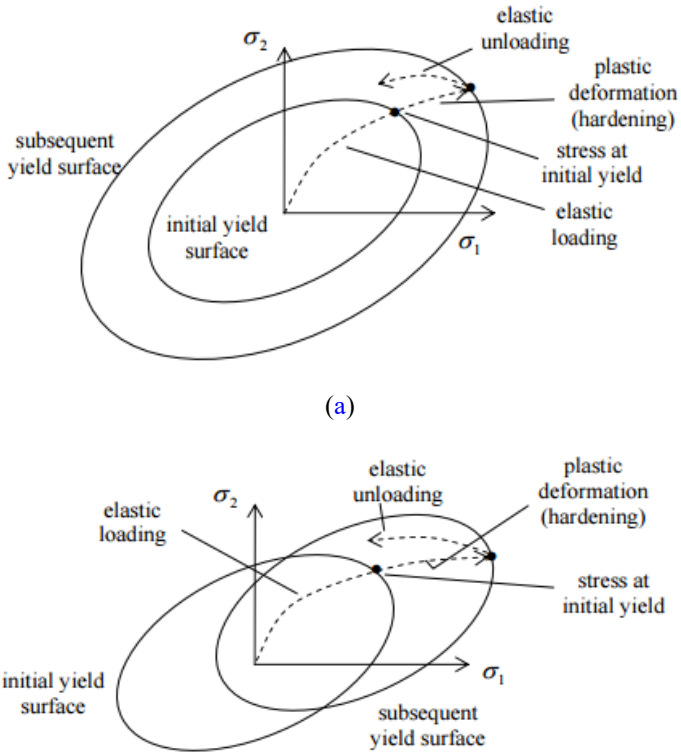

Figure 2-15: Hardening rules (σ_1 and σ_2 are two planar stress components that are mutually perpendicular): (a) isotropic hardening; (b) kinematic hardening.

The existing constitutive models for describing the complex cyclic plasticity of materials can be categorised into two main groups. One is based on the two-surface model proposed by Mroz (1967) and improved by Dafalias & Popov (1975), while the other one is based on the nonlinear kinematic hardening model established by Armstrong & Frederick (1966), also known as A-F model. Although the latter, which is based on the mechanism of strain hardening and dynamic recovery of back stress, has been proved to be more effective for simulating the ratcheting behaviour (Chen et al., 2003), it possesses a large overestimation of ratcheting strain since the influence of cyclic hardening/softening, temperature and time-dependent factors has not been considered. In the past few decades, many endeavours have been contributed to improve the accuracy of modelling the ratcheting behaviour based on the A-F model. Chaboche et al. (1979) introduced a surface in the plastic strain space to

memorise the maximum plastic strain suffered by materials. Ohno (1982) defined a cyclic non-hardening region in the plastic strain space and assumed that if plastic strain falls into the region under cyclic loading, no evolution of isotropic hardening will occur, leading to the dependence of cyclic hardening on strain range. Such memory surface extended was accepted by Chaboche (1986). Burlet & Cailletaud (1986) modified the radial evanescence term and years later, Chaboche (1989) decomposed the backstress term, followed by defining a threshold for the dynamic recovery of decomposed backstress (Chaboche, 1991). Ohno & Wang (1993a & 1994) introduced a critical state of dynamic recovery, also known as the O-W model. McDowell (1995), Jiang & Kurath (1996) and Jiang & Sehitoglu (1996) further modified the O-W model by introducing nonlinear forms of the dynamic recovery term. Voyiadjis & Basuroychowdhury (1998) incorporated the direction of stress-rate in the kinematic hardening rule proposed by Chaboche (1991). Abdel-Karim & Ohno (2000) combined the A-F model and the O-W model to simulate the ratcheting under a steady state. Bari & Hassan (2000 & 2002) reviewed these models and suggested that the major shortcoming of them is the wrong prediction of ratcheting under multiaxial loading cases due to the coupled calculation of plastic modulus with the kinematic hardening rule by the consistency condition. Specifically, the direction and the magnitude of the normal direction of the yield surface translation continuously change during multiaxial loading but these remain unchanged throughout uniaxial loading. This indicates that a more appropriate evolution rule of kinematic hardening is crucial for improving the accuracy of multiaxial ratcheting prediction.

In order to further improve the capability of multiaxial ratcheting prediction, many works were conducted to modify the existing coupled models or the kinematics hardening rules. Bari & Hassan (2002) superposed the Chaboche model (Chaboche, 1991) upon the Burlet-Cailletaud model (Burlet & Cailletaud, 1986) by introducing a new ratcheting parameter. Döring et al. (2003) proposed a new hardening rule with the consideration of the effect of non-proportional factor on ratcheting. Chen et al. (2003) and Chen & Jiao (2004) developed another kinematic hardening rule by superposing the O-W model upon the Burlet-Cailletaud model (Burlet & Cailletaud, 1986). After that, Chen et al.

(2005) established a new kinematic hardening model based on the O-W model. Except for the model proposed by Bari & Hassan (2002), all the others can reasonably predict non-proportional multiaxial ratcheting. However, the evolution of cyclic hardening was assumed to be dependent on the ratcheting strain rate in these models, which is unable to describe the strain amplitude dependence of cyclic hardening and non-saturated feature of cyclic hardening presented in cyclic straining with a higher strain amplitude. Therefore, Kang et al. (2003) extended the O-W model to consider the such features by introducing a notation of critical surface into the evolution rule of isotropic hardening, but ratcheting cannot be simulated reasonably. Kang et al. (2005a) modified the Abdel-Karim-Ohno model (Abdel-Karim & Ohno, 2000) by introducing the temperature-dependent parameters in the kinematic hardening rule to consider the remarkable effect of dynamic strain aging on both uniaxial and multiaxial ratcheting at high temperatures. Yaguchi & Takahashi (2005) proposed a definition of softening index surface based on the O-W model to consider the influence of cyclic softening feature on ratcheting. Based on this model, Kan et al. (2007) introduced a temperature-dependent ratcheting parameter. Koo & Lee (2007) established the constitutive model for ratcheting at high temperatures by combining the Chaboche model (Chaboche, 1991) with the isotropic softening rule. Krishna et al. (2009) combined the same model with the isotropic hardening rule but introduced a softening term. In addition, the Tanaka non-proportional parameter, proposed by Tanaka (1994), was introduced to improve the accuracy of simulating non-proportional cyclic loadings. Such parameter was also applied in Hassan et al. (2008). Recently, there are plenty of similar works which focus on improving the accuracy of simulated ratcheting by modifying the parameters of kinematic hardening and isotropic hardening/softening based on the previous developed modes, i.e. the A-F model and the O-W model. Typical examples include (Abdel-Karim, 2009, Bai & Chen, 2009, Kang, et al., 2009, Abdel-Karim, 2010, Taleb & Cailletaud, 2010, Yu et al., 2012, Khutia et al., 2014, Lee et al., 2014, Pun et al., 2014a, Zhu et al., 2015 & Wang & Liu, 2017).

2.4.3 Summary

In conclusion, ratcheting is one of the essential plastic deformation phenomena of materials under cyclic loading. Both stress-controlled and strain-controlled cyclic loading tests can provide useful information for investigating the ratcheting behaviour of materials. Under stress-controlled cyclic loading, the ratcheting strain and corresponding ratcheting strain rate in each loading cycle are used to quantify the plastic ratcheting of the material and the strain amplitude can be applied to investigate the cyclic deformation characteristics of the material. Under strain-controlled cyclic loading, the cyclic deformation characteristics and the stress relaxation behaviour of the material can be observed. As each type of material has its unique ratcheting behaviour and this doctoral study focuses on flash butt welds high strength rail steels, a systematic experimental study to investigate the uniaxial and biaxial ratcheting behaviour of these welds was carried out and the corresponding results are presented in Chapter 3.

Many studies have been carried out to improve the accuracy of ratcheting prediction by coupling the existing models and modifying the hardening rules. The main reason for these efforts is that ratcheting behaviour is extremely complex, and can be influenced by many factors, i.e. rate-dependent hardening, non-proportional loading history and temperature. Furthermore, ratcheting behaviour usually varies with material characteristics and this indicates that the existing models may not be reasonably and simultaneously describe the ratcheting and cyclic deformation characteristics of rail welds. Therefore, the constitutive cyclic plasticity model for high strength rail steels developed by Pun et al. (2014a) was updated for rail flash butt welds based on the experimental study presented in Chapter 3. More detail regarding the updated model and the method to calibrate the material parameters required can be referred to Chapter 4.

2.5 Numerical Study on Wheel–Rail and Wheel–Rail Weld Contact

2.5.1 General Review

Since 1980s, many researchers have been using the FE method to numerically simulate wheel–rail contact problems due to the high cost of field tests, the applicability of elastic-plastic materials and no limitations of the half-space assumption. As introduced in Chapter 2.2.3, two different methods, quasi-static analysis and dynamic transient analysis, are commonly used. Some simulation works also combined analytical solutions with FE simulations to improve the computational efficiency. In this sub-chapter, representative literature regarding numerical studies on the wheel–rail/weld contact in the past 30 years are reviewed.

2.5.2 Wheel–Rail Contact

Kulkarni et al. (1990) created a 3D FE model to investigate the plastic deformation of elastic-perfectly plastic (EPP) and elastic-linear-kinematic-hardening-plastic (ELKP) bearing steels under cyclic pure rolling contact at the plastic shakedown limit. The Hertzian contact pressure distribution with a load factor of 4.68 was applied, and this value corresponds to the shakedown limit for pure rolling according to the shakedown map as shown in Fig. 2-10a. The cyclic rolling contact was simulated by translating the contact pressure distribution on the steel surface along the longitudinal direction. The results showed that this approach can successfully capture the stress–strain history and the cyclic plastic deformation. In addition, both materials can rapidly achieve cyclic stabilisation. Later, Kulkarni et al. (1991a) repeated this work to study the plastic deformation of both materials under a load factor of 6, which is above the plastic shakedown limit. The results revealed that the plastic deformation mainly occurred at the subsurface for the ELKP material, while it was observed on the surface for the EPP material. Additionally, the ELKP material became cyclically stabilised after one loading cycle while ratcheting was found in the case of EPP material. Following the same approach, Kulkarni et al. (1991b) implemented the actual properties of wheel and rail materials to the ELKP material model to investigate the ratcheting in the rail under a load factor of 9.2.

The results highlighted that the rail material became cyclically stabilised after one cycle and no ratcheting occurred.

Ringsberg et al. (2000b) developed a 3D wheel–rail model to simulate the plastic strain and residual stress fields in the rail head. This model was then applied to simulate a wheel–rail two-point cyclic rolling contact (wheel flange–rail gauge corner and wheel tread–rail top) problem by translating the distributions of normal contact pressure and surface tangential traction repeatedly (Ringsberg, 2001 & Ringsberg & Josefson, 2001). The surface traction was assumed as proportional to the normal contact pressure and the friction coefficient was obtained from twin-disc tests (Ringsberg et al, 2000a). However, it is worth noted that partial slip usually takes place between the actual wheel and rail contact instead of full slip. The simulations considered both Hertzian contact pressure (Ringsberg, 2001) and non-Hertzian contact pressure distributions (Ringsberg & Josefson, 2001), which were obtained from the commercial software packages: CONTACT and MEDYNA. The results indicated that larger accumulation of plastic strain was observed in the Hertzian case and the non-Hertzian case showed better agreement with the initiation of head checks from field tests. This highlighted that a non-Hertzian contact pressure distribution can provide a more realistic simulation for practical wheel–rail cyclic rolling contact. Additionally, Ringsberg (2001) used an analytical model based on the concepts of energy-density and critical plane to predict the RCF initiation life due to plastic shakedown and ratcheting as reviewed in Chapter 2.3.3.

Xu & Jiang (2002) created a two-dimensional (2D) FE rail model to simulate a steady state of line rolling contact under several partial slip conditions. Same as previous studies, the Hertzian contact pressure distribution was used. The contact area was divided into slip and stick zones according to the contact theory (Johnson, 1985) and the tangential tractions were estimated based on Carter's theory (Carter, 1926). Jiang et al. (2002) extended the same methodology to develop a 3D rail model for analysing the effects of different partial slip rolling contact conditions on the contact stresses. The results from both simulations revealed that slip conditions can significantly affect the contact stresses and

strain fields near the contact surface. Also, the maximum ratcheting strain and corresponding location were sensitive to slip conditions and the enhanced plasticity introduced by the surface traction will accelerate the failure of a rail element. Years later, Wen et al. (2005) applied the same approach as Xu & Jiang (2002) to investigate the influence of different partial slip conditions on a non-steady state of wheel–rail 2D rolling contact. The results showed that the contact stresses are sensitive to not only the surface traction but also the harmonic variation in normal contact pressure. Wen et al. (2011) extended the work on a 3D rail model and their results highlighted that an appropriate constitutive plasticity model, which can reasonably capture the ratcheting behaviour of rail materials, is of paramount importance for simulating wheel–rail cyclic rolling contact problems with an acceptable accuracy. Similar work was also conducted by Chen & Chen (2006), which investigated the effects of an insulated rail joint on the contact stresses under partial slip conditions.

Lu et al. (2011) utilised the same method as Xu & Jiang (2002) and Wen et al. (2005) and meantime introduced the constitutive model established by Jiang & Sehitoglu (1996) to predict the RCF initiation life of rail under different contact pressure distributions. However, their results are limited to 2D wheel–rail cyclic rolling contact problems. Pun et al. (2015a) evaluated the ratcheting performance of rail materials and further predicted their RCF initiation life by simulating the wheel–rail cyclic rolling contact quasi-statically, which was achieved through repeatedly translating the distributions of non-Hertzian normal contact pressure and longitudinal tangential traction on the rail surface. The normal contact pressure distribution was obtained from a quasi-static wheel–rail contact simulation, while the longitudinal tangential traction distribution under different slip conditions was estimated based on the Haines and Ollerton's strip theory (Haines & Ollerton, 1963) and Carter's theory (Carter, 1926). An advanced ratcheting constitutive model was established for the rail materials (Pun et al., 2014a). The results of RCF initiation life were in good agreement with the performance of in-service rail materials. Based on this work, Srivastava et al. (2017) introduced a heat flux distribution to analyse the ratcheting of the temperature-dependent rail steels.

All the previous studies reviewed were applied the quasi-static method to simulate the wheel rail cyclic rolling contact. With the development of high-performance clusters in last 20 years, there is an increasing number of works that used the dynamic transient analysis for the wheel–rail rolling contact simulations. However, none of them can simulate cyclic situations due to an extremely high computational cost as mentioned in Chapter 2.2.3. Despite this, the dynamic transient analysis of 'single pass' can still provide researchers with a better understanding of wheel–rail rolling contact in reality. Zhao et al. (2007) created a 3D vehicle–track FE model to investigate the dynamic stress state of the rail surface and the influence of the tangential traction. The results revealed that the dynamic effects were significant, even on the smooth rail contact surface, and the tangential traction can greatly increase the shear stress at the rail surface and reduce the oscillations of the contact stress. Zhao & Li (2011) developed a 3D transient FE model to solve both the normal and the tangential contact problems simultaneously for arbitrary geometry, which was validated by the HCT and the CONTACT software. Years later, they solved a frictional rolling contact problem in elastic-plasticity by the explicit FE method (Zhao & Li, 2015) and similar work was also conducted by Deng et al. (2015) & Wei et al. (2016). Zhao & Li (2016) further proposed a solution of transient rolling contact with velocity-dependent friction.

Li et al. (2008a) established a transient FE model of vehicle–track interaction to analyse the causes of squats and the numerical results showed good correspondence with observed phenomena at squats. Zhang et al. (2014) combined the dynamic FE model with the ALE method to simulate the unsteady state of wheel–rail rolling contact. Vo et al. (2014) investigated the stress state of a rail under high and low adhesion conditions by a 3D dynamic wheel–rail rolling contact model. The results showed that a higher level of adhesion would enlarge the slip region in the stick/slip contact patch and widen the surface damage to a larger area. Additionally, the rail would be damaged due to ratcheting. Vo et al. (2015) applied the same method to predict the damage formation on curved track for various worn status of wheel/rail profiles. Özdemir & Voltr (2017) analysed the wheel–rail rolling contact under in low adhesion and low speed conditions. Martua & Ng (2018) developed a dynamic

3D FE model to predict the RCF initiation life and identify the crack plane orientation based on the analytical model proposed by Jiang & Sehitoglu (1999).

Dynamic transient analysis is also widely applied to investigate the dynamic effects induced by rail irregularities, i.e. insulated rail joint, weld (see Chapter 2.5.3) and squat. Pang & Dhanasekar (2006) simulated a wheel passing an insulated rail joint through a 3D wheel–rail rolling contact model. The results indicated that in the vicinity of the joint, the normal contact pressure was different from the region away from the joint and the maximum contact pressure occurred just after the impact of the wheel. Li et al. (2008b) investigated the effects of locations with variation in track stiffness on the formation of squats by simulating a dynamic rolling contact at a fish-plated insulated joint. Zhao et al. (2013) established a 3D transient FE model to calculate the vertical and the tangential dynamic wheel–rail contact forces caused by squats. The results showed that the system was mainly excited at two frequencies separately in the vertical and the longitudinal dynamics. As a squat grows up, the magnitude of the excited vibration at a lower frequency increases faster than the one at a higher frequency. After that, Molodova et al. (2014) used the same approach to capture the dynamic features of axle box acceleration related to squats in a high frequency range. Yang et al. (2018) presented an analysis of transient contact solutions to wheel–rail frictional rolling impacts by an explicit FE model of the wheel-insulated rail joint dynamic interaction.

2.5.3 Wheel–Rail Weld Contact

Steenbergen & Esveld (2006) created an FE model to simulate the wheel–rail interaction at rail welds. The results indicated that a good correlation between the maximum dynamic wheel–rail contact forces and the gradient of the rail weld geometry. Following on this, Steenbergen (2008) developed an analytical model to further calculate the dynamic contact forces on the rail weld surface and the solution can be correlated with the simulated results obtained in Steenbergen & Esveld (2006). Wen et al. (2009) studied the influence of surface irregularities at rail flash butt welds on dynamic wheel–rail interaction. A

vehicle–track model was first developed to obtain the dynamic results of wheel–rail contact forces. The normal contact pressure distribution was then calculated based on the HCT and the surface traction was considered to be proportional to the contact pressure distribution. After that, these results were input to a 3D FE rail model to calculate the stress and plastic deformation in the vicinity of the rail welds. The PR and weld regions were considered as elastic-plastic combined with the linear kinematic hardening rule. However, no detail about the properties of the softened region was mentioned. The results revealed that high impact loads caused by the irregularities on the rail weld surface can result in high stress and severe localised plastic deformation at both the rail weld and the PR near the weld. Combined with the deformed rail profile, the damage would be more hazardous. Therefore, it was recommended that the surface irregularities at rail welds need to be controlled to decrease the damage caused by impact loads.

Li et al. (2011) applied the same approach and material properties as Wen et al. (2009) to investigate the plastic deformation of a rail weld caused by train–curved track dynamic interactions. The FASTSIM algorithm was introduced to obtain the surface tangential traction and define the stick and slip zones on the contact patch. In addition, the mechanical properties of the HAZ were applied and the results concluded that it is necessary to consider the effects of the HAZ on the plastic deformation of rail welds. The accumulated plastic deformation caused by the high impact loads changed the rail profile of the welds and hence, increased the impact loads between the wheel and rail. Sichani & Bezin (2018) incorporated vehicle–track dynamic interaction, wheel–rail contact mechanics and wear modelling to predict differential wear due to the material inhomogeneity caused by rail head weld repairs. The results indicated that regardless of the magnitude of hardness variation within the HAZ, the long-term surface degradation can be minimised by limiting the length over which the variation occurs. Pun et al. (2017) extended the same approach (Pun et al., 2015a) to conduct a preliminary analysis of ratcheting performance of rail flash butt welds. Due to lack of a constitutive cyclic plasticity model for rail welds, the ratcheting behaviour of the HAZ was assumed as same as that of the PR. Some material parameters of the HAZ were estimated based on the difference in

hardness among the BL section, the softened region and the PR. This analysis was conducted to simulate only one cyclic rolling contact, the results showed that the softened region experienced a higher degree of plastic deformation, which may lead this area to be a susceptive point for RCF initiation. Deng et al. (2019) used FE simulations to verify their proposed hypothesis of the squat formation process at welds (see Chapter 2.1.3). A dynamic wheel–rail rolling contact simulation was initially performed to obtain the geometric irregularities due to the presence of HAZ. After that, such irregularities were applied to the rail surface. By multiplying the deformation by a specific factor, which was derived based on the field measurements, to account for the effect of multiple wheel passages, the evolution of the change in surface pattern was obtained. Although the weld region was assigned with different yield strength, its hardening behaviour was assumed as the same with the PR.

2.5.4 Summary

In conclusion, wheel–rail rolling contact problems can be simulated by either quasi-static method or dynamic transient analysis. The former is usually conducted by translating both contact pressure distribution and tangential traction distribution on the rail surface. Although many related studies have been performed, most of them applied the Hertzian contact pressure distribution which can cause significant discrepancies between the numerical results and the practical wheel–rail rolling contact situations. Therefore, a non-Hertzian pressure distribution is more suitable. With regard to the dynamic transient method, it can capture the dynamic features caused by the wheel–rail rolling contact, which means that the simulated results are close to the practical situations. However, as mentioned in Chapter 2.2.3, a fine mesh zone may be required on the complete circumference of both wheel and rail. Moreover, a certain length of rolling distance from the initial position of wheel to a quasi-steady state is necessary to damp the oscillations generated by the kinematic and potential energy from breaking the static state of wheel–rail contact. A relatively small-time step has to be selected to guarantee the stability of the explicit integration. These reasons can increase the computational costs

dramatically and thus, current dynamic analysis is limited to only one pass. In addition, a reliable constitutive cyclic plasticity model for rail materials is necessary for ratcheting analysis and further prediction of RCF initiation, particularly for rail welds. Due to the sophisticated plasticity of rail welds, very limited numerical simulations on the wheel–rail weld rolling contact have been carried out. Therefore, challenging tasks for the FE method in the future will be how to simulate the wheel–rail cyclic rolling contact by dynamic transient analysis properly and deal with complex non-linear problems, i.e. ratcheting performance of rail welds, more efficiently.

2.6 Chapter Summary

In this Chapter, basic knowledge of rail flash butt welds has been firstly introduced and it is indicated that more rolling contact fatigue damage associated with welds has become a critical issue in railway systems mainly due to the presence of 'discontinuities', consisting of geometry irregularities, material inhomogeneities and residual stress, which result in welds more susceptible to damage than parent rails. After that, a brief review of wheel–rail interface has been provided, including existing theories and methods for analysing the wheel–rail interface with typical studies, and investigations on rail materials, particularly the ratcheting behaviour and its induced degradation, wear and rolling contact fatigue. Additionally, some existing strategies for controlling or mitigating rail/weld degradation have been discussed. The overall review highlighted that RCF damage in rails caused by ratcheting is still a dominant concern in the wheel–rail interface, even though plenty of related experimental and numerical works have been conducted to investigate the rolling contact fatigue damage in the past few decades.

According to the literature reviewed in this chapter, the demanding conditions imposed by rail transport with higher axle loads and increasing annual haulage rates lead to increased rates of rail degradation. Although these situations can be controlled and mitigated by the development and application of higher strength rail steels, increased sensitivity to more rolling contact fatigue damage

associated with rail flash butt welds has been identified, especially in heavy haul railways. This motivation supports this doctoral research to study the plastic deformation, particularly the ratcheting behaviour, of flash butt welds in the latest generation of high strength rail steels (R400HT) currently used in Australian heavy haul operations. As each material has its unique ratcheting behaviour, experimental study by monotonic tensile tests, uniaxial stress-controlled cyclic loading tests and biaxial compression–torsion cyclic loading tests were firstly carried out on these welds, followed by microstructural analysis (Chapter 3). Based on the experimental results, a developed constitutive cyclic plasticity model for high strength rail steels was updated for these welds (Chapter 4). Finally, numerical simulations on wheel–rail weld cyclic rolling contact were performed to evaluate the ratcheting performance of these welds under in-service conditions and further predict the initiation of rolling contact fatigue (Chapter 5). It is expected that the research outcomes can provide a better understanding of rolling contact fatigue in rail flash butt welds for rail operators and further assist them developing more cost-effective rail maintenance strategies.

Chapter 3

Experimental Study on Ratcheting Behaviour of Flash Butt Welds in High Strength Rail Steels

Experimental study consisting of both uniaxial and biaxial stress-controlled cyclic loading tests was performed to investigate the ratcheting behaviour of new flash butt welds in a heat-treated hypereutectoid rail steel (R400HT) used in Australian heavy haul railways. Digital image correlation technology was applied to capture the heterogeneous strain field and its evolution at every point on the surface of the weld specimen. The results show that the distribution of ratcheting strain can almost correlate with the longitudinal hardness profile of the weld. Moreover, the softened zone with a significant hardness drop is more sensitive to plastic deformation and results in higher ratcheting strain than the region around the bond line. Compared with the parent rail, the softened zone shows much worse ratcheting resistance, while the region around the bond line demonstrates slightly better ratcheting resistance. Metallographic analysis indicates that the microstructure and resulting ratcheting resistance of the weld vary with its longitudinal position. High ratcheting strain in the softened zone is mainly attributed to the existence of the spheroidised microstructure with a

high amount of ferrite. The outcomes of this study can provide valuable information for further establishing the constitutive models to quantify the heterogeneous ratcheting of rail welds under practical wheel–rail cyclic rolling contact situations by finite element simulations.

3.1 Materials and Specimens

The materials considered in this study are new rail flash butt welds in an R400HT (hypereutectoid heat-treated) rail steel grade with a carbon content of 0.88%. The hardness of such a rail steel grade is approximately 400 HV and its chemical composition is listed in Table 3-1. Five tested 68 kg/m weld samples were manufactured by using a Chemetron mobile flash butt welder under the same welding conditions, meaning that the quality of each weld sample is almost identical.

Table 3-1: Chemical compositions of the R400HT flash butt rail welds.

Element type	C	Si	Mn	Ni	P	S	Cr	Cu
Content (%)	0.88	0.31	0.92	0.01	0.014	0.01	0.21	0.02

Thin-walled tubular specimens were extracted from the weld samples for monotonic tensile tests and uniaxial stress-controlled cyclic loading tests due to the loading capacity of the test machine. Such a type of specimen was also used for the biaxial stress-controlled cyclic loading tests to provide a nearly uniform strain distribution through the thickness of the specimen gauge. Each specimen was only used for one test. It is known that RCF cracks currently observed in rails or weld regions for heavy haul operations can propagate up to about 15 mm below the running surface (Marich, 2009). Hence, as presented in Fig. 3-1a, the location of the specimen gauge in the cross-sectional view (transverse direction) of each weld sample have reached such depth. In order to confirm the location of the specimens in the longitudinal direction of the weld sample, the longitudinal hardness of each weld sample was measured approximately 8 mm

below the running surface on the examined section which showed the BL and HAZ boundaries after being macro-etched by 2% Nital solution. It is worth noted that the longitudinal hardness profile is almost constant in each weld sample as all the rail samples were welded under the same welding conditions.

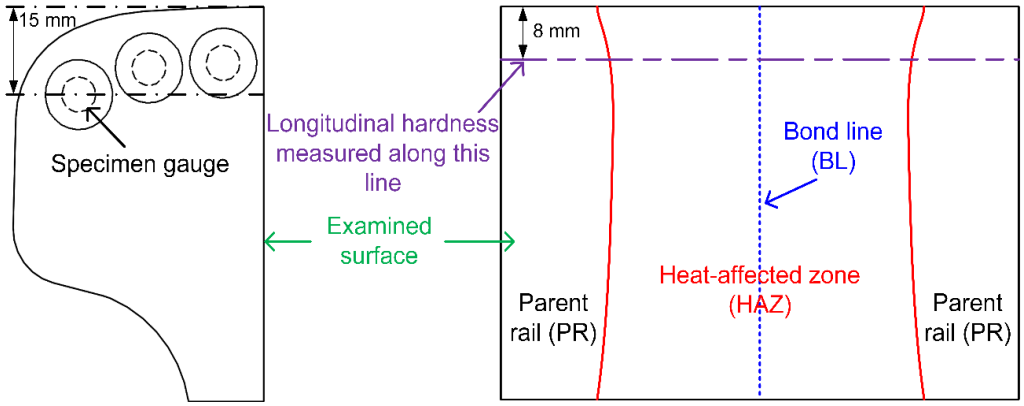

(a)

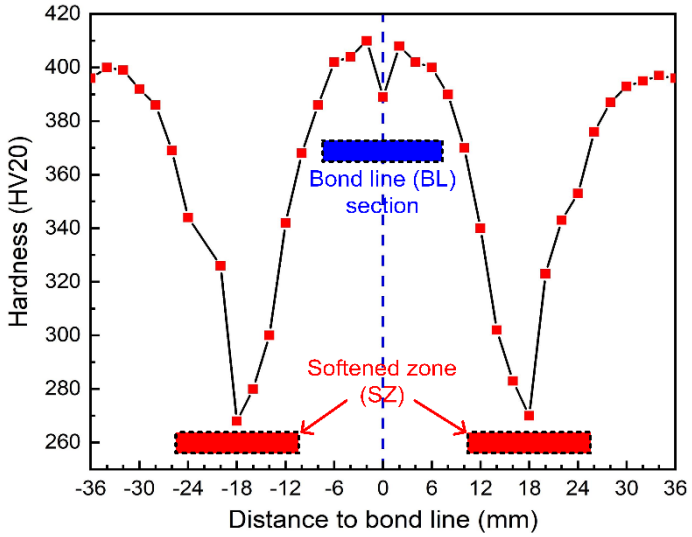

(b)

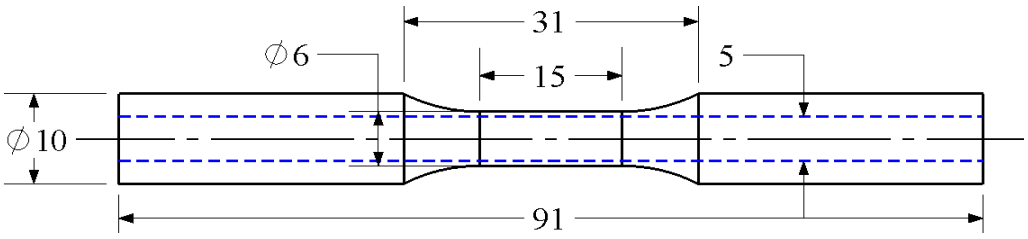

(c)

Figure 3-1: Illustration of the locations and the dimensions of the specimens: (a) specimen locations in the cross-section of a rail weld head sample and the examined surface for longitudinal hardness measurement; (b) longitudinal hardness distribution and specimen gauge locations along the longitudinal direction; (c) dimensions of a thin-walled tubular specimen (mm); (d) a finalised tubular specimen.

(d)

Figure 3-1: Continued.

Fig. 3-1b shows the longitudinal hardness distribution of one of five weld samples. The hardness within the region about 7 mm to the BL is slightly higher than that of PR (396 HV approximately) except for a small drop at the BL, and then reduces significantly to around 270 HV at 18 mm to the BL. Finally, the longitudinal hardness increases back to the value of PR at about 28 mm to the BL. Based on the obtained longitudinal hardness profile, specimens were extracted and machined by electric discharge machining and turning from two positions in each rail weld head sample at the BL and the HAZ with the lowest hardness, so called BL section and SZ, respectively. The hole in each tubular specimen was created by the deep hole drilling method. The machining was performed under the conditions that minimised any heating of the specimens, to avoid introducing microstructural changes. Fig. 3-1c shows the dimensions of the specimens in detail and specifically, each specimen has a total length of 91 mm, an outer diameter of 10 mm for the grip section, an outer diameter of 6 mm for the gauge section and an inner diameter of 5 mm. It is worth noted that each specimen has a gauge length of 15 mm so that both types of the specimens can almost cover the entire weld region. In addition, the hardness value in any cross-section of the specimens is like that measured along the longitudinal direction of the weld sample. The finalised tubular specimen is shown in Fig. 3-1d.

Extra specimens with the same dimensions were also machined at the similar transverse locations from head of the PR at approximately 100 mm to the BL, which is far enough from the weld region. A total of 48 specimens were prepared, which consists of 16 specimens for each tested section (BL section, SZ and PR). It should be noted that the influence of the residual stress in the weld samples is not considered in this work as previous research (Webster et al., 1997, Tawfik

et al., 2006 & Jiang et al., 2013) has shown that most of the residual stress should be released during the machining of the specimens. All the specimens were finally polished by a polisher before the tests. During the preparation of the specimens, the extent of the increase in temperature was not enough to cause any change to the microstructure.

3.2 Experimental Program

All the tests were performed at room temperature using a servo-valve controlled electro-hydraulic testing machine MTS858-Bionix (Fig. 3-2a), which can control axial force and torque simultaneously, and has a maximum loading capacity of 15 kN. The triangular waveform was chosen in the cyclic loading tests without any peak/valley stress holding time. Data covering force, torque, displacement, and rotational angle were collected and recorded by the Flex-Test 40 system during the experiments. The axial and equivalent shear stresses were determined from the axial force and the torque, respectively. To capture the heterogeneity of strain fields in the weld specimens, a 3D non-contact DIC equipment (Fig. 3-2b), ARAMIS-5M from GOM GmbH Ltd. in Germany, was applied to measure the strain field and its evolution during the tests at every point on the gauge surface of the specimens. DIC is a method to evaluate the deformation by image analysis (Nakata et al., 2012). Specifically, the change of random patterns on gauge surface caused by the deformation can be obtained, and then the strain value is determined by correlating the surface brightness distributions before and after the deformation (Peters & Ranson, 1982). Due to this, an extensometer is unable to be employed on the gauge section of the specimens and this indicates that strain-controlled cyclic loading tests cannot be conducted. It should be noted that all the strain results provided in the following contexts of this chapter were obtained by averaging the values within a specific zone. For example, the strain of the SZ means the average of the strain value at each point within the SZ.

Note that, the measurement accuracy of DIC method depends on the quality of random speckle pattern, selection size of statistic domain, lens distortion, image

noise and so on. Therefore, in this work, the DIC equipment was calibrated by the standard procedure before the experimental tests were carried out. To confirm the measurement accuracy of the DIC equipment, two monotonic tensile tests on the BL section were firstly conducted and the corresponding strain data was measured by the DIC method and a conventional extensometer, respectively. As illustrated in Fig. 3-3, two stress – strain curves present a good agreement with each other and this indicates that the accuracy of the calibrated DIC method is acceptable.

(a) (b)

Figure 3-2: Experimental facilities: (a) MTS858-Bionix test machine with the Flex-Test 40 system; (b) DIC system.

All the tests were not repeated and only one specimen from each tested section was tested under each loading conditions due to the limited number of specimens. Monotonic tensile tests were carried out to obtain some basic mechanical parameters of the tested weld samples, such as yield strength and ultimate tensile strength. These parameters were applied to determine the appropriate stress level to be used in uniaxial and biaxial stress-controlled cyclic loading tests for investigating the ratcheting behaviour. Specifically, the applied maximum stress during these tests should be higher than the yield strength to cause ratcheting, but should not be too close to the ultimate tensile strength in order to avoid the specimens failing prematurely (Pun et al., 2014b). All the cyclic loading tests were performed under a loading rate of 100 MPa/s and

stopped at 100 loading cycles which were sufficient to obtain a stabilised ratcheting strain rate. It should be noted that the current study is not to examine the fatigue life of rail welds and the influence of ratcheting on the fatigue life, since the aim is to only investigate the ratcheting behaviour of the rail welds.

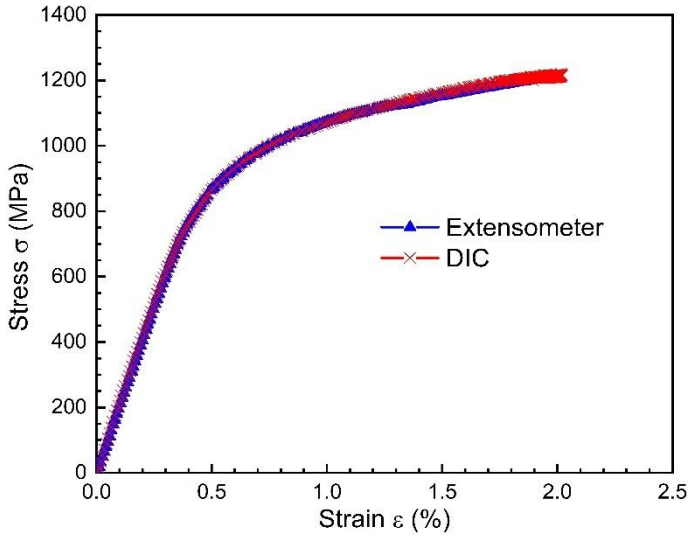

Figure 3-3: Comparison of the stress – strain curves of the BL section by the DIC method and the extensometer under the monotonic tensile tests.

Uniaxial stress-controlled cyclic loading tests were conducted under various mean stresses and stress amplitudes to evaluate their effects on the ratcheting behaviour of the weld region, while biaxial compression–torsion stress-controlled cyclic loading tests were carried out to simulate the loading experienced by wheel–rail weld contact situations. As mentioned in Chapter 3.1, similar tests were also performed on the PR specimens. The specific loading condition of each cyclic loading test is illustrated in Chapter 3.3. From each test, the ratcheting strain (axial: ε_r, torsional: γ_r) in every loading cycle was obtained by averaging the corresponding maximum and minimum strains of a specific zone, see Eqs. (2-1) and (2-2). The ratcheting strain rate (axial: $d\varepsilon_r/dN$; torsional: $d\gamma_r/dN$) was then determined as the increment of the ratcheting strain per loading cycle. Taking the axial direction as an example, the following criterion (Eq. 3-1) is applied to judge if the ratcheting strain rate reaches cyclically stabilised:

$$\left|\frac{(d\varepsilon_r/dN)_{max,N} - (d\varepsilon_r/dN)_{max,N-1}}{(d\varepsilon_r/dN)_{max,N-1}}\right| < 5\% \qquad (3-1)$$

where $(d\varepsilon_r/dN)_N$ is the axial ratcheting strain rate in the current loading cycle and $(d\varepsilon_r/dN)_{N-1}$ is the axial ratcheting strain rate in the previous loading cycle. If such criterion is satisfied in ten continuous loading cycles, the specimen will be considered as cyclically stabilised. In order to judge if the material exhibits cyclic hardening or softening, strain amplitude ε_a in each loading cycle was obtained from half of the difference between the maximum and the minimum strains of a specific zone, see Eq. (2-3). It should be noted that engineering stress and engineering strain are used in the experimental study.

3.3 Results and Discussion

3.3.1 Monotonic Tensile Tests

Fig. 3-4 shows the stress-strain curves of BL section, SZ and PR from the monotonic tensile tests. The basic mechanical properties of Young's modulus E, yield strength $\sigma_{0.2}$, ultimate tensile strength σ_{ult}, elongation δ at specimen fracture, reduction of area R and ductility D are summarised in Table 3-2. The reduction of area is defined as the proportional reduction of the cross-sectional area of the specimen measured after the fracture under the monotonic tensile test. The ductility D is estimated by the same equation used in Pun et al. (2015a):

$$D = ln\left(\frac{1}{1-R}\right) \qquad (3-2)$$

The results show that both the BL section and the SZ have almost the same value of Young's modulus as the PR, while the SZ has the lowest yield strength and ultimate tensile strength among all the test locations due to lower hardness. When the specimens fractured, the BL section gave the smallest elongation of 2% and ductility value of 2.2%. This indicates that the BL section is far less ductile than the SZ and the PR. It is noteworthy that the SZ shows the largest reduction of area and therefore is the most ductile among all the test locations,

with a ductility value of 30.9%. However, the elongation of the SZ is only 4.2%, which was even much lower than that of the PR. This is mainly because the elongation measured is the average value within the entire gauge section of the specimen, while the localised elongation at the fracture point reaches up to 13%. Such results can be attributed to the heterogeneity of the SZ, which will be further explained in the following context.

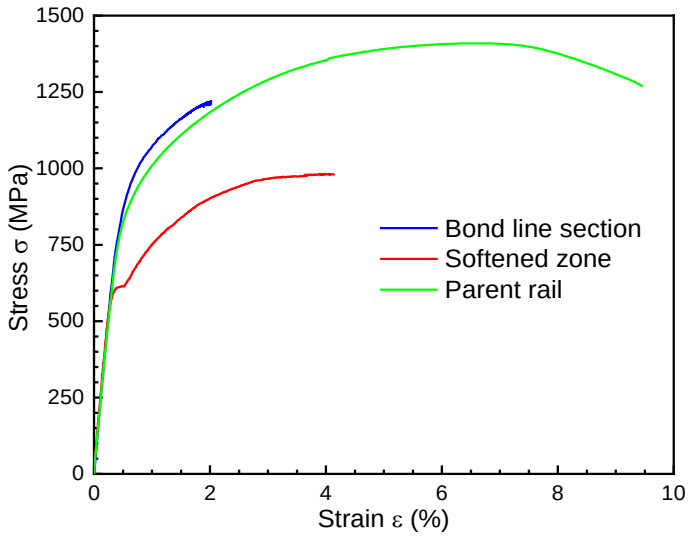

Figure 3-4: Stress–strain curves of the BL section, SZ and PR from the monotonic tensile tests.

Table 3-2: Basic mechanical properties of the BL section, SZ and PR from the monotonic tensile tests.

Test location	Young's Modulus E (GPa)	Yield strength $\sigma_{0.2}$ (MPa)	Ultimate tensile strength σ_{ult} (MPa)	Elongation at specimen fracture δ (%)	Reduction of area R (%)	Ductility D (%)
BL section	210	963	1220	2	2.2	2.2
SZ	212	615	981	4.2	26.6	30.9
PR	210	890	1268	9.5	21.6	24.3

To investigate the evolution of the strain fields, the strain contours of the gauge sections of the BL section and the SZ at different stages of the monotonic tensile tests are presented in Figs. 3-5 and 3-6, respectively. The results show that the strain distribution of the BL section is almost homogeneous with the increase in

stress, even though some fluctuations can be observed along the black dash line. For example, the localised strain along the black dash line fluctuates at around 1.68% at stage d. In comparison, when the applied stress exceeds the localised yield point of the SZ specimen, the strain starts to be concentrated approximately at the midpoint (stage b and afterwards), which corresponds to the position with the lowest hardness as demonstrated in Fig. 3-1b. This indicates that SZ is more sensitive to plastic deformation than the BL section and therefore, it is more valuable to investigate the localised deformation in the SZ under different loading tests.

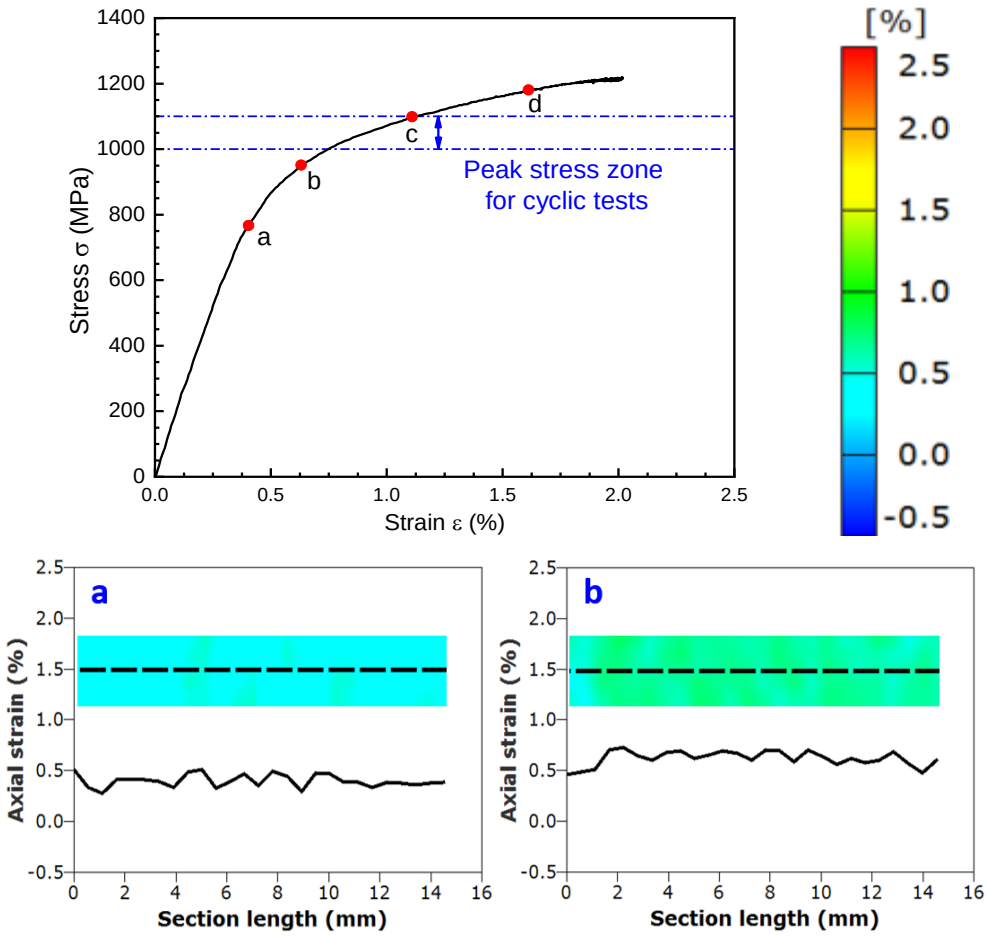

Figure 3-5: Strain contours of the BL section at different stages of the monotonic tensile test.

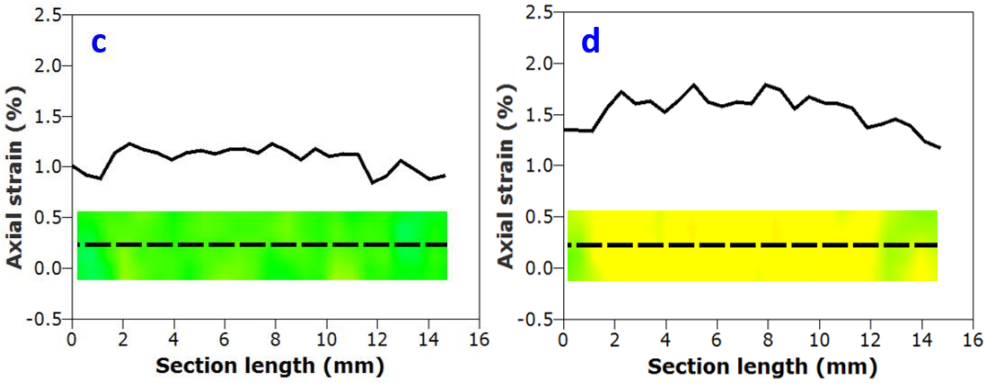

Figure 3-5: Continued.

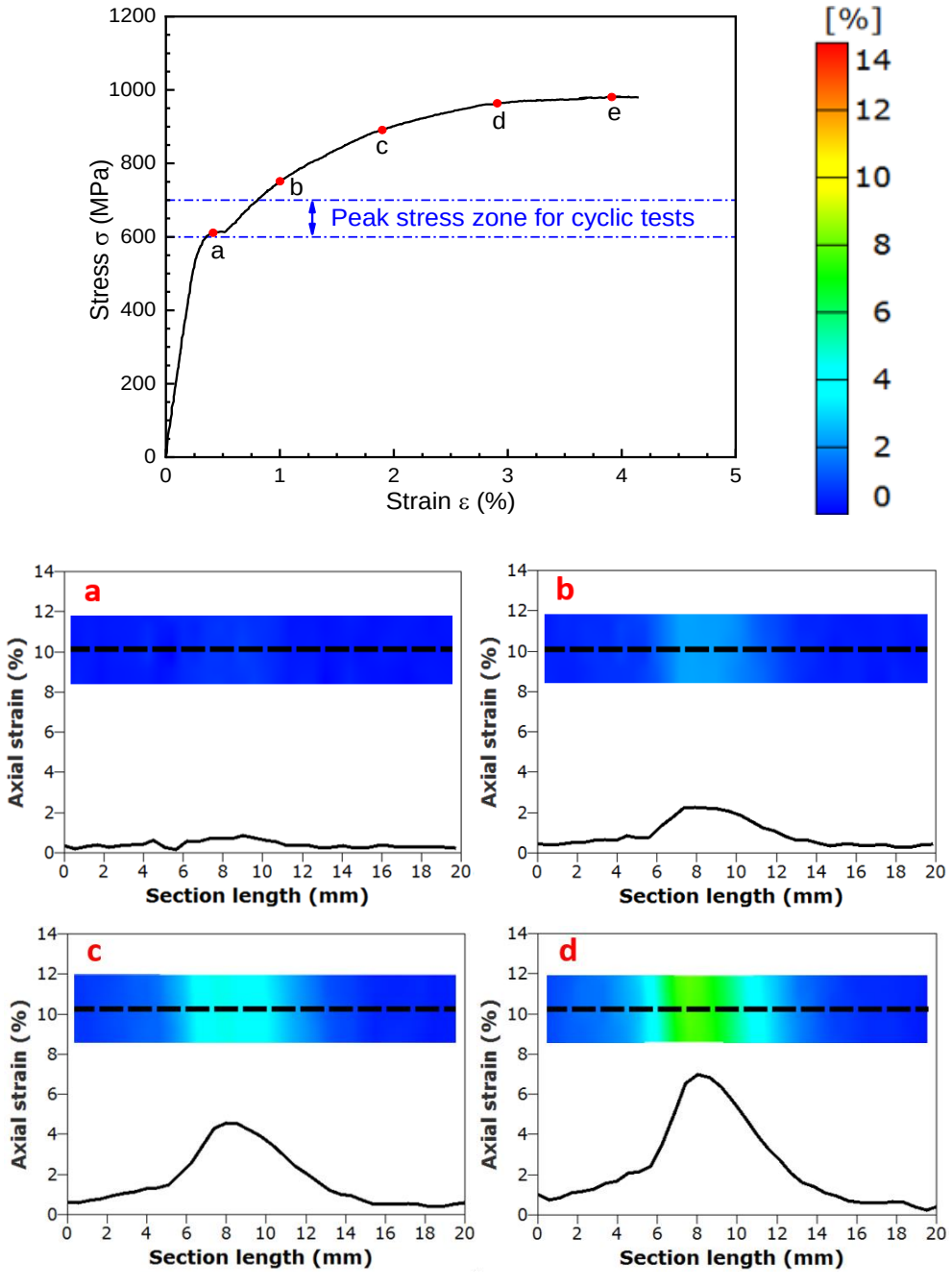

Figure 3-6: Strain contours of the SZ at different stages of the monotonic tensile test.

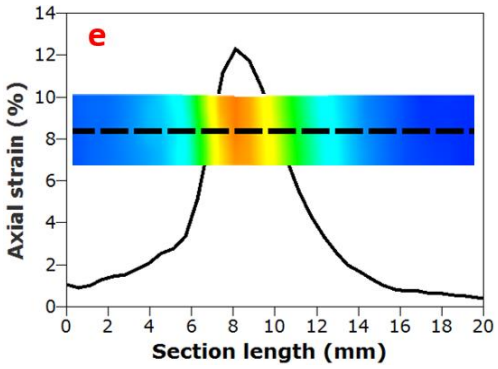

Figure 3-6: Continued.

Subsequently, the SZ has been divided into multiple subzones, and their corresponding hardness and strain at the specimen fracture are presented in Fig. 3-7a. It should be noted that the specimen fracture in the SZ occurred in the subzone 1B, which provides the lowest hardness among the weld region. The results also identify that the strain gradients in the SZ can almost correlate with its hardness gradients. Fig. 3-7b demonstrates the stress–strain curve and the corresponding yield strength of each selected subzone defined in Fig. 3-7a under the monotonic tensile test. It clearly shows that at the specimen fracture, the subzone 1B with the lowest yield strength experiences the highest strain of approximately 13%, which is 4.5% higher than that of the PR. Such phenomenon indicates that the SZ has better ductility than the PR as shown in Table 3-2. In addition, other subzones with a relatively higher yield stress, i.e. the subzone 5B with a strain value of only 3%, offset the strain of the whole SZ when the specimen fractured at the subzone 1B.

As mentioned earlier, carrying out monotonic tensile tests can not only provide some basic parameters of the materials but also help the design of cyclic loading tests for investigating the ratcheting behaviour. Based on the design criteria illustrated in Chapter 3.2 and the obtained yield strength of the weld region, the peak stress applied in the cyclic loading tests was selected within the range of 1000–1100 MPa for the BL section and 600–700 MPa for the SZ as presented by the blue dotted horizontal lines in the stress–strain curves in Figs. 3-5 and 3-6, respectively. According to Table 3-2, the PR has similar values of yield strength and ultimate tensile strength as the BL section. Hence, the same range

of peak stress was applied to the cyclic loading tests on the PR.

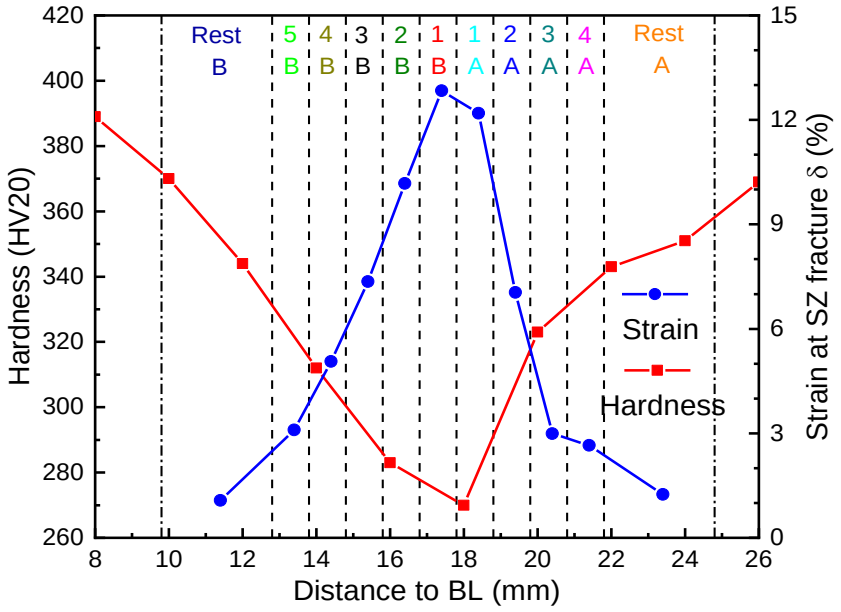

(a)

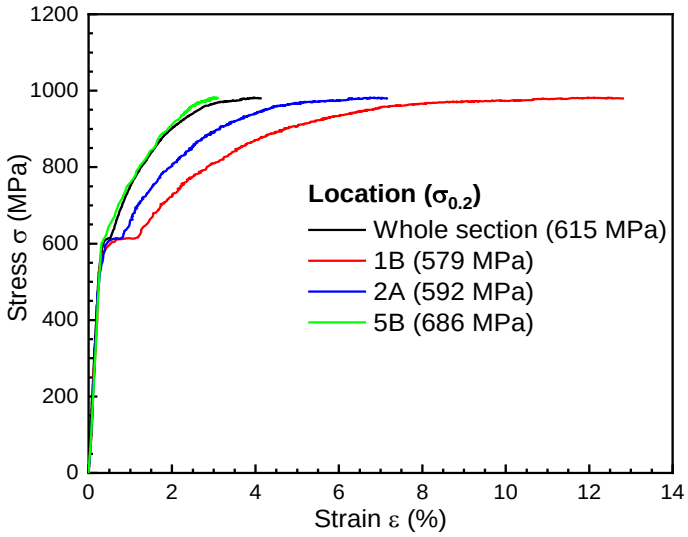

(b)

Figure 3-7: Heterogeneous strain distribution in the SZ under the monotonic tensile test: (a) definition of subzones with corresponding hardness and strain at the fracture of the SZ specimen; (b) stress–strain curves of selected subzones in the SZ with corresponding yield strength $\sigma_{0.2}$.

3.3.2 Uniaxial Stress-Controlled Cyclic Loading Tests

Generally, ratcheting behaviour can be observed when the material is subjected to asymmetrical cyclic loading. According to this, all the uniaxial stress-controlled cyclic loading tests were conducted under a non-zero mean stress. To

clearly illustrate the influence of stress amplitude on the ratcheting behaviour of the entire SZ gauge section, the ratcheting strain ε_r and the ratcheting strain rate $d\varepsilon_r/dN$ versus the number of loading cycles N under different stress amplitudes σ_a and a constant mean stress σ_m of 200 MPa are demonstrated in Figs. 3-8a and 3-8b, respectively. The results show that both ratcheting strain and ratcheting strain rate increase with stress amplitude. Such a relationship was also observed by Kolasangiani et al. (2018). Moreover, the ratcheting strain rate decreases with the increasing number of loading cycles and reaches cyclically stabilised after approximately 80 loading cycles, which reveals that the ratcheting behaviour is dominated by kinematic hardening. Similar information can also be summarised from the results showing the influence of mean stress σ_m on the ratcheting behaviour of the whole SZ in Fig. 3-9. After roughly 90 loading cycles, the ratcheting strain rate in each case becomes almost cyclically stabilised. Additionally, it is found that the evolution of the ratcheting strain under the mean stress of -100 MPa and 100 MPa is not perfectly symmetrical, which indicates that the ratcheting behaviour of the SZ under tension and compression is slightly different. Overall, the stress level applied can significantly affect the ratcheting response of the SZ.

Fig. 3-10 demonstrates the axial strain contours of the SZ gauge section with the defined subzones under the loading case of -100 ± 500 MPa at different loading cycles. Such a test dominated by the compressive stress is close to the practical wheel–rail contact situations. With the increasing number of loading cycles, the strain starts being concentrated mainly in the subzones with relatively lower hardness, i.e. subzones 1B, 1A, 2B and 2A, and gradually extends to other subzones. In addition, the ratcheting strain distribution can roughly correlate with the hardness gradients of the SZ as shown in Fig. 3-11, which demonstrates the relationship between the ratcheting strain distribution ε_r at the 100th loading cycle and the hardness profile of the SZ. Such results indicate that the ratcheting behaviour and its evolution are dependent on the hardness of each subzone.

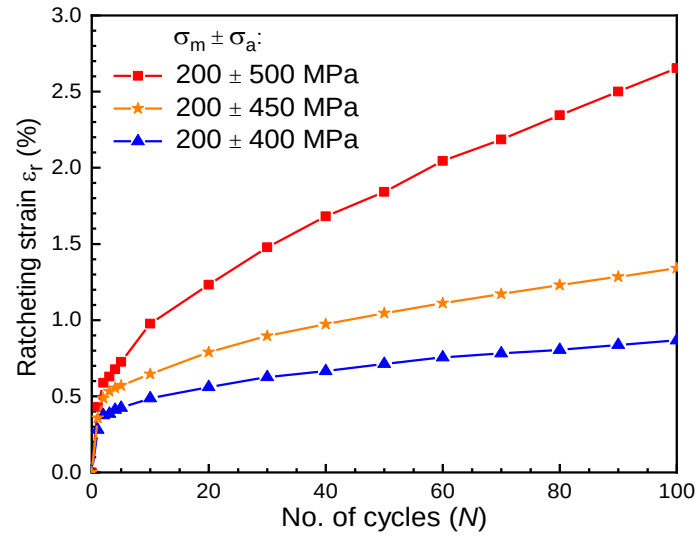

(a)

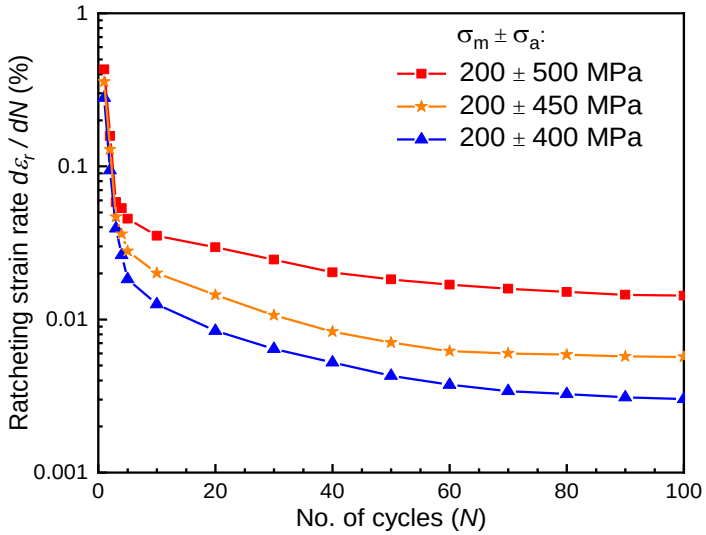

(b)

Figure 3-8: (a) Ratcheting strain ε_r; (b) ratcheting strain rate $d\varepsilon_r/dN$, versus number of loading cycles N under different stress amplitudes σ_a and a constant mean stress σ_m of 200 MPa for the entire SZ.

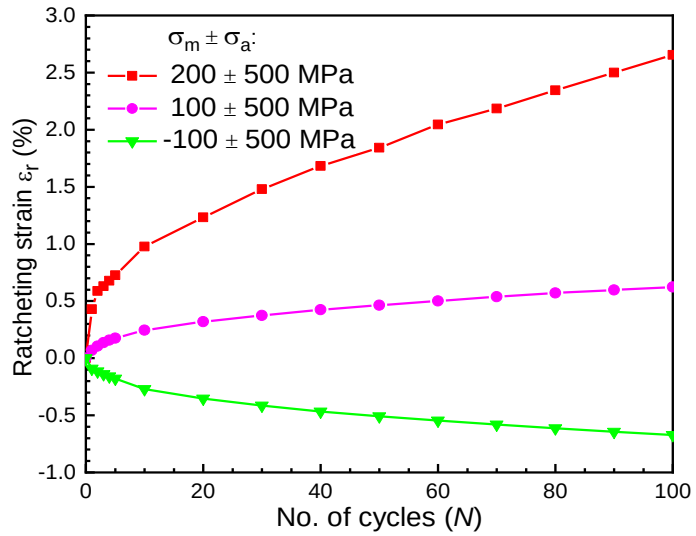

(a)

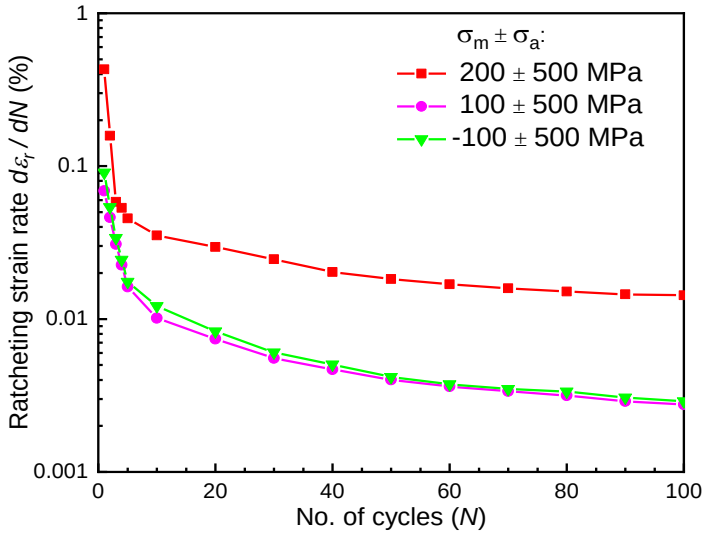

(b)

Figure 3-9: (a) Ratcheting strain ε_r; (b) ratcheting strain rate $d\varepsilon_r/dN$, versus number of loading cycles N under different mean stresses σ_m and a constant stress amplitude σ_a of 500 MPa for the entire SZ.

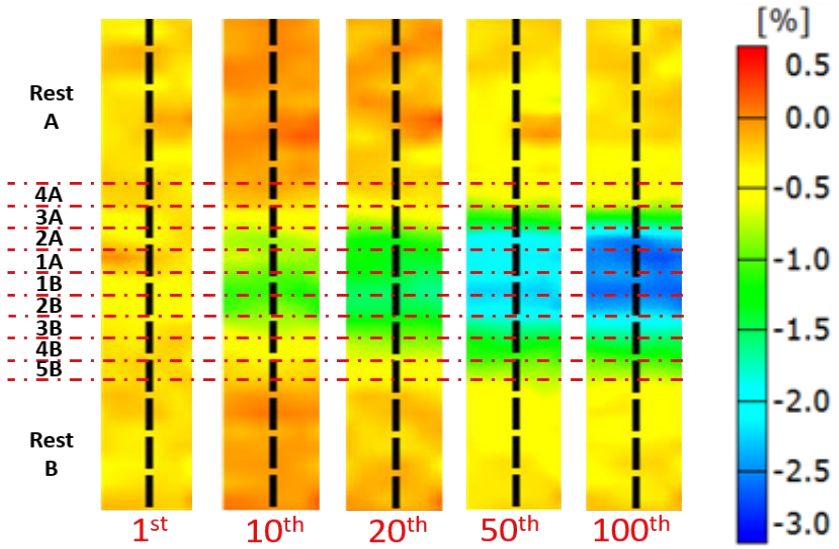

Figure 3-10: Illustration of the heterogeneous strain distributions in the SZ under the loading case of -100 ± 500 MPa.

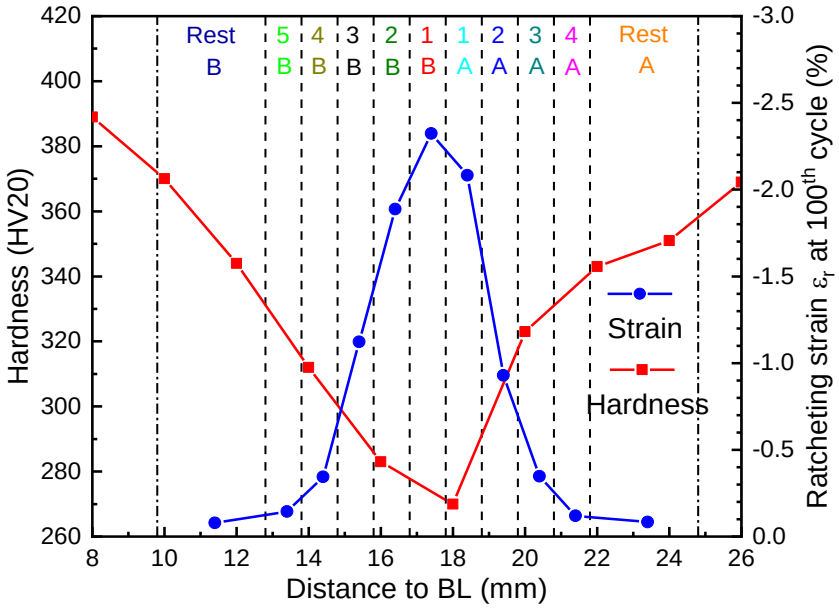

Figure 3-11: The relationship between the ratcheting strain distribution ε_r at the 100th loading cycle under the case of -100 ± 500 MPa and the hardness profile of the SZ.

To further understand the heterogenous nature of ratcheting behaviour in the SZ, the evolutions of ratcheting strain ε_r and ratcheting strain rate $d\varepsilon_r/dN$ for selected subzones in the SZ are shown in Figs. 3-12a and 3-12b, respectively. The results imply that the ratcheting strain of each selected zone increases quickly in the first few loading cycles, particularly the subzones 1B and 2A. After a certain number of loading cycles, the ratcheting strain continues increasing at an almost constant rate. At the 100th loading cycle, the ratcheting

strain of the subzone 1B reaches about -2.4%, approximately four times higher than that of the whole SZ. With regard to the ratcheting strain rate, the subzone 1B shows a stabilised value of 0.012% after 90 loading cycles, while the whole section only gives a stabilised value of 0.003% after 80 loading cycles. Since the yield stress of the subzone 5B (686 MPa) is higher than the subjected peak stress of 600 MPa, the corresponding ratcheting strain can be considered negligible compared with those of other subzones, and the corresponding stabilised ratcheting strain rate is significantly lower than that of the entire section. Such heterogeneities become more evident with the increasing number of loading cycles and directly related to the difference in yield strength and kinematic hardening behaviour of the subzones.

The ratcheting behaviour of the BL section under different stress levels is illustrated in Fig. 3-13. The results also show that both ratcheting strain and ratcheting strain rate increase with stress level, and a stabilised ratcheting strain rate can be obtained after a certain number of loading cycles. However, due to the higher yield stress of the BL section (963 MPa), its ratcheting strain under higher stress levels is much lower than that of the SZ subjected to lower stress levels. For instance, the entire SZ gives a ratcheting strain of 2.65% at the 100th loading cycle under the case of 200 ± 500 MPa as demonstrated in Figs. 3-8a . In contrast, the BL section shows a value of 1.7% even though the applied peak stress (1100 MPa under the loading case of 200 ± 900 MPa) is much higher than that of the SZ. Such discrepancy can also be observed in the tests dominated by compressive loading (the case of -100 ± 500 MPa for the SZ and the case of -100 ± 900 MPa for the BL section). Furthermore, the ratcheting strain under the loading case of -100 ± 900 MPa can be considered negligible, while that under the same stress amplitude σ_a but with a mean stress σ_m of 100 MPa reaches a value of 1.03% at the 100th loading cycle. This information indicates that the region around the BL has the greatest ratcheting resistance and is expected to experience larger ratcheting strain under tension than that under compression.

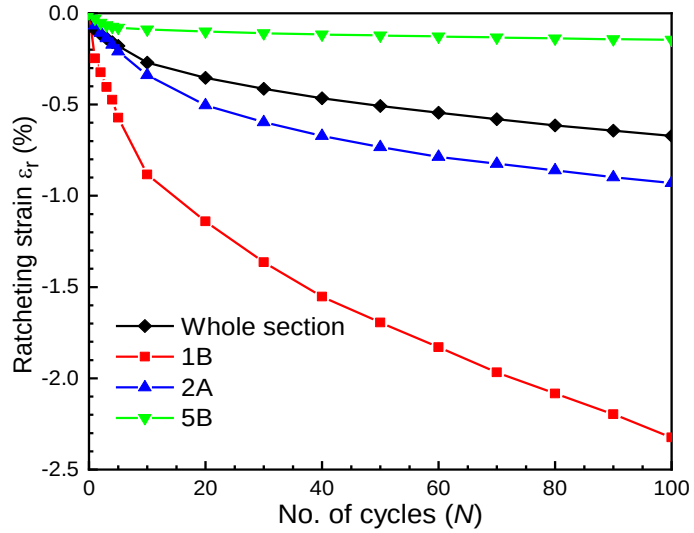

(a)

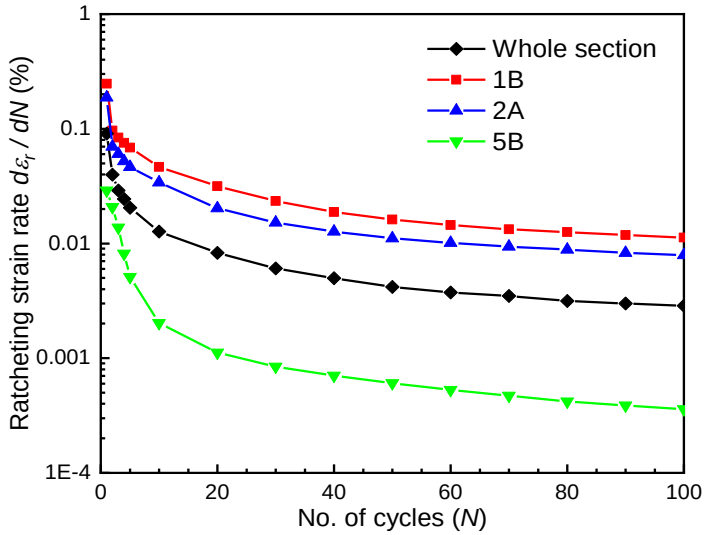

(b)

Figure 3-12: (a) Ratcheting strain ε_r; (b) ratcheting strain rate $d\varepsilon_r/dN$, versus number of loading cycles N under the case of -100 ± 500 MPa for selected subzones in the SZ.

Uniaxial stress-controlled cyclic loading tests were also conducted on the PR, and the results of ratcheting strain ε_r and ratcheting strain rate $d\varepsilon_r/dN$ are compared with those obtained from the tests on the BL section and the subzone 1B as illustrated in Fig. 3-14. The reason why the test conditions are different is that the SZ would fracture earlier if it were tested under the same stress level as the BL section and the PR. The results show that although the subzone 1B is subjected to a peak stress of only 600 MPa, the corresponding ratcheting strain is still much higher than those of both the BL section and the PR under a peak stress of 1000 MPa. Additionally, the PR experiences higher ratcheting strain

than the BL section under such loading conditions, which can be mainly attributed to the difference in yield strength. Regarding the ratcheting strain rate, the subzone 1B also provides the largest value among all the test locations while the BL section gives the smallest value. According to these results, the SZ due to its lower yield strength has the highest sensitivity to ratcheting, followed by the PR and then the region around the BL under cyclic loading. Such findings support the previous evidence that severe plastic deformation was observed in the SZ where the RCF cracks initiated (Mutton et al., 2016).

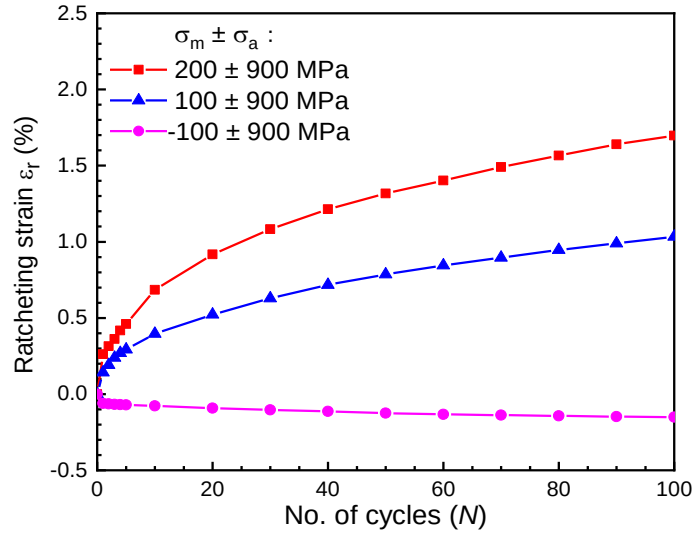

(a)

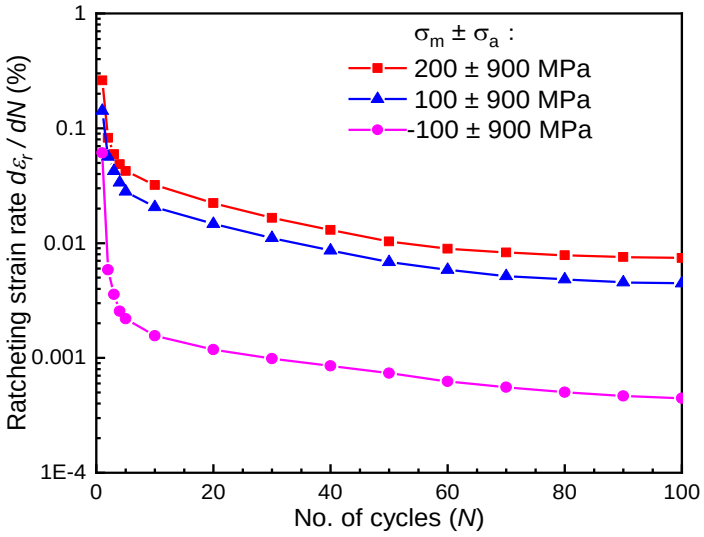

(b)

Figure 3-13: (a) Ratcheting strain ε_r; (b) ratcheting strain rate $d\varepsilon_r/dN$, versus number of loading cycles N under different mean stresses σ_m and a constant stress amplitude σ_a of 900 MPa for the BL section.

Fig. 3-15a demonstrates the strain amplitudes ε_a of the subzone 1B versus the number of loading cycles N under different stress levels. The results demonstrate that the evolution of strain amplitudes depends on the stress applied, but no specific relationship can be identified. It is also found that the subzone 1B exhibits cyclic hardening in the first few loading cycles, then gradually becomes cyclic softening and finally reaches almost cyclically stabilised under most of the tests. Fig. 3-15b compares the evolution of strain amplitudes ε_a under different stress levels for the BL section, the subzone 1B and the PR. It can be identified that both the PR and the BL section exhibit cyclic softening initially and then gradually reach a cyclically stabilised state, while the subzone 1B experiences cyclic hardening at the beginning of the test. A possible explanation for such phenomenon is related to the microstructure, which is determined by the welding process. In particularly the cementite morphology can influence dislocation behaviour, hence the tendency for cyclic hardening/softening of materials (Stephens et al., 2001). Previous research by Sunwoo et al. (1982) indicated that when relatively soft materials (with coarse interlamellar spacing) are subjected to plastic deformation, more dislocations will be generated and constrained to form dislocation cells with the existing dislocations. Such phenomena can enhance dislocation-dislocation interactions and lead to cyclic hardening of the materials. In contrast, cyclic softening occurs more readily in hardened materials (with fine interlamellar spacing) under cyclic loading since the existing dislocations tend to rearrange into a configuration with greater mobility. Additionally, the extent of change in dislocation configuration is also strongly influenced by the cyclic stress which determines the amount of imposed plastic deformation.

To confirm the effect of ratcheting on hardness, the hardness of each tested section presented in Fig. 3-15b was measured after 100 loading cycles. The results reveal that both the BL section and the PR provide slightly lower average hardness (399 HV and 388 HV, respectively) than the original specimens (405 HV and 396 HV, respectively), which indicates that both tested sections became slightly soft. However, the hardness of the subzone 1B increases from 272 HV to 294 HV, and this means that apparent hardening occurred in the subzone 1B.

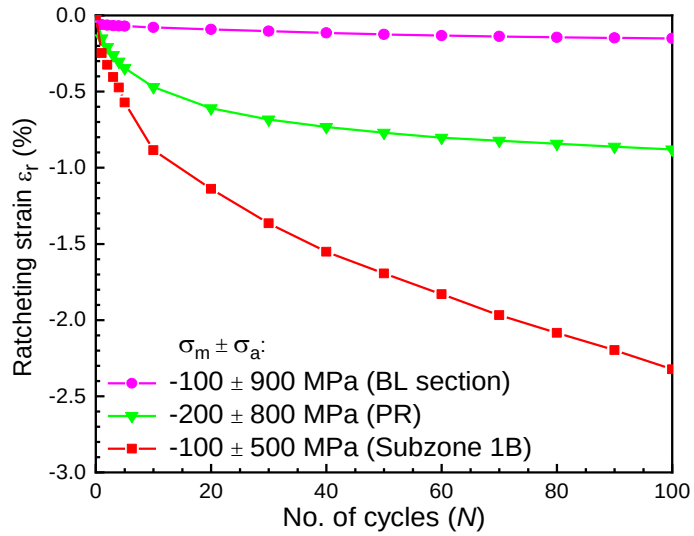

(a)

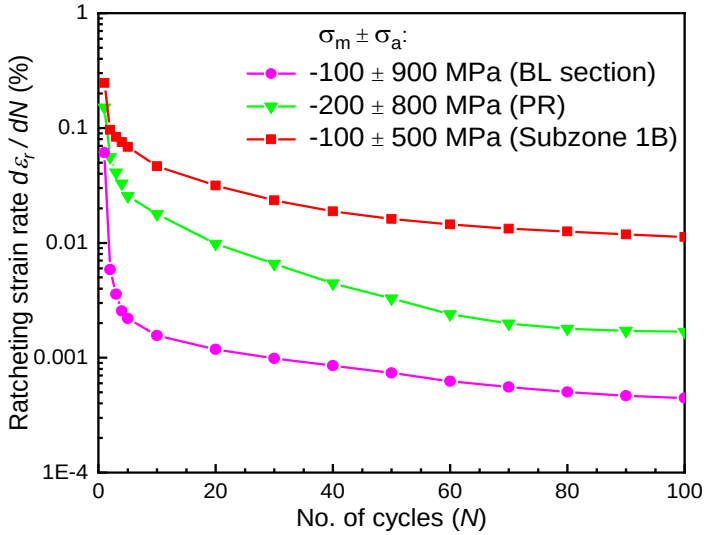

(b)

Figure 3-14: (a) Ratcheting strain ε_r; (b) ratcheting strain rate $d\varepsilon_r/dN$, versus number of loading cycles N under different stress levels for the BL section, the subzone 1B and the PR.

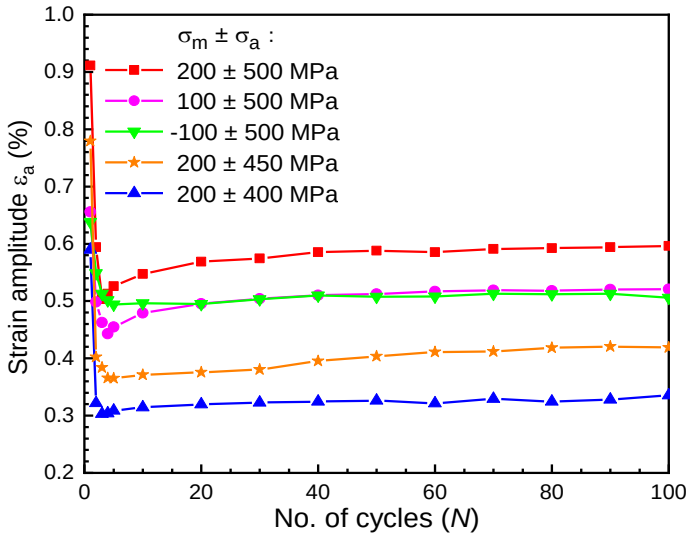

(a)

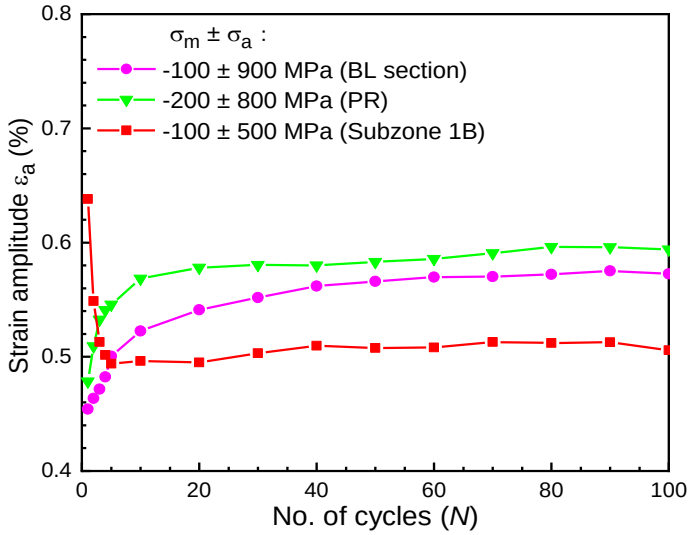

(b)

Figure 3-15: Strain amplitude ε_a versus number of loading cycles N under different stress levels for: (a) the subzone 1B; (b) the BL section, the subzone 1B and the PR.

Previous work by Luo et al. (2017 & 2020) investigated the heterogeneous ratcheting behaviour of SUS301L stainless steel butt weld joint under uniaxial cyclic loading. The width of the HAZ is approximately 12 mm, which is much less than the weld considered in current work owing to the different welding technique applied. Five subzones were defined, and one of them so called the fusion zone with a yield stress of only 314 MPa is the weakest region of the welded joint. Nevertheless, the ratcheting strain also gradually concentrated at the fusion zone and extended to other surrounding zones under the loading case of 100 ± 340 MPa. More severe ratcheting was observed with the increase in

stress level. Furthermore, the fusion zone experienced cyclic hardening, which is similar to the cyclic deformation characteristics of the SZ in the present study. Yu et al. (2019) reported the heterogeneous ratcheting behaviour of a gas tungsten arc welding welded joint for primary coolant piping under a uniaxial cyclic loading case of 290 ± 150 MPa. It is worth noted that the hardness of the HAZ is higher than the base metal and no SZ was observed in such welded joint, so the most remarkable ratcheting strain was found in the base metal and gradually extended to the HAZ. According to such information, each type of weld has unique hardness distribution, which can affect its ratcheting heterogeneity significantly.

3.3.3 Biaxial Compression–Torsion Stress-Controlled Cyclic Loading Tests

To investigate the ratcheting behaviour of the weld region in both axial and torsional directions under biaxial compression–torsion cyclic loading, two types of tests, non-zero mean axial stress with symmetrical equivalent shear stress and non-zero mean equivalent shear stress with symmetrical axial stress, were performed, respectively. As shown in Fig. 3-16, the loading path for both types of the biaxial tests was set as elliptical, which is more relevant to the actual wheel–rail cyclic rolling contact situations (Pun et al., 2014).

Fig. 3-17 presents the axial ratcheting strain ε_r and the axial ratcheting strain rate $d\varepsilon_r/dN$ versus the number of loading cycles N under an axial stress σ of -300 ± 300 MPa and an equivalent shear stress $\sqrt{3}\tau$ of 0 ± 600 MPa (equivalent stress σ_{eq} = 671 MPa) for selected subzones in the SZ. Similar to the results obtained from the uniaxial stress-controlled cyclic loading tests, the subzones 1B and 2A with relatively lower hardness provide much higher axial ratcheting strain (-6.6% and -5.7% at the 100th loading cycle, respectively) than the whole section (-3.3% at the 100th loading cycle). With regard to the subzone 5B with relatively higher hardness, the axial ratcheting strain is lower than those of the other subzones. This relationship is also reflected between the axial ratcheting strain rate and the hardness of the subzone. The axial ratcheting strain rate of

each subzone shows a dramatic decreasing trend in the first few loading cycles and finally reaches a cyclically stabilised state. Moreover, such findings are also applied to the ratcheting behaviour in torsional direction as presented in Fig. 3-18, which demonstrates the shear ratcheting strain γ_r and the shear ratcheting strain rate $d\gamma_r/dN$ versus the number of loading cycles N under an axial stress σ of 0 ± 300 MPa and an equivalent shear stress $\sqrt{3}\tau$ of 100 ± 600 MPa (equivalent stress σ_{eq} = 700 MPa) for selected subzones in the SZ.

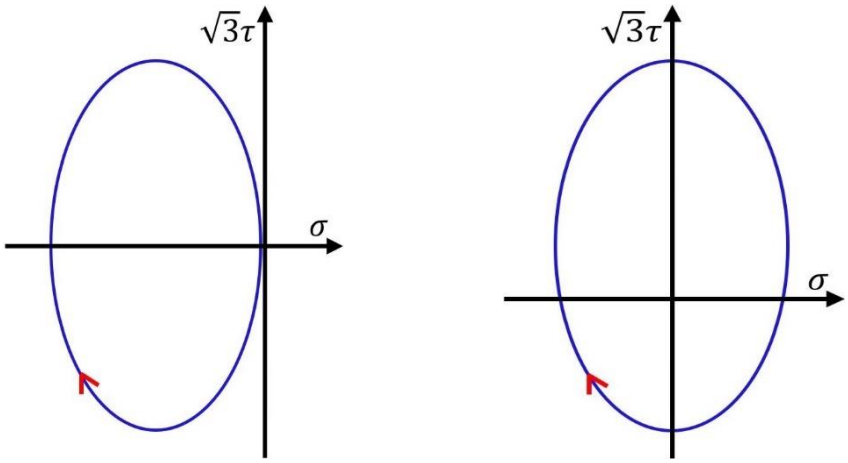

(a) (b)

Figure 3-16: Elliptical loading paths for biaxial compression–torsion stress-controlled cyclic loading tests: (a) asymmetrical loading in axial direction; (b) asymmetrical loading in torsional direction.

Fig. 3-19 demonstrates the cyclic hysteresis shear-axial strain loops of the subzone 1B under the biaxial compression–torsion stress-controlled cyclic loading tests. It clearly shows that with the increasing number of loading cycles, the loops shift along both axial and torsional directions simultaneously, but mainly along the direction in which the asymmetric loading was employed. This indicates that ratcheting also slightly evolves in the direction in which the symmetric loading was applied, i.e. the torsional direction in Fig. 3-19a. Since such phenomena are also found in other subzones, i.e. 1A, 2A and 2B, but much less obvious in the BL section and PR, it is more likely to be related to the heterogenous microstructure in the SZ. According to Fig. 3-19b, the hysteresis loop shifts towards the tensile direction when the SZ is subjected to symmetrical loading in the axial direction. As these phenomena can also be observed in other

subzones, this implies that the SZ may be more sensitive to deformation under tensile loading than that under compressive loading. Similar feature was also reported by Lim et al. (2009), which investigated the ratcheting behaviour of a copper alloy under uniaxial cyclic loading. It is also worth noted that the hysteresis loop changes from an open loop at the initial stage of the tests to an almost closed one at the 100th loading cycle, which reveals that the SZ gradually becomes cyclically stabilised after a certain number of loading cycles.

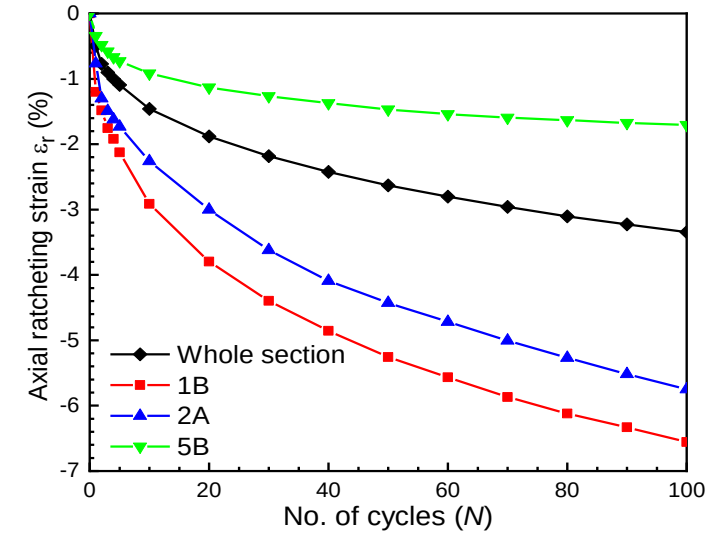

(a)

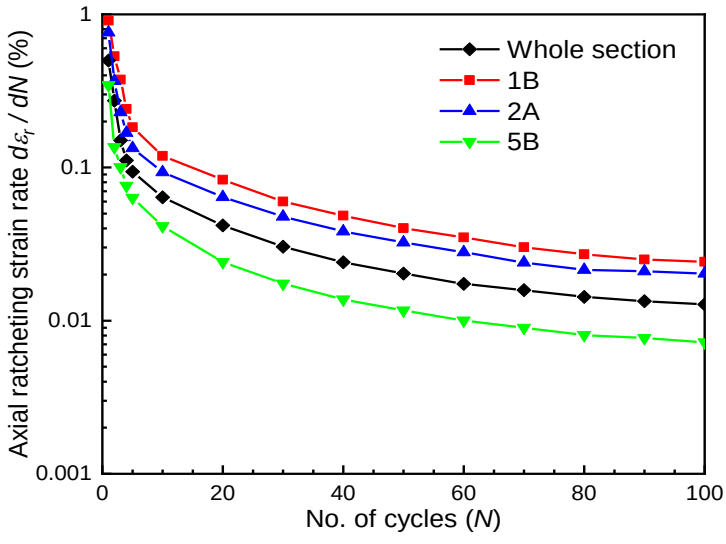

(b)

Figure 3-17: (a) Axial ratcheting strain ε_r; (b) axial ratcheting strain rate $d\varepsilon_r/dN$ versus number of loading cycles N under axial stress σ of -300 ± 300 MPa and equivalent shear stress $\sqrt{3}\tau$ of 0 ± 600 MPa (equivalent stress σ_{eq} = 671 MPa) for selected subzones in the SZ.

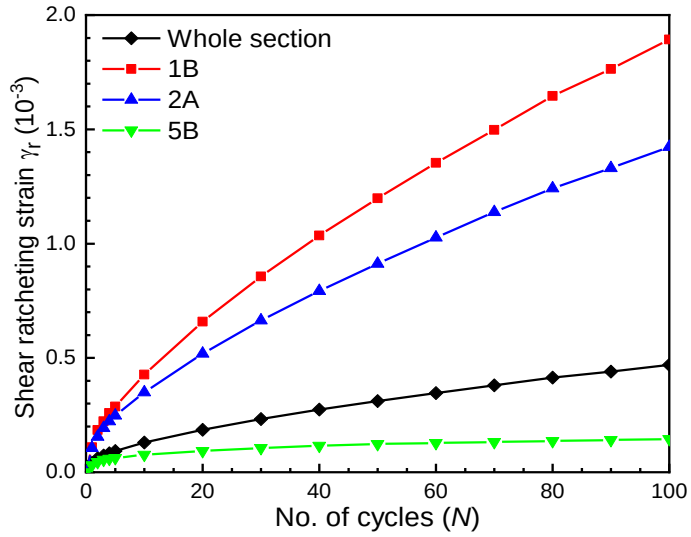

(a)

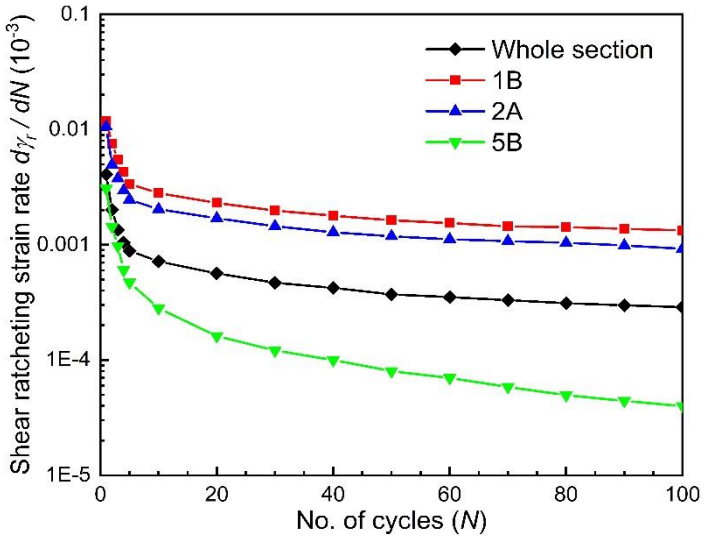

(b)

Figure 3-18: (a) Shear ratcheting strain γ_r; (b) shear ratcheting strain rate $d\gamma_r/dN$ versus number of loading cycles N under axial stress σ of 0 ± 300 MPa and equivalent shear stress $\sqrt{3}\tau$ of 100 ± 600 MPa (equivalent stress σ_{eq} = 700 MPa) for selected subzones in the SZ.

Figs. 3-20a and 3-20b compare the axial ratcheting strain ε_r and the shear ratcheting strain γ_r of the BL section, the entire SZ and the PR versus the number of loading cycles N under the biaxial compression–torsion stress-controlled cyclic loading tests, respectively. The results indicate that the ratcheting strain of the whole SZ in both axial and torsional directions is significantly higher than those of the BL section and the PR, even though the peak equivalent stress applied is the lowest among three types of specimens. Combining the results of ratcheting strain in the subzones 1B and 2A presented

in Figs. 3-17a and 3-18a, it is predicted that the SZ, particularly the region with the lowest hardness, is the most sensitive to ratcheting under actual wheel–rail cyclic rolling contact situations. In comparison, the PR with higher hardness is expected to sustain much less ratcheting than the SZ. Based on the results from Figs. 3-13a and 3-20, the region around the BL with the highest hardness in the weld region presents almost negligible axial ratcheting strain under both uniaxial and biaxial cyclic loading tests dominated by compressive loading in the axial direction, and the lowest shear ratcheting strain under the biaxial cyclic loading test dominated by torsional loading. These phenomena highlight that the region around the BL has the best resistance to ratcheting and is unlikely to be the critical location for rail degradation initiated by ratcheting.

Fig. 3-21 illustrates the evolutions of axial strain amplitudes ε_a of the BL section, the entire SZ, the subzone 1B and the PR under biaxial compression–torsion stress-controlled cyclic loading tests. The results reveal that the axial strain amplitudes of both the BL section and the PR increase in the first few loading cycles and then gradually become almost constant, while that of the SZ decreases initially. This indicates that both the BL section and the PR firstly exhibit cyclic softening and then gradually become cyclically stabilised after approximately 10 loading cycles, while the SZ exhibits cyclic hardening initially and stabilises after around 20 loading cycles, particularly the subzone 1B with the lowest hardness. Furthermore, the measured average hardness of the BL section and the PR after 100 loading cycles decreases by 8 HV and 10 HV, respectively while that of the subzone 1B increases by 27 HV. Such finding is consistent with the cyclic hardening/softening behaviour identified from the uniaxial stress-controlled cyclic loading tests mentioned in Chapter 3.3.2 and also supports the fact from the previous research by (Sunwoo et al., 1982) that softened materials tend to become harder under cyclic loading, and vice versa. Another possible explanation for the cyclic hardening behaviour of the SZ is related to the elliptical loading path. According to Fig. 3-16, the ratio of the axial stress to the torsional stress varies during each loading cycle as the torsional loading was applied 90° phase lag. This means that the direction of maximum shear stress is always changing, which can cause crystal planes in the SZ slipping with each other and therefore may lead to additional hardening

(Stephens et al., 2001).

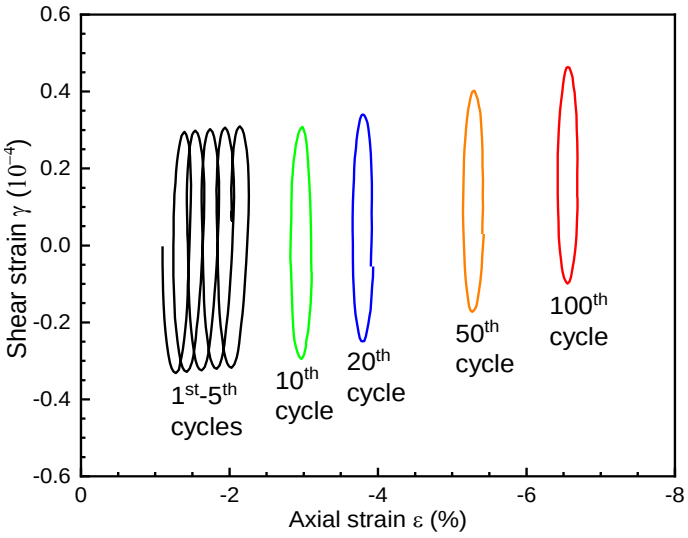

(a)

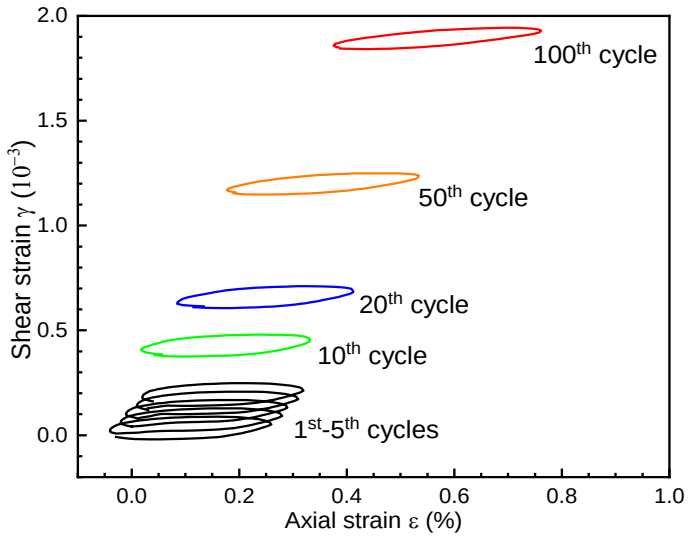

(b)

Figure 3-19: Cyclic hysteresis shear-axial strain loops of the subzone 1B under biaxial compression–torsion stress-controlled cyclic tests: (a) axial stress σ of -300 ± 300 MPa and equivalent shear stress $\sqrt{3}\tau$ of 0 ± 600 MPa (equivalent stress σ_{eq} = 671 MPa); (b) axial stress σ of 0 ± 300 MPa and equivalent shear stress $\sqrt{3}\tau$ of 100 ± 600 MPa (equivalent stress σ_{eq} = 700 MPa).

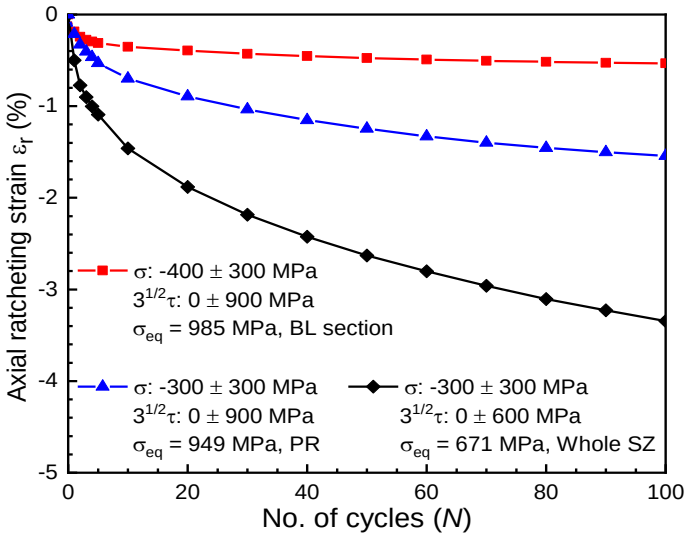

(a)

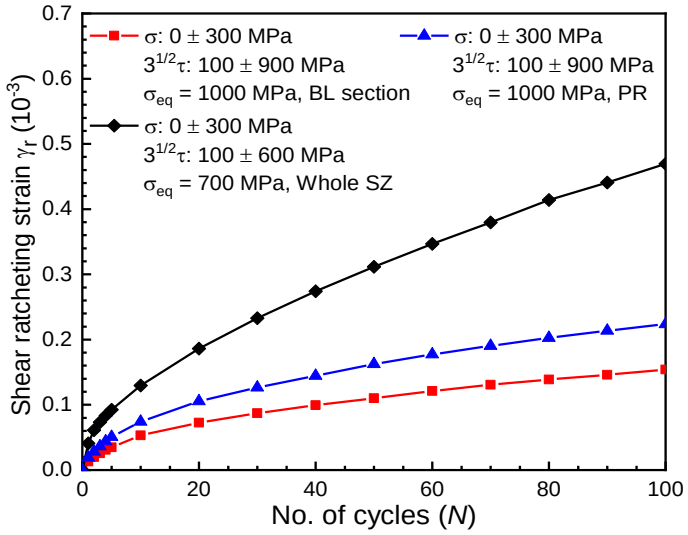

(b)

Figure 3-20: Ratcheting strain of the BL section, the entire SZ and the PR versus number of loading cycles N under biaxial compression–torsion stress-controlled cyclic tests: (a) axial ratcheting strain ε_r; (b) shear ratcheting strain γ_r.

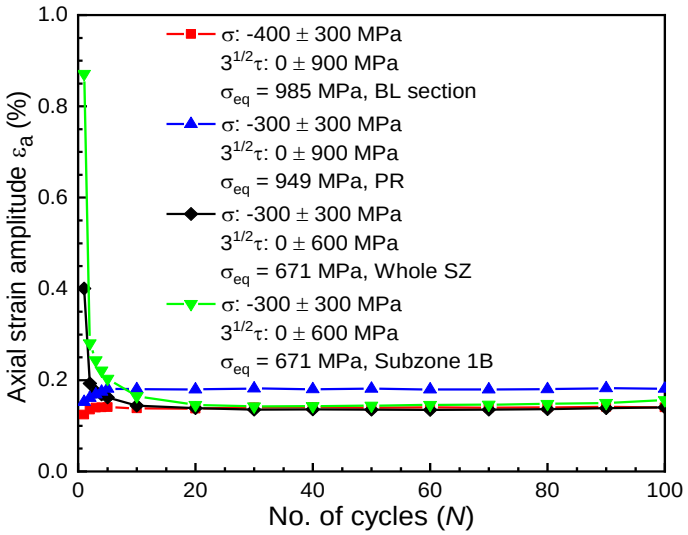

Figure 3-21: Axial strain amplitude ε_a of the BL section, the entire SZ, the subzone 1B and the PR versus number of loading cycles N under the biaxial compression–torsion stress-controlled cyclic loading tests.

3.3.4 Metallographic Analysis

Extra specimens with the same geometry as shown in Figs. 3-1c and 3-1d were prepared from the new weld samples for metallographic analysis. According to Fig. 3-22, the gauge section was cut out from each specimen, and then cut into half along the longitudinal direction by an abrasive cutter. The cross-section of the half gauge section was the examined surface. It was firstly ground, polished, and etched using 2% Nital solution to reveal the HAZ boundary, followed by SEM under × 20000 magnification to characterise the microstructure. The same procedures were also applied to selected specimens after the biaxial cyclic loading tests demonstrated in Chapter 3.3.3.

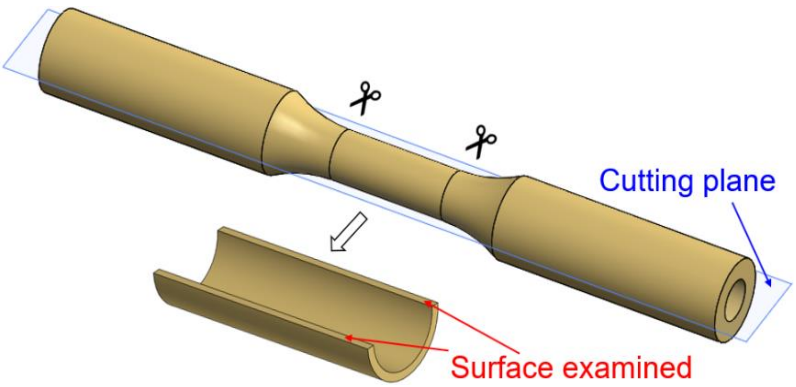

Figure 3-22: Illustration of the specimen preparation for metallographic surface examination.

Figs. 3-23, 3-24, 3-25, 3-26 and 3-27 show representative SEM micrographs for both the original weld material and the one after the biaxial cyclic loading test with asymmetrical axial stress. According to the welding thermal cycles (Weingrill et al., 2017), the peak temperature in the region near the BL is high enough to cause the re-austenitisation and formation of fine pearlite as presented in Fig. 3-23a, which was at 3 mm to the BL. The compact microstructure with small interlamellar spacing can significantly prevent the cementite lamellae moving when being subjected to external loading. This may be the main reason why the BL section shows a strong ratcheting resistance, and also explains the much lower ductility of the BL section obtained from the monotonic tensile test. From Fig. 3-23b, no obvious lamellae distortion occurs and most of the lamellae are still predominantly linear, which demonstrates that less plastic deformation occurs in this region. Such phenomena correspond to the ratcheting strain of the BL section demonstrated in Fig. 3-20a.

In the subzone 5B, partial re-austenitisation occurs due to the relatively lower peak temperature than that at the BL section. It is observed from Fig. 3-24a that the pearlite morphology was changed distinctly with partial cementite spheroidisation and increased amount of ferrite (dark area). Previous research by Eden et al. (2005) and Garnham & Davis (2008) indicated that ferrite, with lower hardness and higher ductility, tends to deform readily under external loading. However, there is no obvious change in appearance induced by plastic deformation after the biaxial test (Fig. 3-24b) and this is mainly because the applied peak stress is lower than the yield stress (686 MPa). Fig. 3-25a presents the SEM micrograph of the subzone 1B before the biaxial test. It clearly shows that the pearlite morphology becomes almost fully spheroidised and large amount of ferrite exists, which can significantly decrease the overall hardness of the subzone 1B that corresponds to the position of the minimum hardness in the weld region as shown in Fig. 3-7a. After the biaxial test, it is found that some spheroidised carbides were distorted to a shape with polygonal-like boundaries by plastic deformation (Fig. 3-25b). Garnham & Davis (2008) identified that thick ferrite zones lightly constrained by pearlite have less resistance to deformation. According to Fig. 3-25a, large ferrite mean free paths

between spheroidised carbides can provide much less resistance to dislocation movement than the cementite lamellae in the BL section and the subzone 5B. Such information can explain why the subzone 1B provides the highest ratcheting strain.

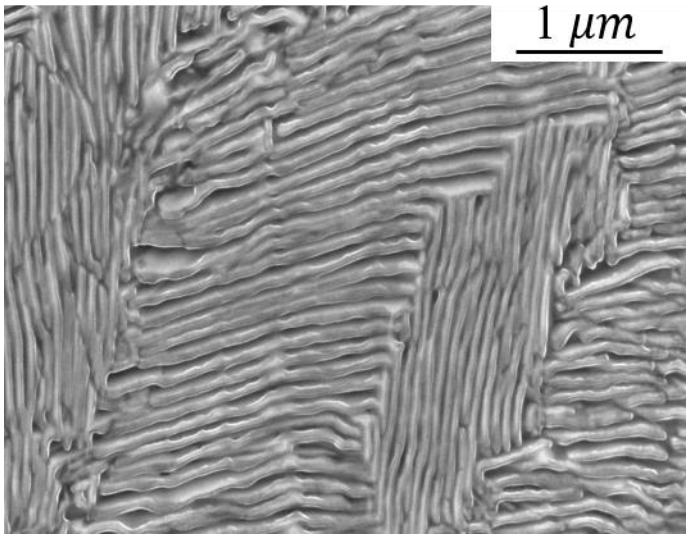

(a)

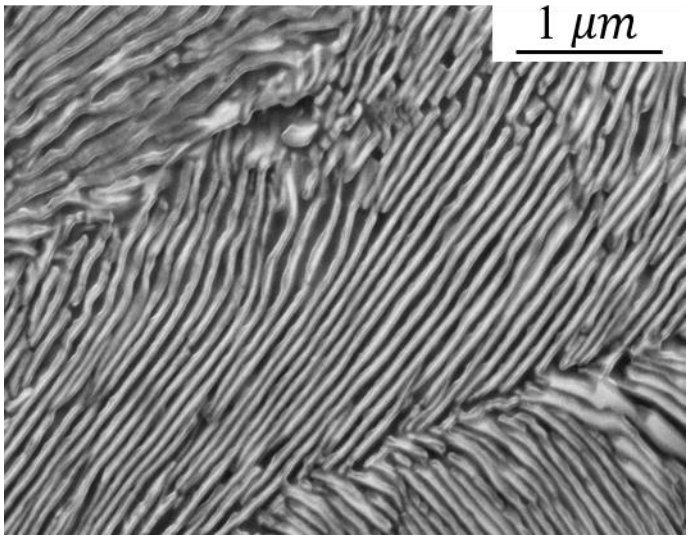

(b)

Figure 3-23: SEM micrographs at 3 mm to the BL: (a) original specimen; (b) After biaxial cyclic loading l test with axial stress σ of -400 ± 300 MPa and equivalent shear stress $\sqrt{3}\tau$ of 0 ± 900 MPa (equivalent stress σ_{eq} = 985 MPa).

The subzone 2A is located in the HAZ–PR transition zone based on Fig. 3-7a. The SEM micrograph before the biaxial test (Fig. 3-26a) shows the co-existence of spheroidised carbides and cementite lamellae. Such microstructure reflects

the fact that the subzone 2A is slightly harder than the subzone 1B with fully spheroidised microstructure. Nevertheless, the cementite lamellae after the biaxial test present a 'zigzag' feature and appear to be fractured in some area (Fig. 3-26b), which indicates that the subzone 2A also suffered severe ratcheting. For the original PR speciman, the SEM micrograph at 100 mm to the BL also shows fine pearlite microstructure (Fig. 3-27a) but not as compact as that in the BL section. In addition, the relatively thinner cementite lamellae are more ductile than the slightly coarser cementite lamellae close to the BL and provides slightly wider pearlite spacing, which may decrease the resistance to plastic deformation. After the biaxial test, the 'zigzag' character and fracture are also observed in some lamellae as demonstrated in Fig. 3-27b. This phenomenon reveals that the PR deforms more than the BL section, which supports the ratcheting results presented in Fig. 3-20a.

According to the microstructural characterisation presented above, the spheroidised region in the SZ reduces the overall mechanical strength of rail welds and increases the sensitivity to ratcheting. Therefore, it is considered essential to minimise the effects of such a region and improve the weld quality by reducing the width of HAZ. To achieve this, some research work has modified the welding process by, i.e. decreasing the preheating cycles (Micenko & Li, 2013) and increasing the upsetting force (Saita et al., 2017). However, no further investigation has been conducted on the influence of such procedures on the ratcheting behaviour of these welds with a narrow width of HAZ. Additionally, the residual stress levels may be higher than those in welds manufactured through the conventional welding process and therefore increase the sensitivity to fatigue failures in the web region under high axle loads (Mutton et al., 2011 & 2016). Another option would be altering the chemical composition of PR since the extent of carbide spheroidisation during the welding process depends on the presence of alloying elements, i.e. silicon and vanadium (Han et al., 2001, Tokaji et al., 2006 & Efremenko et al., 2014). Further optimisation of the welding process and comprehensive evaluation of the weld quality are still required to weaken the influence of microstructure difference on the performance of rail welds.

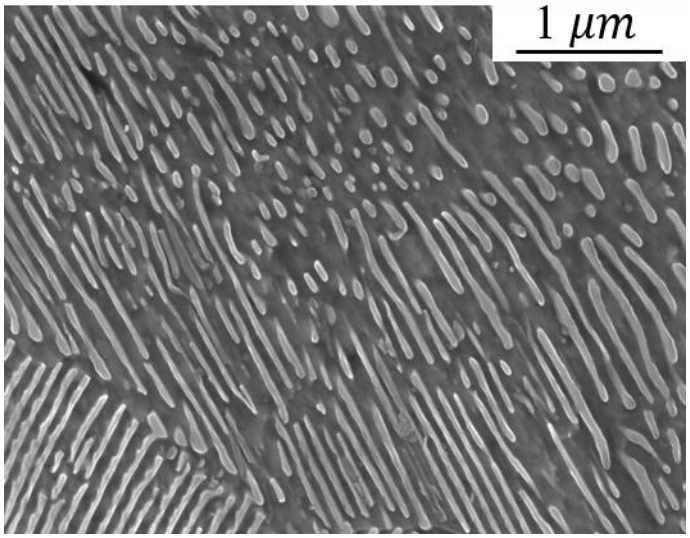

(a)

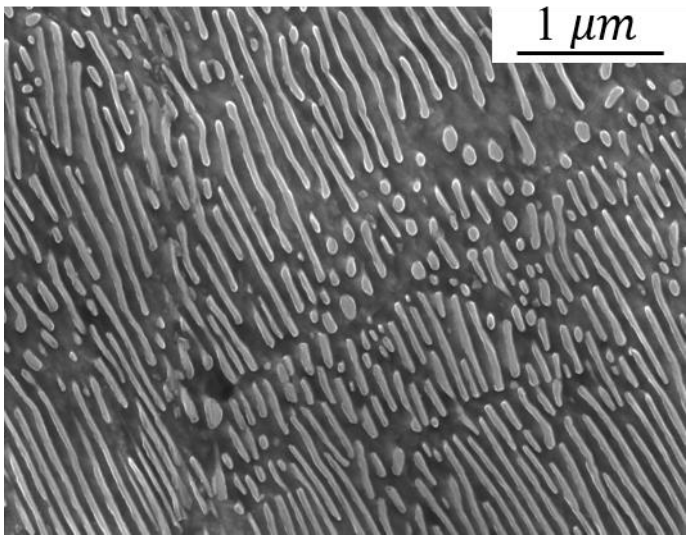

(b)

Figure 3-24: SEM micrographs of the subzone 5B: (a) original specimen; (b) after biaxial cyclic loading test with axial stress σ of -300 ± 300 MPa and equivalent shear stress $\sqrt{3}\tau$ of 0 ± 600 MPa (equivalent stress σ_{eq} = 671 MPa).

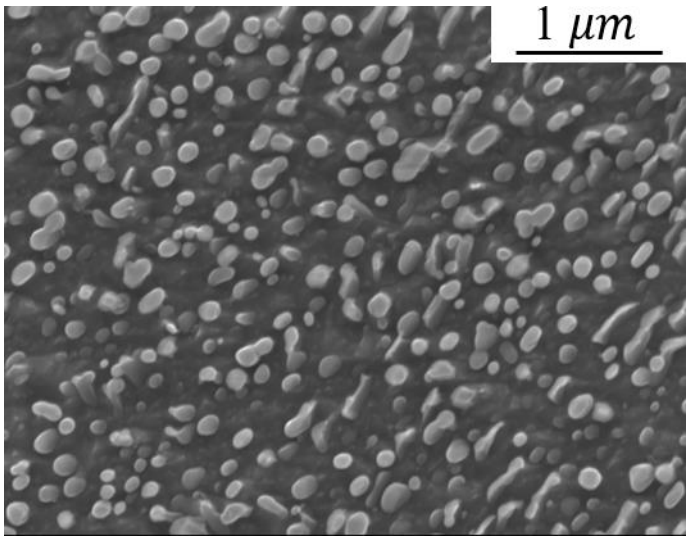

(a)

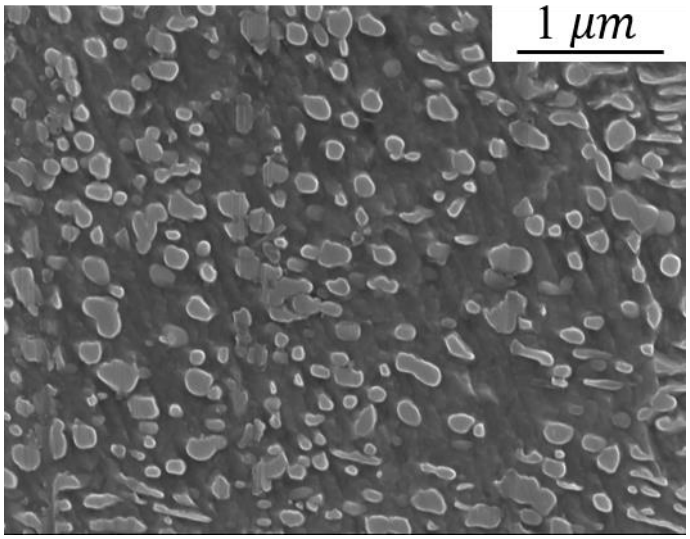

(b)

Figure 3-25: SEM micrographs of the subzone 1B: (a) original specimen; (b) after biaxial cyclic loading test with axial stress σ of -300 ± 300 MPa and equivalent shear stress $\sqrt{3}\tau$ of 0 ± 600 MPa (equivalent stress σ_{eq} = 671 MPa).

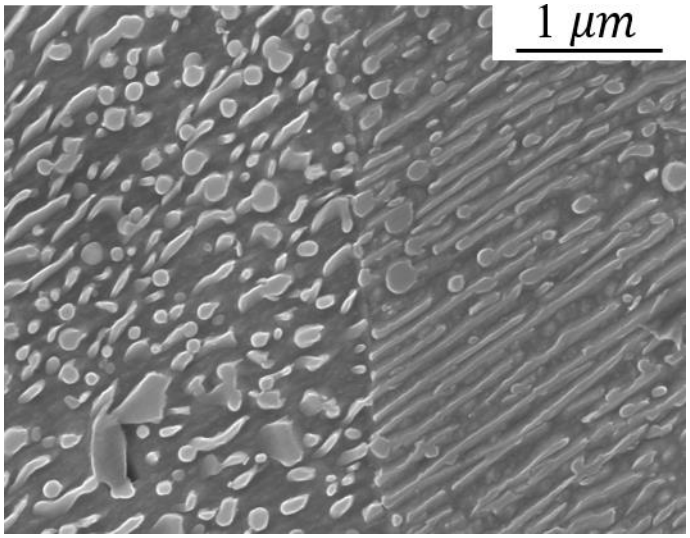

(a)

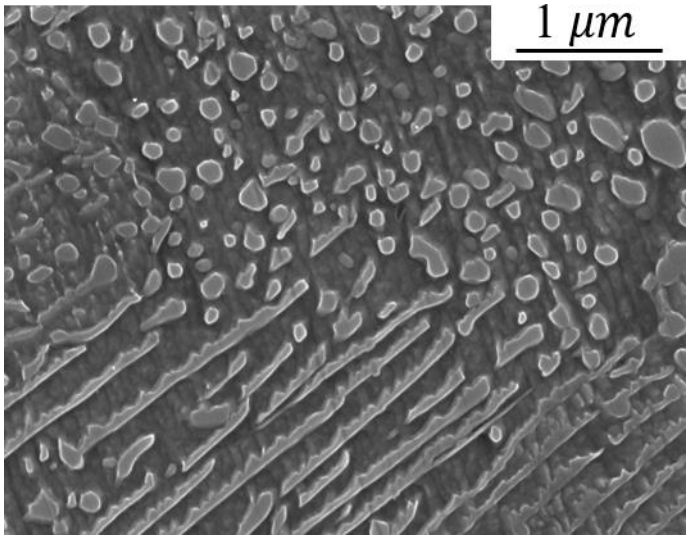

(b)

Figure 3-26: SEM micrographs of the subzone 2A: (a) original specimen; (b) after biaxial cyclic loading test with axial stress σ of -300 ± 300 MPa and equivalent shear stress $\sqrt{3}\tau$ of 0 ± 600 MPa (equivalent stress σ_{eq} = 671 MPa).

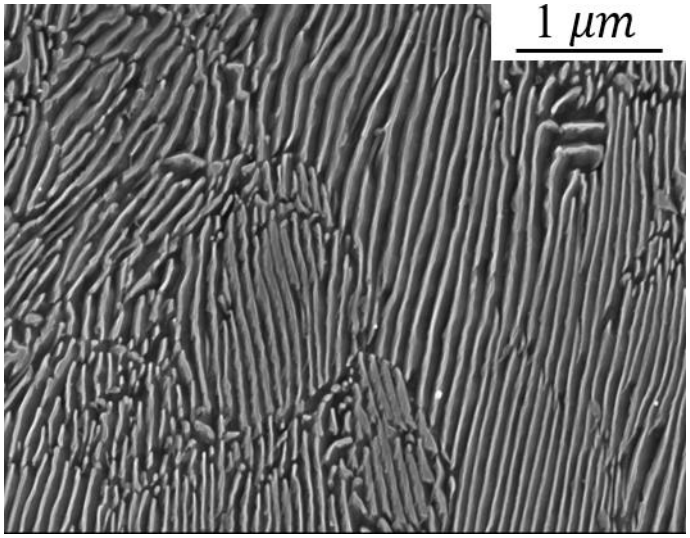

(a)

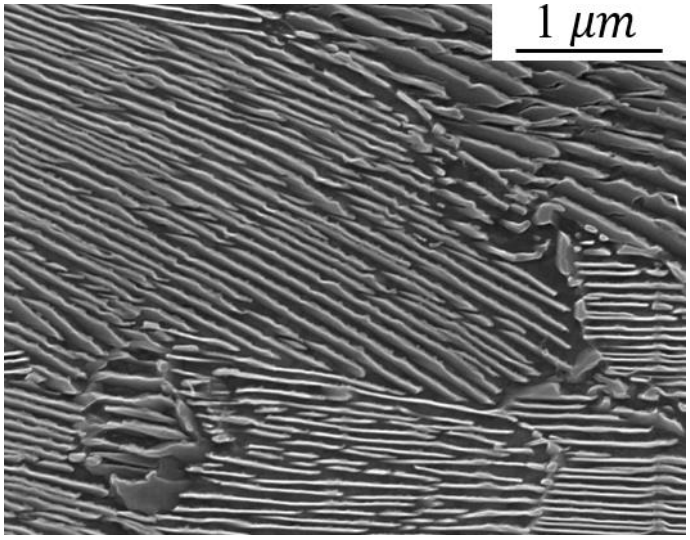

(b)

Figure 3-27: SEM micrographs of the PR (100mm to BL): (a) original specimen; (b) after biaxial cyclic loading test with axial stress σ of -300 ± 300 MPa and equivalent shear stress $\sqrt{3}\tau$ of 0 ± 900 MPa (equivalent stress σ_{eq} = 949 MPa).

3.4 Chapter Summary

The ratcheting behaviour of new rail flash butt welds in R400HT steel grade, which is currently used in Australian heavy haul operations, has been investigated by uniaxial stress-controlled and biaxial compression–torsion stress-controlled cyclic loading tests. The results indicate that the ratcheting strain and its heterogeneity can correlate with the longitudinal hardness profile (yield strength) within the heat-affected zone of the weld. Furthermore, the

softened zone with a significant hardness drop is more sensitive to ratcheting, while the region around the bond line provides much lower or almost negligible ratcheting. The ratcheting strain rate decreases dramatically in the first few loading cycles and then gradually becomes almost cyclically stabilised within the applied loading cycles.

Compared with the ratcheting behaviour of parent rails, it is expected that the softened zone, particularly the region with the lowest hardness, will suffer more severe ratcheting than the parent rail under actual wheel–rail cyclic contact situations, while the region around the bond line has the best resistance to ratcheting and is almost unlikely to fail due to ratcheting. The softened zone tends to exhibit cyclic hardening initially and become cyclically stabilised after a certain number of loading cycles. In contrast, both the regions around the bond line and the parent rail are more likely to exhibit cyclic softening initially and then reach a cyclically stabilised state. It was also observed that slight ratcheting can be observed along the direction in which the symmetric loading was applied under the biaxial cyclic loading, which is probably attributed to the variability of the microstructure in rail welds.

The microstructure and resulting mechanical properties of the weld vary with the longitudinal position to the BL due to the thermal history. The spheroidised microstructure with high amounts of ferrite and longer ferrite mean free paths can significantly reduce the hardness and therefore the ratcheting resistance of the softened zone, while the region around the BL shows great ratcheting resistance due to the presence of fine pearlite. Future work on optimising the welding process is required to address the negative effects of the differences in microstructure on the performance of rail welds.

The outcomes of this study will be useful for the numerical description of the heterogeneous ratcheting behaviour of R400HT rail flash welds (see Chapters 4 and 5) and assist rail operators further understanding the initiation of localised degradation in these welds, especially RCF.

Chapter 4

An Updated Cyclic Plasticity Constitutive Model for Rail Flash Butt Welds

In order to numerically investigate the ratcheting performance of rail flash butt welds in practice, it is essential to employ an appropriate and reliable cyclic plasticity constitutive model in wheel–rail cyclic rolling contact simulations. In this chapter, a developed cyclic plasticity constitutive model for high strength rail steels was updated for flash butt welds in R400HT rail steel. The method for calibrating the material parameters required by the updated constitutive model is demonstrated and the material parameters for these welds are determined from the experimental results of the monotonic tensile tests and stress-controlled cyclic loading tests presented in Chapter 3. The comparison between the simulated results and the experimental data conclude that the updated constitutive model has the capacity to simulate the ratcheting behaviour of the rail flash butt welds with acceptable accuracy, even though some discrepancies can still be observed between the simulated results and the experimental data.

4.1 A Developed Cyclic Plasticity Constitutive Model

In order to numerically study the ratcheting performance of flash butt welds in R400HT rail steels under in-service conditions, the cyclic plasticity constitutive model for high strength rail steels developed by Pun et al. (2014) was updated for these welds based on the experimental results presented in Chapter 3. According to the initial isotropic elasticity and associated plastic flow rules at small deformation, the governing equations adopted in the cyclic plasticity constitutive model are as follows,

$$\boldsymbol{\varepsilon}^{\boldsymbol{T}} = \boldsymbol{\varepsilon}^{\boldsymbol{e}} + \boldsymbol{\varepsilon}^{\boldsymbol{p}} \qquad (4-1)$$

$$\boldsymbol{\varepsilon}^{\boldsymbol{e}} = \boldsymbol{D}^{-1} : \boldsymbol{\sigma} \qquad (4-2)$$

$$\dot{\boldsymbol{\varepsilon}}^{\boldsymbol{p}} = \sqrt{\frac{3}{2}}\dot{\lambda}\frac{\boldsymbol{s}-\boldsymbol{\alpha}}{\|\boldsymbol{s}-\boldsymbol{\alpha}\|} \qquad (4-3)$$

$$F_y = \sqrt{\frac{3}{2}(\boldsymbol{s}-\boldsymbol{\alpha}) : (\boldsymbol{s}-\boldsymbol{\alpha})} - Q \qquad (4-4)$$

where $\boldsymbol{\varepsilon}^{\boldsymbol{T}}$, $\boldsymbol{\varepsilon}^{\boldsymbol{e}}$, $\boldsymbol{\varepsilon}^{\boldsymbol{p}}$ and $\dot{\boldsymbol{\varepsilon}}^{\boldsymbol{p}}$ are total strain, elastic strain, plastic strain and plastic strain rate, respectively. $\boldsymbol{D}$ is the fourth order tensor of elasticity. $\boldsymbol{s}$ is the deviatoric components of stress, which is expressed as $\boldsymbol{\sigma} - \frac{1}{3}tr(\boldsymbol{\sigma})\boldsymbol{I}$ ($\boldsymbol{I}$ is the unit tensor). $\boldsymbol{\alpha}$ is the deviatoric components of backstress. Q is the isotropic deformation resistance and F_y is the von Mises yield function. $\dot{\lambda}$ is the rate of plastic multiplier and $\|\ \|$ denotes the norm.

The Abdel-Karim and Ohno kinematic hardening rule is adopted in the model (Abdel-Karim & Ohno, 2000), which combines the A-F model and the O-W model. The evolution equations of deviatoric backstress $\boldsymbol{\alpha}$ for the kinematic

hardening rule is shown as follows,

$$\boldsymbol{\alpha} = \sum_{i=1}^{M} \boldsymbol{\alpha_i} \quad (i = 1,2,\dots,M) \tag{4-5}$$

$$\dot{\boldsymbol{\alpha}}_{\boldsymbol{i}} = \zeta_i \left[\frac{2}{3} r_i \dot{\boldsymbol{\varepsilon}}^{\boldsymbol{p}} - \mu_i \boldsymbol{\alpha_i} \dot{p} - H(f_i) \boldsymbol{\alpha_i} \left\langle \dot{\boldsymbol{\varepsilon}}^{\boldsymbol{p}} : \frac{\boldsymbol{\alpha_i}}{\|\boldsymbol{\alpha_i}\|} - \mu_i \dot{p} \right\rangle \right] \tag{4-6}$$

The deviatoric backstress $\boldsymbol{\alpha}$ is divided into M parts and each one is represented as $\boldsymbol{\alpha_i}$. H stands for the Heaviside function. $\langle\ \rangle$ is the Macaulay's bracket and means that: if $x \leq 0$, $\langle x \rangle = 0$, else $\langle x \rangle = x$. $\dot{p}$ is the effective plastic strain rate, which is determined by $\sqrt{\frac{2}{3}\dot{\boldsymbol{\varepsilon}}^{\boldsymbol{p}} : \dot{\boldsymbol{\varepsilon}}^{\boldsymbol{p}}}$. ζ_i and r_i are the material parameters which are used to describe the evolution of the backstress. μ_i stands for the ratcheting parameter, which is assumed as a constant for different components of backstress. The critical state of dynamic recovery is described by the critical surfaces f_i:

$$f_i = \|\boldsymbol{\alpha_i}\|^2 - {r_i}^2 = 0 \tag{4-7}$$

The cyclic softening rule adopted in the model is used with the combined hardening model which considers both isotropic and kinematic hardening rules to capture the cyclic softening feature and the ratcheting behaviour. The following evolution equation for the isotropic deformation resistance Q is applied in the model,

$$\dot{Q} = \gamma_m (Q_{sa} - Q)\dot{p} \tag{4-8}$$

where Q_{sa} is saturated isotropic deformation resistance. The initial value of Q is denoted as Q_0, which is the stress value when the plastic strain is zero under the monotonic tensile test. γ_m is the material parameter to control the evolution rate of Q.

4.2 Calibration of Material Parameters

Previous studies demonstrated in Chapter 2.4.2 have already shown that an appropriate method to calibrate the material parameters for the constitutive material model is crucial for accurate simulation of ratcheting behaviour of a material. Parameter calibration for applying the updated cyclic plasticity constitutive model for rail flash butt welds was performed by non-linearly fitting the experimental results of monotonic tensile tests and uniaxial stress-controlled cyclic loading tests as presented in Chapter 3. The method to calibrate the material parameters for these welds is illustrated below.

The material constants ζ_i and r_i in Eqs. (4-8) and (4-9) can be determined by,

$$\zeta_i = \frac{1}{\varepsilon_i^p} \tag{4-8}$$

$$r_i = \left(\frac{\sigma_i - \sigma_{i-1}}{\varepsilon_i^p - \varepsilon_{i-1}^p} - \frac{\sigma_{i+1} - \sigma_i}{\varepsilon_{i+1}^p - \varepsilon_i^p} \right) \varepsilon_i^p \tag{4-9}$$

respectively, where σ_i and ε_i^p are the yield stress and the corresponding plastic strain obtained from a stress-plastic strain curve of a monotonic tensile test. Ten sets of data (σ_i, ε_i^p) are extracted from each curve to calibrate eight sets of (ζ_i, r_i) since M = 8 is usually closer to the experimental results (Ohno & Wang, 1993b). As an example, Fig. 4-1 shows how a set of ten data pairs (σ_i, ε_i^p) are extracted from the stress-plastic strain curve of the subzone 1B for using Eqs. (4-8) and (4-9) to calibrate eight sets of (ζ_i, r_i). The ratcheting parameter μ, which reflects the kinematic hardening in uniaxial tests, can be determined by an optimising process:

$$\delta(\mu) = \sum_{k=1}^{n} \left| \frac{\varepsilon_r^{exp} - \varepsilon_r^{simu}}{\varepsilon_r^{exp}} \right|_k \tag{4-10}$$

where ε_r^{exp} and ε_r^{simu} are experimental and simulated strains at a certain cycle (i.e., the 100th cycle in the present study), respectively. k is the number of uniaxial loading tests. Due to lack of the uniaxial symmetrical strain-controlled cyclic loading tests (the extensometer cannot be applied due to the employment of DIC as mentioned in Chapter 3.2), the material parameters related to cyclic softening: γ_m and Q_{sa} can only be determined by the trial-error method. It should be noted that cyclic softening may not be applied (γ_m = 0 and Q_{sa}= Q_0) in some subzones in the SZ if the simulated results of uniaxial stress-controlled cyclic tests agree well with the corresponding experimental results by only applying a suitable value of μ.

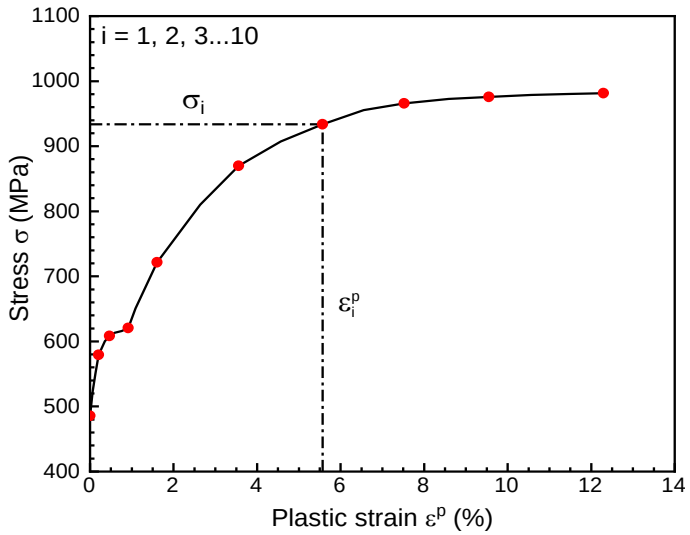

Figure 4-1: The stress-plastic strain curve from the monotonic loading test for the subzone 1B in the SZ for calibrating the backstress of the updated cyclic plasticity constitutive model.

The material parameters obtained for each subzone are summarised in Table 4-1. It should be noted that some subzones have the same sets of data (σ_i, ε_i^p) for calibrating the backstress and the ratcheting parameter μ since these subzones demonstrate similar trends of the strain hardening behaviour under the monotonic tensile tests and the evolutions of ratcheting strain under the uniaxial stress-controlled cyclic loading tests. For these subzones, different parameters related to the cyclic softening: Q_0, Q_{sa} and γ_m, are applied to adjust the magnitudes of ratcheting strain under the same test. It should be noted that the subzones 2A and 3B in the SZ have the same material parameters since the experimental results in both subzones are quite close to each other.

Table 4-1: Calibrated material parameters used in the updated cyclic plasticity constitutive model for the R400HT flash butt welds (r_i: MPa, E: GPa, Q_0: MPa and Q_{sa}: MPa).

	1B	1A	2B	2A	3B	3A	4A	5B	4B	Rest	BL	PR
ζ_1	494.2		499.8	508.4		857.6			866.4	1988	943.5	495.7
ζ_2	214.4		285.7	246.7		476.1			505.1	882.4	485.5	244.8
ζ_3	109.3		172	182		141.7			258	455	248.8	90.62
ζ_4	62.2		107.1	126.2		84.8			166.1	282.3	166.1	49.5
ζ_5	28.1		50.4	51.7		72.9			89.5	201.4	123.3	32.4
ζ_6	18		28.9	32.7		56.9			45.9	158.6	94.7	23.7
ζ_7	13.3		16.4	23.2		49.8			31.8	142.3	76.8	19.6
ζ_8	10.5		10.9	17.9		41.2			24.1	128.3	69.5	17.3
r_1	71.6		44.5	39.1		16.6			23.4	35.3	77.8	130.3
r_2	38.5		58.3	41.4		16.2			36.1	32.5	79.1	73.3
r_3	-108.5		-53.9	-129		29.3			-27.7	44.9	60.6	102.9
r_4	112.2		23.7	102.5		60			-21.2	40.5	49.7	109.8
r_5	157.4		45.9	125		30.7			71.2	41.9	74.7	113.9
r_6	84.6		148.6	101.5		36.3			104.2	69.9	68.6	99.8
r_7	87.9		153.9	113.7		87			136.2	29	91	61.6
r_8	27.6		38	28.8		68.9			60.9	64.2	31.3	31.9
E	212										210	210
ν	0.33											
μ	0.5		0.011	0.01		0.004			0.0055	0.005	0.006	0.007
Q_0	485	494	502	528		570	595	578	546	605	720	677
Q_{sa}	485	494	345	373		440	463	448	408	475	615	550
γ_m	0	0	18	25		30			29.8	15	1.5	1.2

4.3 Numerical Simulations by Using the Updated Constitutive Model

With the calibrated material parameters listed in Table 4-1, the applicability of the updated cyclic plasticity constitutive model as described in Chapter 4.2 was first verified by simulating the monotonic tensile tests with Abaqus 2019 with the User Subroutine program. Fig. 4-2 compares the simulated stress-strain curves of the BL section and the PR with the corresponding experimental results,

while Fig. 4-3 presents the comparison of selected subzones in the SZ. Both simulated results agree well with the corresponding experimental ones. Since the calibrated material parameters of the subzones 2A and 3B are the same according to Table 4-1, the results of both subzones from the simulations are identical. It is worth noting that engineering strain and stress are used for both simulated and experimental results.

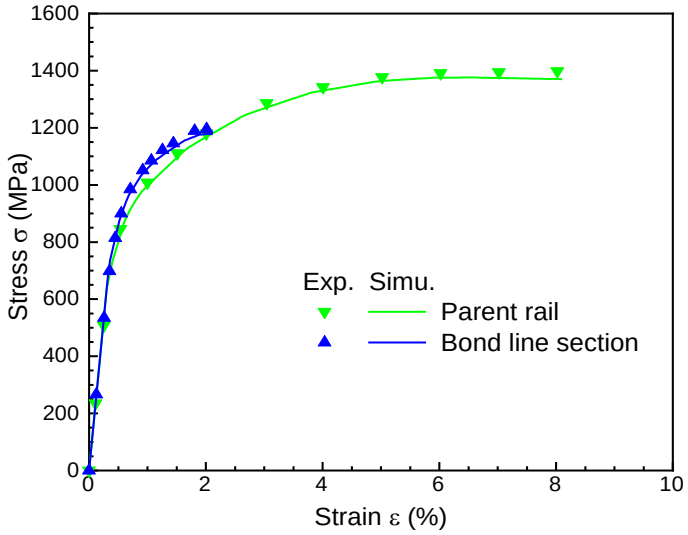

Figure 4-2: Comparison between the experimental and simulated stress-strain curves of the BL section and the PR under the monotonic tensile tests.

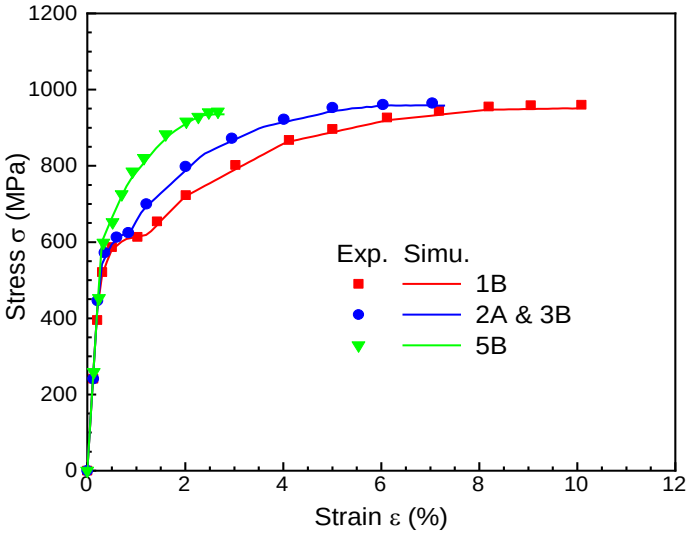

Figure 4-3: Comparison between the experimental and simulated stress-strain curves of selected subzones in the SZ under the monotonic tensile tests.

The updated cyclic plasticity constitutive model with the calibrated material

parameters was then applied to simulate the evolution of ratcheting strain ε_r under the uniaxial stress-controlled cyclic loading tests with different mean stress values of σ_m. Fig. 4-4 compares the simulated results of selected subzones in the SZ with the corresponding experimental ones, while Figs. 4-5a and 4-5b present the comparison of the BL section and the PR, respectively. The results indicate that the simulated evolutions of ratcheting strain in the PR and selected subzones in the SZ agree well with the corresponding experimental results. Even though discrepancies are observed in the first few cycles for the subzone 5B, the main features of evolution tendency, such as the negligible ratcheting strain at the 100th cycle and the insignificant ratcheting rate after about 20 cycles, are captured with acceptable accuracy. In addition, the simulated results of the subzone 1B under the loading case of 200 ± 500 MPa and the PR under the loading case of 200 ± 900 MPa are slightly lower than the corresponding experimental results. However, such discrepancies are unlikely to affect the numerical results obtained from further wheel–rail weld cyclic rolling contact simulations since the rail will be dominantly subjected to compressive loading.

For the BL section, large discrepancies can be found between the simulated and experimental results. One of the possible reasons is related to the significant asymmetry in the evolution of ratcheting strain under the loading cases with the same stress amplitude but symmetrical mean stresses. Such phenomena have been described in Chapter 3.3.2. Therefore, it is difficult to use only one set of calibrated material parameters to fit the curves of all the loading cases. However, the simulated results of the BL section under the loading case of -100 ± 900 MPa and the PR under the loading case of -200 ± 800 MPa capture the feature that the ratcheting strain of the BL section is lower than that of the PR under the same peak compressive stress (the BL section provides a better ratcheting resistance than the PR). From this perspective, the calibrated parameters for the BL section is reasonable.

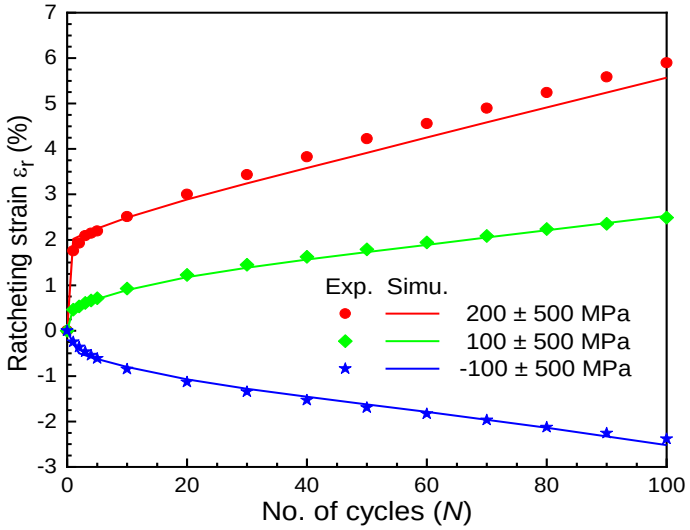

(a)

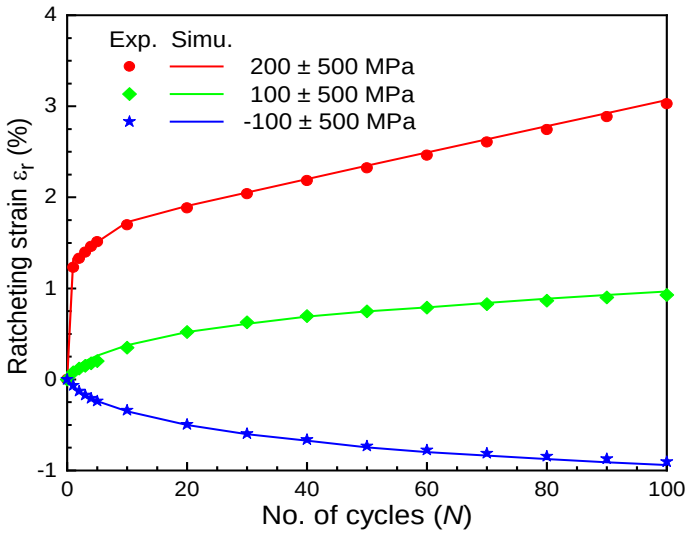

(b)

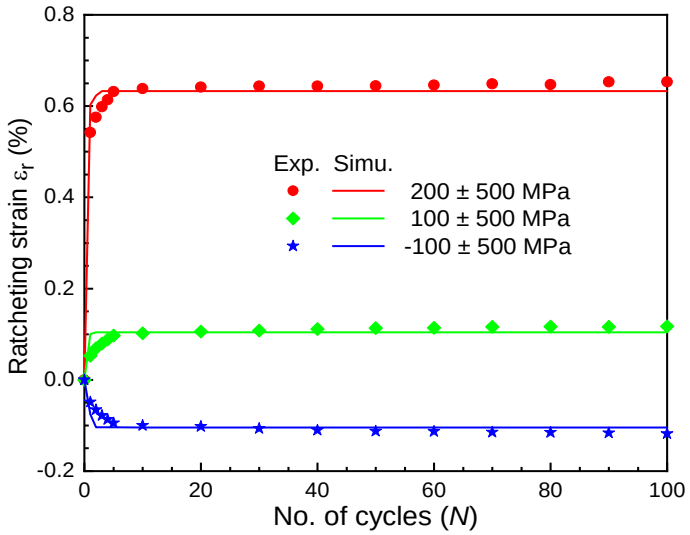

(c)

Figure 4-4: Comparison between the experimental and simulated evolutions of ratcheting strain ε_r in: (a) the subzone 1B; (b) the subzones 2A and 3B; (c) the subzone 5B under the uniaxial

stress-controlled cyclic loading tests with different mean stresses σ_m.

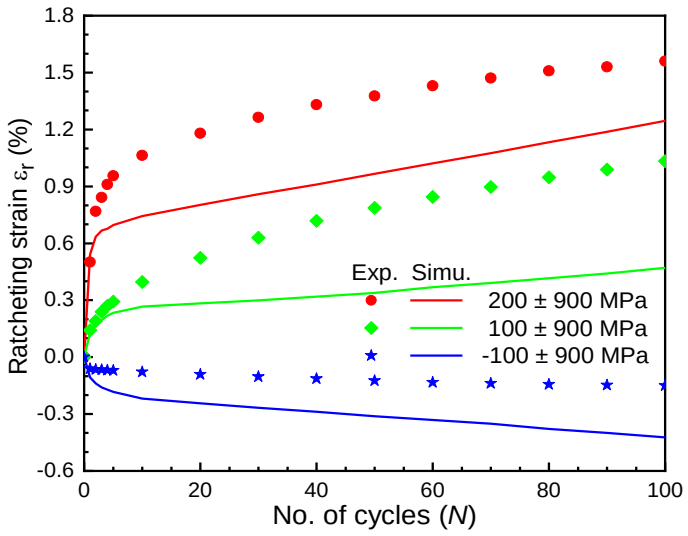

(a)

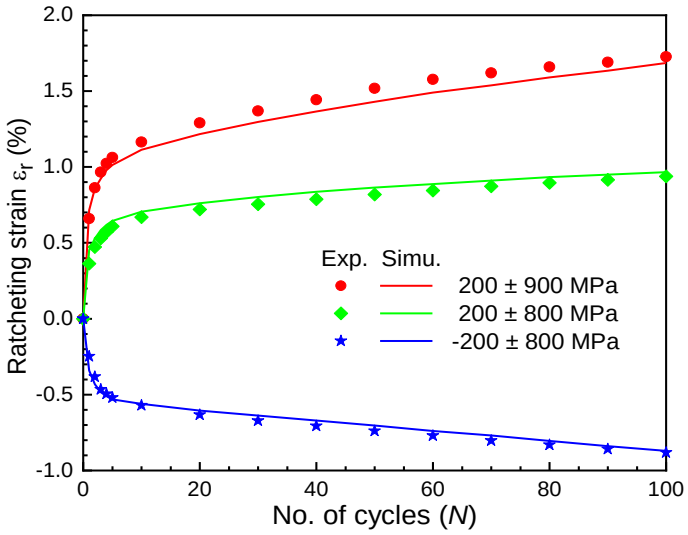

(b)

Figure 4-5: Comparison between the experimental and simulated evolutions of ratcheting strain ε_r in: (a) the BL section; (b) the PR under the uniaxial stress-controlled cyclic loading tests with different mean stresses σ_m.

4.4 Chapter Summary

An existing cyclic plasticity constitutive model for high strength rail steels was updated for flash butt welds in R400HT rail steels. The method for calibrating the material parameters required by the updated constitutive model is demonstrated and the material parameters for the SZ, the BL section and the PR

are determined from the experimental results of the monotonic tensile tests and stress-controlled cyclic loading tests presented in Chapter 3. The comparison between the simulated results and the experimental data conclude that the updated constitutive model has the capacity to simulate the ratcheting behaviour of the rail flash butt welds with acceptable accuracy, even though some discrepancies can still be observed between the simulated results and the experimental data, particularly in the region around the bond line. Therefore, this updated constitutive model for the rail flash butt welds can be applied to simulate the wheel–rail weld cyclic rolling contact under practical situations, which will be presented in the next Chapter.

Chapter 5

Numerical Study on the Ratcheting Performance of Rail Flash Butt Welds in Service

The ratcheting performance of new R400HT rail flash butt welds was numerically evaluated under a typical heavy haul in-service condition. A dynamic finite element simulation of wheel–rail weld rolling contact was firstly carried out to obtain the total vertical contact force, and its variation with the rolling distance. Multiple quasi-static wheel–rail weld contact simulations were then performed by applying the obtained total vertical contact force to determine the non-Hertzian contact pressure distribution when the wheel was located at different positions on the rail weld top surface along the rolling direction. Based on each normal contact pressure distribution, the Haines and Ollerton's strip theory and Carter's theory were then employed to estimate the corresponding longitudinal tangential traction distribution on the running surface. Finally, a cyclic loading simulation was conducted to evaluate the ratcheting performance of the rail weld in terms of RCF initiation life by repeatedly translating these normal contact pressure and longitudinal tangential traction distributions on the running surface. The results reveal that the subzone with the lowest hardness in

the softened zone is predicted to have the shortest RCF initiation life among the weld region, followed by the region around the bond line. The parent rail provides the longest RCF initiation life and therefore has the best resistance to RCF. Additionally, the existence of the softened zone can shorten the RCF initiation life of the parent rail and the bond line section, particularly the regions located adjacent to the softened zone. The possible location of RCF initiation in the softened zone of the rail head can reach to a depth of 4 mm from the running surface and extend up to 3 mm away from the wheel–rail initial contact point towards both sides in the transverse direction, while in the parent rail and the region around the bond line can reach to a depth of 2 mm beneath the running surface and extend up to 1 mm transversely from the wheel–rail initial contact point.

5.1 Methodology

As discussed in Chapters 2.2 and 2.5, a certain number of previous studies applied the Hertzian contact pressure distribution in FE analysis to simulate wheel–rail cyclic rolling contact problems quasi-statically. However, it has been found that the application of Hertzian contact pressure distribution can result in significant discrepancies between numerical results and practical situations owing to the assumptions in the HCT, i.e. linear-elastic materials and the half-space assumption. Therefore, a non-Hertzian contact pressure distribution, which can be obtained from a quasi-static FE simulation of wheel–rail contact, should be considered. Additionally, dynamic transient analysis of wheel–rail rolling contact is limited to single pass due to extremely high computational cost, even if it can capture the dynamic features effectively, particularly the dynamic contact forces generated when a wheel is passing an irregularity like a region of rail weld. In order to investigate the ratcheting performance of rail flash butt welds under in-service conditions, a combination of a dynamic transient wheel–rail weld rolling contact simulation, multiple quasi-static wheel–rail weld contact simulations and a cyclic loading simulation on a rail weld was applied in this study and the detailed procedure is illustrated in Fig. 5-1. All the simulations were performed by using the commercial software

Abaqus 2019.

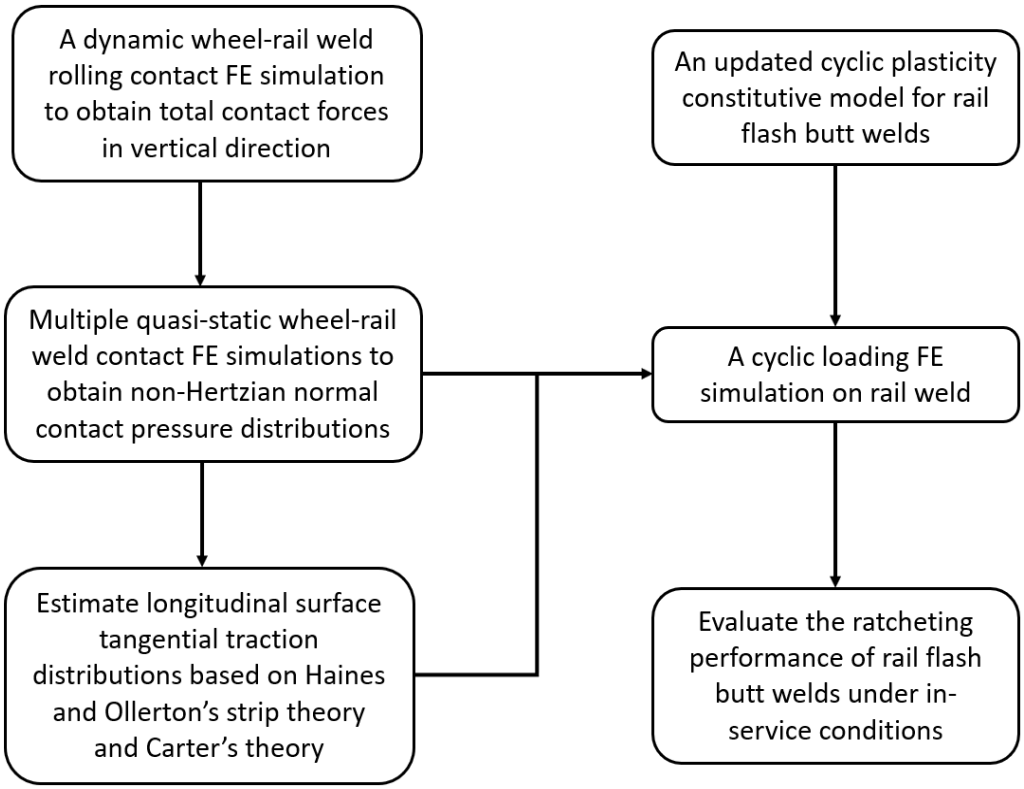

Figure 5-1: Flow chart of the research methodology to evaluate the ratcheting performance of rail flash butt welds under in-service conditions.

A dynamic transient FE simulation of wheel–rail weld rolling contact under a typical condition in Australian heavy haul railways was firstly carried out. From this analysis, the total vertical contact force between the wheel and the rail weld, and its variation with the rolling distance (longitudinal direction of the rail) were obtained. It should be highlighted that due to the application of a fairly long rail model assigned with relatively coarse mesh in the dynamic simulation (more detail illustrated in Chapter 5.2.1), the normal contact pressure distribution obtained from this simulation is less accurate and not used for further analysis. After that, multiple quasi-static wheel–rail weld contact simulations were performed by applying the total vertical contact force obtained from the dynamic simulation to determine the non-Hertzian contact pressure distribution when the wheel was located at different positions on the top surface of the rail weld along the rolling direction.

Based on the results of each normal contact pressure distribution, the Haines and Ollerton's strip theory (Haines & Ollerton, 1963) and Carter's theory (Carter, 1926) were then employed to estimate the corresponding longitudinal tangential traction distribution on the running surface. Finally, a cyclic loading simulation was conducted to evaluate the ratcheting performance of the rail weld by repeatedly translating these normal contact pressure and longitudinal tangential traction distributions on the running surface. It is noteworthy that the rail considered in the current study was a tangent track. Therefore, lateral creepage and spin and their corresponding effects were not considered.

5.1.1 Material Properties

The wheel material considered in the current study is identical with that used in Pun et al. (2015a). The wheel steel grade corresponds to AAR Class C, with a yield strength of 855 MPa (AAR, 2017). The properties are described by a classical von Mises elastic-plastic constitutive model combined with the isotropic hardening rule. The Young's Modulus and the Poisson's ratio are 210 GPa and 0.3, respectively. The work hardening exponent is 0.16. For the rail material, the rail steel grade is R400HT and the cyclic plasticity constitutive model demonstrated in Chapter 4 is used to describe both weld region and PR, while the corresponding material parameters are listed in Table 4-1.

5.1.2 Wheel/Rail Profiles

The rail profile considered is an as-rolled 68 kg/m flat-bottom rail (AS1085.1-2002/Amdt1, 2005) as shown in Fig. 5-2, while the wheel profile corresponds to an M-107/M-208 wheel with a standard wide flange contour (AAR Type D-38) as specified in AAR (2017) and presented in Fig. 5-3. Both rail and wheel profiles are in new condition, which are the same profiles applied in Pun et al. (2015a). The geometrical parameters of the rail profile include a height of 186 mm, a width of 74 mm, a crown radius of 254 mm and a gauge corner radius of 32 mm. A rail cant of 1:40 is applied. The geometrical parameters of the wheel profile include a flange radius of 16 mm, a width of 145 mm and a diameter of

965 mm. Since the contact case considered in this study is for tangent tracks, the initial contact position between the wheel and the rail was determined when the centreline of the rail profile coincided with that of the wheel profile. At first, the wheel was placed above the rail with distances. The point which provided the shortest vertical distance between the wheel and the rail is known as the initial contact point. The wheel was then moved towards the rail in accordance with the shortest vertical distance to establish the initial contact.

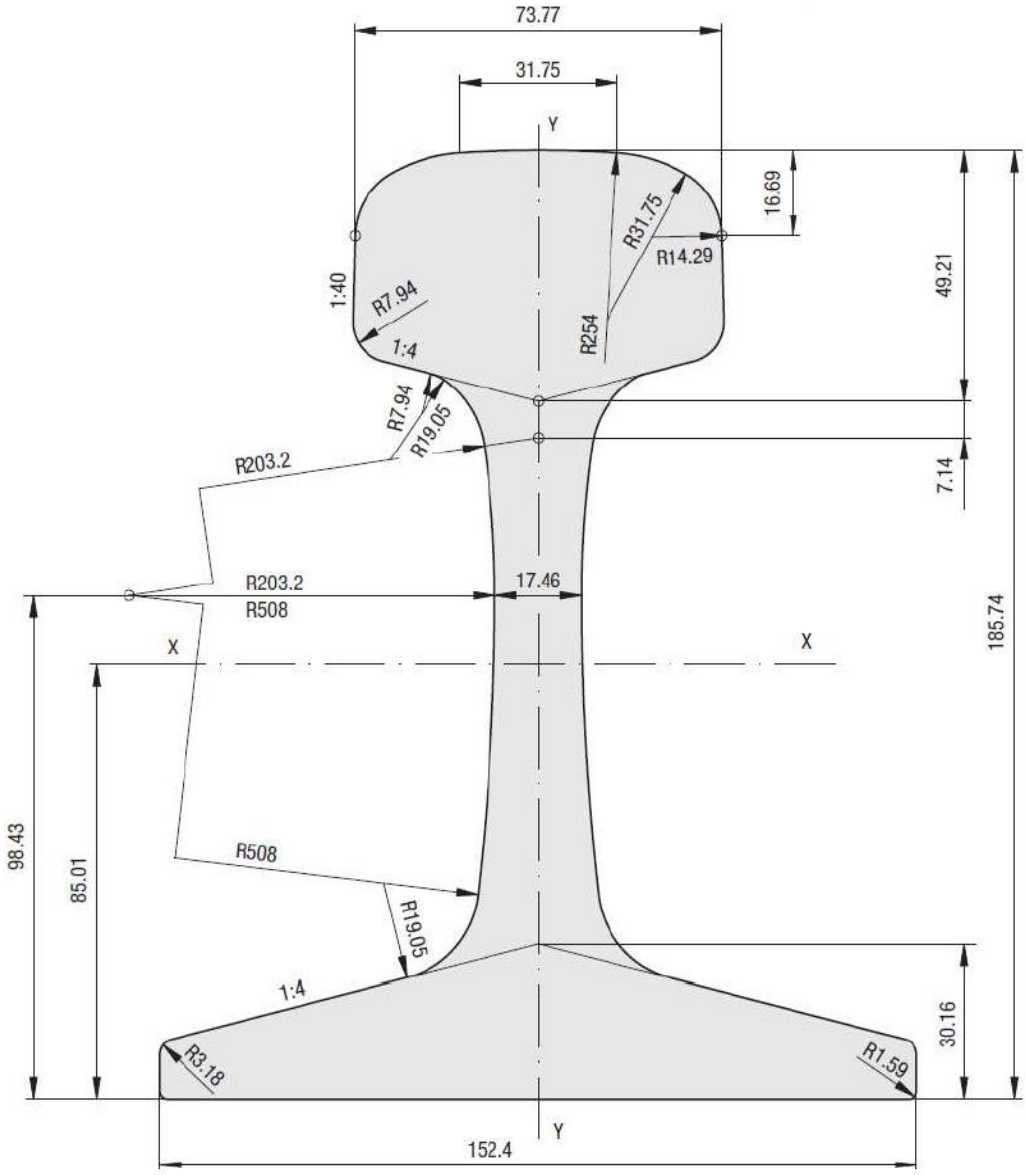

Figure 5-2: Dimensions of the rail profile (AS1085.1-2002/Amdt1, 2005).

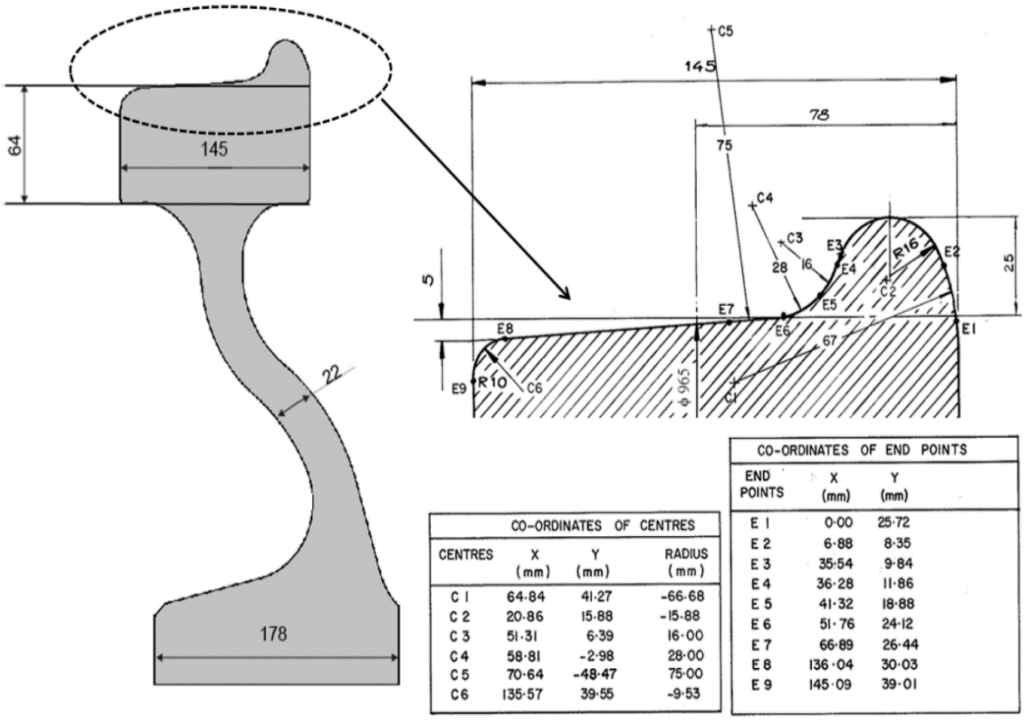

CO-ORDINATES OF CENTRES			
CENTRES	X (mm)	Y (mm)	RADIUS (mm)
C 1	64·84	41·27	-66·68
C 2	20·86	15·88	-15·88
C 3	51·31	6·39	16·00
C 4	58·81	-2·98	28·00
C 5	70·64	-48·47	75·00
C 6	135·57	39·55	-9·53

CO-ORDINATES OF END POINTS		
END POINTS	X (mm)	Y (mm)
E 1	0·00	25·72
E 2	6·88	8·35
E 3	35·54	9·84
E 4	36·28	11·86
E 5	41·32	18·88
E 6	51·76	24·12
E 7	66·89	26·44
E 8	136·04	30·03
E 9	145·09	39·01

Figure 5-3: Dimensions of the wheel profile (AAR, 2017).

5.2 Dynamic Wheel–Rail Weld Rolling Contact Simulation

In order to obtain the total vertical contact force (instead of normal contact pressure distribution) and its change with respect to the rolling distance during a wheel passing a region of rail weld, a dynamic simulation of wheel–rail weld rolling contact was carried out under a typical condition in heavy haul railways.

5.2.1 Finite Element Model

The entire FE model consists of a half track and a half wheelset due to symmetry. The 3D rail model with a length of 8.15 m was generated by extruding the 2D transverse rail section as presented in Fig. 5-2, while the 3D wheel model was created by revolving the 2D transverse wheel profile as shown in Fig. 5-3. At first, the wheel was placed at one end of rail top surface to establish the initial wheel–rail contact based on the method illustrated in Chapter 5.1.2. As demonstrated in Fig. 5-4, the weld region has a length of 54 mm and is located

at 6.323 m from the wheel–rail initial contact position. This position is also the midpoint of two 'virtual' sleepers. It is noteworthy that the function of sleepers was achieved by constraining the rail bottom surface that should be attached with rail pads in reality, along both longitudinal (Z, rolling direction) and lateral (X) directions. Therefore, no practical sleepers were modelled in current simulations. Each 'virtual' sleeper has a width of 250 mm and the sleeper spacing is 600 mm. Since the axle load applied in Australian heavy haul railways for iron ore haulage is typically in the range of 30–40 t, a point sprung mass of 17.5 tonnes, which represents the full axle load of 35 tonnes under in-service conditions, was connected to the wheel centre by the virtual primary suspension with a stiffness of 2 MN/m and a damping coefficient of 50 kNs/m. Both parameters were selected based on the fact that the vehicle body and the bogie frame have a negligible effect on high-frequency wheel–rail dynamic interactions (Baeza et al., 2006). Furthermore, both parameters are used in typical track designs for Australian heavy haul railways. A kinematic coupling constraint was set to connect the wheel centre with the wheel inner surface. In this way, the wheel and the sprung mass have the same degree of freedom as the wheel centre. The density ρ of the wheel/rail materials and the gravity g are 7800 kg/m^3 and 9.81 m/s^2, respectively. All the key parameters applied in this dynamic simulation are summarised in Table 5-1.

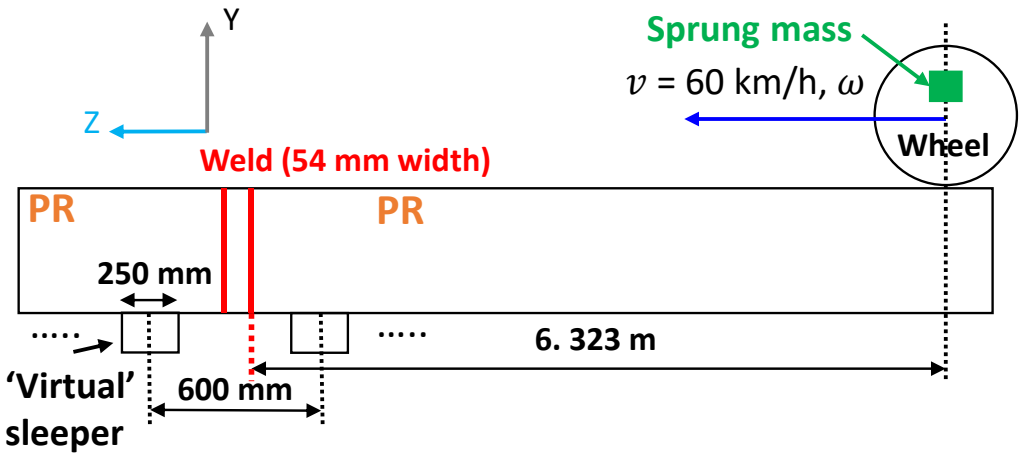

Figure 5-4: Illustration of the dynamic wheel–rail weld rolling contact simulation.

Table 5-1: Key parameters applied in the dynamic simulation.

Rail length (m)	8.15
Rolling distance to start of weld region (m)	6.323
Length of weld region (mm)	54
Translational velocity v (km/h)	60
Creepage (%)	0.15
Friction coefficient f	0.4
Time (s)	0.048
Total rolling distance d (m)	8
Sleeper width (mm)	250
Sleeper spacing (mm)	600
Sleeper stiffness (MN/m)	Infinite
Sprung mass (tonnes)	17.5
Stiffness of primary suspension (MN/m)	2
Damping for primary suspension (kNs/m)	50
Gravity g (m/s^2)	9.81
Density ρ (kg/m^3)	7800
Parameters of wheel material properties	Refer to Chapter 5.1.1
Parameters of rail material properties	Refer to Table 4-1

As illustrated in Fig. 5-5, the mesh at the contact zone was refined in order to ensure the accuracy of contact forces, while coarse mesh was applied to the other part of the model in order to reduce the computational time. The surface-based mesh tie constraints, which enable the active degrees of freedom equal for a pair of surfaces with uneven mesh densities (Abaqus, 2019), were employed to connect coarse and fine mesh regions. Fine mesh with an element size of 4 mm was applied in the complete circumference of both wheel and rail contact, except for the contact in the weld region, which was assigned with finer mesh with an element size of 4 mm × 1 mm × 4 mm (XZY). According to the definition of different subzones for the tested weld specimens presented in Figs. 3-10 and 5-6, the weld region in the rail model was partitioned into 23 segments,

consisting of one for the BL section with a width of 18 mm, two for the SZRest subzone adjacent to the BL section (each with a width of 4 mm), two for the SZRest subzone adjacent to the PR (each with a width of 5 mm) and eighteen for the other subzones covering the lowest hardness in the SZ and its surrounding region (each with a width of 1 mm). The developed cyclic plasticity constitutive model for the rail material, which is illustrated in Chapter 4, was assigned to each segment of the weld region in the rail model. The entire wheel–rail weld model consists of 243294 C3D8 elements and 315433 nodes in total.

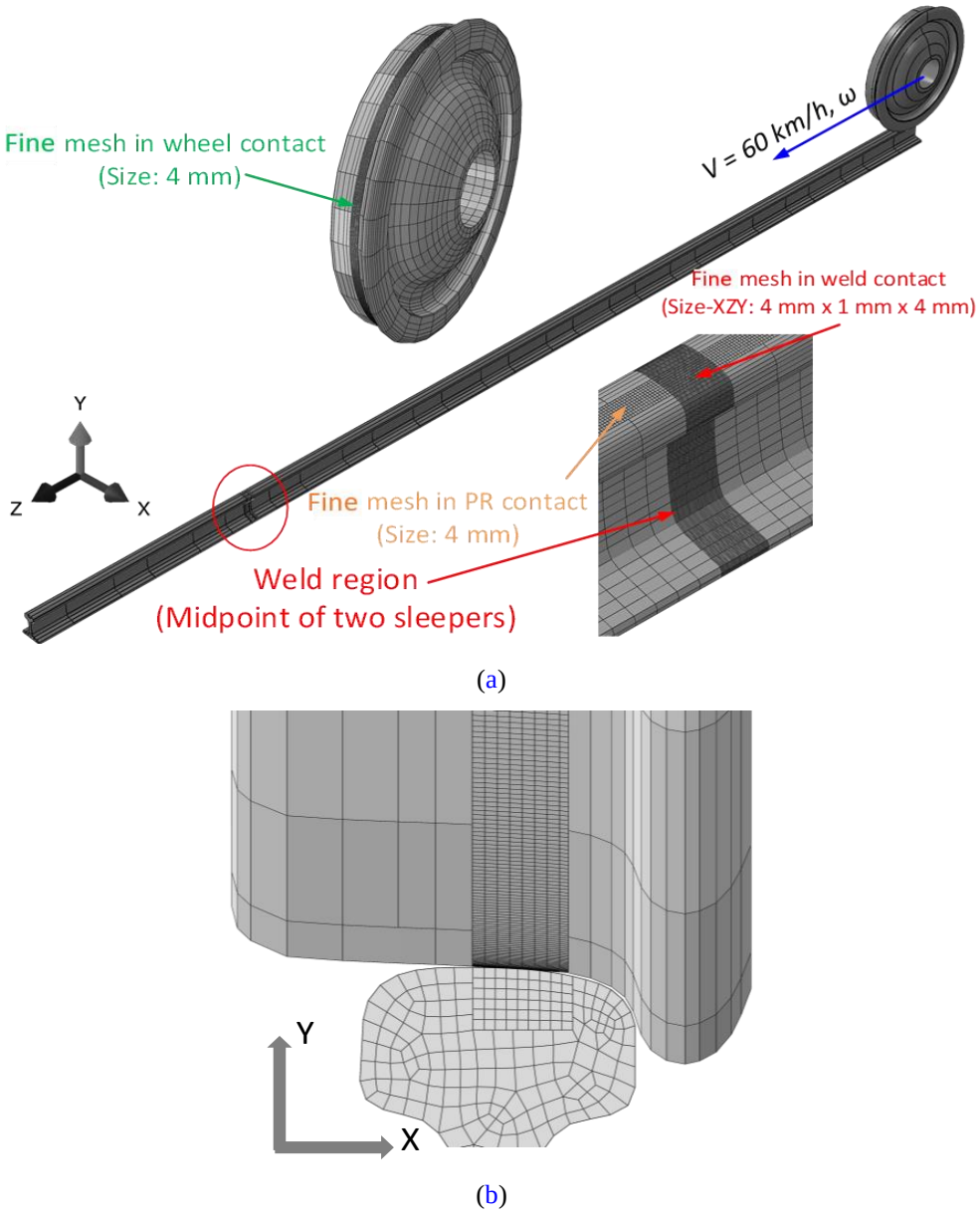

Figure 5-5: The FE model with detailed mesh for the dynamic wheel–rail weld rolling contact simulation: (a) Isometric view; (b) Transverse view.

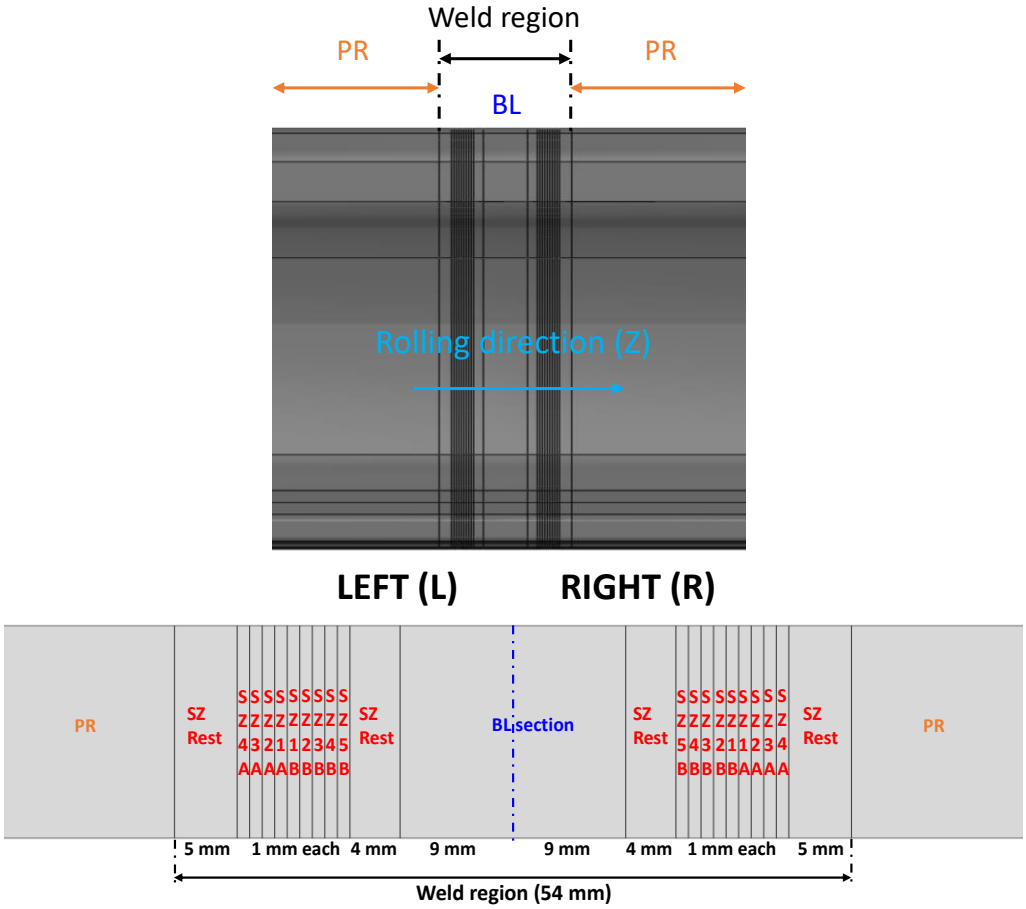

Figure 5-6: The weld region in the rail model, which was partitioned into 23 segments.

A wheel–rail quasi-static equilibrium analysis was firstly performed to obtain the deformation of wheel and rail materials caused by the gravitational load, which was subsequently considered as the initial conditions for the following wheel–rail weld dynamic rolling contact simulation. Throughout the quasi-static simulation, the wheel centre was constrained in both longitudinal (Z) and lateral (X) directions to prevent the wheel and the sprung mass from undesired movement. From this analysis, the obtained resultant vertical contact force (static axle load) is 176.3 kN. Subsequently, the dynamic-implicit simulation of wheel–rail weld rolling contact was carried out. During this analysis, the constraint that limited the wheel movement in the longitudinal direction (Z) was released. Simultaneously, a translational velocity v of 60 km/h and an angular velocity ω, which generated a creepage of 0.15%, were gradually applied on the wheel centre. A gradually increased driving force, instead of a sudden exertion, can avoid the excitation as much as possible and minimise the dynamic

relaxation (Wei et al., 2016). The frictional coefficient f at the contact was set as 0.4 and it should be noted that the aim of the dynamic simulation is to determine the total vertical contact force and its variation induced by the rail weld only, instead of the creep forces. In addition, both ends of the rail model were constrained in the longitudinal direction (Z). As listed in Table 5-1, the rolling distance to the start of the weld region d is 6.323 m, which is long enough to damp out the oscillations caused by the initial kinematic and potential energy from the imperfect wheel–rail static equilibrium and therefore for the system to reach a quasi-steady state before the wheel enters the weld region of the rail model. The maximum size of the time increment is 2.4×10^{-6} s and the total simulation time is 0.048s, which provides a rolling distance of 8 m.

5.2.2 Dynamic Wheel–Rail/Weld Contact Forces

Fig. 5-7 demonstrates the relationship between the total dynamic vertical contact force F_2 and the rolling distance d of the wheel. It is found that the resultant vertical contact force increases slightly until the rolling distance reaches roughly 3.4 m, although significant oscillations can be observed. After that, the resultant vertical contact force continues oscillating between 164.6 kN and 188.8 kN before the wheel reaches the beginning of the rail weld region. Such a range is less than 10 % of the static axle load of 176.3 kN and this indicates that a quasi-steady state of the wheel–rail contact is considered to be achieved based on the explanation proposed by Yang et al. (2016). When the wheel is rolling on the rail weld region, the maximum total vertical contact force $F_{2,max}$ of 190.5 kN occurs at approximately 3 mm right to the BL and the corresponding dynamic factor is only 1.081, which is determined by the following equation:

$$Dynamic\ factor = \frac{Max.total\ vertical\ contact\ force}{Static\ axle\ load} \qquad (5-1)$$

Such a phenomenon is directly related to the variation of the material properties in the weld region, particularly the lower yield strength of the SZ. Furthermore, the average of peak resultant dynamic vertical contact force is 184.2 kN when

the rolling distance is from 3.4 m to 7.5 m, which gives a dynamic factor of 1.045 according to Eq. (5-1). These outcomes imply that the existence of the new rail weld can cause an increase in the vertical contact force, but the overall influence is insignificant.

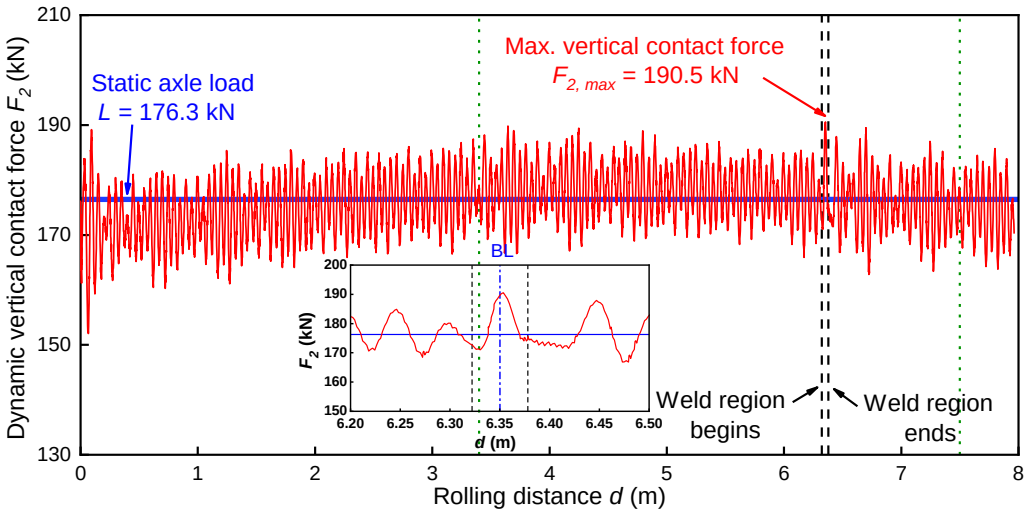

Figure 5-7: The relationship between the total dynamic vertical contact force F_2 and the rolling distance d. The average of peak total dynamic vertical contact force was calculated from the range between two green dot lines when the rolling distance is from 3.4 m to 7.5 m. The maximum total vertical contact force $F_{2,max}$ occurs at roughly 3 mm right to the BL (when the rolling distance is 6.353 m).

5.3 Quasi-Static Wheel–Rail Weld Contact Simulations

According to the history of the resultant dynamic vertical contact force F_2 demonstrated in Fig. 5-7, multiple quasi-static wheel–rail weld contact simulations were carried out to obtain the non-Hertzian normal contact pressure distribution when the wheel was located at the different positions on the running surface of the rail weld along the longitudinal direction (Z). After that, the corresponding longitudinal surface tangential traction distribution was estimated based on the Haines and Ollerton's strip theory (Haines & Ollerton, 1963) and Carter's theory (Carter, 1926). The lateral creepage and spin and their influences were not considered because this study only focuses on a tangent

track.

5.3.1 Finite Element Model

The FE model for the quasi-static wheel–rail weld contact simulations was updated based on that used for the dynamic simulation as introduced in Chapter 5.2.1. As shown in Fig. 5-8, the length of the rail model was shortened to 850 mm which includes the segment supported by two 'virtual' sleepers and the weld region at the middle. It should be noted that such length is sufficient to get the results of contact pressure converged and no geometry change was made for the wheel model. A fine mesh region with 1 mm element size was set in the vicinity of the contact in the model to capture high contact pressure and its gradient. Specifically, the fine mesh in the rail head covers the region with a length of 134 mm (54 mm for the weld region and 40 mm for each side of the PR) and a depth of approximately 16 mm, while the fine mesh in the wheel model covers the region with a 10 degree of its circumference and also a depth of 16 mm. For the rest of the model, coarse mesh was applied to reduce the computational time. The whole model consists of 125544 C3D8 elements and 143796 nodes. A detailed mesh convergence check was performed to avoid the influence of the mesh density on the accuracy of results prior to the simulations, which is presented in Appendix A.

The quasi-static simulations were conducted by simply applying the axle load at the wheel centre instead of the gravitational load on the whole model, which is the values of the resultant dynamic vertical contact force F_2 obtained from the previous dynamic rolling simulation, as presented in Fig. 5-7. According to Fig. 5-9a, a simulation was initially carried out when the wheel was placed on the PR (42 mm left to the BL). Then the simulation was repeated at different wheel–rail contact locations along the longitudinal direction (Z) of the rail until the wheel passed the weld region and reached the position of 42 mm right to the BL. The considered wheel–rail contact locations are every 3 mm within the PR and every 1 mm within the weld region, as denoted by the green cross in Fig. 5-9a. Therefore, the total number of simulations is 63. By using this method, the

change of the normal contact pressure distribution due to the presence of the weld region can be reasonably captured. Fig. 5-9b shows the corresponding axle load *L* applied in each simulation. To consider the worst condition and the dynamic effects caused by the weld region, the value of the axle load applied was 184.2 kN, which is the average of peak resultant dynamic vertical contact forces when the rolling distance is from 3.4 m to 7.5 m in the dynamic simulation (Fig. 5-7). For the weld region between 9 mm left and 11 mm right to the BL, the axle load applied corresponded to the total dynamic vertical contact force when the rolling distance is from 6.341 m to 6.361 m in the dynamic simulation, which is higher than the average. Throughout each simulation, the wheel centre was constrained in both longitudinal (Z) and lateral (X) directions to prevent the wheel from undesired movement.

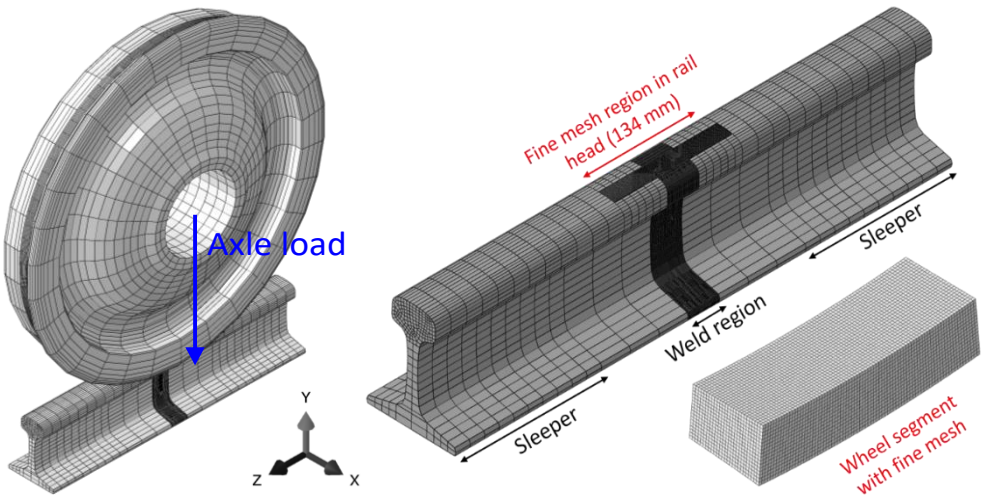

(a)

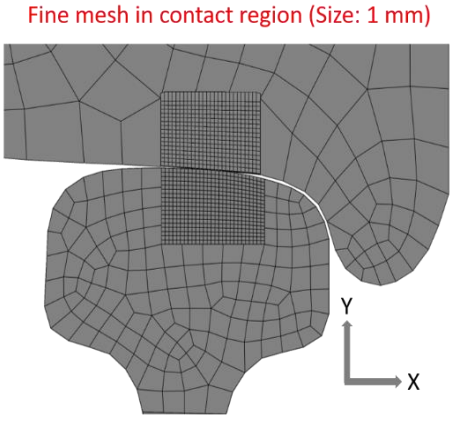

(b)

Figure 5-8: The FE model with detailed mesh for the quasi-static wheel–rail weld contact simulations: (a) Isometric view; (b) Transverse view.

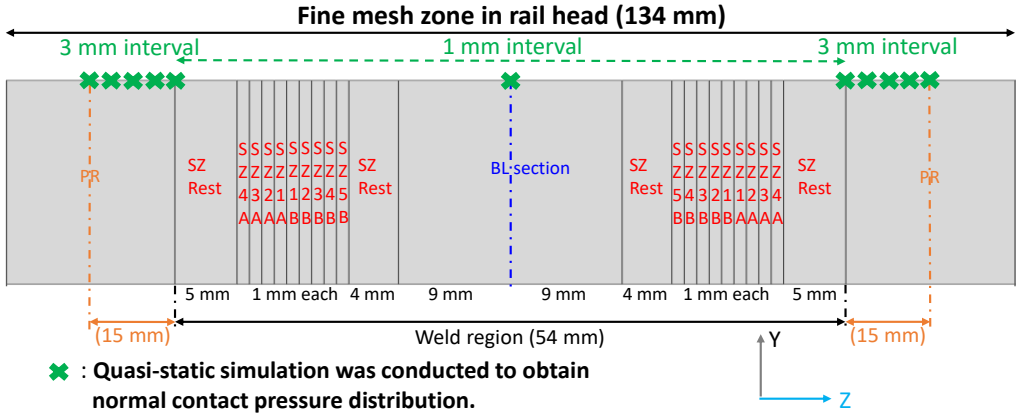

(a)

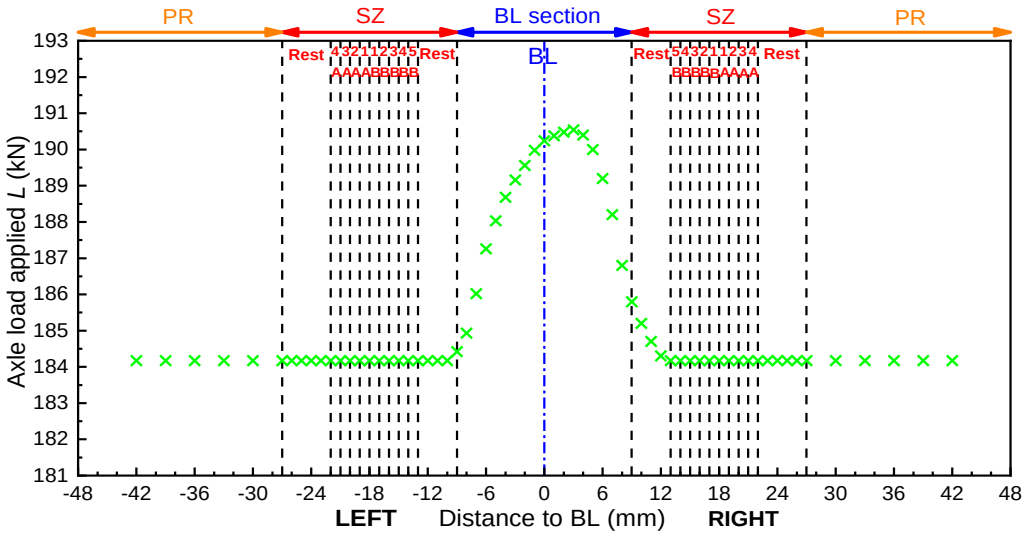

(b)

Figure 5-9: (a) Illustration of the method to perform the quasi-static wheel–rail weld contact simulations. The simulation was conducted with a 3 mm interval when the wheel was placed on the PR, while 1 mm interval when the wheel was placed on the weld region (63 simulations in total); (b) the corresponding axle load *L* applied in each simulation.

5.3.2 Normal Contact Pressure Distribution

Fig. 5-10 presents the non-Hertzian contact pressure distribution obtained from selected quasi-static wheel–rail weld contact simulations when the wheel was located at different positions with respect to the BL. The results indicate that the maximum contact pressure firstly decreases as the wheel entered from the PR (1765 MPa in Fig. 5-10a) to the SZ (1597 MPa in Fig. 5-10c) and then increases when it entered the BL section (1798 MPa in Fig. 5-10e). After that, the maximum value drops again when the wheel entered the SZ located right side

of the BL (1610 MPa in Fig. 5-10g) and finally increases as the wheel approached the PR again (1765 MPa in Fig. 5-10i). Additionally, each contact patch is not perfectly symmetric, particularly those obtained when the wheel was placed on the SZ and its adjacent region. Such phenomena are mainly due to the presence of the weld region and its associated inhomogeneous mechanical properties in the SZ.

5.3.3 Longitudinal Surface Tangential Traction Distribution

In order to simulate the wheel–rail weld cyclic rolling contact problem, both normal contact pressure and longitudinal tangential traction distributions were applied on the rail top surface. To estimate the longitudinal tangential traction distribution, the Haines and Ollerton's strip theory (Haines & Ollerton, 1963) was employed to identify the stick and slip zones in each contact patch obtained from the quasi-static simulations. The Carter's theory (Carter, 1926) was then applied to determine the corresponding longitudinal tangential traction distribution. Johnson (1985) mentioned that the estimated results based on these theories have almost no difference to those obtained from Kalker (1967). A partial slip condition, which represents the general in-service wheel–rail contact condition, was considered in this study.

Based on the mesh width (1 mm) in the contact surface of the rail model, the contact patch was divided into multiple thin strips parallel to the rolling direction by ignoring the interaction between adjacent strips. Fig. 5-11 provides an example of a strip, which is illustrated by the black arrows, based on the contact patch presented in Fig. 5-10a. a_i is the semi-width of a strip along the rolling direction (Z) and a_0 represents the longest semi-width of the strip, also known as the major width of the contact patch. b_0 denotes the longest semi-width of the contact area along the lateral direction (X). Under a steady-state rolling contact, the stick zone usually dominates in the leading area of a contact patch when a rail material is approaching to be in contact (Johnson, 1985 & Kalker, 1990). The semi-width of the stick zone in each strip is denoted as a_i' as shown in Fig. 5-12.

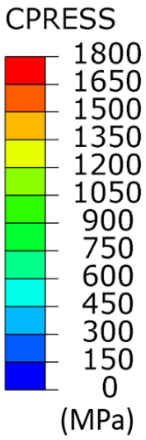

(a) PR (47 mm left to BL)

(b) PR–SZRest (27 mm left to BL)

(c) SZ (18 mm left to BL)

(d) SZRest–BL section (9 mm left to BL)

(e) BL

(f) BL section–SZRest (9 mm right to BL)

(g) SZ (18 mm right to BL)

(h) SZRest–PR (27 mm to right BL)

(i) PR (47 mm right to BL)

Figure 5-10: Normal contact pressure distribution obtained from selected quasi-static wheel–rail weld contact simulations when the wheel was located at different positions with respect to the BL.

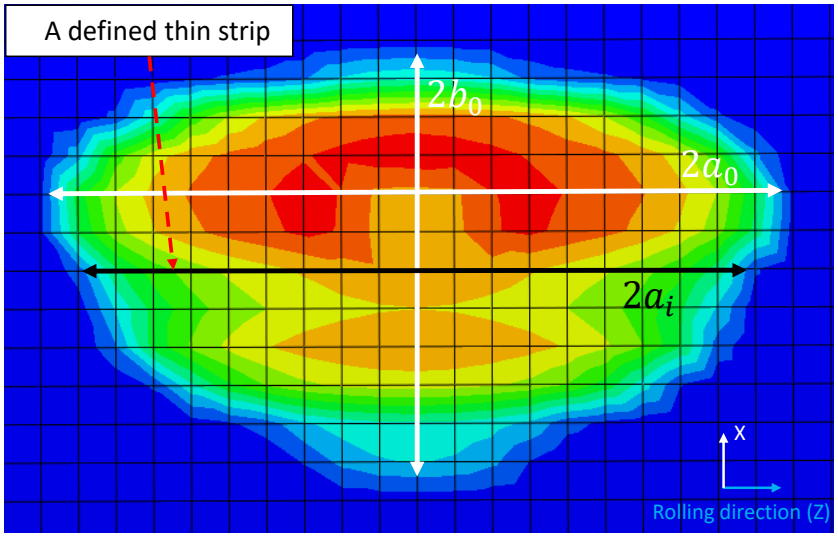

Figure 5-11: An example of this strip defined based on the contact patch presented in Fig. 5-10a.

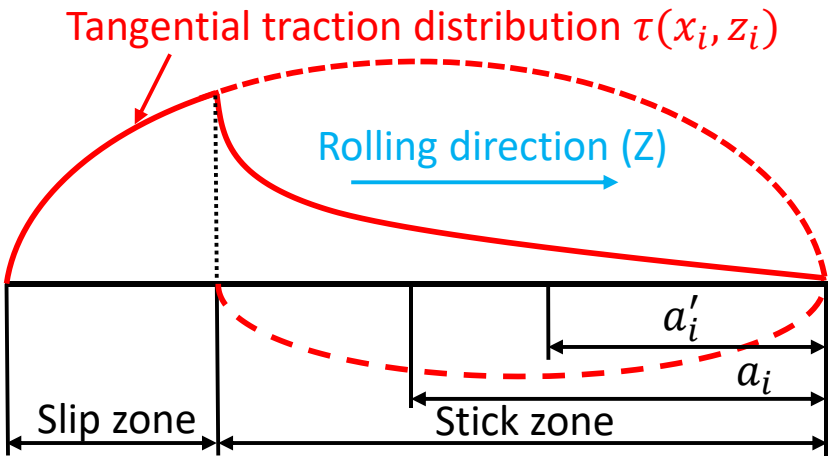

Figure 5-12: Illustration of longitudinal tangential traction distribution in the stick and slip zones of a strip.

According to the contact theory (Johnson, 1985), the sizes of the slip and stick zones for a strip are reflected by the normalised tangential traction coefficient ξ, which is defined by,

$$\xi = \frac{|F_t|}{fL} \qquad (5-2)$$

Where F_t is the tangential traction force. f is the friction coefficient and L is the normal force which is the axle load in current study. Eq. (5-2) indicates that the upper limit of the tangential traction force F_t is the value of fL. When $\xi = 0$,

the contact area is fully sticking, which represents a free rolling condition. When $\xi = 1$, the stick zone vanishes, and the condition becomes fully slipping. In general, partial slip $(0 < \xi < 1)$ occurs in wheel–rail cyclic rolling contact situations. For example, the tangential traction force transmitted is half of the maximum driving capacity if $\xi = 0.5$. Based on the strip theory (Haines & Ollerton, 1963), the relationship between the normalised tangential traction coefficient ξ and the major width of a contact patch can be described by,

$$\xi = 1 - \frac{3}{2} \times \left[\sqrt{2K - K^2} \left(1 - \frac{2}{3}K + \frac{1}{3}K^2 \right) - (1 - K) sin^{-1} \sqrt{2K - K^2} \right] \quad (5-3)$$

Where $K = \frac{a_0'}{a_0}$ (a_0' is the major semi-width of the stick zone in the contact patch), is the normalised size of the stick zone at the major width of the contact patch. If the normalised tangential traction coefficient ξ is known, the major semi-width of the stick zone in the contact patch a_0' can be determined by Eq. (5-3). After that, the size of the stick zone for each strip can be obtained by,

$$a_i - a_i' = a_0 - a_0' \quad (5-4)$$

For a 2D contact patch, the semi-width of the stick zone along the lateral direction (X) b_0' is also required and it can be determined by,

$$b_0' = \sqrt{[2K - K^2]} \quad (5-5)$$

Based on the coordinates of the nodes within the contact patch obtained from previous quasi-static simulations, the nodes in the stick zone for each strip are identified when $a_i - 2a_i' \leq z \leq a_i$ and $x \leq b_0'$, while those in the slip zone are identified when $-a_i \leq z \leq a_i - 2a_i'$ and $b_0' \leq x \leq b_0$. With the defined stick and slip zones, the longitudinal tangential traction distribution within the contact patch can be estimated by the following Carter's theory (Carter, 1926),

$$\tau_z(x_i, z_i) = fp(x_i, z_i) - \frac{a_i'}{a_i} fp(x_i, z_i), a_i - 2a_i' \le z \le a_i \; and \; x \le b_0' \quad (5-6)$$

$$\tau_z(x_i, z_i) = fp(x_i, z_i), -a_i \le z \le a_i - 2a_i' \; and \; b_0' \le x \le b_0 \quad (5-7)$$

Where $\tau_z(x_i, z_i)$ and $p(x_i, z_i)$ are the estimated longitudinal tangential traction and the normal contact pressure obtained from the quasi-static simulations, respectively. Fig. 5-12 indicates that the longitudinal tangential traction distribution in each strip can be regarded as the difference of two half elliptical traction distributions by a proper scale factor under Hertzian contact pressure distribution. Since the non-Hertzian contact pressure distribution is employed in this study, the longitudinal tangential traction distribution in each strip can be treated as the difference of two half non-elliptical traction distributions by a scale factor of $\frac{a_i'}{a_i}$.

According to Eqs. (5-3 to 5-7), the longitudinal tangential traction distribution under a friction coefficient f of 0.4 and a normalised tangential traction coefficient ξ of 0.5 was determined based on the normal contact pressure distributions obtained from 63 quasi-static simulations. This combination of parameters can represent typical dry conditions in Australian heavy haul operations and was also used as a reference in the parametric study on the ratcheting performance of high strength rail steels by Pun et al. (2015a). Fig. 5-13 presents the corresponding longitudinal tangential traction distribution under the normal contact pressure distribution shown in Fig. 5-11. The results reveal that the maximum longitudinal tangential traction is reduced when the wheel approached the left SZ from the left side of the PR and the right SZ from the right side of the BL section. In contrast, the maximum longitudinal tangential traction is increased when the wheel entered from the right SZ to the right side of the PR and from the left SZ section to the left side of the BL section.

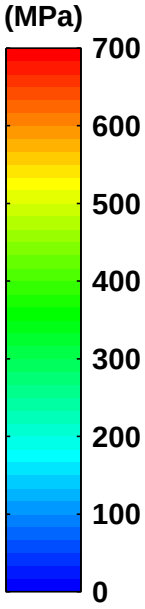

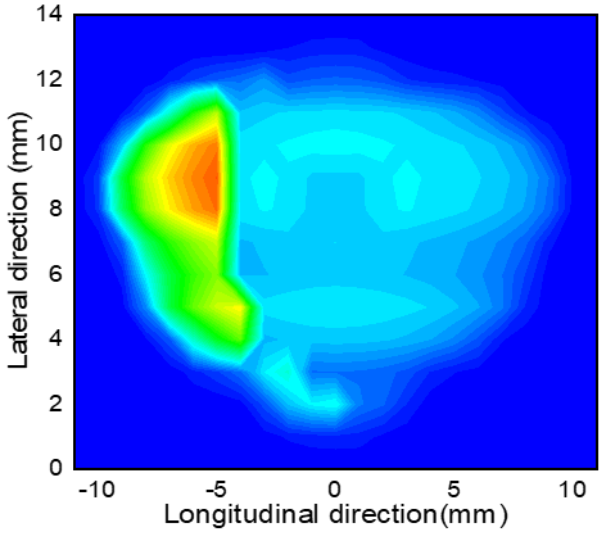

(a): PR (47 mm left to BL)

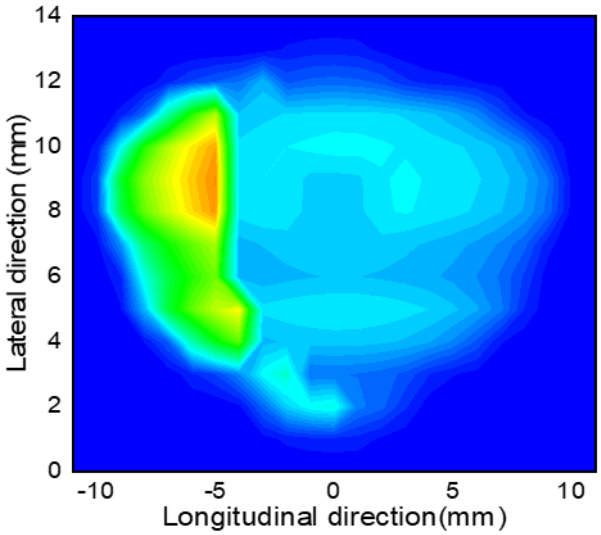

(b): PR–SZRest (27 mm left to BL)

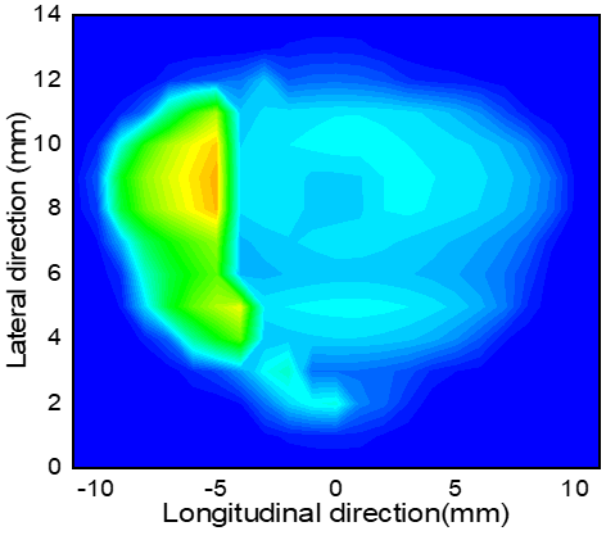

(c): SZ (18 mm left to BL)

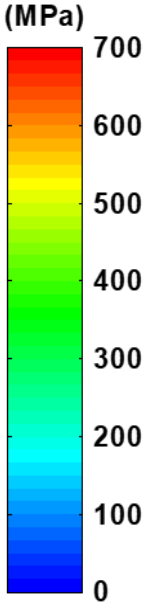

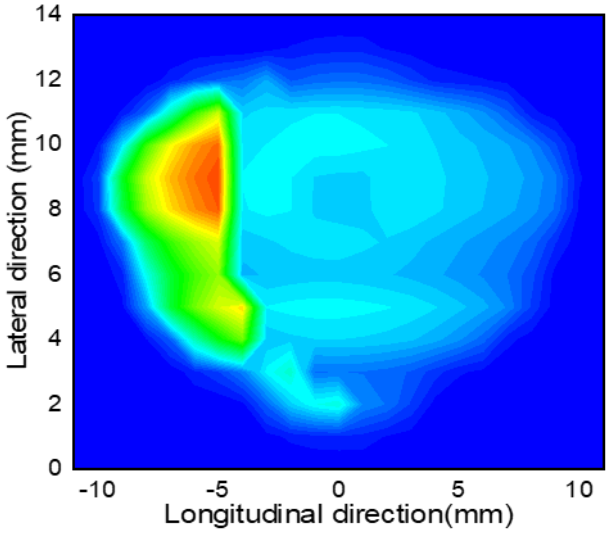

(d) SZRest–BL section (9 mm left to BL)

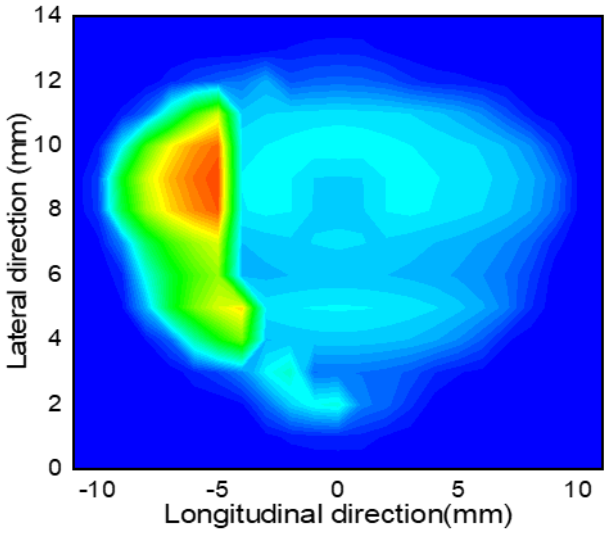

(e) BL

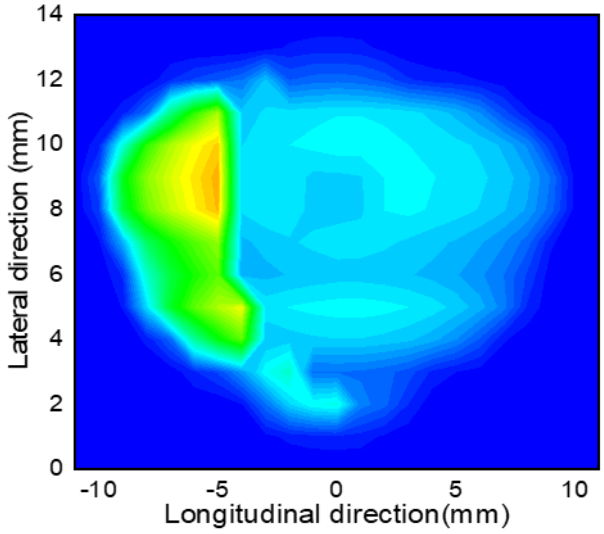

(f) BL section–SZRest (9 mm right to BL)

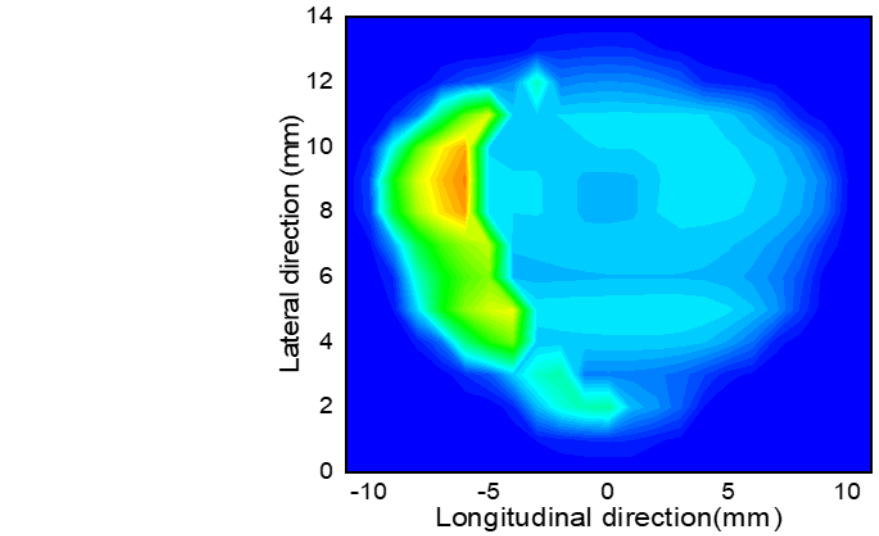

(g) SZ (18 mm right to BL)

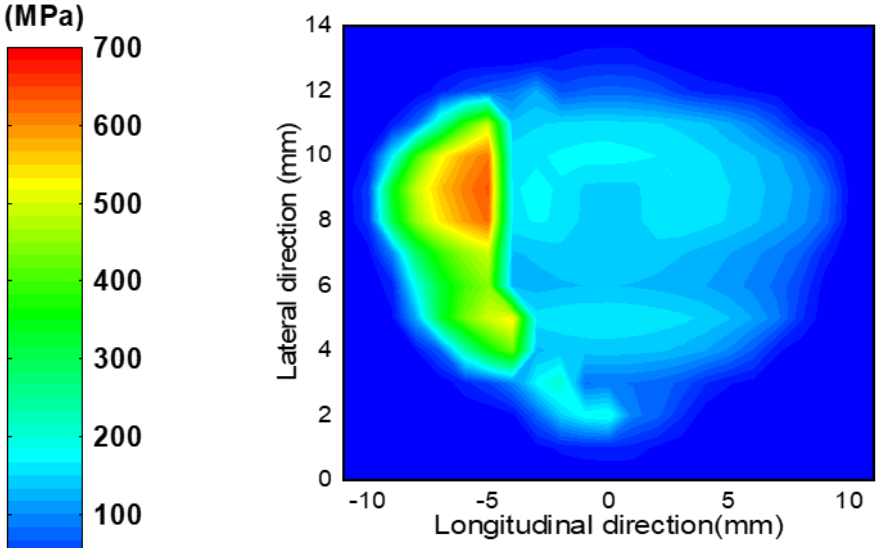

(h) SZRest–PR (27 mm to right BL)

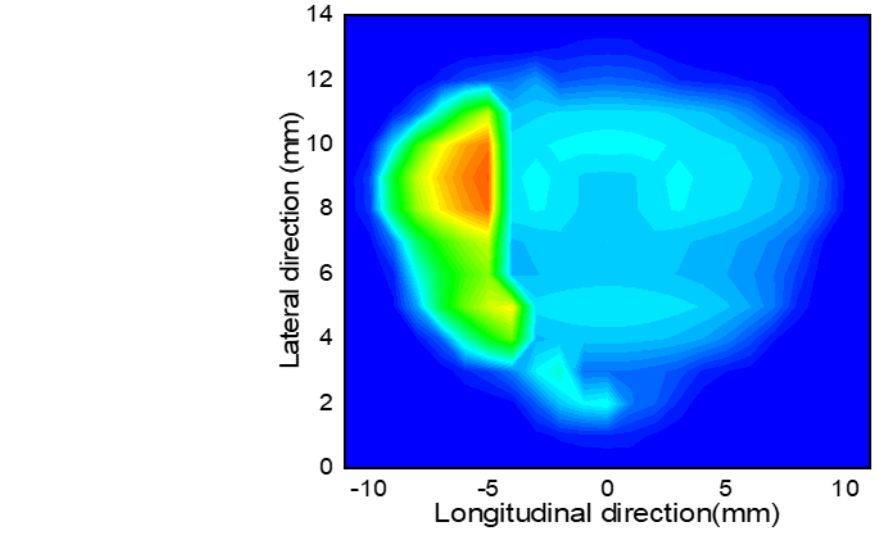

(i) PR (47 mm right to BL)

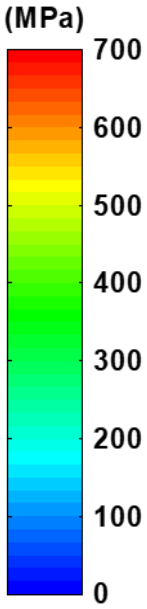

Figure 5-13: The corresponding longitudinal tangential traction distribution under a friction coefficient f of 0.4 and a normalised tangential traction coefficient ξ of 0.5 based on the normal

contact pressure distribution shown in Fig. 5-11.

5.4 Cyclic Loading Simulation on Rail Weld

In order to investigate the ratcheting performance in terms of RCF initiation life of the rail weld under the practical situation, a cyclic loading simulation was carried out by repeatedly translating the normal contact pressure and longitudinal tangential traction distributions presented in Chapter 5.3 on the top surface of the rail weld.

5.4.1 Finite Element Model

The FE rail model used is exactly the same as the one applied in previous quasi-static wheel–rail weld contact simulations, which consists of 81116 C3D8 elements and 92796 nodes. As demonstrated in Fig. 5-14, the cyclic loading simulation was conducted by repeatedly translating the normal contact pressure and longitudinal tangential traction distributions from left to right on the top surface of the fine mesh zone in the rail model through the time-dependent amplitude function with a fixed time interval (Abaqus, 2019). The translating distance was 114 mm (54 mm on the weld region and 30 mm on each side of the PR) in each loading cycle and the total number of loading cycles performed was 100. Based on the results from the quasi-static simulations, the contact pressure distribution was changed as the wheel was moving along the longitudinal direction (Z). Therefore, the translated normal contact pressure and longitudinal tangential traction distributions were varied with the location of the element surface at the rail top, which experienced the cyclic loading.

To define the loading translated on a specific element surface at the rail top, all the contact patches that once covered this element surface were firstly identified from the results of quasi-static simulations in a chronological order which corresponded to the shifting of the wheel. The value of contact pressure applied on this element surface in each patch was then represented by the average of the corresponding nodal pressure values. According to these results, the normal

contact pressure distribution translated on this element surface was eventually determined by applying its elemental pressure value from each identified contact patch. Similar procedure was used to obtain the corresponding longitudinal tangential traction distribution translated on this element surface from all the traction distributions estimated previously. Since the total distance of translation was 134 mm and the width of each contact patch along the lateral direction (X) was 14 mm, normal contact pressure and longitudinal tangential traction distributions translated were defined on 134 columns of element surfaces at the rail top for the cyclic loading simulation. Each column consisted of 14 element surfaces.

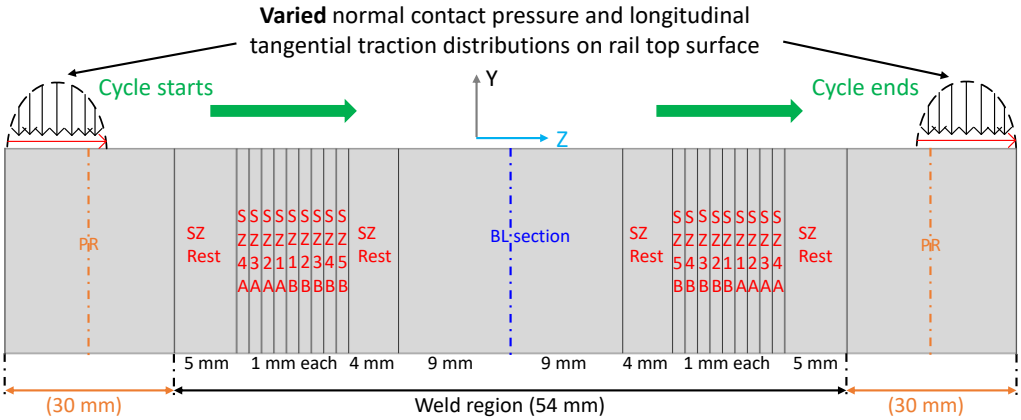

Figure 5-14: Cyclic loading simulation by repeatedly translating the normal contact pressure and longitudinal tangential traction distributions from left to right on the top surface of the weld region and the PR.

Fig. 5-15 demonstrates 21 wheel–rail initial contact positions (denoted by green cross) in the quasi-static simulations, the corresponding contact patches of which covered 14 element surfaces located at the top of the SZ1B (17.5 mm left to the BL). It is shown that when the wheel was placed at 27 mm left to the BL, these element surfaces were firstly covered by the corresponding contact patch. As the wheel passed 7 mm left to the BL, the corresponding contact patch left these element surfaces completely. Based on the 21 contact patches, the normal contact pressure and longitudinal tangential traction distributions translated on these element surfaces are illustrated in Figs. 5-16 and 5-17 in the chronological order, respectively. It is worth noted that the normal contact pressure translated on the top of the SZ1B at the beginning were the right two columns of elemental

pressure values in the contact patch obtained from the quasi-static simulation in which the wheel position was 27 mm left to the BL. In this contact patch, the SZ1B is located at the second column from right, see Fig. 5-16a, while the adjacent contact patch obtained from the last simulation as the wheel was placed at 30 mm left to the BL, did not cover the SZ1B. This approach was also applied for defining the normal contact pressure distributions translated on the element surfaces at the top of other subzones that are located between 56.5 mm and 17.5 mm left to the BL as well as between 17.5 mm and 56.5 mm right to the BL.

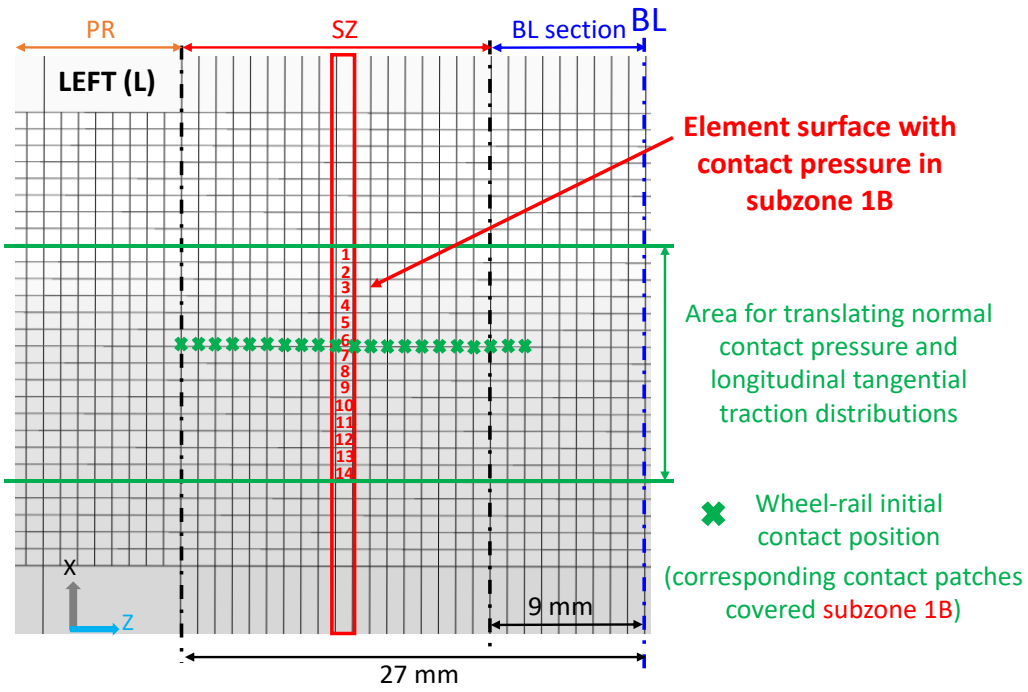

Figure 5-15: Illustration of the wheel–rail initial contact positions in the quasi-static simulations, the corresponding contact patches of which covered 14 element surfaces on the top of SZ1B.

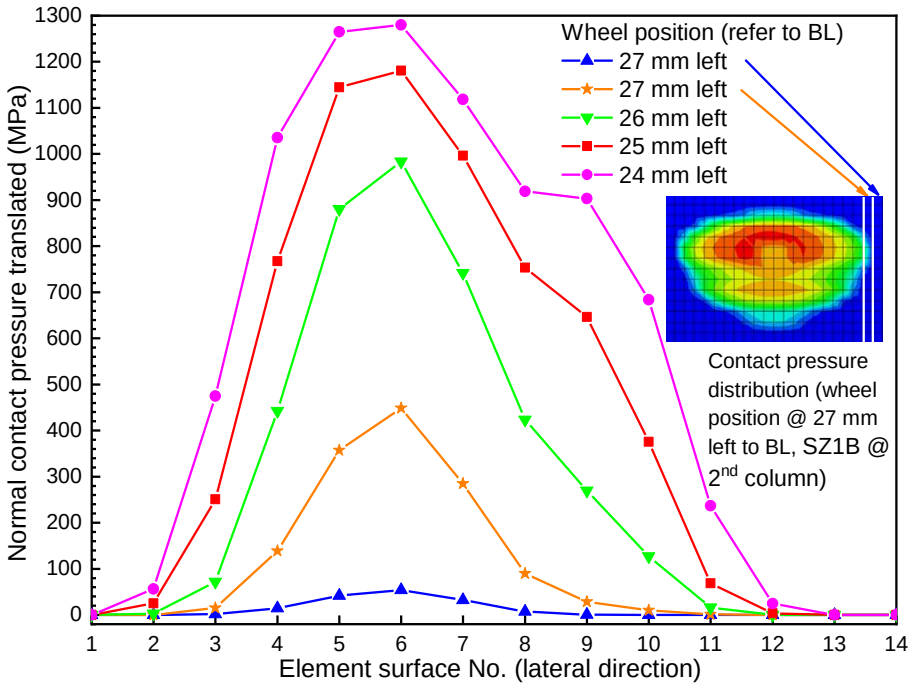

(a)

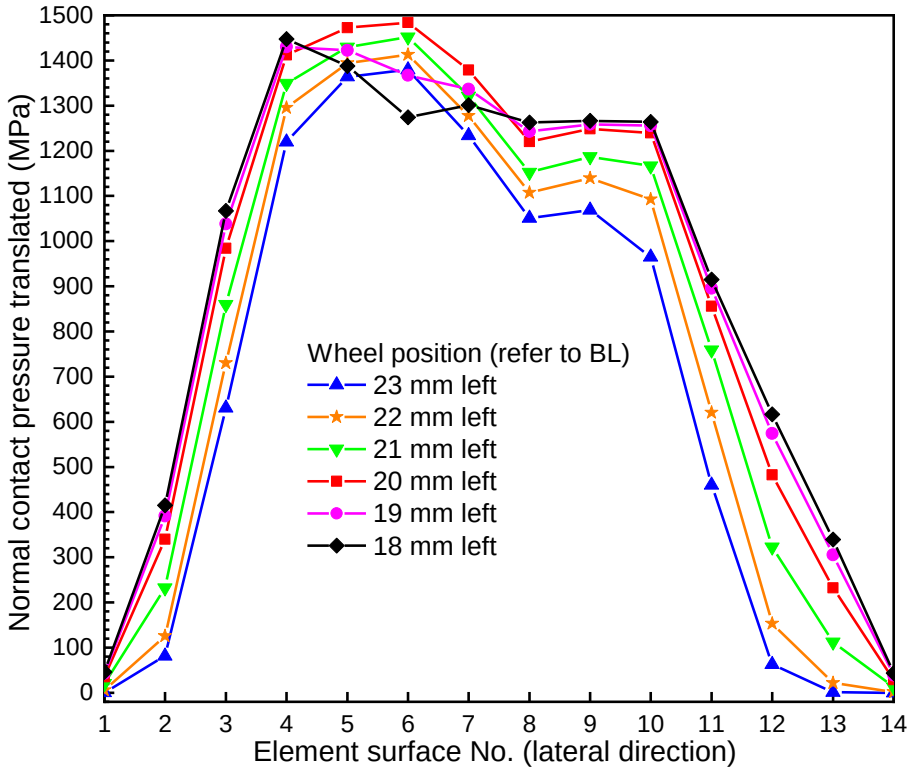

(b)

Figure 5-16: Normal contact pressure distribution translated in the chronological order on 14 element surfaces located at the top of SZ1B (17.5 mm left to the BL).

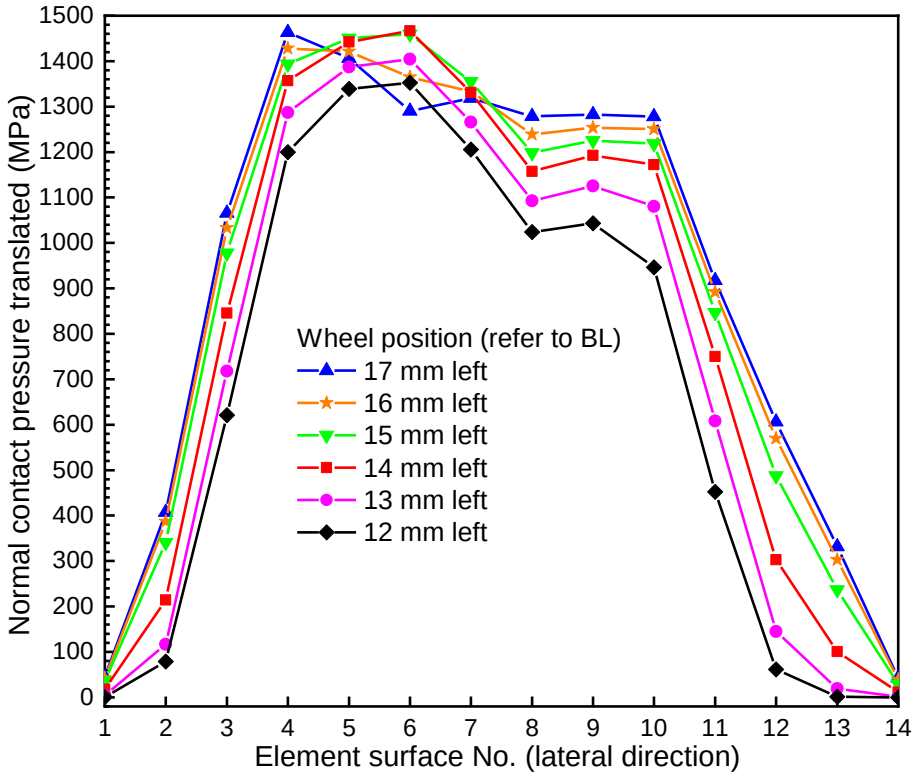

(c)

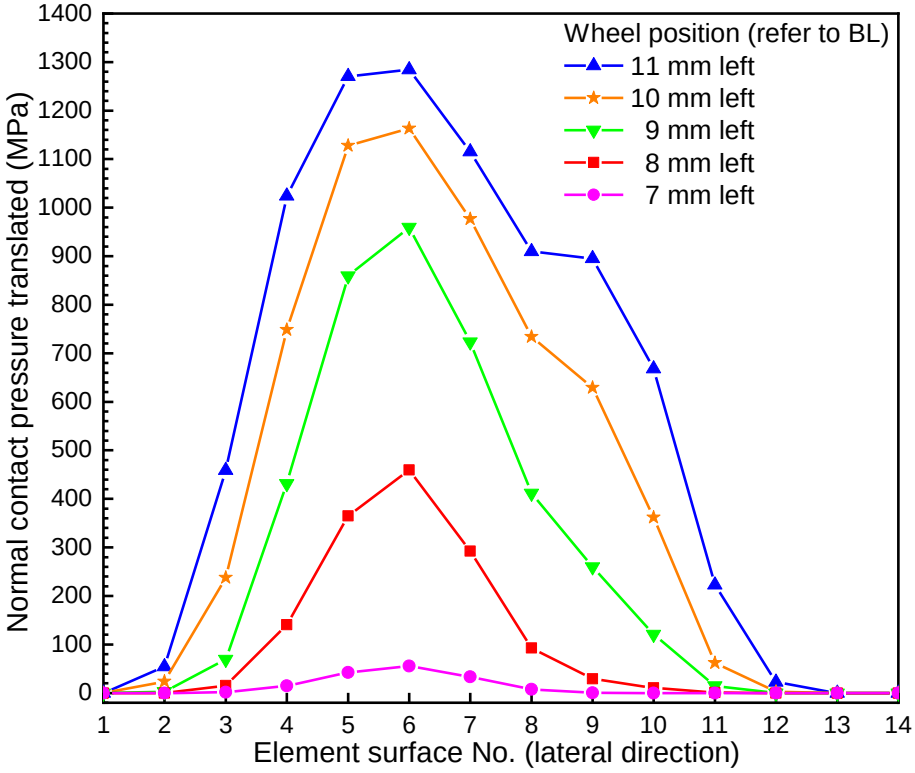

(d)

Figure 5-16: Continued.

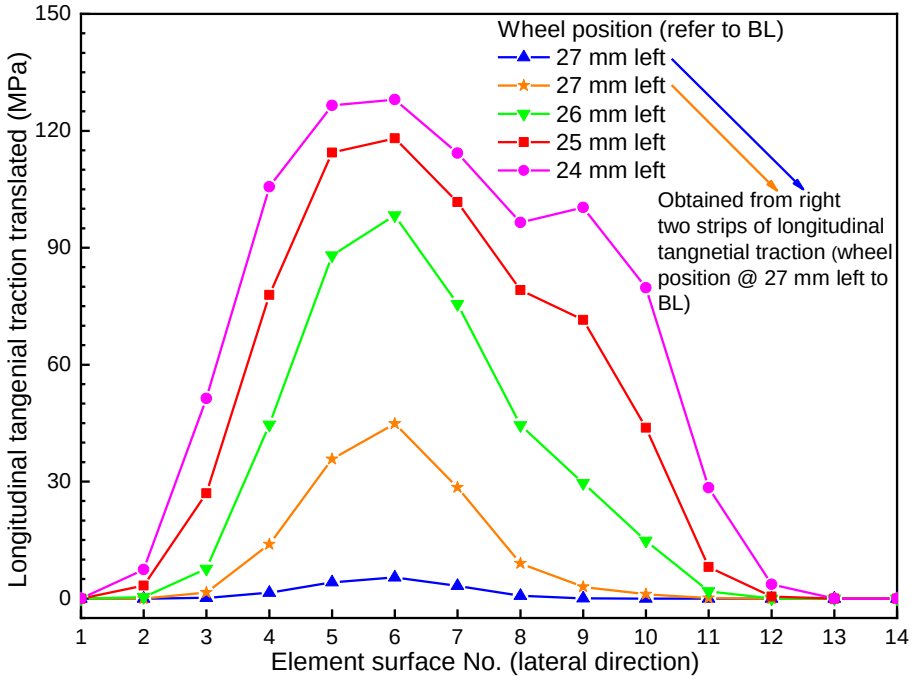

(a)

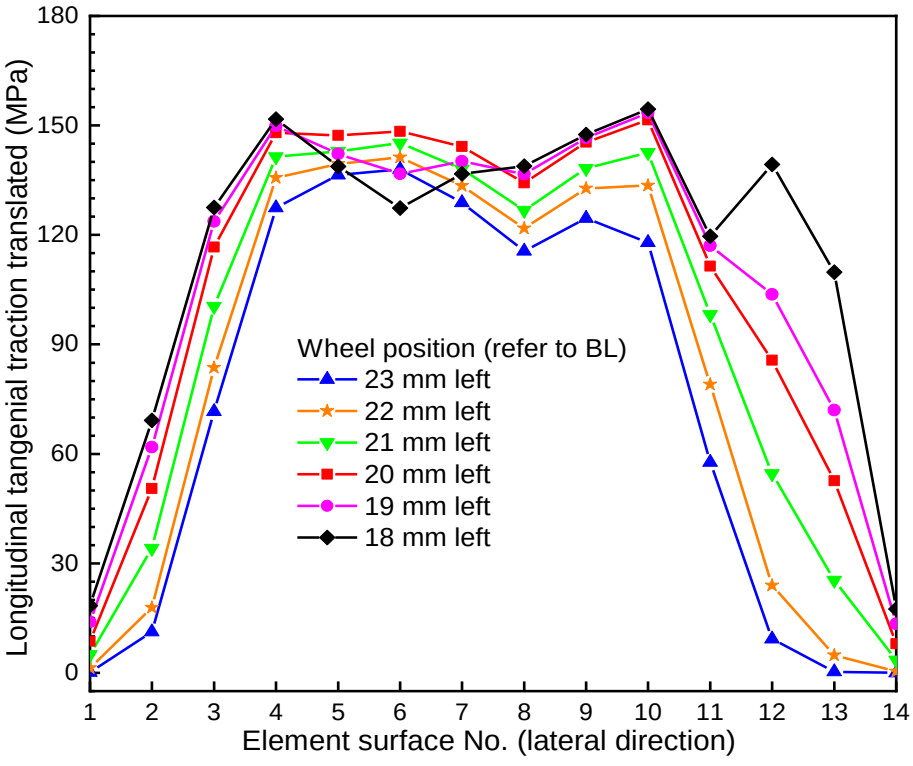

(b)

Figure 5-17: Longitudinal tangential traction distribution translated in the chronological order on 14 element surfaces located at the top of SZ1B (17.5 mm left to the BL).

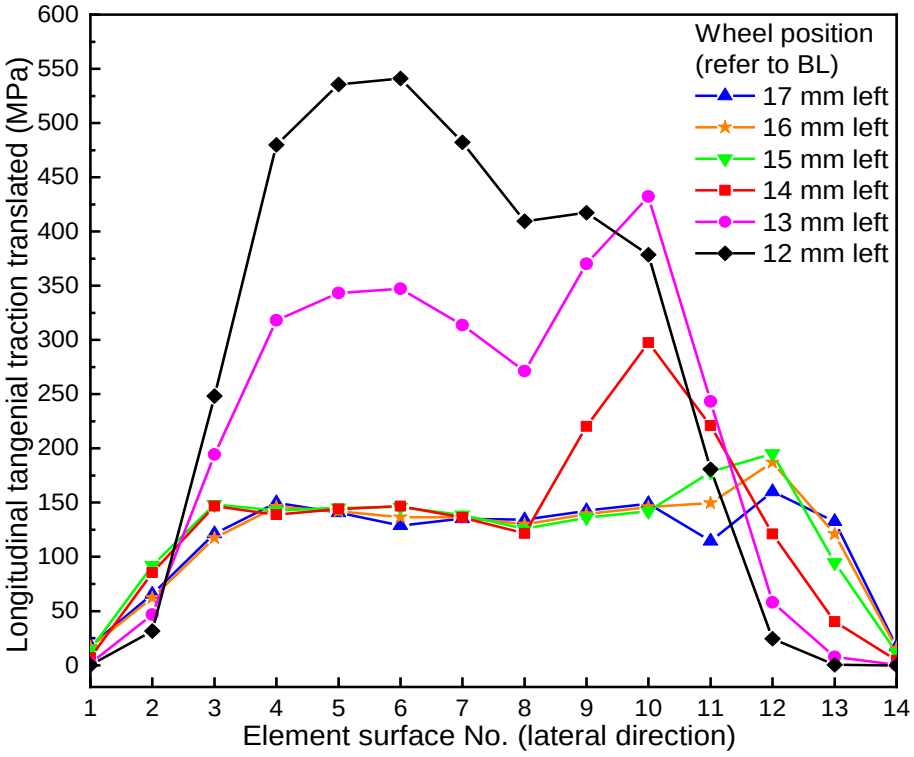

(c)

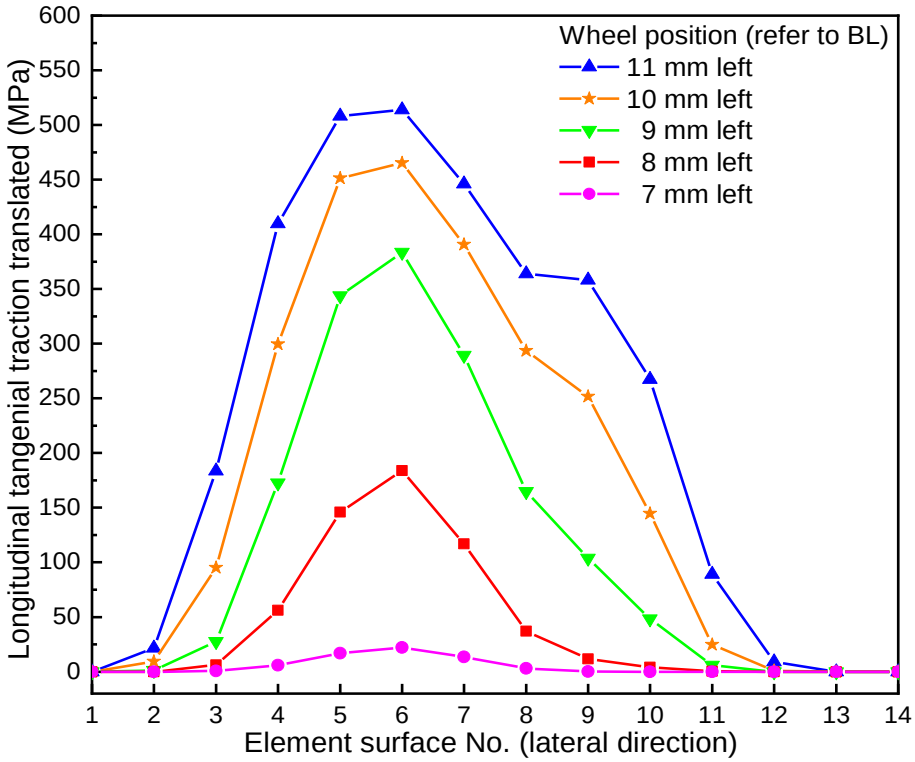

(d)

Figure 5-17: Continued.

During the cyclic loading simulation, both ends of the rail model were constrained in the longitudinal direction (Z). In addition, 60 target sections (54 for the weld region and 3 for each side of the PR) that cover all the fine elements below the top surface of the rail in the fine mesh region were created to output the plastic strain components for ratcheting analysis. The three target sections for each side of the PR are located at 45.5 mm, 30.5 mm and 27.5 mm to the BL, respectively. In this way, the influence of the weld region on the ratcheting performance of the PR can be quantified. Fig. 5-18 details an example of the target sections from the cross-sectional view of the rail model.

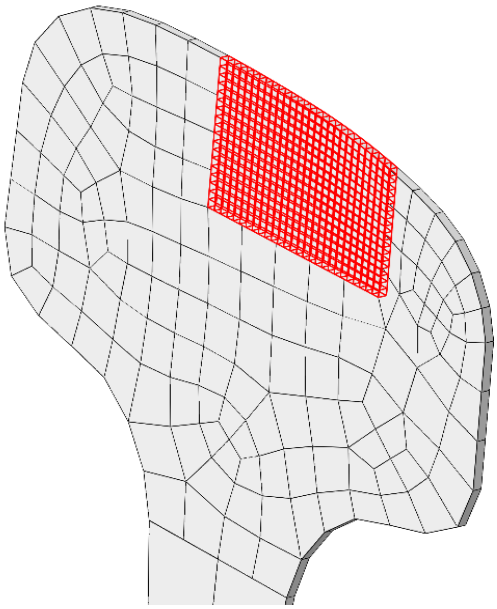

Figure 5-18: An example of the target sections (highlighted in red) to output the plastic strain components from the cross-sectional view of the rail model.

5.4.2 Evaluation of Ratcheting Performance

The cyclic loading simulation can provide both normal and shear plastic strain components of each previously defined target section in the fine mesh region since the rail head is subjected to multi-axial loading. The effective plastic strain ε_{eff}^{p} can be applied to obtain the ratcheting strain ε_r, which is the maximum value of effective plastic strain $(\varepsilon_{eff}^{p})_{max}$ of the rail material in each loading cycle. It is defined in terms of both normal and shear plastic strain components by the following equation (Yan et al., 2000),

$$\varepsilon_r = (\varepsilon_{eff}^{p})_{max} = \left(\sqrt{\frac{2}{3}\boldsymbol{\varepsilon}_\mathbf{p}:\boldsymbol{\varepsilon}_\mathbf{p}}\right)_{max} \qquad (5-8)$$

Where $\boldsymbol{\varepsilon}_\mathbf{p}$ is the plastic strain tensor. Then the ratcheting strain rate $d\varepsilon_r/dN$ in each loading cycle can be determined, which is used to predict the RCF initiation life N_i of the rail material. As mentioned in Chapter 1, rail degradation can be in the form of wear or RCF due to ratcheting. In other words, ratcheting behaviour can manifest itself in material damage in the form of wear or RCF, which are concurrent damage mechanisms (Hiensch & Steenbergen, 2018). In the case of high strength rail steels and their welds used in heavy haul operations, RCF is the dominant damage mode. According to this, the ratcheting performance is evaluated in terms of RCF initiation life.

It is assumed that RCF would initiate when the ratcheting strain ε_r reaches the material's ductility D. The time, i.e. number of loading cycles, to accumulate the plastic deformation to the material's ductility D is therefore treated as the RCF initiation life N_i, which is then used as a measure of the ratcheting performance of the rail weld in this study. The RCF initiation life N_i can be predicted from the stabilised maximum ratcheting strain rate $(d\varepsilon_r/dN)_{max,sta}$ of each target section under specific loading conditions. The following criterion is applied to judge if the rail material reaches a cyclically stabilised state:

$$\left|\frac{(d\varepsilon_r/dN)_{max,N} - (d\varepsilon_r/dN)_{max,N-1}}{(d\varepsilon_r/dN)_{max,N-1}}\right| < 5\% \qquad (5-9)$$

where $(d\varepsilon_r/dN)_{max,N}$ is the maximum ratcheting strain rate in the current loading cycle and $(d\varepsilon_r/dN)_{max,N-1}$ is the maximum ratcheting strain rate in the previous loading cycle. If Eq. (5-9) is satisfied in ten continuous loading cycles and the maximum ratcheting strain rate fluctuates during this period (instead of presenting a continuously increasing/decreasing trend), the position with the maximum ratcheting strain rate reaches cyclically stabilised and is most

likely to be where RCF will initiate. Knowing the ductility D of the weld region and the PR as given in Table 3-2, the RCF initiation life N_i can be predicted by,

$$N_i = \frac{D}{(d\varepsilon_r/dN)_{max,sta}} \qquad (5-10)$$

It is worth noted that the ductility of the rail materials was obtained under the monotonic tensile tests (Chapter 3.3.1) and might not be suitable for practical wheel–rail contact situations, which are dominated by compressive and shear stresses. This indicates that the actual ductility may be higher and therefore, a longer RCF initiation life can be expected by using Eq. (5-10). A more relevant approach to determine the strain level at which RCF initiates would be to conduct twin disc tests under conditions that are aimed at developing RCF damage, as used in other studies, e.g. by Garnham & Beynon (1991).

5.4.3 Numerical Results and Discussion

To clearly demonstrate the numerical results of ratcheting, the label of subzones that are located at the left side of the BL are presented in the format of '[subzone name]$_{Left}$', i.e. SZ1A $_{Left}$ and PR $_{Left}$, while the label of subzones that are located at the right side of the BL are presented in the format of '[subzone name]$_{Right}$', i.e. SZ1A$_{Right}$ and PR$_{Right}$. Additionally, a detailed mesh convergence check was performed to avoid the influence of the mesh density on the accuracy of ratcheting results prior to the cyclic loading simulation, which is presented in Appendix B.

Fig. 5-19 shows the evolution of the maximum ratcheting strain distribution $\varepsilon_{r,max}$ within each target section of the weld region and the PR. The results clearly indicate that the ratcheting strain mainly concentrates at the SZ with lower hardness. With the increase in the number of loading cycles, such a phenomenon becomes more evident. For instance, the maximum ratcheting strain of the BL at the 1st loading cycle is only -0.1%, while the SZ1B$_{Left}$ provides a value of -0.5%. At the 100th loading cycle, the maximum ratcheting

strain increases to -0.22% and -1.3%, respectively. Moreover, the shape of the maximum ratcheting strain distribution can almost correlate with the longitudinal hardness profile of the weld region presented in Fig. 3-1b, but is not symmetrical with the BL since the loading translated on the running surface of the weld region varies with the position to the BL.

According to the definition of the subzones illustrated in Chapter 3.3.1 and the cyclic plasticity constitutive model established in Chapter 4, the SZRest is not further divided into multiple subzones and hence, it is treated as homogenous as the PR and the BL section. However, the maximum ratcheting strain distribution in four regions (two at each side adjacent to the PR and the BL section, respectively) of the SZRest presents sharper gradients than that in the PR and the BL section. For example, at the 100^{th} loading cycle, the maximum ratcheting strain in the $SZRest_{Left}$ increases from -0.41% (26.5 mm to the BL) to -0.62% (22.5 mm to the BL). In comparison, the values in the PR_{Left} and the left side of the BL section increase slightly from -0.28% (45.5 mm to the BL) to -0.34% (27.5 mm to the BL) and from -0.22% (at the BL) to -0.26% (8.5 mm to the BL), respectively. The variations of the ratcheting train in three homogenous regions are not mainly caused by the change of the loading subjected within the region itself, but by their adjacent regions with different material properties. Specifically, both the PR and the BL section that have higher hardness, are connected with the softer SZRest. The relatively high deformation subjected by the SZRest causes higher ratcheting strain in the PR and the BL section adjacent to the SZRest than that in the same region but far from the SZRest (i.e. 45.5 mm to the BL and at the BL). Similarly, the SZRest is located between the harder PR/BL section and the softer subzones in the SZ. The relatively slighter deformation subjected by the former and the more severe deformation subjected by the latter result in the sharp change of the maximum ratcheting strain within the SZRest. These phenomena indicate that the existence of the weld region with various material properties in its SZ, i.e. hardness and ratcheting behaviour, can significantly affect the overall ratcheting strain distribution in the rail.

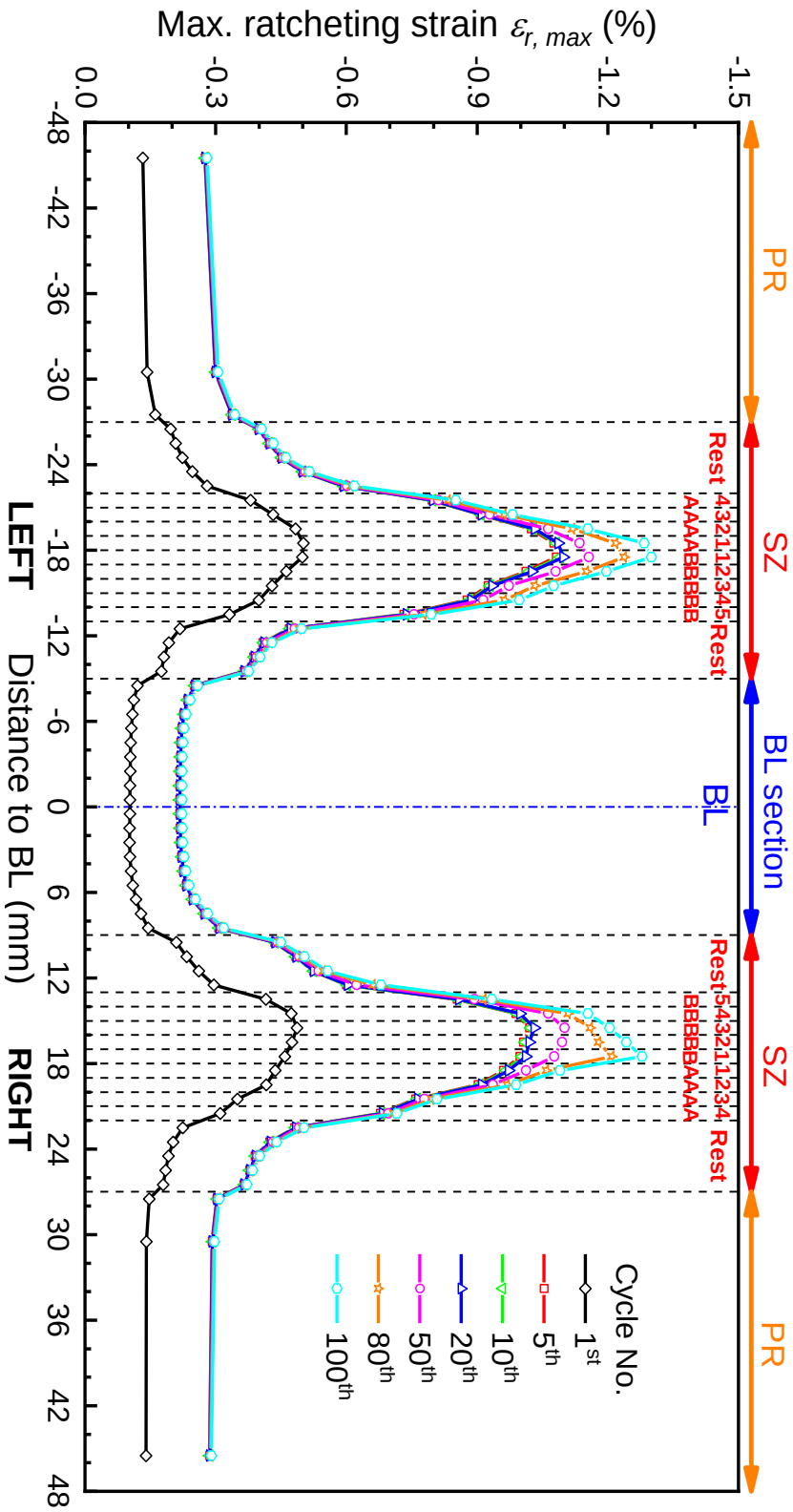

Figure 5-19: The evolution of the maximum ratcheting strain distribution $\varepsilon_{r,max}$ within the rail weld and the PR.

Fig. 5-20 demonstrates the locations of the maximum ratcheting strain $\varepsilon_{r,max}$ in the rail head within all the target sections throughout the entire simulation. The results imply that the maximum ratcheting strain is always found at about 2 mm below the running surface for both the PR and the BL section. The corresponding transverse (lateral) location of the maximum ratcheting strain is shifted roughly 2 mm away from the wheel–rail initial contact point towards the X direction. For the SZ, the maximum ratcheting strain is located at approximately 3 mm below the running surface and around 1 mm away from the wheel–rail initial contact point towards the X direction. It is worth noted that the location of the maximum ratcheting strain may change after a certain number of loading cycles. Based on the criteria defined in Chapter 5.4.2, RCF initiation is likely to occur at the location with the maximum stabilised ratcheting strain rate instead of the maximum ratcheting strain. Therefore, it is more valuable to investigate the ratcheting strain rate of each target section.

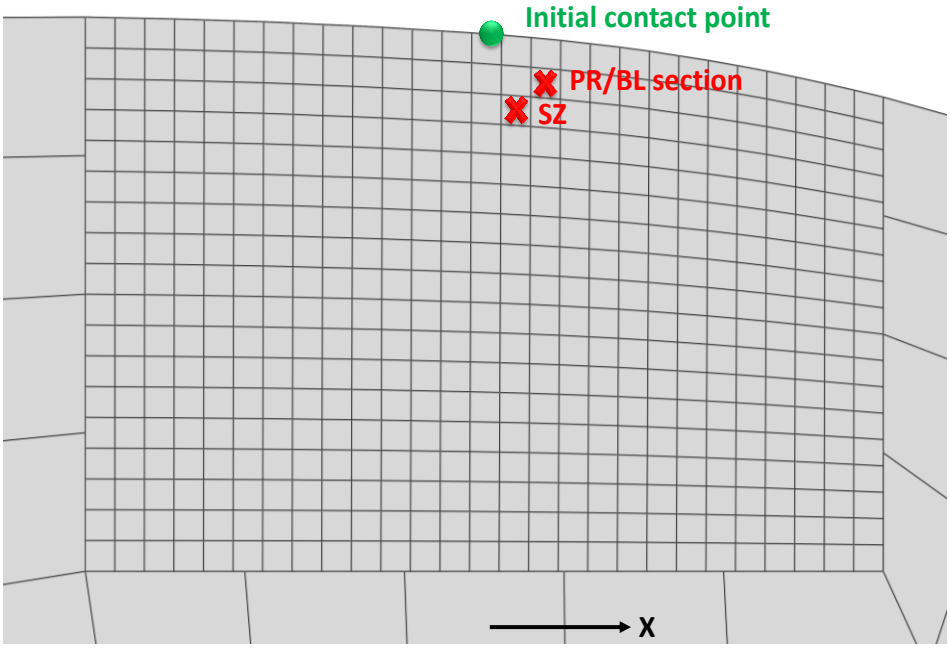

Figure 5-20: The location of the maximum ratcheting strain $\varepsilon_{r,max}$ in the target sections of the rail head.

Fig. 5-21 presents the evolution of the maximum ratcheting strain rate distribution $(d\varepsilon_r/dN)_{max}$ within each target section of the weld region and the PR. Similar to the maximum ratcheting strain distribution, the shape of the

maximum ratcheting strain rate distribution can also roughly correlate with the longitudinal hardness profile of the rail weld presented in Fig. 3-1b, but it is not symmetrical with respect to the BL. Among all the target sections, the softer subzones in the SZ always provide much higher maximum ratcheting strain rate than the PR and the BL section. In addition, the maximum ratcheting strain rate distribution in four regions of the SZRest demonstrates sharper gradients than that in the PR and the BL section owing to the location of the SZRest, between the harder PR/BL section and the softer subzones in the SZ. For example, at the 100^{th} loading cycle, the maximum ratcheting strain rate in the $SZRest_{Left}$ increases from 1.57×10^{-6} (26.5 mm to the BL) to 9.61×10^{-6} (22.5 mm to the BL). In comparison, the values in the PR_{Left} and the left side of the BL increase slightly from 8.09×10^{-7} (45.5 mm to the BL) to 1.27×10^{-6} (27.5 mm to the BL) and from 8.7×10^{-7} (at the BL) to 1.34×10^{-6} (8.5 mm to the BL), respectively. These results reveal that the presence of the weld region with various material properties in its SZ, can also influence the overall ratcheting strain rate distribution in the rail remarkably.

It has been found that higher ratcheting strain rate dominates in the SZ with lower hardness as shown in Fig. 5-21. In order to identify the target section which provides the highest maximum ratcheting strain rate in the whole rail, the evolution of the highest maximum ratcheting strain rate $(d\varepsilon_r/dN)_{max}$ in the whole rail with the corresponding target section is presented in Fig. 5-22. The results illustrate that the highest maximum ratcheting strain rate in the entire rail decreases dramatically in the first ten loading cycles, followed by the fluctuation between 4.8×10^{-6} and 6.8×10^{-6} in the next 60 loading cycles. During this stage, the target section with the highest maximum ratcheting strain rate changes frequently in multiple softer subzones, i.e. $SZ1A_{Left}$, $SZ2B_{Left}$ and $SZ1B_{Right}$. Subsequently, the highest maximum ratcheting strain rate in the whole rail becomes cyclically stabilised based on the criterion demonstrated in Eq. (5-9), which is identified in the softest target section $SZ1B_{Left}$ of the weld region. Therefore, the net plastic deformation in the $SZ1B_{Left}$ is more likely to accumulate to its ductility more rapidly than that in other subzones. The stabilised maximum ratcheting strain rate can be further applied to estimate the

RCF initiation life, which will be discussed later.

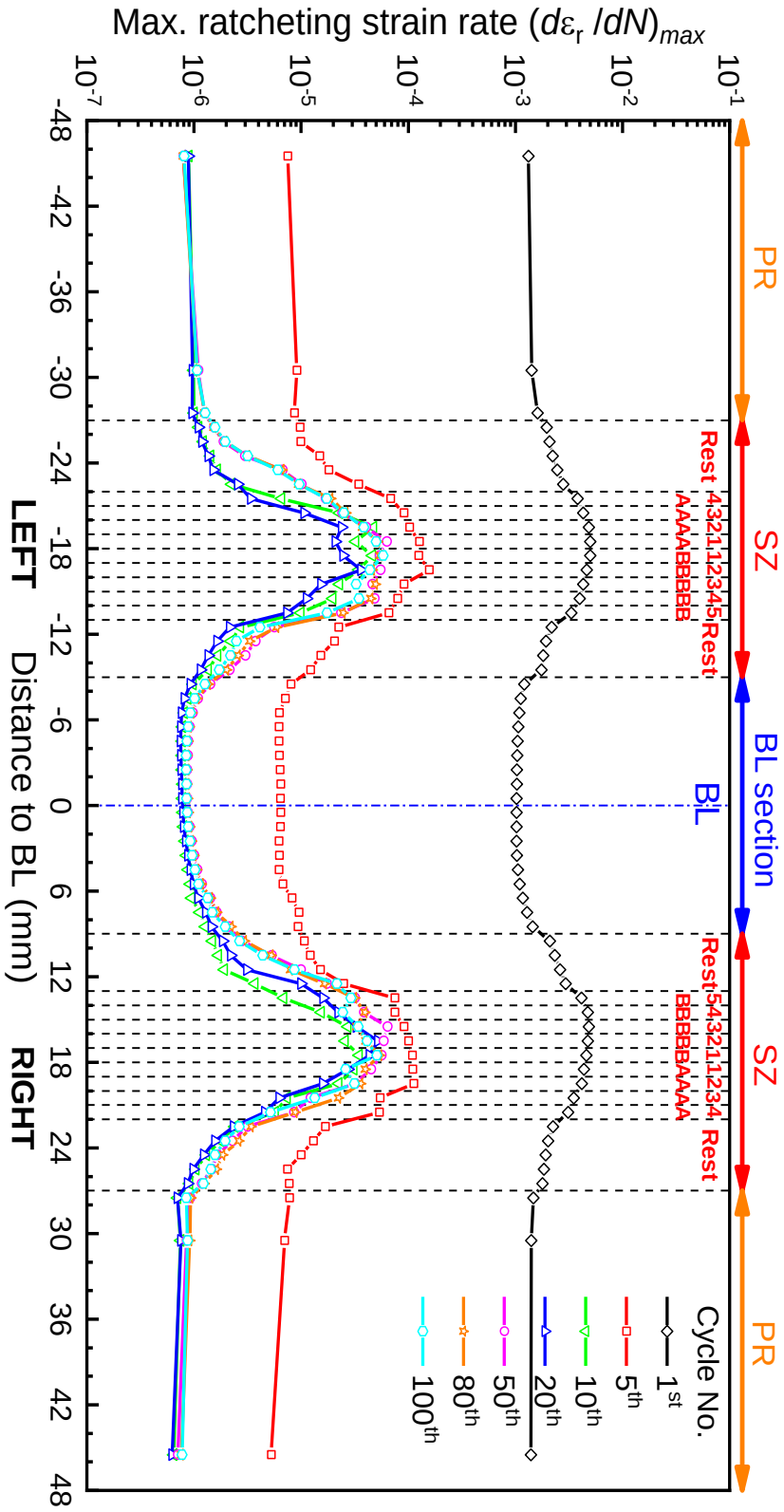

Figure 5-21: The evolution of the maximum ratcheting strain rate distribution $(d\varepsilon_r/dN)_{max}$ within the rail weld and the PR.

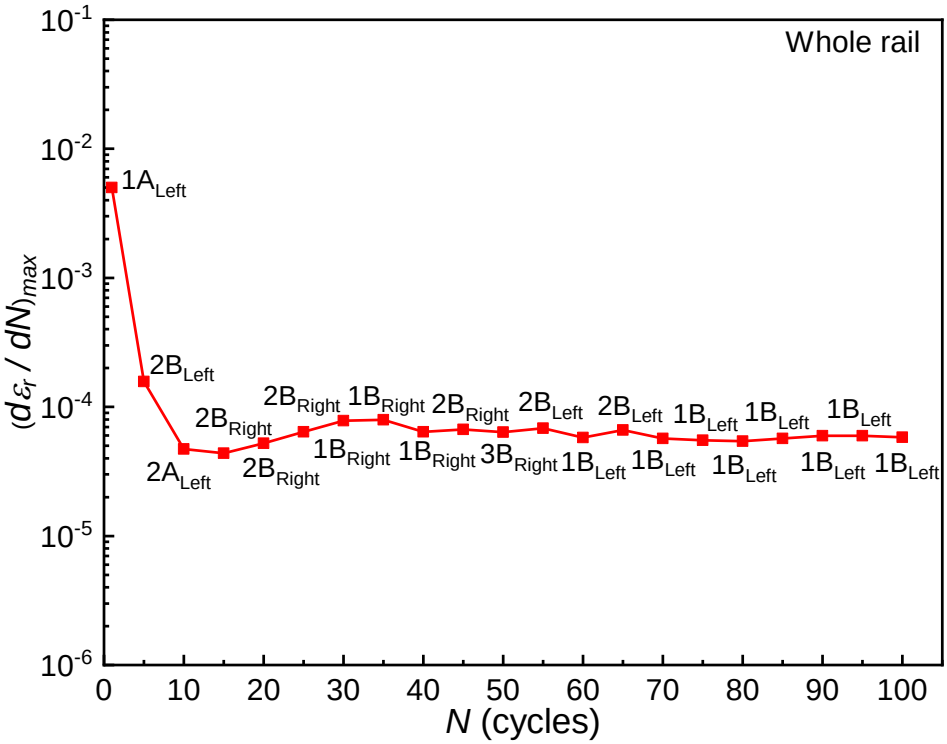

Figure 5-22: The highest maximum ratcheting strain rate $(d\varepsilon_r/dN)_{max}$ in the whole rail with its position versus the number of loading cycles N.

The cyclic stability of the maximum ratcheting strain rate has been analysed from the prospective of the entire rail in Fig. 5-22. However, it is also important to judge if each target section reaches cyclically stabilised within 100 loading cycles and further identify the positions at which RCF most likely initiates in each target section. Fig. 5-23 shows the relationships between the maximum ratcheting strain rate $(d\varepsilon_r/dN)_{max}$ in selected target sections within the BL section and the number of loading cycles N. The results clearly demonstrate that the maximum ratcheting strain rate in the BL section also decreases significantly in the first ten loading cycles, but after that becomes cyclically stabilised rapidly. It is noteworthy that for the target sections within the BL section but fairly close to the SZRest (blue/black plots), the corresponding maximum ratcheting strain rate increases slightly before reaching a cyclically stabilised state. Moreover, an increasing trend of the maximum ratcheting strain rate can be found from the BL to either side of the SZRest. Due to the higher load experienced by the right side of the BL section, see Fig. 5-9b, the maximum ratcheting strain rate in any target section within this region is always higher than that in the one located at

the same distance left to the BL. Since the maximum stabilised ratcheting strain rate in these target sections is identified at roughly 2 mm below the running surface and within 1 mm away from the wheel–rail initial contact point towards the X direction, initiation of RCF in the BL section is most possibly to occur at such positions.

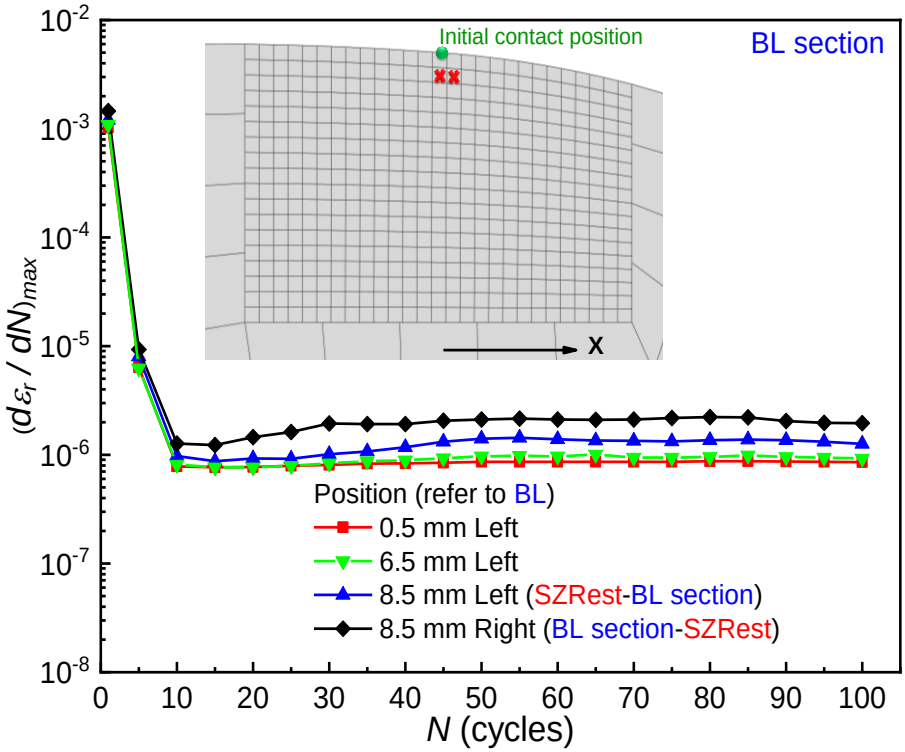

Figure 5-23: The maximum ratcheting strain rate $(d\varepsilon_r/dN)_{max}$ in selected target sections within the BL section versus the number of loading cycles N (red cross: RCF most likely initiates at).

Fig. 5-24 illustrates the relationships between the maximum ratcheting strain rate $(d\varepsilon_r/dN)_{max}$ in selected target sections within the PR and the number of loading cycles N. Similarly, the maximum ratcheting strain rate in the PR is reduced dramatically in the first ten loading cycles and reaches a cyclically stabilised state very quickly. Owing to the influence of the adjacent SZRest, the maximum ratcheting strain rate in the target sections close to the SZRest (black plots) is higher than that further away from the SZ. Additionally, the target sections on the left side of the BL always provide a higher maximum ratcheting strain rate than those located at the same location but on the right side of the BL. One of the possible explanations is attributed to the loading history. Specifically,

the load was translated from the harder PR towards the SZ on the PRL top surface, while it was translated reversely on the PR_{Right} top surface. Regarding the positions at which RCF initiates most likely in the PR, they are also located approximately 2 mm below the running surface but within 1 mm away from the wheel–rail initial contact point towards both sides in the lateral direction in comparison with those in the BL section, which are identified within 1 mm away from the wheel–rail initial contact point towards the X direction only.

The relationships between the maximum ratcheting strain rate $(d\varepsilon_r/dN)_{max}$ in selected target sections within the SZRest and the number of loading cycles N are presented in Fig. 5-25. Compared with the maximum ratcheting strain rates in the BL section and the PR, the maximum ratcheting strain rate in the SZRest gives a more evident increasing tread after the rapid decrease in the first ten loading cycles, especially in the target sections adjacent to both sides of the SZ4A and the SZ5B. Therefore, such target sections adjacent to the softer subzones in the SZ require more loading cycles to become cyclically stabilised than those adjacent to the harder PR and BL section. For example, approximately 70 loading cycles for the target section located at 12.5 mm right to the BL, while only 49 and 36 loading cycles for the ones located at 9.5 mm and 26.5 mm right to the BL, respectively. It is also identified that relatively significant cyclic instability of the maximum ratcheting strain rate occurs in the target section located at 12.5 mm right to the BL before the 70^{th} loading cycle, and this phenomenon may result from the collective effects of adjacent softer region and the higher load translated on the $SZRest_{Right}$ and the right side of the BL section (Fig. 5-9b). RCF in the SZRest most likely initiates from the running surface to 2 mm below the running surface and within 2 mm away from the wheel–rail initial contact point towards either side of the lateral direction (area with the red crosses). It is noteworthy that although the maximum ratcheting strain rate in some target sections within the SZRest reaches a cyclically stabilised state, its specific location may alter within this region as the number of loading cycles increases. The expanded region in the SZRest, in which RCF is likely to initiate, compared with those in the PR and the BL section, is more possibly associated with its softer feature.

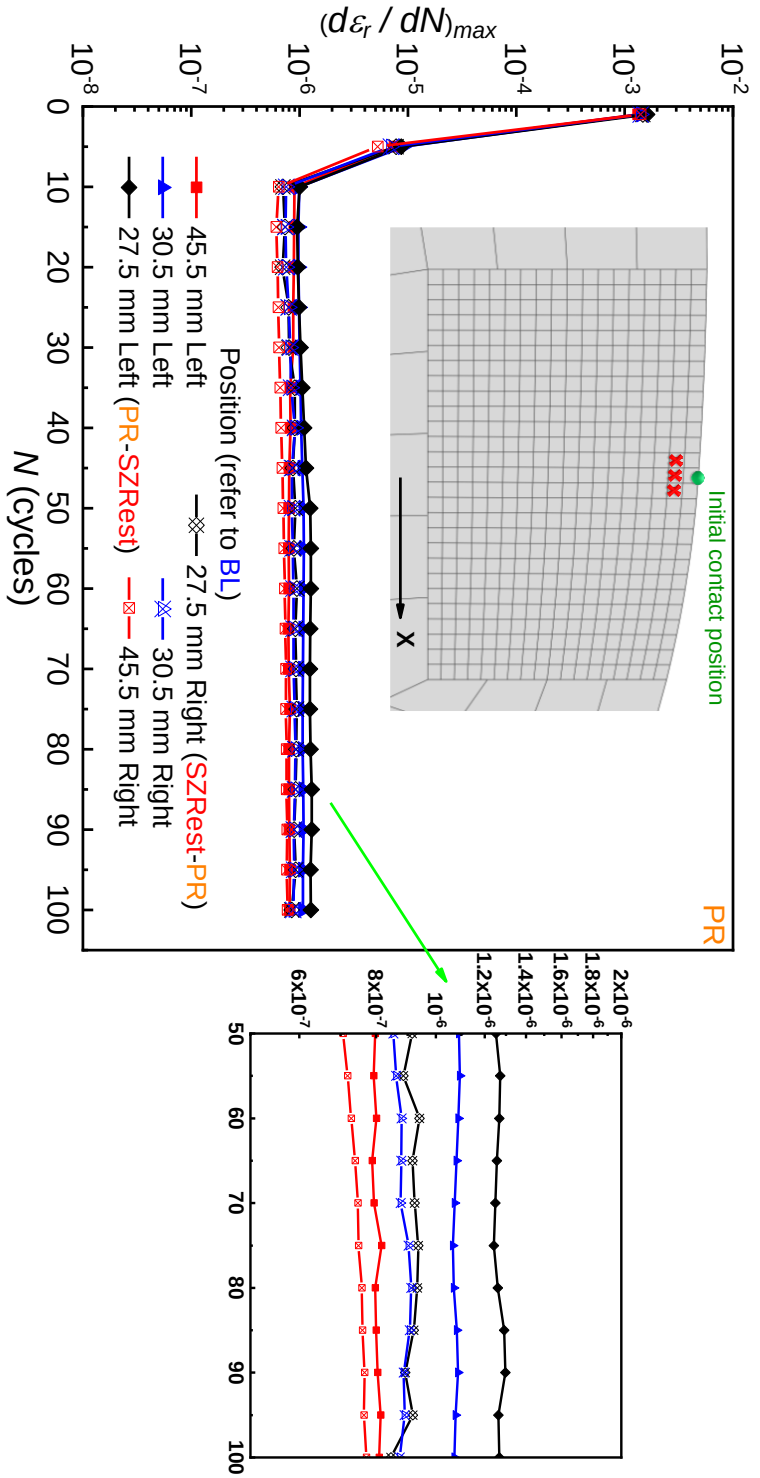

Figure 5-24: The maximum ratcheting strain rate $(d\varepsilon_r/dN)_{max}$ in selected target sections within the PR versus the number of loading cycles N (red cross: RCF most likely initiates at).

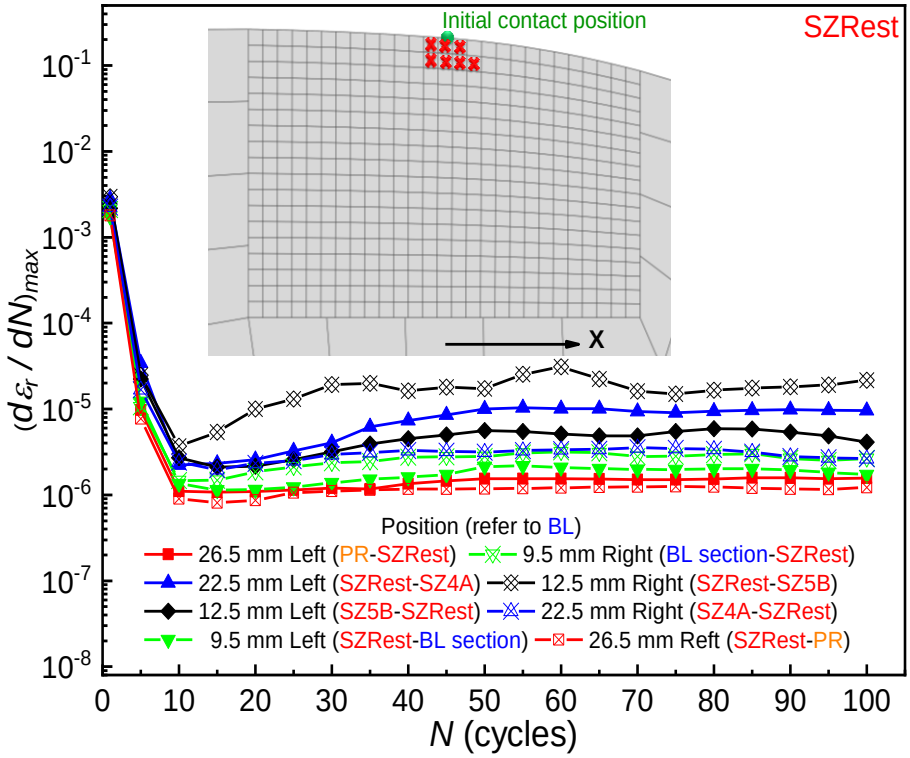

Figure 5-25: The maximum ratcheting strain rate $(d\varepsilon_r/dN)_{max}$ in selected target sections within the SZRest versus the number of loading cycles N (red cross: RCF most likely initiates at).

Fig. 5-26 shows the relationships between the maximum ratcheting strain rate $(d\varepsilon_r/dN)_{max}$ in selected target sections within the softer subzones in the SZ and the number of loading cycles N. Since each target section in this region has its unique hardness and ratcheting behaviour, more evident cyclic instability can be observed between the 10th and the 50th loading cycles. The SZ1B in both sides of the BL, which has the lowest hardness in the weld region, becomes cyclically stabilised after around 65 loading cycles. Furthermore, the stabilised maximum ratcheting strain rate in the $SZ1B_{Left}$ is slightly higher than that in the $SZ1B_{Right}$. It is worth noted that based on the criterion defined by Eq. (5-9), a cyclically stabilised is not achieved in the target sections adjacent to the BL section ($SZ5B_{Left}$ and $SZ5B_{Right}$) and the PR_{Right} ($SZ4A_{Right}$) except for the $SZ4A_{Left}$. They are the only three target sections within the weld region, in which a cyclically stabilised state is not reached. Despite this, the maximum ratcheting strain rates in these target sections fluctuate after a certain number of loading cycles, and it is expected that such behaviour would be sustained if more loading cycles were carried out. Among all the target sections within the softer

subzones in the SZ, the positions at which RCF most possibly initiates are found from the running surface to 4 mm beneath the running surface and within up to 3 mm away from the wheel–rail initial contact point towards both sides in the lateral direction (area with the red crosses). In contrast with those in the SZRest, these positions are located within a more expanded region. Similarly, the specific position with the maximum ratcheting strain rate also changes within this region even if some target sections reach cyclically stabilised in 100 loading cycles, i.e. $SZ1B_{Left}$, $SZ1B_{Right}$ and $SZ4A_{Left}$.

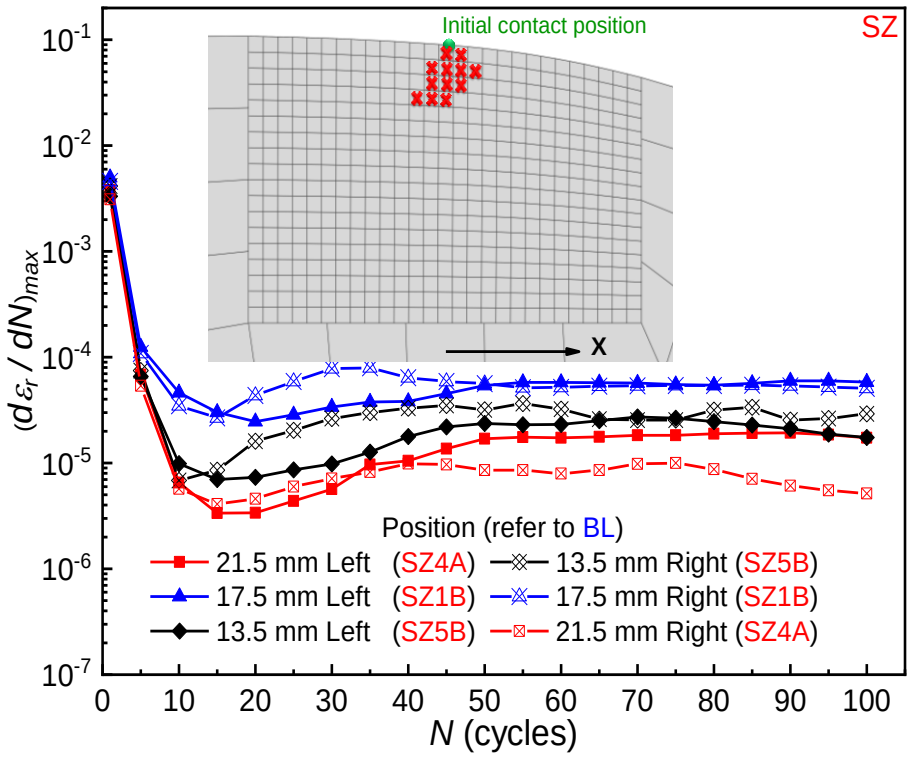

Figure 5-26: The maximum ratcheting strain rate $(d\varepsilon_r/dN)_{max}$ in selected target sections within the softer subzones in the SZ versus the number of loading cycles N (red cross: RCF most likely initiates at).

After analysing the evolution of the maximum ratcheting strain rate in the target sections within the weld region and the PR, the loading cycles required for each target section to reach cyclically stabilised N and the corresponding stabilised maximum ratcheting strain rate $(d\varepsilon_r/dN)_{max,sta}$ are summarised in Fig. 5-27. The results show that the SZ generally needs more loading cycles to become cyclically stabilised than the BL section and the PR. One of the possible explanations is that the softer characteristics can lead multiple positions (area

with the red crosses in Figs. 5-25 and 5-26) in each target section within the SZ to suffer the maximum ratcheting strain rate during the loading history. For the target section that reaches a cyclically stabilised state, its stabilised maximum ratcheting strain rate was determined by averaging all the maximum ratcheting strain rates from the first loading cycle at which the target section becomes cyclically stabilised to the 100th loading cycle. As mentioned above, a cyclically stabilised state is not reached in the SZ4A$_{Right}$ and both sides of the SZ5B, but the maximum ratcheting strain rates in these target sections keep fluctuating after a certain number of loading cycles. For these target sections, the stabilised maximum ratcheting strain rate was determined by averaging all the maximum ratcheting strain rates from the 50th to the 100th loading cycle. Based on this method, the highest stabilised maximum ratcheting strain rate (5.74×10^{-5}) is found in the SZ1B$_{Left}$, while the lowest value (7.54×10^{-7}) occurs in the PR located at 45.5 mm right to the BL.

With the stabilised maximum ratcheting strain rate $(d\varepsilon_r/dN)_{max,sta}$ and the ductility D presented in Table 3-2, the RCF initiation life N_i of the weld region and the PR can be estimated by Eq. (5-10) and used to evaluate the ratcheting performance. Since the ductility of the SZ was determined based on the reduction of cross-sectional area R of the specimen after the fracture at the SZ1B under the monotonic test as demonstrated in Chapter 3.3.1, the RCF initiation life of the SZ is only estimated for the SZ1B. Unfortunately, the RCF initiation life of other subzones in the SZ is unable to be predicted due to lack of their ductility. Fig. 5-28 summaries the estimated RCF initiation life of the weld region and the PR. The results show that the SZ1B$_{Left}$ provides the shortest RCF initiation life within the weld region due to the highest stabilised maximum ratcheting strain rate, which is approximately 5380 loading cycles. For the SZ1B$_{Right}$, the corresponding value increases to 5810 loading cycles. Although the ductility of the PR is lower than that of the SZ1B, the PR still gives the longest RCF initiation life. Specifically, the RCF initiation life of the PR, which is located at 45.5 mm to the BL, exceeds 0.3 million loading cycles. Owing to the influence of the SZ, this value drops to about 0.19 and 0.27 million loading cycles for the PR adjacent to the left and the right PR–SZRest boundaries,

respectively. Similarly, the RCF initiation life is about 2.5×10^4 loading cycles at the BL and is reduced to approximately 1.6×10^4 and 10^4 loading cycles for the region adjacent to the left and the right BL section–SZRest boundaries, respectively. Due to the worst ductility among all the regions, the RCF initiation life of the BL section is much shorter than that of the PR. Such information indicates that a rail material with poor ductility can cause a significant decrease in RCF initiation life, even if it may demonstrate high resistance to ratcheting. However, the lower stabilised maximum ratcheting rate in the BL section leads to longer RCF initiation life than the SZ1B.

According to the results of RCF initiation life, the SZ with the lowest hardness is predicted to be the first location in which RCF most likely initiates within the weld region, followed by the region around the BL. The PR presents the longest RCF initiation life and therefore has the best resistance to RCF. Meanwhile, RCF is likely to initiate beneath the running surface more deeply in the SZ with lower hardness based on Figs. 5-25 and 5-26 and thus, more frequent attention should be employed at this region after the rail welds are subjected to in-service loading conditions.

The region around the BL on the right side (towards rolling direction) is more sensitive to RCF than that on the left side, mainly due to the higher dynamic load on the running surface at right side of the BL. It is also identified that the right side of the PR adjacent to the SZ is less hazardous than the left one, which is more related to the difference in loading history caused by the symmetry of the weld region with respect to the BL. Furthermore, the variation of RCF initiation life in the BL section and the PR reveals that the presence of the SZ can offset their resistance to RCF, particularly in the regions adjacent to the SZ. From this point of view, it is suggested that additional attention may also be required for the PR and the BL section that are located close to the SZ.

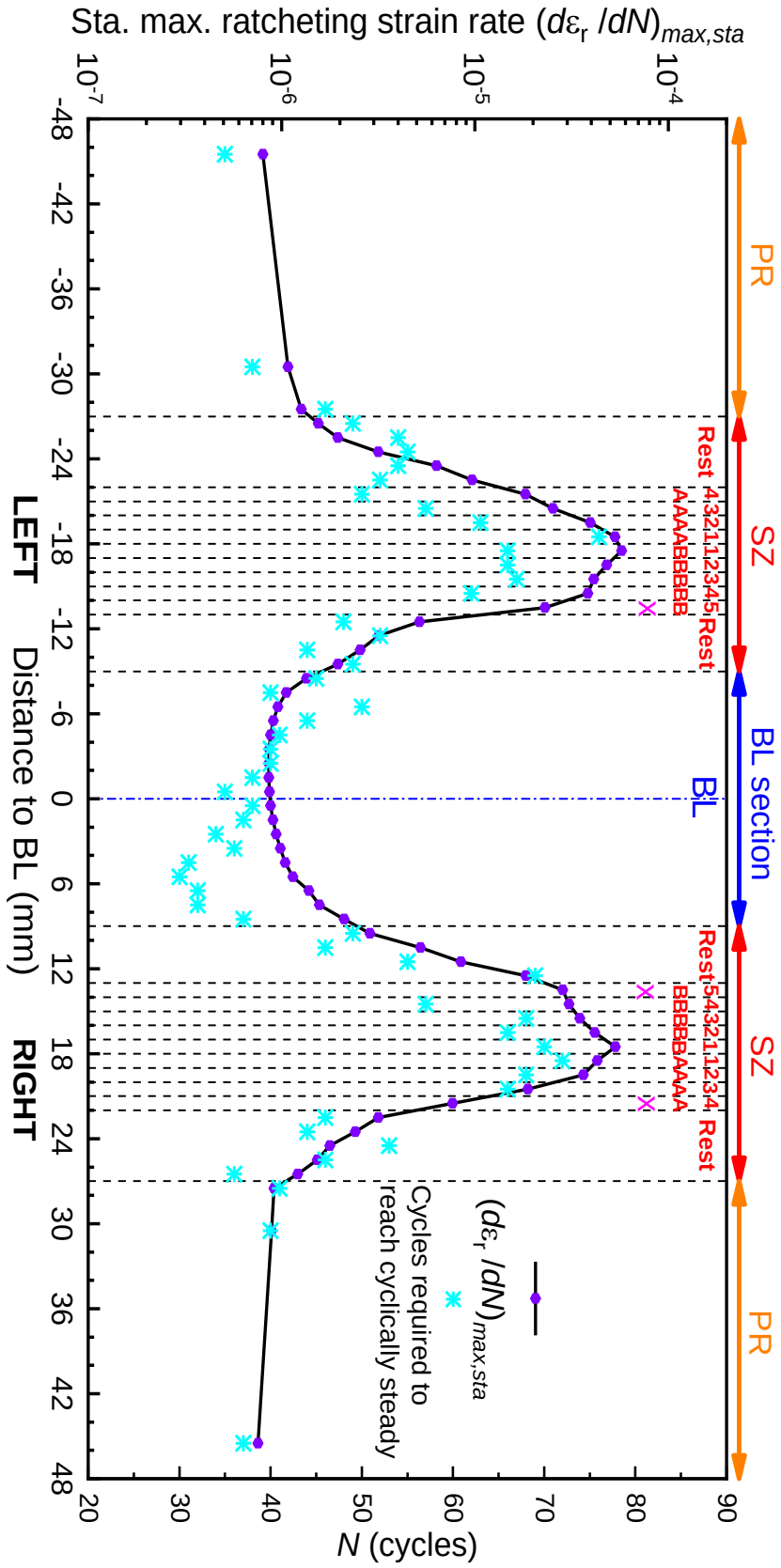

Figure 5-27: The loading cycles required for each target section to reach cyclically stabilised N and the distribution of the stabilised maximum ratcheting strain rate $(d\varepsilon_r/dN)_{max,sta}$ within the rail weld and the PR.

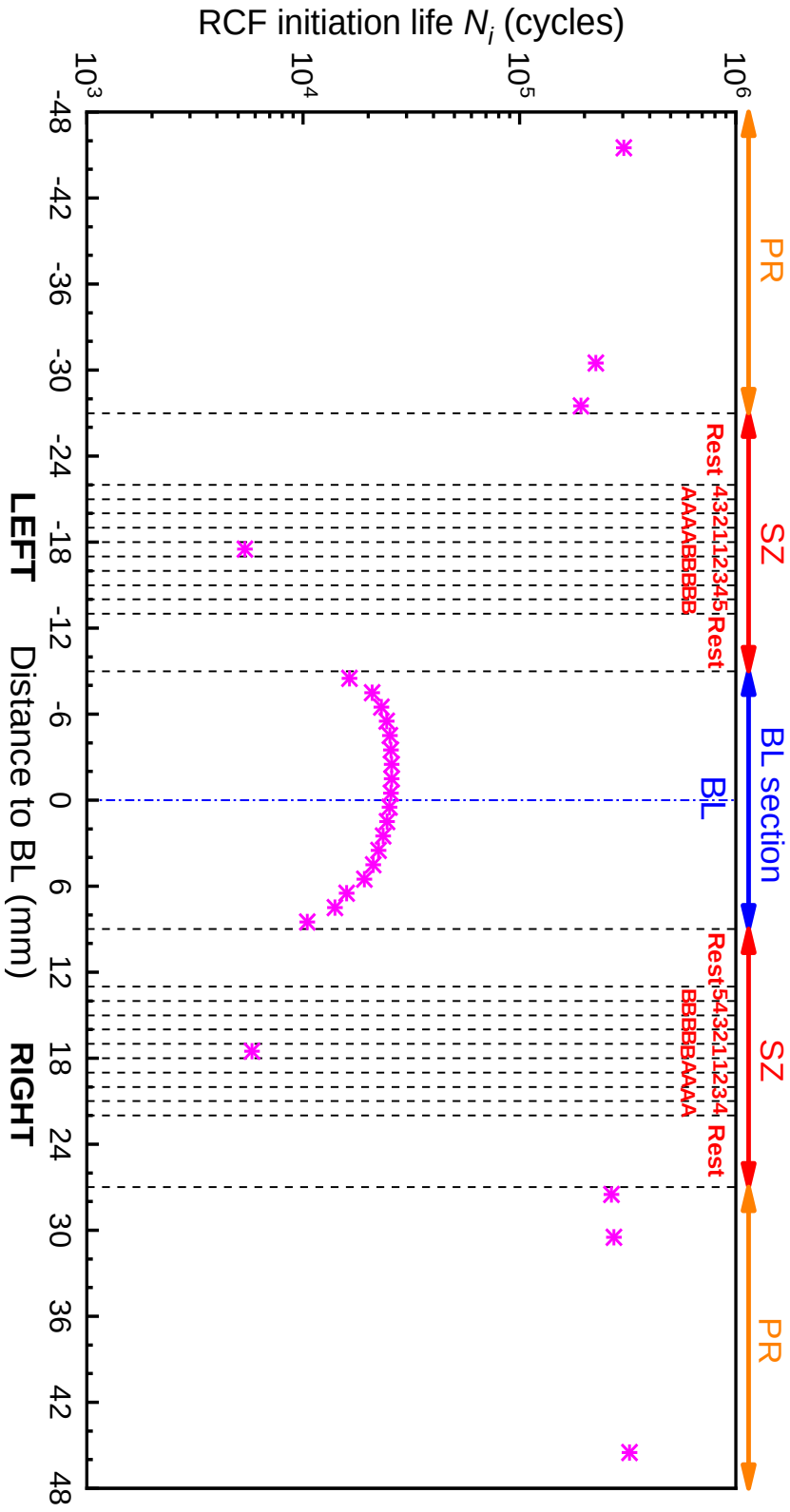

Figure 5-28: The RCF initiation life N_i of the weld region and the PR.

Mutton et al. (2016) observed severe plastic deformation around the RCF initiation regions in the SZ of ex-service rail flash butt welds. However, RCF damage was not observed at the BL in general. One of the possible reasons is

that the width of the BL region is very narrow compared with the SZ. Therefore, the tendency for ratcheting to occur at the BL is constrained by the surrounding harder material. This is a possible limitation of the modelling approach. Other limitations of the current numerical study are also outlined herein. The most significant one should be the change of contact patch due to the plastic deformation at the running surface, particularly the weld region, is ignored over multiple loading cycles. Practically, the contact stresses will be continuously reduced as the contact patch tends to become larger. It is worth mentioned that the original rail and wheel profiles will be worn over in-service loading conditions, which will also lead to the enlargement of contact patch. According to these facts, the ratcheting strain rate is likely to be overestimated and therefore the RCF initiation life might be underestimated based on the lower ductility of the rail materials obtained from the monotonic tensile tests. To overcome these limitations in the future, dynamic cyclic rolling simulations (with an actual wheel) might be a suitable solution, but an extremely high computational cost can be expected. Furthermore, residual stress in the weld region is neglected in the simulations, which can also affect the prediction of RCF initiation life.

In Australian heavy haul railways, a friction coefficient greater than 0.4 and operating conditions in high traction area, i.e. banking section with steep uphill gradient for loaded trains, can generally occur in the wheel–rail interface. This indicates that only one combination of traction and friction conditions considered in the present work is unable to represent all the practical loading conditions. Therefore, more simulations should be carried out to evaluate the ratcheting performance of rail welds under different combinations of traction and friction conditions in future. A comprehensive understanding of the effects of traction conditions on the RCF initiation in rail welds can be expected. Additionally, the current modelling work did not consider environmental factors or the third body layers, i.e. water, oxygen and temperature, which can also influence the RCF initiation.

Last but not least, lack of ductility for other subzones in the SZ limits the feasibility of estimating the RCF initiation life of these subzones. Since the

ductility is inhomogeneous within the SZ, an approach to quantify the ductility with acceptable accuracy by linking the microstructure characteristics is considered necessary for future work on the ratcheting performance of rail welds. As mentioned in Chapter 5.1, the current work focuses on the RCF initiation at the weld region in tangent tracks only. Since more RCF damage associated with welds have been identified in curved tracks, particularly with the wheel–rail contact at the gauge corner, the next stage would be conducting the similar work on the weld region in curved tracks.

5.5 Chapter Summary

A comprehensive study has been conducted to evaluate the ratcheting performance of new flash butt welds in R400HT rail steel under a typical wheel–rail cyclic rolling contact condition (35 tonnes axle load and 0.4 friction coefficient) in Australian heavy haul systems. A dynamic finite element simulation of wheel–rail weld rolling contact was firstly carried out. From this analysis, the total vertical contact force between the wheel and the rail/weld, and its variation with the rolling distance were obtained. The results indicate that the existence of the new rail weld can result in an increase in the vertical contact force due to the variation of the material properties in the weld region, particularly the lower yield strength of the SZ. However, the overall influence is insignificant. The maximum total vertical contact force is captured at roughly 3 mm right to the bond line. After that, multiple quasi-static wheel–rail/weld contact simulations were performed by applying the total vertical contact force obtained from the dynamic simulation to determine the non-Hertzian contact pressure distribution when the wheel was placed at different positions on the top surface of the rail weld along the rolling direction. The results reveal that when the wheel is located on the softened zone, the maximum normal contact pressure is lower than that obtained when it is located on the parent rail and the region around the bond line.

Based on the results of the normal contact pressure distribution, the Haines and Ollerton's strip theory (Haines & Ollerton, 1963) and Carter's theory (Carter,

1926) were then applied to estimate the longitudinal tangential traction distributions on the running surface of the rail weld under the condition of 0.5 normalised tangential traction coefficient and 0.4 friction coefficient. Finally, a cyclic loading simulation was conducted to evaluate the ratcheting performance of the rail weld by repeatedly translating these normal contact pressure and longitudinal tangential traction distributions on the rail weld top surface. The results indicate that the ratcheting strain mainly concentrates at the softened zone with lower hardness. With the increase in the number of loading cycles, this phenomenon becomes more evident. Furthermore, the shape of the maximum ratcheting strain distribution can almost correlate with the longitudinal hardness profile of the weld region. Similar phenomena can also be identified in the maximum ratcheting strain rate distribution. The numerical results also demonstrate that the maximum ratcheting strain rate in every subzone decreases dramatically in the first few loading cycles. Subsequently, both the parent rail and the region around the bond line become cyclically stabilised after a certain number of loading cycles, whereas most of the subzones in the softened zone experience quite significant cyclic instability before reaching a cyclically stabilised state eventually. Generally, the softened zone requires more loading cycles to become cyclically stabilised than the parent rail and the region around the bond line.

According to the stabilised maximum ratcheting strain rate and the ductility of the rail material, the RCF initiation life is estimated under the typical in-service condition. The subzone with the lowest hardness in the softened zone is predicted to have the shortest RCF initiation life among the weld region, followed by the region around the bond line. Therefore, more frequent attention should be employed at the subzones with lower hardness in the softened zone after the welds are subjected to in-service loading conditions. The parent rail presents the longest RCF initiation life and therefore has the best resistance to RCF. Furthermore, the presence of the softened zone can shorten the RCF initiation life of the parent rail and the bond line section, particularly the regions located adjacent to the softened zone. Such information indicates that additional attention may also be required for these regions in practice.

The possible location of RCF initiation from the cross-sectional view of the rail head in the softened zone with lower hardness can reach to a depth of 4 mm from the running surface and extend up to 3 mm away from the wheel–rail initial contact point towards either side of the transverse direction, while in the softened zone with relatively higher hardness (adjacent to the parent rail or the region around the bond line) can reach to a depth of 2 mm below the running surface and extend up to 2 mm transversely from the wheel–rail initial contact point. Regarding the parent rail and the region around the bond line, the corresponding critical region can still reach to a depth of 2 mm from the running surface but extend up to only 1 mm transversely from the wheel–rail initial contact point. Although the current work has some typical limitations, the outcomes can assist researchers further understanding the ratcheting performance in terms of RCF initiation in rail welds and potentially provide useful information for the railway operators to develop more reliable and cost-effective maintenance strategies for these welds, i.e. grinding the RCF damage more frequently.

Chapter 6

Numerical Study on the Ratcheting Performance of Heavy Haul Rails in Curved Tracks

The ratcheting performance of heavy haul rails in curved tracks under different in-service conditions was numerically evaluated through a recently developed approach. The wheel–high rail cyclic rolling contact was simulated by translating the non-Hertzian contact pressure and the estimated longitudinal tangential traction distributions repeatedly on the running surface of a high rail. The maximum ratcheting strain rate of the rail was obtained in each loading cycle. Based on the known ductility of the rail materials and the maximum stabilised ratcheting strain rate, the RCF initiation life of the rail was predicted. The results indicate that the RCF initiation life the rail investigated decreases with the increase in normalised tangential traction coefficient, friction coefficient, ratio of lateral/vertical load and axle load. Under the same in-service loading condition, the ratcheting performance of the rail in curved tracks is relatively worse than the one in tangent tracks. The hypereutectoid rail steel with a lower carbon content always shows the best ratcheting performance and is likely to be the most reliable choice for high rails in curved tracks. Moreover,

RCF is predicted to initiate around 1 mm beneath from the wheel–rail initial contact point under low traction conditions. As the traction condition becomes more severe, the location of RCF initiation may shift from the subsurface to the running surface. The results can provide valuable information to assist rail operators in the selection of rail steel grades and the development of rail maintenance strategies.

6.1 Background and Research Aims

As a train passes a curved track, the vehicle is subjected to the centrifugal force and may shift transversely towards the high rail. Under such situation and depending on the wheel and rail profiles in use, two-point contact between wheel and high rail may occur as the wheel flange can touch the rail gauge (Zhang et al., 2009 & Vo et al., 2014). The area of wheel tread/flange–rail gauge contact can be smaller than that under wheel tread–rail crown contact in tangent tracks, so the high rail surface can be subjected to cyclic rolling and sliding condition with higher contact stresses. As mentioned in Chapter 1, if the rail stress level resulted from the wheel–rail cyclic rolling contact is above the plastic shakedown limit, new plastic deformation will generate and accumulate in each loading cycle, which is known as plastic ratcheting. The increment of plastic deformation in one loading cycle may be small, but it can accumulate to large values after many loading cycles. Initiation of rail degradation, such as wear and RCF, will primarily occur where the ratcheting strain reaches the ductility of rail materials.

Throughout the past few decades, the introduction of higher axle loads and annual haulage rates has placed more emphasis on the performance of rails in curved track. During this period, there has also been a shift in the dominant damage mode from wear to RCF, as was illustrated by Wessels et al. (2015) in relation to the Rio Tinto heavy haul operation in Australia. This transition was, in part, due to the more widespread application of higher strength rail steels, but also other changes in wheel–rail management practices including the introduction of modified wheel and rail profiles that improved the curving

performance of rolling stock. Lubrication of the wheel–rail interface (to control wear) has historically found to be not cost-effective in these heavy haul operations, due to the limited effectiveness of such an approach and the remoteness of much of the rail network (Welsby et al., 2014). More recently, however, there has been renewed interest in the application of TOR–FM strategies to limit the extent of rail surface degradation due to RCF in some track locations.

Since the initial application of higher strength rail steels for heavy haul operations, rail manufacturers have continued to develop rail steels of higher strength levels through a combination of alloy design and thermomechanical processing, all of which offer the potential for improved performance. However, the relationship between the basic material characteristics such as tensile properties (yield strength, ultimate tensile strength and ductility) that are covered in rail standards and specifications are not comprehensive. In addition, RCF behaviour is complex as reviewed in Chapter 2.3.3, depending on the wheel–rail contact conditions in service. For this reason, it is essential to evaluate the ratcheting behaviour of such steels and further predict their service performance with greater certainty.

In the literature, limited studies have been performed to simulate the wheel–rail cyclic rolling contact in curved tracks. Jin et al. (2011) developed a 3D wheel–rail FE model to predict the wear of wheel flange and rail gauge corner for Japanese railways. The results compared with the field measurements indicated that the wear prediction model is feasible to be applied in the actual railway system. However, the axle load applied was not sufficient for the situation in Australia heavy haul railways and no information about the material deformation was presented. Another study conducted by Vo et al. (2015) predicted the damage in curved tracks with various status of wheel and rail profiles. The results highlighted that the high rail gauge corner is prone to the damage caused by ratcheting when suffering higher contact pressure.

A comprehensive approach for numerically evaluating the ratcheting performance of the rail steels under in-service cyclic loading has been

developed by Pun et al. (2015a). Different wheel–rail cyclic rolling contact conditions, i.e. free rolling, partial slip and full slip conditions, different friction coefficients and different axle loads were investigated under single-point contact on tangent tracks. The wheel–rail cyclic rolling contact was simulated by repeatedly translating a non-Hertzian contact pressure distribution obtained from a separate quasi-static FE analysis, and a longitudinal tangential traction predicted from Haines and Ollerton's strip theory (Haines & Ollerton, 1963) and Carter's theory (Carter, 1926). A cyclic plasticity constitutive model was developed and employed to simulate the ratcheting behaviour of three rail steel grades (Pun et al., 2014a). The results indicated that the increase in normalised tangential traction coefficient, friction coefficient and axle load can reduce the crack initiation life. The hypereutectoid rail steel grade with a lower carbon content showed the best ratcheting performance among all the rail steel grades investigated. The research outcomes can provide useful information to assist in the application of premium rail grades and the development of improving rail maintenance strategies.

In the current study, the same procedure developed by Pun et al. (2015a) was further applied to numerically evaluate the ratcheting performance of the same rail steel grades for high rails in curved tracks under cyclic rolling contact conditions. The influence of axle load, ratio of lateral/vertical load, normalised tangential traction coefficient and friction coefficient were considered. The results obtained can be useful to predict the crack initiation life of high rails in curved tracks and such information can further improve rail maintenance strategies for mitigating rail degradation. It should be noted that such results and their interpretation in the current paper are for heavy haul operations. They may not always generalise to other situations such as metros or mixed traffic, for which the balance of wear and RCF that results from the ratcheting of rail steels may be different.

The structure of this chapter is as follows: the comprehensive approach consisting of the material properties, the FE models and the methodology to evaluate the ratcheting performance of the rail steels under different in-service conditions, is demonstrated in Chapter 6.2, followed by the numerical results

described and discussed in Chapter 6.3. Conclusions are provided in Chapter 6.4.

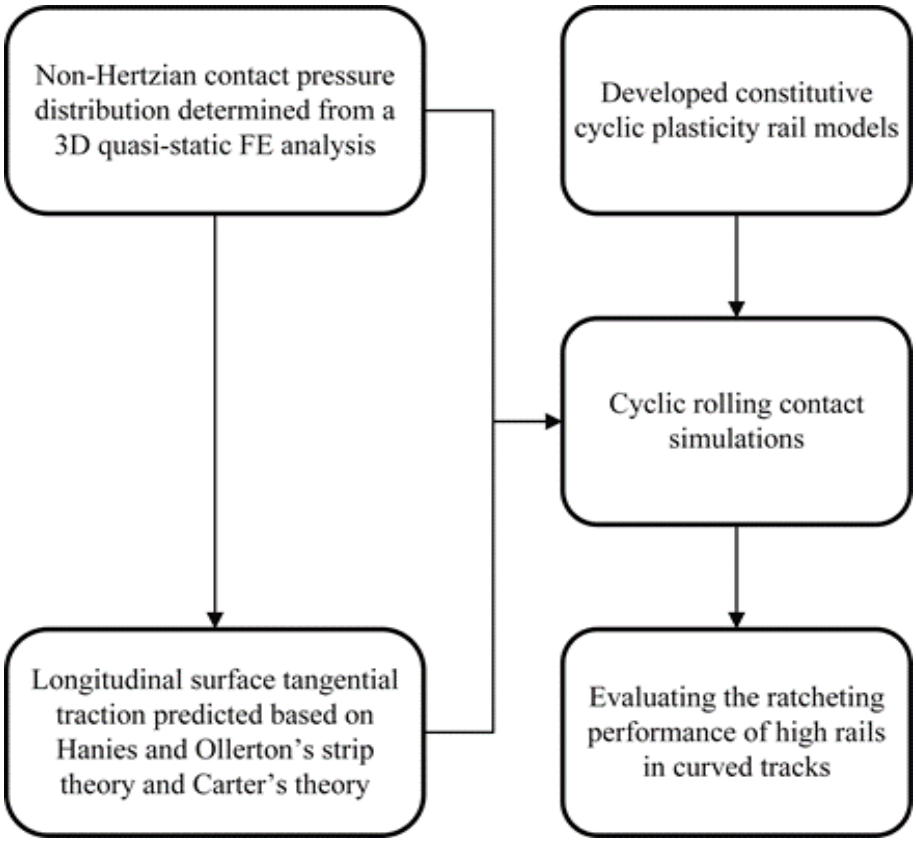

Figure 6-1: Flow chart of the research methodology to evaluate the ratcheting performance of high rails in curved tracks.

6.2 Methodology

The comprehensive approach developed by Pun et al. (2015a) was updated for cyclic rolling contact of high rails in curved tracks. The research methodology is illustrated in the flowchart as shown in Fig. 6-1.

6.2.1 Material Properties

The wheel and rail materials applied in current study are identical with those used in Pun et al. (2015a). The wheel grade corresponds to AAR Class C with a yield strength of 855 MPa (AAR, 2017). The properties are described by an elastic-plastic constitutive model combined with the isotropic hardening rule.

The work hardening exponent is 0.16. The wheel material is also the same as that used in the wheel–rail weld simulations (Chapter 5.1.1). Three types of fully pearlitic rail steel grades considered include a low alloy heat-treated (LAHT) rail steel with 0.8% carbon content and two hypereutectoid rail steels (HE1 and HE2) with 1% and 0.85% carbon content, respectively. The nominal hardness levels of these grades ranging from 380 HV to 420 HV and the development of the cyclic plasticity constitutive model can be found in Pun et al. (2014a). The yield stress $\sigma_{0.2}$ of LAHT rail steel is 1000 MPa, while the corresponding values of HE1 and HE2 rail steels are 850 MPa and 905 MPa, respectively.

6.2.2 Finite Element Model

To simulate the cyclic rolling contact problems, the distributions of normal contact pressure and longitudinal tangential traction were applied on the running surface of the rail model. Johnson (1985) indicated that only a minor loss of accuracy occurs if the normal contact pressure distribution is determined with the assumption that the contact pressure is independent of the friction and shear forces for two bodies with similar elastic properties. According to this, the non-Hertzian contact pressure distribution was firstly obtained from a separate frictionless quasi-static FE analysis. A 3D half wheel–high rail model due to symmetry was generated in Abaqus 6.14-1 as shown in Fig. 6-2a. Since the length of the rail model (390 mm) is very short comparing to the radius of the curvature applied in railway systems, a straight rail segment can be used to simulate a curved one. To set the initial wheel–rail contact, the centreline of the rail profile first coincided with that of the wheel profile and the wheel was placed above the rail with distances. Then the wheel was shifted horizontally towards the rail for a fairly short distance (0.2 mm) and then was moved towards the rail to check if a two-point contact was established. If not, the wheel was moved back to the position above the rail with distances and repeated the horizontal shift and the movement towards the rail until a two-point contact was finally established. Both axle force, which represents the axle load, and lateral force were simultaneously applied at the wheel centre to obtain the normal contact pressure distribution. A kinematic coupling constraint was set to connect

the wheel centre with the wheel inner surface. In this way, the wheel body has the same degree of freedom as the wheel centre. To prevent the model from undesired movement during the quasi-static simulations, the wheel centre was constrained in the longitudinal direction, while the rail bottom surface was pinned.

Both rail and wheel profiles considered in this study are in new condition and the same as those used in the wheel–rail weld simulations, which are presented in Chapter 5.1.2. Specifically, the rail profile is an as-rolled 68 kg/m flat-bottom rail (AS1085.1-2002/Amdt1, 2005) with a rail cant of 1:40, while the wheel profile is an M-107/M-208 wheel with a standard wide flange contour (AAR Type D-38) as detailed in AAR (2017). Additionally, both profiles used are also exactly identical to those in Pun et al. (2015a). Therefore, the ratcheting performance of high rails in curved tracks from this study can be compared with that of the rails in tangent tracks. It is also worth mentioned that the presented method can be directly applied to deal with a worn wheel–rail situation. The fine mesh region with an element size of 0.8 mm was designed to capture the high stress and its gradient near the wheel–rail initial contact points shown in Fig. 6.2b, while the coarse mesh was applied to the rest of the model for the reduction of computational cost. The surface-based mesh tie constraints, which enable the active degrees of freedom equal for a pair of surfaces with uneven mesh densities (Abaqus, 2014), were used to connect coarse and fine mesh regions. A mesh convergence check was carried out to avoid the influence of the mesh density on the accuracy of simulations, which is presented in Appendix C. According to this, the entire FE model consists of 175413 C3D8 elements and 185877 nodes. The value of contact pressure of each element on the rail surface was represented by the average of the corresponding nodal pressure values.

Based on the obtained numerical results of the non-Hertzian contact pressure distribution, the Haines and Ollerton's strip theory (Haines & Ollerton, 1963) was applied to identify the slip and stick zones along the rolling direction in the contact patch, and the longitudinal tangential traction distribution was estimated by Carter's theory (Carter, 1926). Johnson (1985) stated that the estimated

results obtained from these theories have almost no difference with the results obtained from Kalker (1967). According to the contact theory (Johnson, 1985), the sizes of the slip and stick zones are reflected by the normalised tangential traction coefficient ξ, which is defined by Eq. (5-2), where F_t is the tangential traction force and fL is the upper limit of the tangential traction force F_t or the saturated value of driving capacity (f is the friction coefficient and L is the axle load). When $\xi = 0$, the contact area is fully sticking, which represents a free rolling condition. When $\xi = 1$, the condition becomes fully slipping. In general, partial slip ($0 < \xi < 1$) occurs in wheel–rail cyclic rolling contact situations. For example, the tangential traction force transmitted is half of the maximum driving capacity if $\xi = 0.5$, which is the situation considered in the wheel–rail weld simulations, see Chapter 5.3.3. According to this, Fig. 6-3a illustrates the normal contact pressure distribution obtained from the FE analysis for LAHT steel in high rails when the applied axle load L is 35 tonnes and the ratio of lateral/vertical load η is 0.3. Based on Eqs. (5-3 to 5-7), the determined longitudinal tangential traction distributions with the normalised tangential traction coefficients of ξ= 0.25, 0.5 and 0.75 and a friction coefficient f of 0.4 are shown in Figs. 6-3b, 6-3c and 6-3d, respectively.

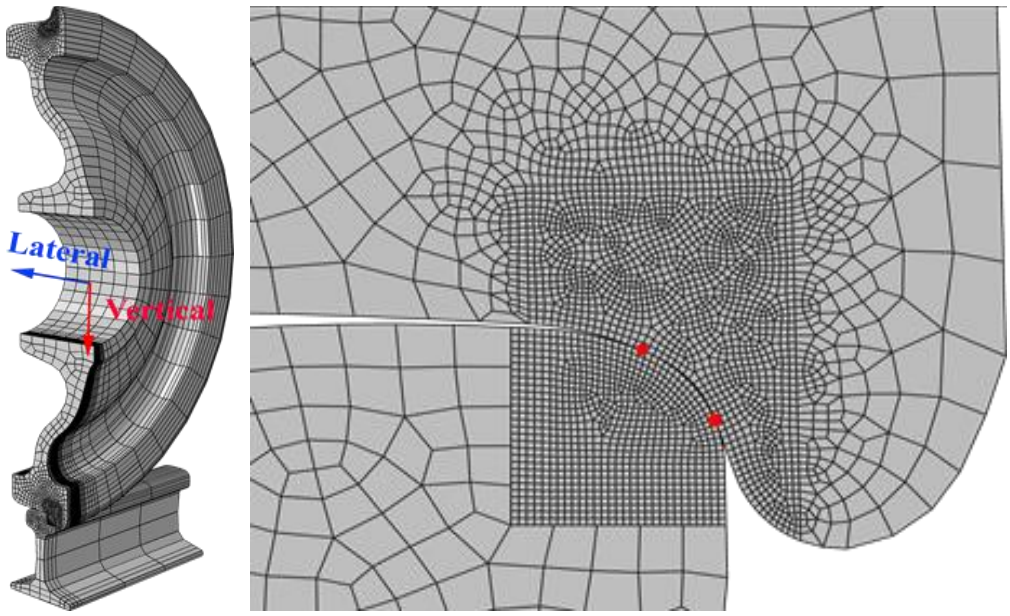

(a) (b)

Figure 6-2: The FE wheel–high rail model for quasi-static analysis: (a) the whole model; (b) the fine mesh region near the wheel–rail initial contact points (red dots).

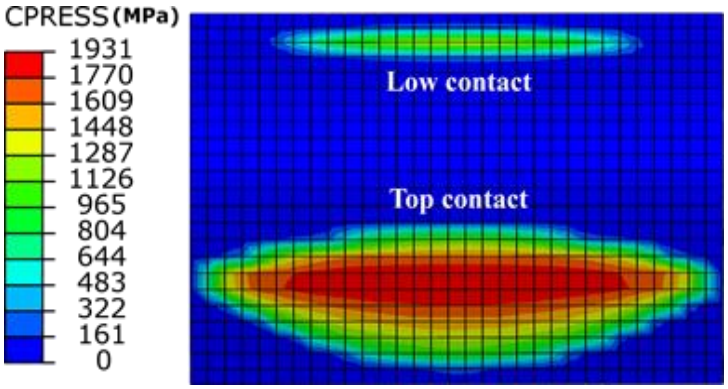

(a)

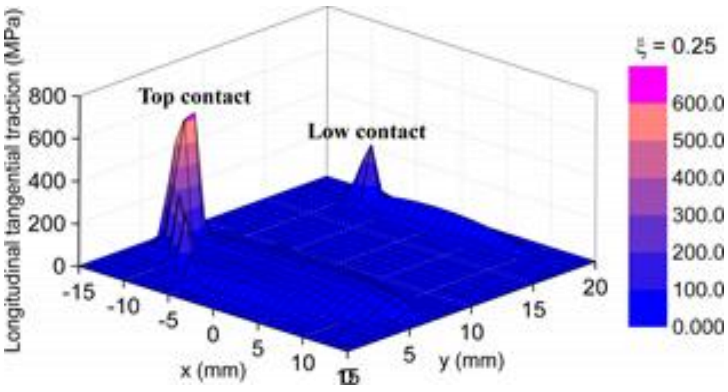

(b)

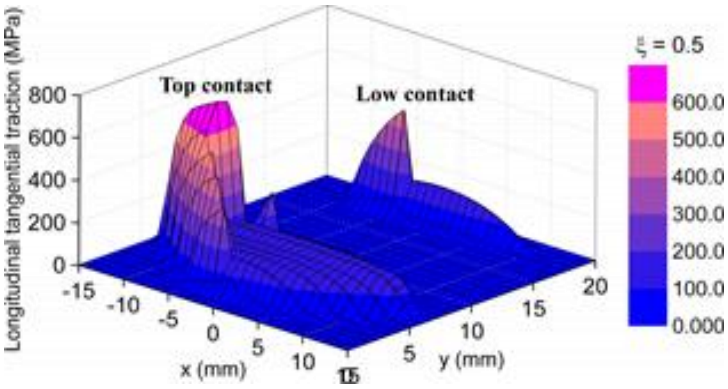

(c)

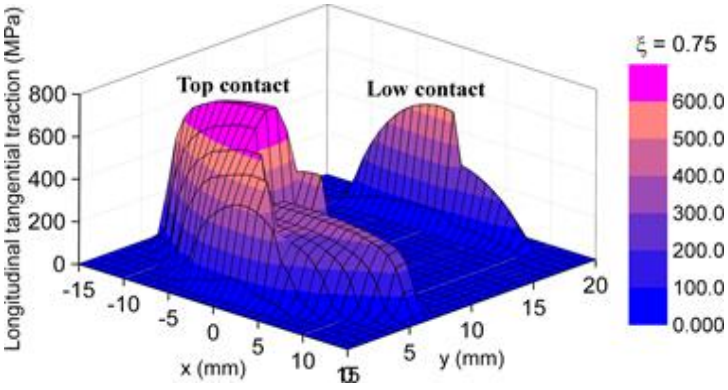

(d)

Figure 6-3: (a) Normal contact pressure distribution and (b-d) longitudinal tangential traction distribution under different values of normalised tangential traction coefficient: (b) $\xi = 0.25$; (c)

ξ = 0.5; (d) ξ = 0.75, for LAHT steel in high rails with axle load of L = 35 tonnes, ratio of lateral/vertical load η = 0.3 and friction coefficient of f = 0.4.

The FE rail model for the cyclic loading simulations is shown in Fig. 6-4. The fine mesh zone where the cyclic loading was translated, is almost identical to that used in the quasi-static simulations except for the double length of the rail model. The whole model consists of 51014 C3D8 elements and 56035 nodes. As demonstrated in Figs. 6-4b and 6-4c, a target section which covers all the corresponding fine elements below the running surface of the rail model was created in the middle of the fine mesh region to output the plastic strain components. Fig. 6-5 illustrates the process of the cyclic loading simulation for ratcheting analysis. The normal contact pressure and the estimated longitudinal tangential traction distributions were translated repeatedly from left to right on the top surface of the fine mesh zone through the time-dependent amplitude function with a fixed time interval (Abaqus, 2014). The bottom surface of the rail model was also pinned throughout the whole simulation to constrain the movements of the rail model in three translational directions.

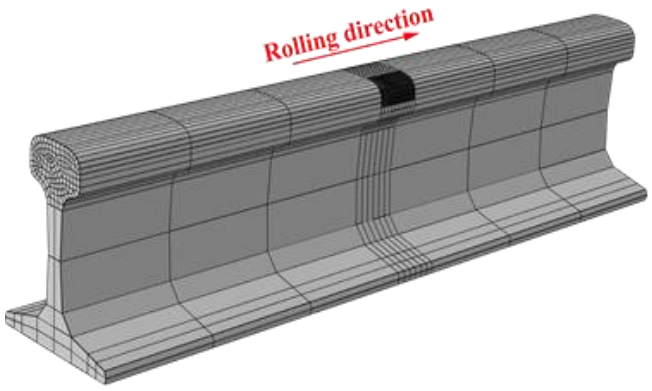

(a)

Figure 6-4: The FE model for the cyclic loading simulations: (a) the full rail model; (b) the fine mesh region where the cyclic loading was translated; (c) the target section in detail from the cross-sectional view.

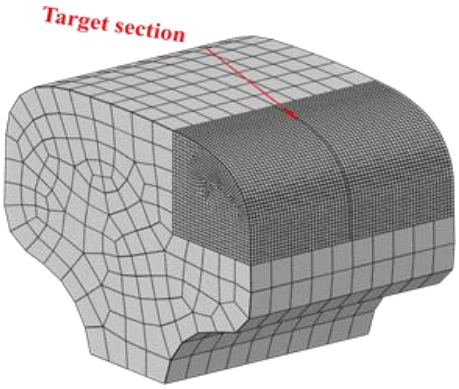

(b)

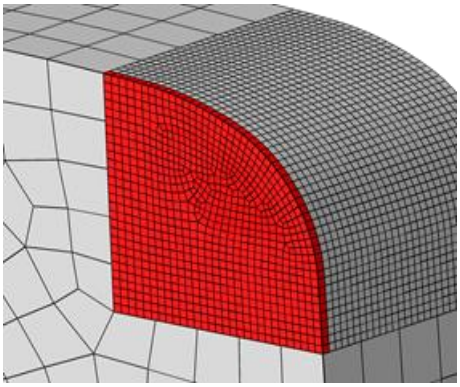

(c)

Figure 6-4: Continued.

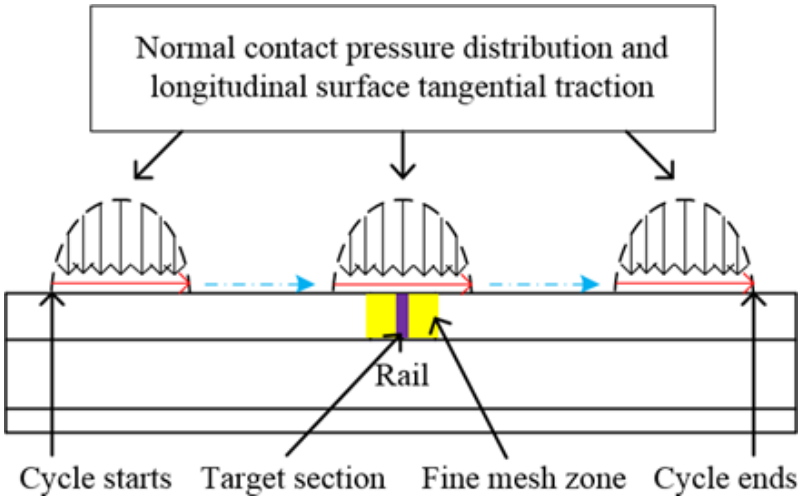

Figure 6-5: Cyclic loading simulation by repeatedly translating the normal contact pressure and longitudinal tangential traction distributions from left to right on the top surface of the rail.

6.2.3 Evaluation of Ratcheting Performance

The approach to evaluate the ratcheting performance of rails under different loading conditions is illustrated in Chapter 5.4.2. The cyclic loading simulation

can provide both normal and shear components of plastic strain, and then the effective plastic strain ε_{eff}^{p} determined through Eq. (5-8) can be applied to obtain the ratcheting strain ε_r, which is the maximum value of effective plastic strain $(\varepsilon_{eff}^{p})_{max}$ of the rail material in each loading cycle. Then the ratcheting strain rate $d\varepsilon_r/dN$ in each loading cycle can be determined and further used to predict the crack initiation life N_i of the rail material. As mentioned in Chapter 6.1, rail degradation can be in the form of wear or RCF due to ratcheting. In other words, ratcheting behaviour can manifest itself in material damage in the form of wear or RCF, which are concurrent damage mechanisms (Hiensch & Steenbergen, 2018). In the case of high strength rail steels used in heavy haul operations and examined in this study, RCF is the dominant damage mode under wheel–rail cyclic rolling contact. According to this, it is assumed that RCF would initiate when the ratcheting strain ε_r reaches the material's ductility D. The time, i.e. number of loading cycles, to accumulate the plastic deformation to the material's ductility D is therefore treated as the RCF initiation life N_i, which is then used as a measure of the ratcheting performance of the rail steels in this study. The RCF initiation life N_i can be predicted from the stabilised maximum ratcheting strain rate $(d\varepsilon_r/dN)_{max,sta}$ of the target section under different cyclic rolling contact conditions. The following criterion is applied to judge if the rail material reaches cyclically stabilised:

$$\left|\frac{(d\varepsilon_r/dN)_{max,N} - (d\varepsilon_r/dN)_{max,N-1}}{(d\varepsilon_r/dN)_{max,N-1}}\right| < 0.5\% \qquad (6-1)$$

where $(d\varepsilon_r/dN)_{max,N}$ is the maximum ratcheting strain rate in the current loading cycle and $(d\varepsilon_r/dN)_{max,N-1}$ is the maximum ratcheting strain rate in the previous loading cycle. If Eq. (6-1) is satisfied in ten continuous loading cycles and the maximum ratcheting strain rate fluctuates during this period (instead of presenting a continuously increasing/decreasing trend), the position with the maximum ratcheting strain rate reaches a cyclically stabilised state is most likely to be where RCF will initiate. Knowing the ductility D of each rail steel as given in Table 6-1, the RCF initiation life N_i under different cyclic loading conditions can be predicted by Eq. (5-10).

Table 6-1: Ductility of three rail steel grades (Pun et al., 2015a).

Steel grade	LAHT	HE1	HE2
Ductility D (%)	44.43	15.91	50.25

It should be noted that the ductility of the rail steels was obtained under the monotonic tensile tests and might not be suitable for practical wheel–rail contact situations, which are dominated by compressive and shear stresses. This implies that the actual ductility may be higher and therefore, a longer RCF initiation life can be expected by using Eq. (5-10). A more relevant method to determine the strain level at which RCF initiates would be to perform twin disc tests under conditions that are aimed at developing RCF damage, as used in other studies, e.g. by Garnham & Beynon (1991).

6.3 Numerical Results and Discussion

With the existing approach and the developed FE model for cyclic loading simulations, several case studies have been conducted on the ratcheting performance of three rail steels for high rails within curves under various loading conditions in service. The effects of axle load, ratio of lateral/vertical load, normalised tangential traction coefficient and friction coefficient have been investigated. The number of loading cycles conducted in each case depended on the number of loading cycles required for the location with the maximum ratcheting strain rate to reach a cyclically stabilised state which is judged by Eq. (6-1). Based on the results of all the cases considered as shown in Figs. 6-6, 6-9, 6-12 and 6-15, the stabilised maximum ratcheting strain rate is non-zero. This means that the net plastic deformation will accumulate continuously in each following loading cycle even if its value may be very small. As illustrated in Chapter 6.1, initiation of RCF will occur when the ratcheting strain reaches the ductility of the rail materials.

6.3.1 Influence of Normalised Tangential Traction Coefficient

Fig. 6-6 demonstrates the maximum ratcheting strain rate $(d\varepsilon_r/dN)_{max}$ versus the number of loading cycles N under different values of normalised tangential traction coefficient ξ for each rail steel. It is shown that the maximum ratcheting strain rate decreases with the increasing number of loading cycle but increases with the normalised tangential traction coefficient. The stabilised maximum ratcheting strain rate is around 10^{-6} when the normalised tangential traction coefficient is less than or equal to 0.5. When the normalised tangential traction coefficient increases to 0.75, HE2 steel has the lowest stabilised maximum ratcheting strain rate of 1.14×10^{-5} while it is 7.2×10^{-5} and 9.71×10^{-5} for LAHT and HE1 steels, respectively. In addition, the number of loading cycles required for the position with the maximum ratcheting strain rate to become cyclically stabilised increases with the normalised tangential traction coefficient. According to the information above, it is predicted that the rail materials will need more loading cycles to become cyclically stabilised and its corresponding stabilised maximum ratcheting strain rate will further increase under the full slip condition ($\xi = 1$).

Fig. 6-7 presents the influence of the normalised tangential traction coefficient ξ on the stabilised maximum ratcheting strain rate $(d\varepsilon_r/dN)_{max,sta}$ for each rail steel. The results illustrate that the stabilised maximum ratcheting strain rate almost keeps constant when the normalised tangential traction coefficient is less than or equal to 0.25. A minor increase on the stabilised maximum ratcheting strain rate is observed when the normalised tangential traction coefficient increases to 0.5. As the normalised tangential traction coefficient is greater than 0.5, the stabilised maximum ratcheting strain rate for both LAHT and HE1 steels increases significantly while a slight increase is observed on HE2 steel which gives the lowest value. Based on the obtained stabilised maximum ratcheting strain rate, and the known ductility listed in Table 6-1 and Eq. (5-10), the RCF initiation life under different values of the normalised tangential traction coefficient for all three steels can be predicted.

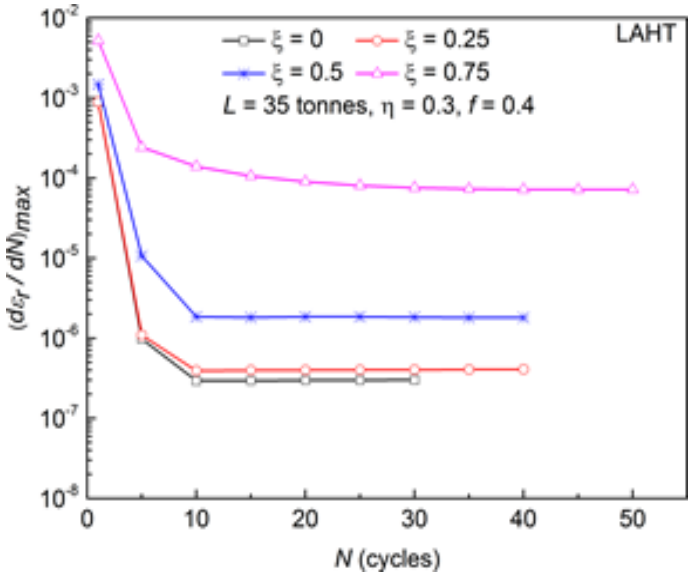

(a)

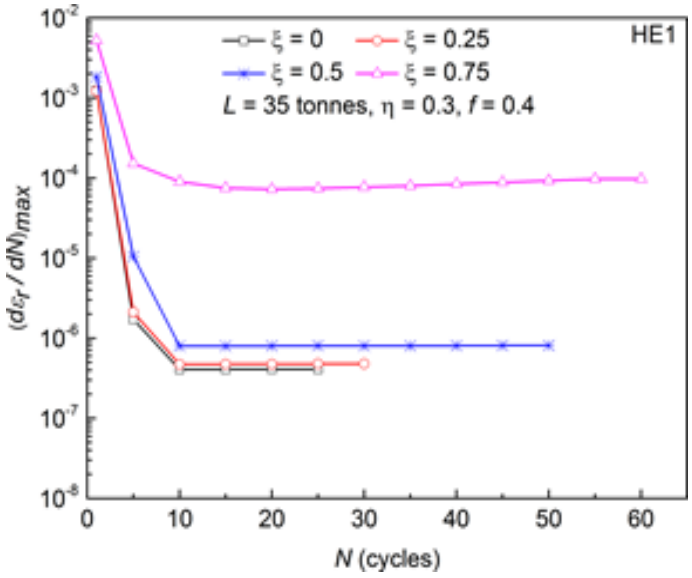

(b)

Figure 6-6: The maximum ratcheting strain rate $(d\varepsilon_r/dN)_{max}$ versus the number of loading cycles N under different values of normalised tangential traction coefficient ξ for (a) LAHT; (b) HE1; (c) HE2, with an axle load of L = 35 tonnes, a ratio of lateral/vertical load η = 0.3 and a friction coefficient of f = 0.4.

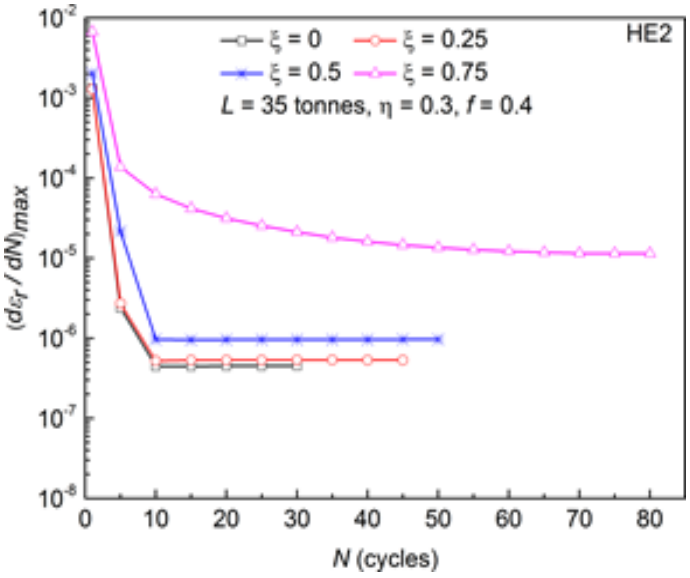

(c)

Figure 6-6: Continued.

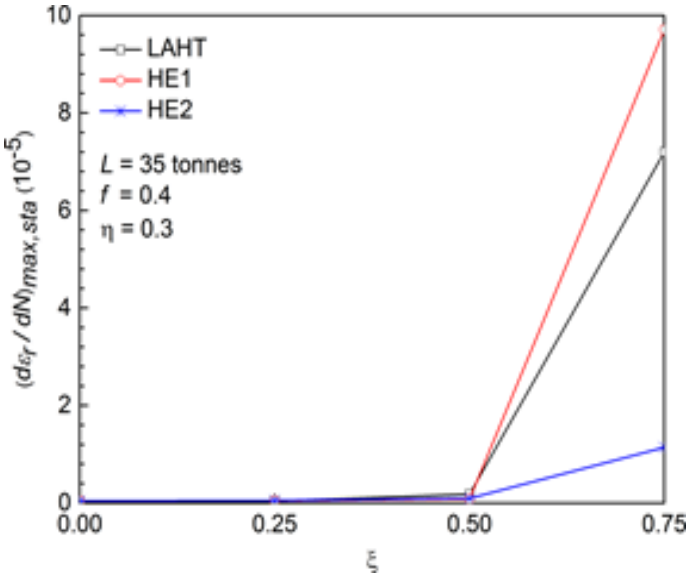

Figure 6-7: The stabilised maximum ratcheting strain rate $(d\varepsilon_r/dN)_{max,sta}$ versus the normalised tangential traction coefficient ξ for all three rail steels with an axle load of L = 35 tonnes, a ratio of lateral/vertical load η = 0.3 and a friction coefficient of f = 0.4.

Fig. 6-8 demonstrates the relationship between the RCF initiation life N_i and the normalised tangential traction coefficient ξ. It is found that the RCF initiation life decreases as the normalised tangential traction coefficient increases. The RCF initiation life of LAHT steel is up to 1.5 million cycles under the free rolling condition, while it is 0.39 million cycles and 1.1 million cycles for HE1 and HE2 steels, respectively. When the normalised tangential traction

coefficient increases to 0.75, the RCF initiation life of HE2 steel is reduced to 4×10^4 cycles, which is the longest among all three steels. The results also indicate that under mild tangential traction conditions, i.e. $\xi \leq 0.25$, LAHT steel shows the best ratcheting performance while HE2 steel gives the best one under severe tangential traction conditions, i.e. $\xi \geq 0.5$. Additionally, HE1 steel always has the shortest RCF initiation life although its reduction is not as dramatic as the other two steels.

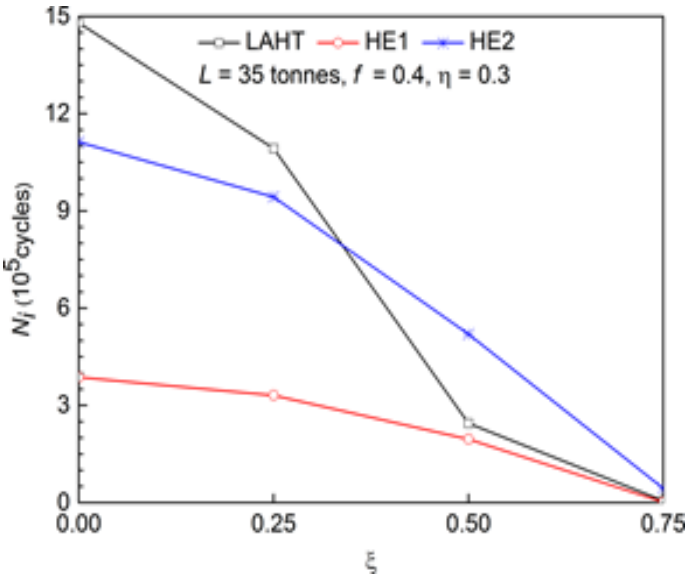

Figure 6-8: The predicted RCF initiation life N_i versus the normalised tangential traction coefficient ξ for all three rail steels with an axle load of L = 35 tonnes, a ratio of lateral/vertical load η = 0.3 and a friction coefficient of f = 0.4.

6.3.2 Influence of Friction Coefficient

Fig. 6-9 illustrates the maximum ratcheting strain rate $(d\varepsilon_r/dN)_{max}$ versus the number of loading cycles N under different values of the friction coefficient f for each rail steel. The results demonstrate that the maximum ratcheting strain rate decreases with the increasing number of loading cycles but increases with the friction coefficient. The stabilised maximum ratcheting strain rate for all three steels is approximately 10^{-6} when the friction coefficient is less than or equal to 0.4. When the friction coefficient increases to 0.5, the stabilised maximum ratcheting strain rate for HE2 steel only increases to 7.64×10^{-6} while the one for both LAHT and HE1 steels almost increases to the range of

10^{-5}. It is also shown that higher friction coefficient results in the position with the maximum ratcheting strain rate requiring more loading cycles to reach a cyclically stabilised state.

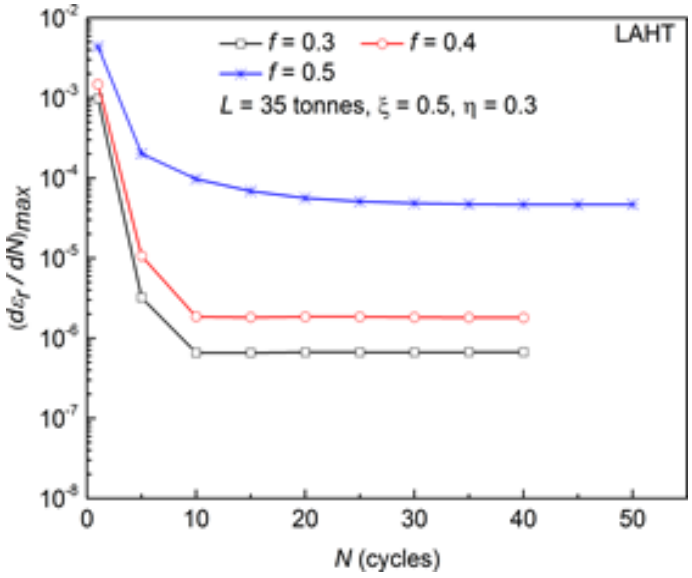

(a)

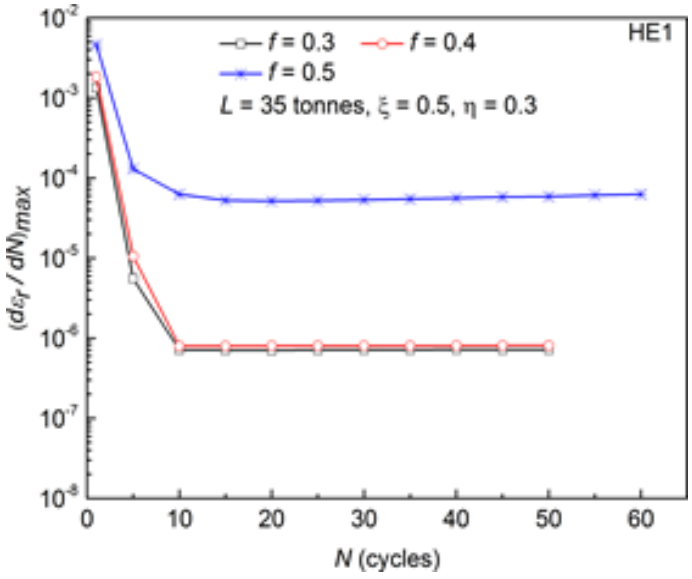

(b)

Figure 6-9: The maximum ratcheting strain rate $(d\varepsilon_r/dN)_{max}$ versus the number of loading cycles N under different values of friction coefficient f for (a) LAHT; (b) HE1; (c) HE2, with an axle load of L = 35 tonnes, a ratio of lateral/vertical load η = 0.3 and a normalised tangential traction coefficient of ξ = 0.5.

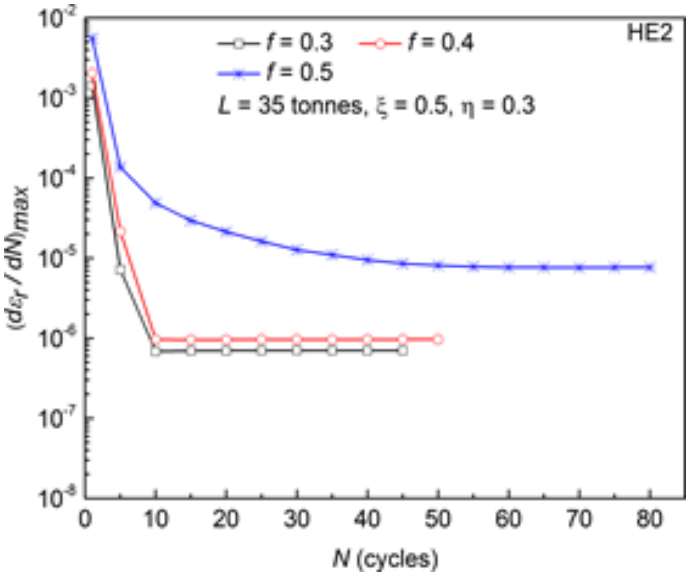

(c)

Figure 6-9: Continued.

The influence of the friction coefficient f on the stabilised maximum ratcheting strain rate $(d\varepsilon_r/dN)_{max,sta}$ for all three steels is presented in Fig. 6-10. It is apparent that there is no significant change in the stabilised maximum ratcheting strain rate when the friction coefficient increases from 0.3 to 0.4. As the friction coefficient further increases to 0.5, the stabilised maximum ratcheting strain rate increases slightly for HE2 steel whereas it increases rapidly for both LAHT and HE1 steels.

According to Fig. 6-11, it is found that HE1 steel always has the shortest RCF initiation life while HE2 steel provides the longest one. When the friction coefficient is 0.5, the RCF initiation life of HE2 steel is 6.57×10^4 cycles while it is less than 10^4 cycles for both LAHT and HE1 steels. It is worth noting that when the friction coefficient increases from 0.3 to 0.5, the RCF initiation life is reduced by 98% and 91% for LAHT and HE2 steels, respectively. However, the RCF initiation life of HE1 steel shows a relatively slight decrease when the friction coefficient is greater than 0.4. This information indicates that the performance of LAHT and HE2 steels is more sensitive to the friction coefficient than HE1 steel and the application of effective lubrication may be required.

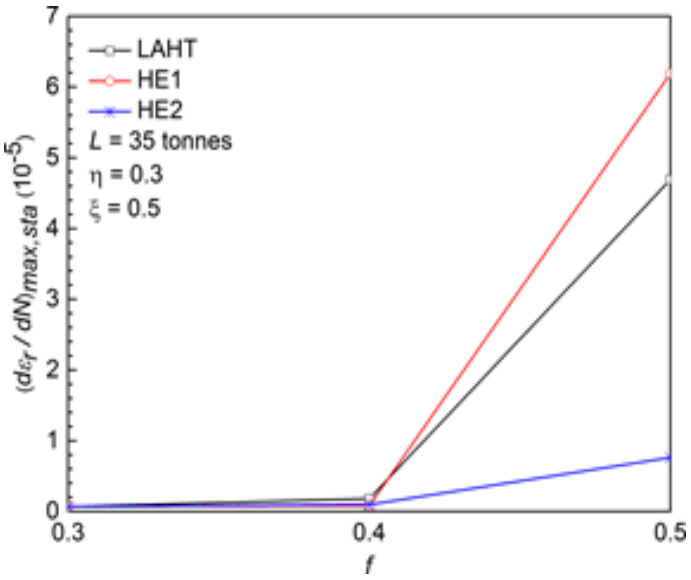

Figure 6-10: The stabilised maximum ratcheting strain rate $(d\varepsilon_r/dN)_{max,sta}$ versus the friction coefficient f for all three rail steels with an axle load of L = 35 tonnes, a ratio of lateral/vertical load η = 0.3 and a tangential traction coefficient of ξ = 0.5.

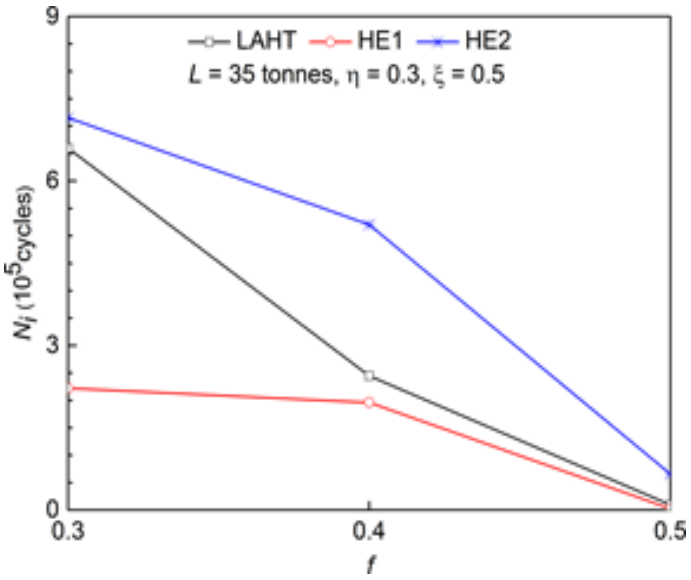

Figure 6-11: The predicted RCF initiation life N_i versus the friction coefficient f for all three rail steels with an axle load of L = 35 tonnes, a ratio of lateral /vertical load η = 0.3 and a tangential traction coefficient of ξ = 0.5.

6.3.3 Influence of Lateral/Vertical Load Ratio

In Australian heavy haul railways for iron ore haulage, the radius of the sharpest curves in the mainline can be less than 400 m, while the operating speed on tangent tracks can be up to 85 km/h. When a train passes a sharp-curved track,

a high rail can be subjected to a large lateral load from the wheelset and hence it is necessary to evaluate the ratcheting performance of the rail steels under different lateral loading conditions. In this study, the ratios of lateral/vertical load η: 0.1, 0.3, and 0.5 were analysed. These parameters can cover most of the loading situations in Australian heavy haul systems (Ranjha et al., 2012).

Fig. 6-12 shows the maximum ratcheting strain rate $(d\varepsilon_r/dN)_{max}$ versus the number of loading cycles N under different values of the ratio of lateral/vertical load η for all three steels. Like the influence of friction-related parameters: ξ and f, the maximum ratcheting strain rate decreases as the number of loading cycles increases. For LAHT steel, the stabilised maximum ratcheting strain rate increases from 6.42×10^{-7} to 3.81×10^{-6} when the ratio of lateral/vertical load increases from 0.1 to 0.5. In contrast, the influence of the ratio of lateral/vertical load on the stabilised maximum ratcheting strain rate for both hypereutectoid steels is insignificant. All the results of the stabilised maximum ratcheting strain rate lie between 6.5×10^{-7} and 9×10^{-7}.

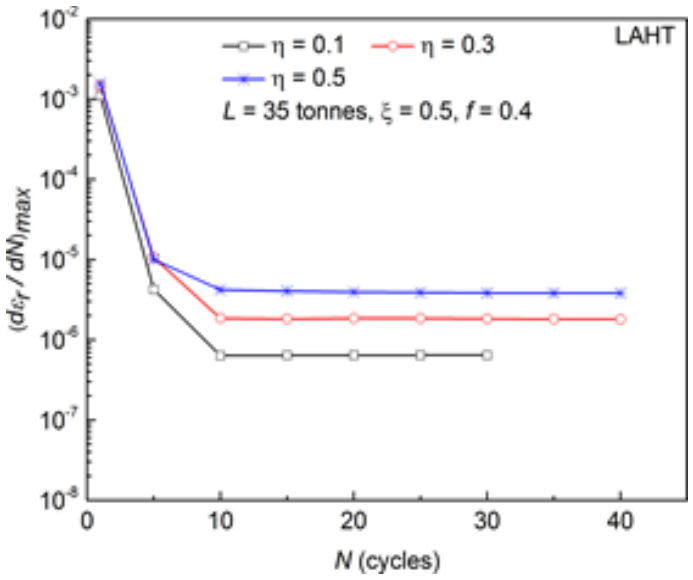

(a)

Figure 6-12: The maximum ratcheting strain rate $(d\varepsilon_r/dN)_{max}$ versus the number of loading cycles N under different values of the ratio of lateral/vertical load η for (a) LAHT; (b) HE1; (c) HE2, with an axle load of L = 35 tonnes, a friction coefficient of f = 0.4 and a normalised tangential traction coefficient of ξ = 0.5.

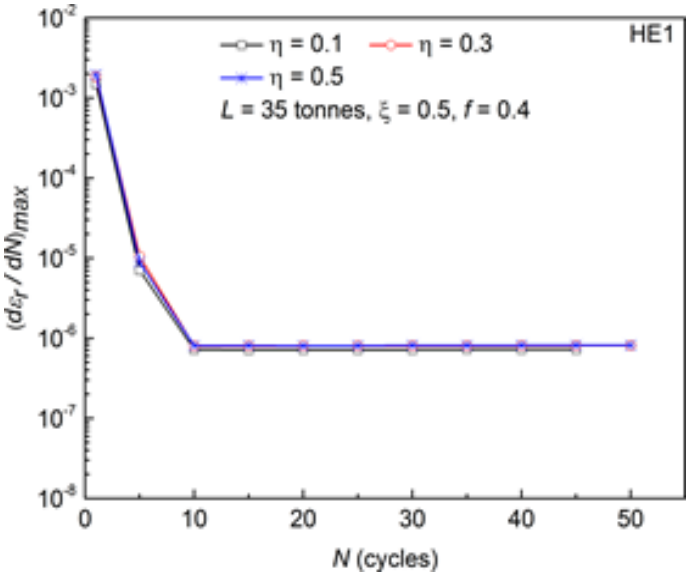

(b)

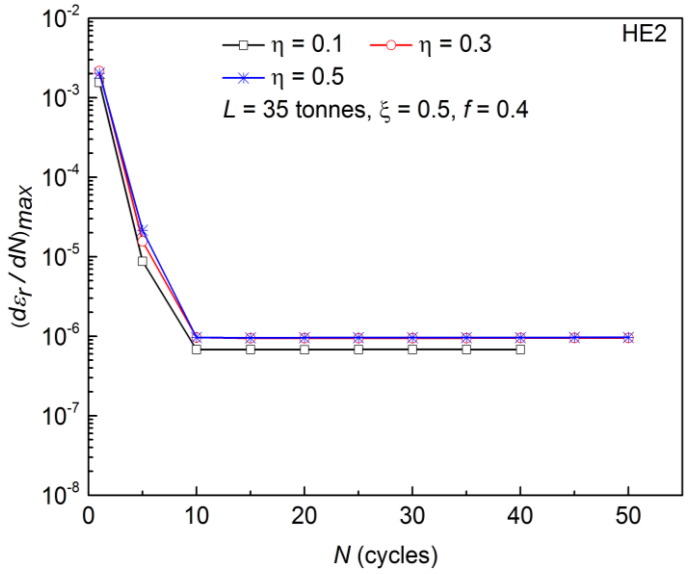

(c)

Figure 6-12: Continued.

Fig. 6-13 further illustrates the relationship between the ratio of lateral/vertical load η and the stabilised maximum ratcheting strain rate $(d\varepsilon_r/dN)_{max,sta}$ for each rail steel. It is found that the stabilised maximum ratcheting strain rate is almost identical for all three steels when the ratio of lateral/vertical load is 0.1. However, the stabilised maximum ratcheting strain rate for LAHT steel increases rapidly with the increase of the ratio of lateral/vertical load. In comparison, the one for both hypereutectoid steels is almost constant, although there is a minor increase for HE2 steel when the ratio of lateral/vertical load increases from 0.1 to 0.3.

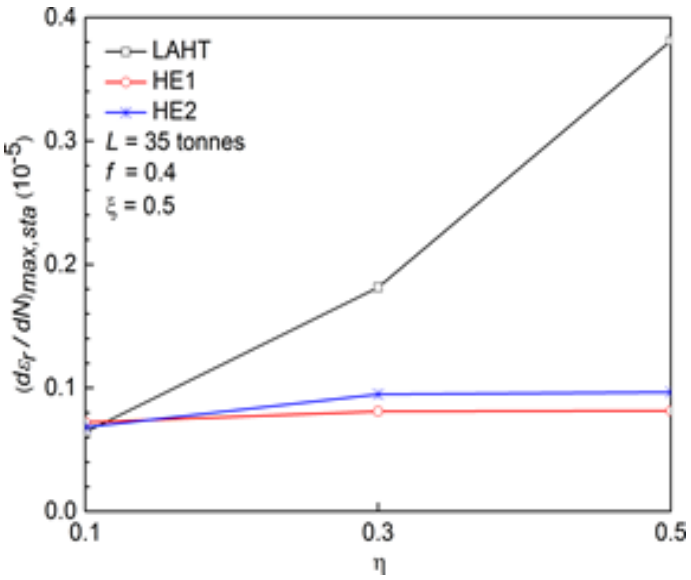

Figure 6-13: The stabilised maximum ratcheting strain rate $(d\varepsilon_r/dN)_{max,sta}$ versus the ratio of lateral/vertical load η for all three rail steels with an axle load of L = 35 tonnes, a friction coefficient of f = 0.4 and a normalised tangential traction coefficient of ξ = 0.5.

The influence of the ratio of lateral/vertical load η on the RCF initiation life N_i for all three steels is demonstrated in Fig. 6-14. It is clearly shown that when the ratio of lateral/vertical load is 0.1, HE1 steel has the shortest RCF initiation life which is around 0.2 million cycles. As the ratio of lateral/vertical load increases to 0.5, the RCF initiation life of HE1 steel keeps almost constant, while the one of LAHT steel decreases rapidly from 0.7 million cycles to 0.1 million cycles and becomes the shortest among all three steels. These results reveal that if assessed only based on ratcheting performance, both LAHT and HE1 steels are likely to require additional attention when installed in a high rail with a sharp curve or high allowable speed of the rolling stock. Moreover, HE2 steel always shows the best ratcheting performance even though a significant reduction of the RCF initiation life is observed as the ratio of lateral/vertical load increases from 0.1 to 0.3.

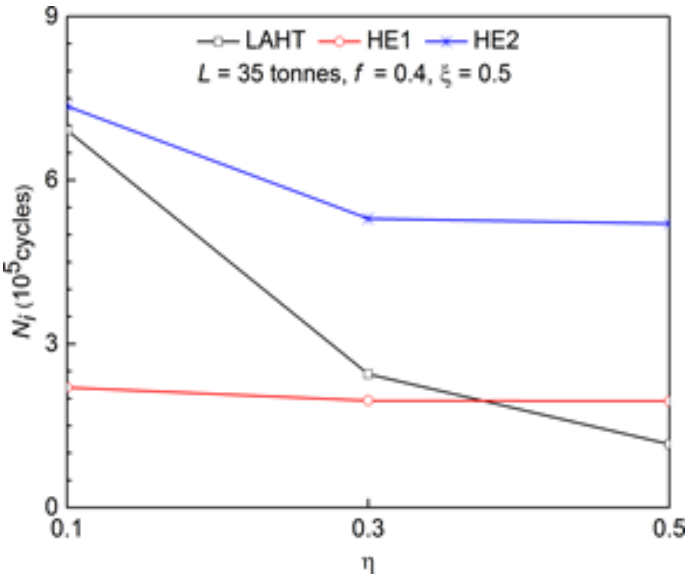

Figure 6-14: The predicted RCF initiation life N_i versus the ratio of lateral/vertical load η for all three rail steels with an axle load of L = 35 tonnes, a friction coefficient of f = 0.4 and a normalised tangential traction coefficient of ξ = 0.5.

6.3.4 Influence of Axle Load

The axle load applied in Australian heavy haul railways for iron ore haulage is typically in the range of 30–40 tonnes. Therefore, it is also essential to evaluate the ratcheting performance of the rail steels under different axle loads. Fig. 6-15 shows the maximum ratcheting strain rate $(d\varepsilon_r/dN)_{max}$ versus the number of loading cycles N under different values of axle load L for all three steels. The results demonstrate that the maximum ratcheting strain rate decreases with the increasing number of loading cycles. The stabilised maximum ratcheting strain rate for LAHT steel increases from 8×10^{-7} to 7.76×10^{-6} as the axle load increases from 30 tonnes to 40 tonnes. Regarding HE1 steel, the stabilised maximum ratcheting strain rate is almost constant when the axle load is less than or equal to 35 tonnes. When the axle load further increases to 40 tonnes, the stabilised maximum ratcheting strain rate increases to 2.82×10^{-6}. In comparison, the influence of the axle load on the stabilised maximum ratcheting strain rate for HE2 steel is minor. All the results of the stabilised maximum ratcheting strain rate are approximately 10^{-6}.

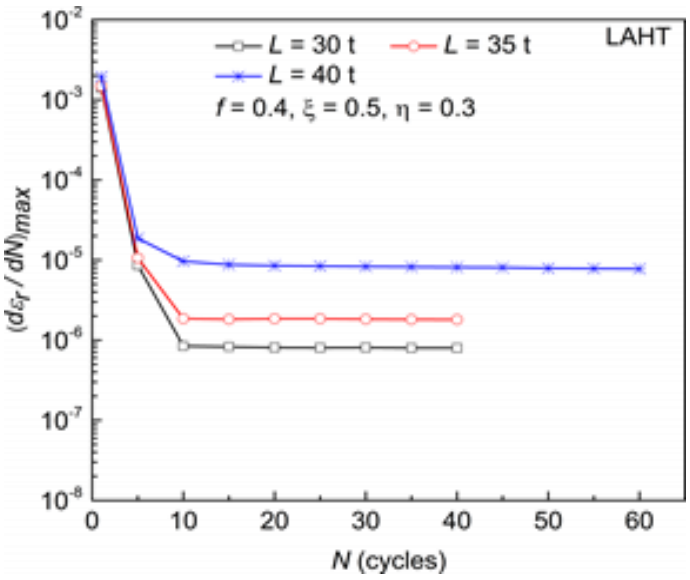

(a)

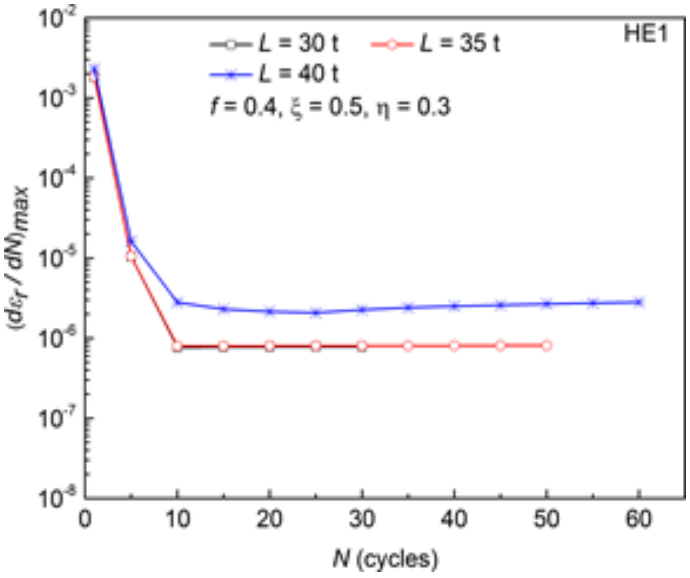

(b)

Figure 6-15: The maximum ratcheting strain rate $(d\varepsilon_r/dN)_{max}$ versus the number of loading cycles N under different values of axle load L for (a) LAHT; (b) HE1; (c) HE2, with a ratio of lateral/vertical load η = 0.3, a friction coefficient of f = 0.4 and a normalised tangential traction coefficient of ξ = 0.5.

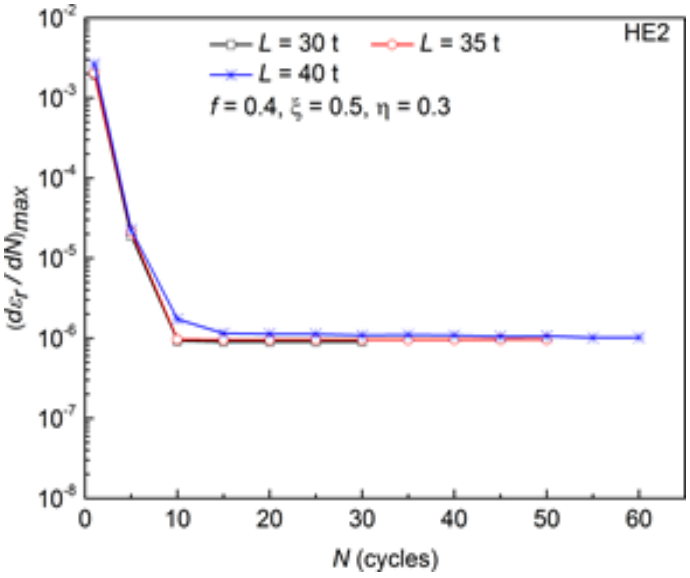

(c)

Figure 6-15: Continued.

Fig. 6-16 summarises the influence of the axle load L on the stabilised maximum ratcheting strain rate $(d\varepsilon_r/dN)_{max,sta}$ for each rail steel. The results indicate that when the axle load is 30 t, the stabilised maximum ratcheting strain rate for all three steels is almost identical. As the axle load increases to 40 tonnes, the stabilised maximum ratcheting strain rate for LAHT steel increases dramatically and becomes the highest value among all three steels whereas HE2 steel gives the lowest one which almost keeps constant. For HE1 steel, an increase in the stabilised maximum ratcheting strain rate is observed when the axle load is larger than 35 tonnes.

The relationship between the RCF initiation life N_i and the axle load L for all three steels is demonstrated in Fig. 6-17. It is clearly shown that the RCF initiation life decreases with the increase of the axle load although there is almost no change for HE1 steel when the axle load increases from 30 tonnes to 35 tonnes. In addition, HE2 steel always provides the longest RCF initiation life even though it is reduced gradually with the increase of the axle load. In contrast, HE1 steel always has the shortest RCF initiation life among all three steels. It is noteworthy that LAHT steel is more sensitive to the axle load as the RCF initiation life is reduced by almost 90% with the axle load increasing from 30 tonnes to 40 tonnes. These results reveal that both LAHT and HE1 steels

installed in high rails may need additional attention.

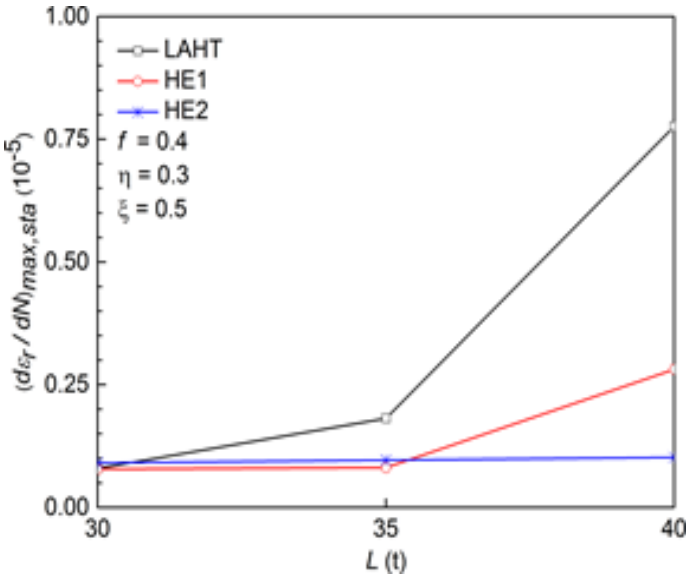

Figure 6-16: The stabilised maximum ratcheting strain rate $(d\varepsilon_r/dN)_{max,sta}$ versus the axle load L for all three rail steels with a ratio of lateral/vertical load η = 0.3, a friction coefficient of f = 0.4 and a normalised tangential traction coefficient of ξ = 0.5.

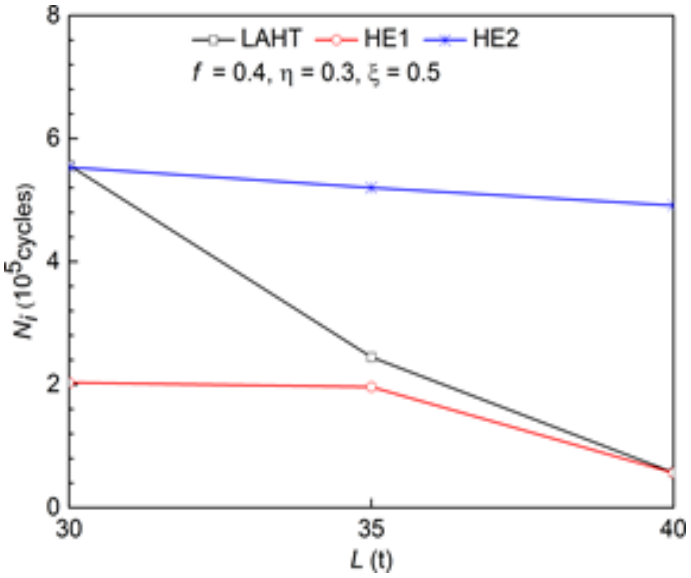

Figure 6-17: The predicted RCF initiation life N_i versus the axle load L for all three rail steels with a ratio of lateral/vertical load η = 0.3, a friction coefficient of f = 0.4 and a normalised tangential traction coefficient of ξ = 0.5.

6.3.5 Discussion

As shown in Figs. 6-8, 6-11, 6-14 and 6-17, HE1 steel always shows shorter

RCF initiation life when compared with HE2 steel, even though HE1 steel has a lower stabilised maximum ratcheting strain rate in some cases, i.e. $\eta \geq 0.3$. The main reason is that as shown in Table 6-1 (Pun et al., 2015a), HE1 steels have lower ductility, which decreases with the increase of carbon content for hypereutectoid steels (Ueda et al., 2013). Moreover, the presence of pro-eutectoid Fe_3C has a negative effect on controlling rail degradation. In some situations, RCF initiated at pearlite colony boundaries and tended to propagate along the pro-eutectoid Fe_3C (Franklin et al., 2009). It is also found that HE2 steel always has the best ratcheting performance among all three steels, particularly under more severe rolling contact conditions, i.e. $\xi \geq 0.5$, $f \geq 0.4$, $\eta \geq 0.3$ and $L \geq 35$ tonnes. For LAHT steel, the RCF initiation life is same as or even longer than HE2 steel under mild loading conditions, i.e. $\xi \leq 0.25$. However, as the loading conditions become severe, the stabilised maximum ratcheting strain rate increases and the corresponding RCF initiation life decreases more significantly than both hypereutectoid steels. The reason is that LAHT steel has the smallest interlamellar spacing of three rail steels, which means that LAHT steel is most sensitive to cyclic softening and is likely to suffer higher deformation (Pun et al., 2015b & Athukorala et al., 2016). Szablewski et al. (2011) conducted the RCF tests for LAHT and HE2 steels on a curved track with a radius of 350 m. The results show that LAHT steel has more surface damage than that of HE2 steel after a traffic of 81.1 MGT. Such information indicates that HE2 steel has the most reliable resistance to RCF and are potentially the best choice to be applied in high rails, particularly installed in the sharper curved tracks, for Australian heavy haul operations.

As presented in Chapter 6.2.3, the RCF initiation life of the rail steels can be predicted from the stabilised maximum ratcheting strain rate. Therefore, the possible location of RCF initiation should correspond to the position with the stabilised maximum ratcheting strain rate. Based on the obtained numerical results, the stabilised maximum ratcheting strain rate or the RCF initiation in curved tracks is always located around 1 mm beneath from the wheel–rail initial contact point under low traction conditions. When the traction condition becomes more severe, i.e. $\xi \geq 0.5$, $f \geq 0.4$ in the current study, the location of

the RCF initiation may shift from the sub-surface to the running surface as shown in Fig. 6-18. Generally, RCF defects observed at high rails in heavy haul operations, such as gauge corner checking, shelling and flaking, are originated from the rail surface or 2-8 mm underneath the gauge corner of the rail head (Marich, 2009). The difference may be attributed to the consideration of only one combination of wheel and rail profiles in this study. Ekberg et al. (2014) highlighted that the contact geometry can affect the contact stresses between wheel and rail and may result in RCF initiating at various depths. Additional considerations, such as steel cleanliness and defect size, can also affect the location of RCF initiation (Kabo & Ekberg, 2005). In spite of these factors, the numerical approach can still roughly predict the possible location of RCF initiation.

The ratcheting performance of all three steels in tangent tracks evaluated by Pun et al., (2015a) concludes that the stabilised maximum ratcheting strain rate increases with normalised tangent traction coefficient, friction coefficient and axle load. Meanwhile, the corresponding RCF initiation life shows a decreasing trend. The same conclusion is also obtained from current analysis for high rails within curves. However, the ratcheting performance in all considered cases is relatively worse than that on tangent tracks. As an example, the stabilised maximum ratcheting strain rate for LAHT steel in tangent tracks is in the range of 10^{-7} and the RCF initiation life is over 3 million cycles under ξ = 0.5, f = 0.4 and L = 35 tonnes, while the stabilised maximum ratcheting strain rate increases to 1.82×10^{-6} and the corresponding RCF initiation life is reduced to less than 0.5 million cycles for high rails in curved tracks with the introduction of η = 0.3. Another typical example is that the influence of the axle load, which is in the range of 30–40 tonnes, on both hypereutectoid steels in tangent tracks is not significant while the ratcheting performance of HE1 steel in high rails becomes worse when the axle load is over 35 tonnes. These examples indicate that the rail steels in high rails need a more frequent maintenance than those in tangent tracks because the smaller contact patch on high rails results in a larger critical area on the running surface suffering higher normal contact pressure and longitudinal tangential traction as shown in Fig. 6-

3. According to such information, it is predicted that the ratcheting performance of high rails would become worse if lateral tangential traction and influence of wheel spin were considered. Additionally, due to the feature of cyclic softening investigated in Pun et al. (2014b) and the higher stress suffered, the position with the maximum ratcheting strain rate in high rails needs more loading cycles than that in tangent tracks to become cyclically stabilised, i.e. 80 cycles in high rails while only 10 cycles in tangent tracks for HE2 steel under f = 0.5.

Pun et al. (2015a) also mentioned that among all three steels in tangent tracks, LAHT steel has the best resistance to ratcheting and the longest RCF initiation life under mild loading conditions: $\xi \leq 0.5$, $f \leq 0.4$ and $L \leq 35$ tonnes. However, in high rails, HE2 steel provides almost the same or even better ratcheting performance than LAHT steel except for $\xi \leq 0.25$ as demonstrated in Figs. 6-8, 6-11 and 6-17. As the loading conditions become more severe, both LAHT and HE1 steels provide relatively worse ratcheting performance of high rails in curved tracks while LAHT steel shows the worst one in tangent tracks. These outcomes highlight that HE2 steel is the best option to be applied in both tangent and curved tracks in Australian heavy haul railways due to its higher ductility and relatively better resistance to RCF.

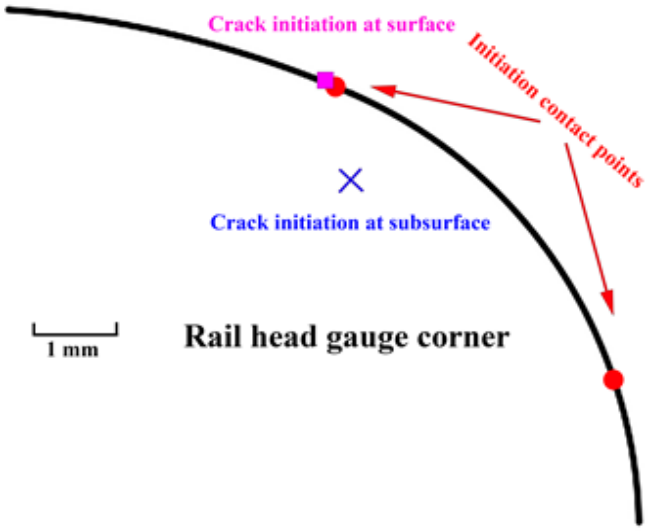

Figure 6-18: The RCF initiation location at the rail head gauge corner will shift from the subsurface (blue) to the running surface (pink) as the surface traction becomes more severe.

So far, the approach developed by Pun et al. (2015a) has been applied to

evaluate the ratcheting performance of the steels for tangent rails and high rails in curved tracks under a combination of new rail and wheel profiles. Practically, the profiles should be modified and implemented in rail systems with the aim of avoiding hazardous contact situations, i.e. the rail profile for heavy haul operations is ground to improve more resistance to gauge corner damage by spreading the contact load on high rails in curved tracks (Kerr & Marich, 2001). The near-conformal or conformal contact formed between the rail gauge and the wheel flange is able to ensure a larger contact area and hence reduces the normal stress (Fröhling, 2007). This approach can also be applied to evaluate the ratcheting performance of rail steels under such situations. The results can then assist rail operators in developing cost-effective maintenance strategies and optimizing the rail performance for particular circumstances.

However, several limitations of the present work should be identified. It is worth mentioning that the change of the contact pressure and tangential traction over the loading cycles is considered small and neglected in this study. Practically, the contact patch will become larger and so result in a reduced contact stresses over multiple loading cycles due to plastic deformation. From this point of view, the ratcheting strain rate from this study might be overestimated. Additionally, some factors were not considered during the cyclic loading simulation, including change of both wheel and rail profiles, lateral tangential traction, influence of wheel spin, impact of leading vs. trailing axles, and influence of lubrication. These factors could also affect the ratcheting performance of rail materials. More numerical studies are needed to overcome these limitations in the future.

6.4 Chapter Summary

The present work investigated the ratcheting performance of three premium high strength rail steels in curved tracks under different in-service heavy haul loading conditions based on a previous approach developed by Pun et al. (2015a). The numerical results obtained for high rails indicate that the stabilised maximum ratcheting strain rate for all three steels increases with normalised

tangent traction, friction coefficient, ratio of lateral/vertical load and axle load, and the corresponding RCF initiation life shows a decreasing trend. Among all three steels, HE2 steel always has the longest RCF initiation life and is the best choice to be installed in high rails, particularly under severe cyclic loading conditions, i.e. $\xi \geq 0.5$, $f \geq 0.4$, $\eta \geq 0.3$ and $L \geq 35$ tonnes, due to its highest ductility and relatively better resistance to ratcheting. RCF is predicted to initiate around 1 mm beneath from the wheel–rail initial contact point under low traction conditions. As the traction condition becomes more severe, the location of RCF initiation may shift from the subsurface to the running surface.

Compared with the results obtained from tangent tracks, the overall ratcheting performance of high rails within curves is relatively worse and one of the dominant reasons is that the narrower contact area on high rails leads to higher contact pressure and longitudinal tangential traction under the new rail and wheel contact situations (without considering the changes of the wheel and rail profiles due to wear and plastic deformation). This means that the rail steels in high rails may require a more frequent maintenance than those in tangent tracks. Additionally, both LAHT and HE1 steels are more prone to suffering rail degradation when installed in high rails even though the ratcheting performance of LAHT steel is better or almost the same as that of HE2 steel under mild rolling contact conditions i.e. $\xi \leq 0.25$, $f = 0.3$, $\eta = 0.1$ and $L = 30$ tonnes. Although significant limitations exist in the current work, these outcomes can further supply useful information about the application of rail steel grades and the development of rail maintenance strategies, such as rail grinding and friction modification, to the track owners and operators.

Chapter 7

Conclusions and Recommendations

The objectives of this research project have been achieved by conducting several tasks to investigate the plastic deformation of flash butt welds in high strength rail steels in Australian heavy haul railways. In this chapter, significant findings of each task are summarised. Some recommendations for further research are also outlined.

7.1 Conclusions

The major aim of this doctoral study is to investigate the plastic deformation, particularly ratcheting behaviour, of flash butt welds which are currently used in Australian heavy haul railway systems. The materials considered are new flash butt welds in R400HT (hypereutectoid heat-treated steel grade with a head hardness roughly 400 HV) rail steel grade with a carbon content of 0.88%. To achieve the main aim, there are three major objectives involved in this research:

(a) To investigate the ratcheting behaviour by experimental study consisting of monotonic tensile tests and cyclic loading tests.

(b) To establish a cyclic plasticity constitutive model which can describe the ratcheting behaviour with reasonable accuracy.

(c) To quantify the ratcheting performance and further estimate the RCF initiation life of the rail head under practical heavy haul loading conditions by finite element simulations.

7.1.1 Ratcheting Behaviour under Laboratory Conditions

The ratcheting behaviour of new flash butt welds in R400HT rail steel was investigated under uniaxial and biaxial stress-controlled cyclic loading tests. The results indicate that:

(a) The ratcheting strain (rate) and its heterogeneity can be correlated to the longitudinal hardness profile (yield strength) within the heat-affected zone of the weld. Moreover, the softened zone with a significant hardness drop is more sensitive to plastic deformation and results in higher ratcheting strain than the region around the bond line.

(b) The ratcheting strain rate for each loading case decreases dramatically in the first few cycles and then gradually becomes almost cyclically

stabilised within the applied loading cycles.

(c) Compared with the parent rail, the softened zone shows much worse ratcheting resistance, while the region around the bond line demonstrates slightly better ratcheting resistance.

(d) The softened zone tends to exhibit cyclic hardening initially and become cyclically stabilised after a certain number of loading cycles. In contrast, both the region around the bond line and the parent rail are more likely to initially exhibit cyclic softening and then reach a cyclically stabilised state.

(e) The microstructure and resulting ratcheting resistance of the weld vary with its longitudinal position. High ratcheting strain in the softened zone is mainly attributed to the existence of the spheroidised microstructure with a high amount of ferrite.

7.1.2 Cyclic Plasticity Constitutive Model

A developed cyclic plasticity constitutive model for high strength rail steels was updated for flash butt welds in R400HT rail steel. The method for calibrating the material parameters required by the updated constitutive model is demonstrated and the material parameters for these welds are determined from the experimental results of the monotonic tensile tests and the stress-controlled cyclic loading tests. The comparison between the simulated results and the experimental data conclude that the updated constitutive model has the capacity to simulate the ratcheting behaviour of the rail flash butt welds with acceptable accuracy, even though some discrepancies can still be observed between the simulated results and the experimental data. Furthermore, the updated constitutive model can be applied to simulate the ratcheting performance of rail welds in practice.

7.1.3 Numerical Study on Ratcheting Performance under Practical Wheel–Rail Weld Cyclic Rolling Contact

With the updated cyclic plasticity constitutive model, dynamic and quasi-static finite element simulations were carried out to evaluate the ratcheting performance of new R400HT rail flash butt welds under an actual wheel–rail weld cyclic rolling contact condition.

The results of the dynamic wheel–rail weld rolling contact simulation imply that that the presence of the new rail weld can lead to an increase in the vertical contact force, but the overall influence is insignificant.

The results of multiple quasi-static wheel–rail/weld contact simulations indicate that when the wheel is located on the softened zone, the maximum normal contact pressure is lower than that when it is located on the parent rail and the region around the bond line. Similar conclusion can also be applied to the estimated longitudinal tangential traction based on the normal contact pressure.

The results of the cyclic loading simulation on the rail weld reveal that:

(a) The ratcheting strain mainly concentrates at the softened zone with lower hardness. As the number of loading cycles increases, this phenomenon becomes more evident. Moreover, the shape of the maximum ratcheting strain distribution can almost correlate with the longitudinal hardness profile of the weld region. Similar conclusions can also be identified in the maximum ratcheting strain rate distribution.

(b) The maximum ratcheting strain rate in every subzone within the weld region and the parent rail decreases dramatically in the first few loading cycles. Both the parent rail and the region around the bond line become cyclically stabilised after a certain number of loading cycles, while most of the subzones in the softened zone experience quite

significant cyclic instability before reaching a cyclically stabilised state eventually. Generally, the softened zone requires more loading cycles to become cyclically stabilised than the parent rail and the region around the bond line.

The ratcheting performance of the weld region and the parent rail is evaluated in terms of the corresponding RCF initiation life:

(c) The subzone with the lowest hardness in the softened zone is predicted to has the shortest RCF initiation life among the weld region, followed by the region around the bond line. The parent rail presents the longest RCF initiation life and therefore has the best resistance to RCF. Furthermore, the presence of the softened zone can shorten the RCF initiation life of the parent rail and the bond line section, especially the regions located adjacent to the softened zone.

(d) The possible location of RCF initiation from the cross-sectional view of the rail head in the softened zone with lower hardness can reach to a depth of 4 mm from the running surface and extend up to 3 mm away from the wheel–rail initial contact point towards either side of the transverse direction, while in the softened zone with relatively higher hardness (adjacent to the parent rail or the region around the bond line) can reach to a depth of 2 mm below the running surface and extend up to 2 mm transversely from the wheel–rail initial contact point. Regarding the parent rail and the region around the bond line, the corresponding critical region can still reach to a depth of 2 mm from the running surface but extend up to only 1 mm transversely from the wheel–rail initial contact point.

The outcomes can assist researchers further understanding the RCF initiation in rail welds and potentially provide useful information for the railway operators to development more reliable and cost-effective maintenance strategies for these welds, i.e. grinding to control RCF damage more frequently. Therefore, a more efficient and safer heavy haul environment can be expected to meet the

continuously increasing demand for freight transportation.

7.1.4 Numerical Study on Ratcheting Performance of High Strength Rail Steels in Curved Tracks

The ratcheting performance of three types of high strength rail steels in curved tracks under different Australian heavy haul in-service conditions was evaluated through the quasi-static wheel–high rail contact simulations and the cyclic loading simulations. The results highlight that:

(a) The stabilised maximum ratcheting strain rate for all three steels increases with normalised tangent traction, friction coefficient, ratio of lateral/vertical load and axle load, and the corresponding RCF initiation life shows a decreasing trend.

The ratcheting performance of all three rail steels is evaluated in terms of the corresponding RCF initiation life:

(b) Under the same in-service loading condition, the ratcheting performance of high rails in curved tracks is relatively worse than the one in tangent tracks.

(c) The hypereutectoid rail steel with a lower carbon content always shows the best RCF resistance and is likely to be the most reliable choice for high rails in curved tracks.

(d) RCF is predicted to initiate around 1 mm beneath from the wheel–rail initial contact point under low traction conditions. As the traction condition becomes more severe, the location of RCF initiation is likely to shift from the subsurface to the running surface.

Although significant limitations exist in the current work, the results can supply valuable information to assist rail operators in the selection of rail steel grades

and the development of rail maintenance strategies, particularly for curved tracks.

7.2 Recommendations for Future Research

Some recommendations for future research in this field are listed below:

(a) Extend the numerical study of ratcheting performance to flash butt welds installed in curved tracks.

(b) Application of dynamic cyclic loading simulations for the ratcheting of rail materials.

(c) Research into the influence of flash butt welding parameters and high strength steel grades on the ratcheting behaviour of rail flash butt welds.

(d) Comprehensive study on the propagation of RCF cracks initiated at rail flash butt welds.

(e) Extending the above to aluminothermic welds with wider softened zone and less ductile fusion zone (weld metal).

(f) Research into the influence of environmental factors or the third body layers, i.e. water, oxygen and temperature, on the wheel–rail interface study.

References

Abaqus (2014). Abaqus Analysis User's Manual Version 6.14-1, Dasssault Systemes Simulia Corp, Providence, RI, United States.

Abaqus (2019). Abaqus Analysis User's Manual Version 2019, Dasssault Systemes Simulia Corp, Providence, RI, United States.

Abdel-Karim, M. (2009). Modified kinematic hardening rules for simulations of ratcheting. *International Journal of Plasticity* 25 (8), pp. 1560-1587.

Abdel-Karim, M. (2010). An extension for the Ohno-Wang kinematic hardening rules to incorporate isotropic hardening. *International Journal of Pressure Vessels and Piping* 87 (4), pp. 170-176.

Abdel-Karim, M. & Ohno, N. (2000). Kinematic hardening model suitable for ratcheting with steady-state. *International Journal of Plasticity* 16 (3-4), pp. 225-240.

Aldajah, S., Ajayi, O. O., Fenske, G. R. & Kumar, S. (2003). Investigation of top of rail lubrication and laser glazing for improved railroad energy efficiency. *Journal of Tribology* 125 (3), pp. 643-648.

Al-Juboori, A., Wexler, D., Li, H., Zhu, H., Lu, C., McCusker, A., Mcleod, J., Pannila, S. & Wang, Z. (2017). Squat formation and the occurrence of two distinct classes of white etching layer on the surface of rail steel. *International Journal of Fatigue* 104, pp. 52-60.

Al-Juboori, A., Zhu, H., Wexler, D., Li, H., Lu, C., McCusker, A., Mcleod, J., Pannila, S. & Barnes, J. (2019). Characterisation of White Etching Layers formed on rails subjected to different traffic conditions. *Wear* 436, 202998.

Armstrong, P. J. & Frederick, C. O. (1966). A mathematical representation of the multiaxial Bauschinger effect. *Central Electricity Generating Board*, Report RD/B/N731, Berkely Nuclear Laboratories, Berkely, UK.

References

Archard, J. (1953). Contact and rubbing of flat surfaces. *Journal of Applied Physics* 24 (8), pp. 981-988.

AREMA Manual for Railway Engineering (2013), vol. 1, section 4.11, Recommended Practices for Wheel–rail Friction Control.

Asaro, R. & Lubarda, V. (2006). Mechanics of solids and materials. Cambridge University Press, Cambridge.

Association of American Railroads (AAR) (2017). Manual of Standards and Recommended Practices Section G, Part II – Wheel and Axle Shop Manual: Wheels, Carbon Steel-Specification: M-107/M-208 (Revised: 2017), AAR Publications.

Athukorala, A. C., De Pellegrin, D. V. & Kourousis, K. I. (2016). Characterisation of head-hardened rail steel in terms of cyclic plasticity response and microstructure for improved material modelling. *Wear* 366, pp. 416-424.

Australian Standard AS1085.1-2002/Amdt1 (2005). Railway track materials-Steel rails.

Australian Standard AS1085.20 (2020). Railway Track Materials, Part 20, Welding of Steel Rail.

Ayasse, J. B. & Chollet, H. U. G. U. E. S. (2005). Determination of the wheel rail contact patch in semi-Hertzian conditions. *Vehicle System Dynamics* 43 (3), pp. 161-172.

Baeza, L., Roda, A., Carballeira, J. & Giner, E. (2006). Railway train–track dynamics for wheelflats with improved contact models. *Nonlinear Dynamics* 45 (3-4), pp. 385-397.

Bai, N. & Chen, X. (2009). A new unified constitutive model with short and long-range back stress for lead-free solders of Sn–3Ag–0.5 Cu and Sn–0.7 Cu. *International Journal of Plasticity* 25 (11), pp. 2181-2203.

Bari, S. & Hassan, T. (2000). Anatomy of coupled constitutive models for ratcheting simulation. *International Journal of Plasticity* 16 (3-4), pp. 381-409.

References

Bari, S. & Hassan, T. (2002). An advancement in cyclic plasticity modelling for multiaxial ratcheting simulation. *International Journal of Plasticity* 18 (7), pp. 873-894.

Beretta, S., Boniardi, M., Carboni, M. & Desimone, H. (2005). Mode II fatigue failures at rail butt-welds. *Engineering Failure Analysis* 12 (1), pp. 157-165.

Beynon, J. H., Garnham, J. E. & Sawley, K. J. (1996). Rolling contact fatigue of three pearlitic rail steels. *Wear* 192 (1-2), pp. 94-111.

Bolton, P. J. & Clayton, P. (1984). Rolling—sliding wear damage in rail and tyre steels. *Wear* 93 (2), pp. 145-165.

Bower, A. F. (1989). Cyclic hardening properties of hard-drawn copper and rail steel. *Journal of the Mechanics and Physics of Solids* 37(4), pp. 455-470.

Bower, A. F. & Johnson, K. L. (1991). Plastic flow and shakedown of the rail surface in repeated wheel–rail contact. *Wear* 144 (1-2), pp. 1-18.

BREE. (2020) *Resources and Energy Quarterly, March Quarter 2020*, Bureau of Resources and Energy Economics, Australia.

Burlet, H. & Cailletaud, G. (1986). Numerical techniques for cyclic plasticity at variable temperature. *Engineering Computations* 3, 143-153.

Burstow, M. C., Benyon, J., Watson, A. S., Beagles, A. E. & Beagles, M. (2003). Current developments in the whole life rail model to predict rolling contact fatigue in rails. In*: Proceedings of the World Congress on Railway Research*, pp. 445-451, Edinburgh, UK.

Busquet, M., Chollet, H., Baillet, L., Dagorn, C., Ayasse, J. B. & Berthier, Y. (2006). From railway dynamics to wheel/rail contact mechanics, an approach for the modelling of the wheel/rail contact: elasto-plastic response of the railhead. In: *Proceedings of the Institution of Mechanical Engineers, Part F: Journal of Rail and Rapid Transit* 220 (3), pp. 189-200.

Cann, P. M. (2006). The “leaves on the line” problem—a study of leaf residue film

formation and lubricity under laboratory test conditions. *Tribology Letters* 24 (2), pp. 151-158.

Carroll, R. I. & Beynon, J. H. (2006). Decarburisation and rolling contact fatigue of a rail steel. *Wear* 260 (4-5), pp. 523-537.

Carter, F. W. (1926). On the action of a locomotive driving wheel. In: *Proceedings of the Royal Society of London. Series A, containing papers of a mathematical and physical character* 112 (760), pp. 151-157.

Çetinkaya, C. & Arabaci, U. (2006). Flash butt welding application on 16MnCr5 chain steel and investigations of mechanical properties. *Materials & Design* 27 (10), pp. 1187-1195.

Chang, C., Wang, C., Chen, B. & Li, L. (2010). A study of a numerical analysis method for the wheel–rail wear of a heavy-haul train. In: *Proceedings of the Institution of Mechanical Engineers, Part F: Journal of Rail and Rapid Transit* 224 (5), pp. 473-482.

Chaboche, J. L. (1986). Time-independent constitutive theories for cyclic plasticity. *International Journal of Plasticity* 2 (2), pp. 149-188.

Chaboche, J. L. (1989). Constitutive equations for cyclic plasticity and cyclic viscoplasticity. *International Journal of Plasticity* 5 (3), pp. 247-302.

Chaboche, J. L. (1991). On some modifications of kinematic hardening to improve the description of ratcheting effects. *International Journal of Plasticity* 7, pp. 661-678.

Chaboche, J. L., Dang-Van, K. & Cordier, G. (1979). Modelisation of the strain memory effect on the cyclic hardening of 316 stainless steel. In: *Transactions of SMIRT 5*, Vol. L, Paper No. L11/3.

Chen, X. & Jiao, R. (2004). Modified kinematic hardening rule for multiaxial ratcheting prediction. *International Journal of Plasticity* 20 (4-5), pp. 871-898.

Chen, X., Jiao, R. & Kim, K. S. (2003). Simulation of ratcheting strain to a high number of cycles under biaxial loading. *International Journal of Solids and Structures* 40 (26), pp. 7449-7461.

Chen, X., Jiao, R. & Kim, K. S. (2005). On the Ohno-Wang kinematic hardening rules for multiaxial ratcheting modelling of medium carbon steel. *International Journal of Plasticity* 21 (1), pp. 161-184.

Chen, X., Jiao, R. & Tian, T. (2003). Research advances of ratcheting effects and cyclic constitutive models. *Advances in Mechanics* 33(4), pp. 461-470.

Chen, Y. C. (2003). The effect of proximity of a rail end in elastic-plastic contact between a wheel and a rail. In: *Proceedings of the Institution of Mechanical Engineers, Part F: Journal of Rail and Rapid Transit* 217 (3), pp. 189-201.

Chen, Y. C. & Chen, L. W. (2006). Effects of insulated rail joint on the wheel/rail contact stresses under the condition of partial slip. *Wear* 260 (11-12), pp. 1267-1273.

Ciavarella, M. & Monno, F. (2010). A comparison of multiaxial fatigue criteria as applied to rolling contact fatigue. *Tribology International* 43 (11), pp. 2139-2144.

Christoforou, P., Fletcher, D. I. & Lewis, R. (2019). Benchmarking of premium rail material wear. *Wear* 436, 202990.

Clare, A. T., Oyelola, O., Abioye, T. E. & Farayibi, P. K. (2013). Laser cladding of rail steel with Co-Cr. *Surface Engineering* 29 (10), pp. 731-736.

Clare, A., Oyelola, O., Folkes, J. & Farayibi, P. (2012). Laser cladding for railway repair and preventative maintenance. *Journal of Laser Applications* 24 (3), 032004.

Cookson, J. M. & Mutton, P. J. (2011). The role of the environment in the rolling contact fatigue cracking of rails. *Wear* 271 (1-2), pp. 113-119.

Cookson, J. M. & Mutton, P. J. (2016). Flash butt welding specification issues for general freight and transit systems. *CORE 2016: Maintaining the Momentum*, pp. 137-144.

Crossland, B. (1956). Effect of large hydrostatic pressures on the torsional fatigue strength of an alloy steel. In: *Proceedings of International Conference on Fatigue of Metals London: Institution of Mechanical Engineers*, pp. 138-149.

Cuervo, P., Christoforou, P., Lewis, R., Beagles, A., Santa, J. F. & Toro, A. (2018). Twin disc assessment of wear regime transitions in R400HT-E8 Pairs. In: *Proceedings of the 11th International Conference on Contact Mechanics and Wear of Rail/Wheel Systems (CM2018)*, pp. 181-188, Delft, The Netherlands.

Dang, K., Van, K., Cailletaud, G., Flavenot, J. F., LeDouaron, A. & Lieurade, H. P. (1989). Criterion for high cycle fatigue failure under multiaxial loading. In: *Biaxial and multiaxial fatigue*, edited by Brown, M. W. & Miller, K. J., pp. 459-478, Mechanical Engineering Publications, London, UK.

Dafalias, Y. F. & Popov, E. P. (1975). A model of nonlinearly hardening materials for complex loading. *Acta Mechanica*, 21 (3), pp. 173-192.

Date, S., Ishikawa, H., Otani, T. & Takahashi, Y. (2008). Effect of ratcheting deformation on fatigue and creep-fatigue life of 316FR stainless steel. *Nuclear Engineering and Design* 238 (2), pp. 336-346.

Demofonti, G., Mecozzi, E., Guagnelli, M., Drewett, L., Thompson, G. & Jöller, A. (2007). Role of steel composition and welding parameters in the improvement of fatigue behaviour of high-strength welded rails. EUR 22853, pp. 1-225.

Deng, D. & Murakawa, H. (2013). Influence of transformation induced plasticity on simulated results of welding residual stress in low temperature transformation steel. Computational Materials Science 78, pp. 55-62.

Deng, X., Li, Z., Qian, Z., Zhai, W., Xiao, Q. & Dollevoet, R. (2019). Pre-cracking development of weld-induced squats due to plastic deformation: Five-year field monitoring and numerical analysis. *International Journal of Fatigue* (127), pp. 431-444.

Deng, X., Qian, Z. & Dollevoet, R. (2015). Lagrangian explicit finite element modelling for spin-rolling contact. Journal of Tribology 137 (4), pp. 1401-1411.

Ding, H. H., Fu, Z. K., Wang, W. J., Guo, J., Liu, Q. Y. & Zhu, M. H. (2015). Investigation on the effect of rotational speed on rolling wear and damage behaviours of wheel/rail materials. Wear 330, pp. 563-570.

Ding, H. H., He, C. G., Ma, L., Guo, J., Liu, Q. Y. & Wang, W. J. (2016). Wear mapping and transitions in wheel and rail materials under different contact pressure and sliding velocity conditions. Wear 352, pp. 1-8.

Donzella, G., Faccoli, M., Ghidini, A., Mazzu, A. & Roberti, R. (2005). The competitive role of wear and RCF in a rail steel. Engineering Fracture Mechanics 72 (2), pp. 287-308.

Döring, R., Hoffmeyer, J., Seeger, T. & Vormwald, M. (2003). A plasticity model for calculating stress–strain sequences under multiaxial nonproportional cyclic loading. Computational Materials Science 28 (3-4), pp. 587-596.

Dwight, R. & Jiang, J. (2006), On-board wheel–rail noise monitoring for the direction of track maintenance. In: Proceedings of Conference of Railway Excellence (CORE2006), Railway Technical Society of Australia, Melbourne, Australia.

Eadie, D.T., Vidler, B., Hooper, N.E. & Makowsky, T.W. (2003). Top of rail friction control: Lateral force and rail wear reduction in a freight application, International Heavy Haul Association. In: Proceedings of the Specialist Technical Session on Implementation of Heavy Haul Technology for Network Efficiency, pp. 5.73–5.80, Dallas, Texas, USA.

Eden, H. C., Garnham, J. E. & Davis, C. L. (2005). Influential microstructural changes on rolling contact fatigue crack initiation in pearlitic rail steels. Materials Science and Technology 21 (6), pp. 623-629.

Eddy, J., Bourke, M., Arcus, K., Mutton, P. & Cookson, J. (2015). Application of phased array ultrasonic testing for enhanced quality assurance of flash butt welds. In: Proceedings of 11th International Heavy Haul Association Conference, Perth, Australia.

Efremenko, V. G., Shimizu, K., Cheiliakh, A. P., Kozarevskaya, T. V., Kusumoto, K. & Yamamoto, K. (2014). Effect of vanadium and chromium on the microstructural features of V-Cr-Mn-Ni spheroidal carbide cast irons. International Journal of Minerals, Metallurgy, and Materials 21 (11), pp. 1096-1108.

Ekberg, A., Åkesson, B. & Kabo, E. (2014). Wheel/rail rolling contact fatigue–Probe,

predict, prevent. Wear 314 (1-2), pp. 2-12.

Ekberg, A. & Kabo, E. (2014). Surface fatigue initiated transverse defects and broken rails–an International Review. Research report 2014:05, Chalmers University of Technology.

Elwazri, A. M., Wanjara, P. & Yue, S. (2005). The effect of microstructural characteristics of pearlite on the mechanical properties of hypereutectoid steel. *Materials Science and Engineering: A* 404 (1-2), pp. 91-98.

Fletcher, D. I. & Beynon, J. H. (2000). The effect of intermittent lubrication on the fatigue life of pearlitic rail steel in rolling-sliding contact. In*: Proceedings of the Institution of Mechanical Engineers, Part F: Journal of Rail and Rapid Transit*, 214 (3), pp. 145-158.

Fletcher, D. I., Franklin, F. J. & Kapoor, A. (2009). Rail surface fatigue and wear. In: *Wheel–rail interface handbook*, edited by Lewis, R. & Olofsson, U., pp. 280–309, Woodhead Publishing, Cambridge, UK, ISBN 978-1-84569-110-3.

Franklin, F. J., Garnham, J. E., Davis, C. L., Fletcher, D. I. & Kapoor, A. (2009). The evolution and failure of pearlitic microstructure in rail steel–observations and modelling. In: *Wheel–rail interface handbook*, edited by Lewis, R. & Olofsson, U., pp. 311-348, Woodhead Publishing, Cambridge, UK, ISBN 978-1-84569-110-3.

Franklin, F. J., Garnham, J. E., Fletcher, D. I., Davis, C. L. & Kapoor, A. (2008). Modelling rail steel microstructure and its effect on crack initiation. *Wear* 265 (9-10), pp. 1332-1341.

Fröhling, R. D. (2007). Wheel/rail interface management in heavy haul railway operations—applying science and technology. *Vehicle System Dynamics* 45 (7-8), pp. 649-677.

Fu, Z. K., Ding, H. H., Wang, W. J., Liu, Q. Y., Guo, J. & Zhu, M. H. (2015). Investigation on microstructure and wear characteristic of laser cladding Fe-based alloy on wheel/rail materials. *Wear* 330, pp. 592-599.

Fujii, M., Nakanowatari, H. & Nariai, K. (2015). Rail flash butt welding technology.

References

JFE Technical Report 20 (March), pp. 159-163, JFE Steel Corporation.

Garnham, J. E. & Beynon, J. H. (1991). The early detection of rolling-sliding contact fatigue cracks. *Wear* 144, pp. 103-116.

Garnham, J. E. & Davis, C. L. (2008). The role of deformed rail microstructure on rolling contact fatigue initiation. *Wear* 265 (9-10), pp. 1363-1372.

Garnham, J. E. & Davis, C. L. (2009). Rail materials. In: *Wheel–rail interface handbook*, edited by Lewis, R. & Olofsson, U., pp. 125-171, Woodhead Publishing, Cambridge, UK, ISBN 978-1-84569-110-3.

Garnham, J. E. & Davis, C. L. (2011). Very early stage rolling contact fatigue crack growth in pearlitic rail steels. *Wear* 271 (1-2), pp. 100-112.

Godefroid, L. B., Faria, G. L. D., Cândido, L. C. & Viana, T. G. (2015). Failure analysis of recurrent cases of fatigue fracture in flash butt welded rails. *Engineering Failure Analysis* 58, pp. 407-416.

Gutscher, D., Baillargeon, J. & Li, D. (2014). Effects of Heavy-axle Loads on Electric Flash-weld Surface Degradation. *Railway Track and Structures* 110 (7).

Grassie, S. L. (2009a). Maintenance of the wheel–rail interface. In: *Wheel–rail interface handbook*, edited by Lewis, R. & Olofsson, U., pp. 576-607, Woodhead Publishing, Cambridge, UK, ISBN 978-1-84569-110-3.

Grassie, S. L. (2009b). Rail corrugation: characteristics, causes, and treatments. In: *Proceedings of the Institution of Mechanical Engineers, Part F: Journal of Rail and Rapid Transit* 223 (6), 581-596.

Haines, D. J. & Ollerton, E. (1963). Contact stress distributions on elliptical contact surfaces subjected to radial and tangential forces. In: *Proceedings of the Institution of Mechanical Engineers* 177 (1), pp. 95-114.

Han, K., Edmonds, D. V. & Smith, G. D. W. (2001). Optimization of mechanical properties of high-carbon pearlitic steels with Si and V additions. *Metallurgical and Materials Transactions A* 32 (6), pp. 1313-1324.

Hardwick, C., Lewis, R. & Eadie, D. T. (2014). Wheel and rail wear—Understanding the effects of water and grease. *Wear* 314(1-2), pp. 198-204.

Hardwick, C. Lewis, R. & Stock, R. (2017). The effects of friction management materials on raifstripl with pre-existing RCF surface damage. *Wear* 384, pp. 50-60.

Hassan, T. & Kyriakides, S. (1992a). Ratcheting in cyclic plasticity, part I: uniaxial behaviour. *International Journal of Plasticity* 8 (1), pp. 91-116.

Hassan, T., Corona, E. & Kyriakides, S. (1992b). Ratcheting in cyclic plasticity, part II: multiaxial behaviour. *International Journal of Plasticity* 8 (2), pp. 117-146.

Hassan, T. & Kyriakides, S. (1994a). Ratcheting of cyclically hardening and softening materials: I. Uniaxial behavior. *International Journal of Plasticity* 10 (2), pp. 149-184.

Hassan, T. & Kyriakides, S. (1994b). Ratcheting of cyclically hardening and softening materials: II. Multiaxial behaviour. *International Journal of Plasticity* 10 (2), pp. 185-212.

Hassan, T., Taleb, L. & Krishna, S. (2008). Influence of non-proportional loading on ratcheting responses and simulations by two recent cyclic plasticity models. *International Journal of Plasticity* 24 (10), pp. 1863-1889.

Hernandez, F. C. R., Olivares, R. O. & Garcia, C. I. (2008). New rail steels for the 21st century. *Railway Track and Structures* 104 (6).

Hernández, F. R., Okonkwo, A. O., Kadekar, V., Metz, T. & Badi, N. (2016). Laser cladding: The alternative for field thermite welds life extension. *Materials & Design* 111, pp. 165-173.

Hertz, H. (1882). Ueber die Berührung fester elastischer Körper. *Journal für die reine und angewandte Mathematik* 1882 (92), pp. 156-171.

Hiensch, M. & Steenbergen, M. (2018). Rolling Contact Fatigue on premium rail grades: Damage function development from field data. *Wear* 394, pp. 187-194.

References

https://publications.industry.gov.au/publications/resourcesandenergyquarterlymarch2020/index.

http://www.railsystem.net/flash-butt-welding/.

Ichiyama, Y. & Kodama, S. (2006). Flash-butt welding of high strength steels. *SHINNITTETSU GIHO* 385, pp. 74-80.

International Heavy Haul Association. (2015). Guidelines to best practices for heavy haul railway operations: management of the wheel and rail interface. *Simmons-Boardman Books, inc*.

Iwnicki, S., Björklund, S. & Enblom, R. (2009). Wheel–rail contact mechanics. In: *Wheel–rail interface handbook*, edited by Lewis, R. & Olofsson, U., pp. 58-91, Woodhead Publishing, Cambridge, UK, ISBN 978-1-84569-110-3.

Jiang, W., Woo, W., An, G. B. & Park, J. U. (2013). Neutron diffraction and finite element modelling to study the weld residual stress relaxation induced by cutting. *Materials & Design* 51, pp. 415-420.

Jiang, Y. (2001). An experimental study of inhomogeneous cyclic plastic deformation. *Journal of Engineering Materials and Technology* 123 (3), pp. 274-280.

Jiang, Y. & Kurath, P. (1996). Characteristics of the Armstrong-Frederick type plasticity models. *International Journal of Plasticity* 12 (3), pp. 387-415.

Jiang, Y. & Sehitoglu, H. (1994a). Cyclic ratcheting of 1070 steel under multiaxial stress states. *International Journal of Plasticity* 10 (5), pp. 579-608.

Jiang, Y. & Sehitoglu, H. (1994b). Multiaxial cyclic ratcheting under multiple step loading. *International Journal of Plasticity* 10(8), pp. 849-870.

Jiang, Y. & Sehitoglu, H. (1996). Modelling of cyclic ratcheting plasticity, Part I: Development of constitutive relations. *Journal of Applied Mechanics* 63, pp. 720-725.

Jiang, Y. & Sehitoglu, H. (1999). A model for rolling contact failure. *Wear* 224 (1), pp. 38-49.

Jiang, Y., Xu, B. & Sehitoglu, H. (2002). Three-dimensional elastic-plastic stress analysis of rolling contact. *Journal of Tribology* 124 (4), pp. 699-708.

Jin, Y., Ishida, M. & Namura, A. (2011). Experimental simulation and prediction of wear of wheel flange and rail gauge corner. *Wear* 271 (1-2), pp. 259-267.

Johnson, K. L. (1958a). The effect of spin upon the rolling motion of an elastic sphere on a plane. *Journal of Applied Mechanics* 25, pp. 332-338.

Johnson, K. L. (1958b). The effect of spin upon the rolling motion of an elastic sphere on a plane. *Journal of Applied Mechanics* 25, pp. 339-346.

Johnson, K. L. (1985). Contact mechanics. Cambridge University Press, Cambridge.

Kabo, E. & Ekberg, A. (2005). Material defects in rolling contact fatigue of railway wheels—the influence of defect size. *Wear* 258 (7-8), pp. 1194-1200.

Kalker, J. J. (1967). A strip theory for rolling with slip and spin. In: *Proceedings of the Koninklijke Nederlandse Aksdemie Van Wetenschappen, Series B-Physical Sciences* 70 (1), pp. 10-62.

Kalker, J. J. (1972). On elastic line contact. *Journal of Applied Mechanics* 39 (4), pp. 1125-1132.

Kalker, J. J. (1973). Simplified theory of rolling contact. Department of Mathematics, Delft University of Technology, The Netherlands.

Kalker, J. J. (1979a). Survey of wheel–rail rolling contact theory. *Vehicle System Dynamics* 8 (4), pp. 317-358.

Kalker, J. J. (1979b). The computation of three-dimensional rolling contact with dry friction. *International Journal for Numerical Methods in Engineering* 14 (9), pp. 1293-1307.

Kalker, J. J. (1982). A fast algorithm for the simplified theory of rolling contact. *Vehicle System Dynamics* 11 (1), pp. 1-13.

Kalker, J. J. (1990). Three-dimensional elastic bodies in rolling contact. Springer, Kluwer, The Netherlands.

Kalker, J. J. (2001). Rolling contact phenomena – linear elasticity. In: *Rolling contact phenomena*, *CISM Courses and Lectures*, edited by Jacobson, B. & Kalker, pp. 1-84, Wien, New York: Springer.

Kalousek, J. & Magel, E. (1997). Achieving a balance: the 'magic' wear rate. *Railway Track and Structures* 93, pp. 50–52.

Kan, Q., Kang, G. & Zhang, J. (2007). A unified viscoplastic constitutive model for uniaxial time-dependent ratcheting and its finite element implementation. *Theoretical and Applied Fracture Mechanics* 47 (2), pp. 133-144.

Kang, G. & Gao, Q. (2002). Uniaxial and non-proportionally multiaxial ratcheting of U71Mn rail steel: experiments and simulations. *Mechanics of Materials* 34 (12), pp. 809-820.

Kang, G., Gao, Q., Cai, L. & Sun, Y. (2002a). Experimental study on uniaxial and non-proportionally multiaxial ratcheting of SS304 stainless steel at room and high temperatures. *Nuclear Engineering and Design* 216 (1-3), pp. 13-26.

Kang, G., Gao, Q., Cai, L., Yang, X. & Sun, Y. (2001). Experimental study on uniaxial and multiaxial strain cyclic characteristics and ratcheting of 316L stainless steel. *Journal of Materials Science and Technology* 17 (2), pp. 219-223.

Kang, G., Gao, Q. & Yang, X. (2002b). Experimental study on the cyclic deformation and plastic flow of U71Mn rail steel. *International Journal of Mechanical Sciences* 44 (8), pp. 1647-1663.

Kang, G., Gao, Q. & Yang, X. (2004). Uniaxial and non-proportionally multiaxial ratcheting of SS304 stainless steel at room temperature: experiments and simulations. *International Journal of Non-Linear Mechanics* 39 (5), pp. 843-857.

Kang, G. & Kan, Q. (2009). Experimental study on the uniaxial cyclic deformation of 25CDV4. 11 steel. *Journal of Materials Sciences and Technology* 21 (01), pp. 5-9.

Kang, G., Kan, Q., Yu, C., Song, D. & Liu, Y. (2012). Whole-life transformation ratcheting and fatigue of super-elastic NiTi Alloy under uniaxial stress-controlled cyclic loading. *Materials Science and Engineering: A* 535, pp. 228-234.

Kang, G., Kan, Q. Zhang, J. & Sun, Y. (2006a). Time-dependent ratcheting experiments of SS304 stainless steel. *International Journal of Plasticity* 22 (5), pp. 858-894.

Kang, G., Li, Y. & Gao, Q. (2005a). Non-proportionally multiaxial ratcheting of cyclic hardening materials at elevated temperatures: experiments and simulations. *Mechanics of Materials* 37 (11), pp. 1101-1118.

Kang, G., Li, Y. G., Zhang, J., Sun, Y. F. & Gao, Q. (2005b). Uniaxial ratcheting and failure behaviours of two steels. *Theoretical and Applied Fracture Mechanics* 43 (2), pp. 199-209.

Kang, G. & Liu, Y. (2008). Uniaxial ratcheting and low-cycle fatigue failure of the steel with cyclic stabilizing or softening feature. *Materials Science and Engineering: A* 472 (1-2), pp. 258-268.

Kang, G., Liu, Y. & Ding, J. (2008). Multiaxial ratcheting-fatigue interactions of annealed and tempered 42CrMo steels: experimental observations. *International Journal of Fatigue* 30 (12), pp. 2104-2118.

Kang, G., Liu, Y., Ding, J. & Gao, Q. (2009). Uniaxial ratcheting and fatigue failure of tempered 42CrMo steel: damage evolution and damage-coupled viscoplastic constitutive model. *International Journal of Plasticity* 25 (5), pp. 838-860.

Kang, G., Liu, Y. & Li, Z. (2006b). Experimental study on ratcheting-fatigue interaction of SS304 stainless steel in uniaxial cyclic stressing. *Materials Science and Engineering: A* 435, pp. 396-404.

Kang, G., Ohno, N. & Nebu, A. (2003). Constitutive modelling of strain range dependent cyclic hardening. *International Journal of Plasticity* 19 (10), pp. 1801-1819.

Kapoor, A., Fletcher, D. I. & Franklin, F. J. (2003). The role of wear in enhancing rail life. In: *Proceedings of the 29th Leeds-Lyon Symposium on Tribology, Elsevier*

Tribology Series 41, pp. 331-340.

Kapoor, A. & Johnson, K. L. (1994). Plastic ratcheting as a mechanism of metallic wear. In: *Proceedings of the Royal Society of London. Series A: Mathematical and Physical Sciences* 445 (1924), pp. 367-384.

Kapoor, A. (1994). A re-evaluation of the life to rupture of ductile metals by cyclic plastic strain. *Fatigue & Fracture of Engineering Materials & Structures*, 17 (2), pp. 201-219.

Kapoor, A. (1997). Wear by plastic ratcheting. *Wear* 212 (1), pp. 119-130.

Kerr, M. & Marich, S. (2001). At last, compatible wheel and rail profiles for standard gauge lines. In: *Proceedings of the 13th International Rail Track Conference*, Rail Track Association, Canberra, Australia.

Khoddam, S., Shamdani, A. H., Mutton, P., Ravitharan, R., Beynon, J. H. & Kapoor, A. (2014). A new test to study the cyclic hardening behaviour of a range of high strength rail materials. *Wear* 313 (1-2), pp. 43-52.

Khutia, N., Dey, P. P., Sivaprasad, S. & Tarafder, S. (2014). Development of new cyclic plasticity model for 304LN stainless steel through simulation and experimental investigation. *Mechanics of Materials* 78, pp. 85-101.

Kik, W. & Piotrowski, J. (1996). A fast, approximate method to calculate normal load at contact between wheel and rail and creep forces during rolling. In: *Proceedings of the Second Mini Conference on Contact Mechanics and Wear of Rail/Wheel Systems*, edited by Zobory, Budapest, Hungary.

Kim, C. Y., Song, J. H., Hwangbo, Y. & Shim, H. S. (2010). Plastic deformation behaviour of Cu thin films during fatigue testing. *Procedia Engineering* 2 (1), pp. 1421-1430.

Knothe, K. & Le The, H. (1984). A contribution to the calculation of the contact stress distribution between two elastic bodies of revolution with non-elliptical contact area. *Computers & Structures* 18 (6), pp. 1025-1033.

References

Koo, G. H. & Lee, J. H. (2007). Investigation of ratcheting characteristics of modified 9Cr–1Mo steel by using the Chaboche constitutive model. *International Journal of Pressure Vessels and Piping* 84 (5), pp. 284-292.

Kolasangiani, K., Farhangdoost, K., Shariati, M. & Varvani-Farahani, A. (2018). Ratcheting assessment of notched steel samples subjected to asymmetric loading cycles through coupled kinematic hardening-Neuber rules. *International Journal of Mechanical Sciences* 144, pp. 24-32.

Krauss, G. (1992). Microstructure and transformation in steels. In: *Material Science & Technology: A Comprehensive Treatment*, Edited by Cahn, R.W., Haasen, P. & Kramer, E.J., pp. 1-40, VCH-Wiley, Weinheim, Germany.

Krishna, S., Hassan, T., Naceur, I. B., Saï, K. & Cailletaud, G. (2009). Macro versus micro-scale constitutive models in simulating proportional and nonproportional cyclic and ratcheting responses of stainless steel 304. *International Journal of Plasticity* 25 (10), pp. 1910-1949.

Kuchuk-Yatsenko, S. I., Didkovsky, A. V., Shvets, V. I., Antipin, E. V., Wojtas, P. & Kozłowski, A. (2016). Flash-butt welding of high-strength rails. *Mining–Informatics, Automation and Electrical Engineering* 54, pp. 40-49.

Kulkarni, S. M., Hahn, G. T., Rubin, C. A. & Bhargava, V. (1990). Elastoplastic finite element analysis of three-dimensional, pure rolling contact at the shakedown limit. *Journal of Applied Mechanics* 57, pp. 57-65.

Kulkarni, S. M., Hahn, G. T., Rubin, C. A. & Bhargava, V. (1991a). Elastoplastic finite element analysis of three-dimensional, pure rolling contact above the shakedown limit. *Journal of Applied Mechanics* 58, pp. 347-353.

Kulkarni, S. M., Hahn, G. T., Rubin, C. A. & Bhargava, V. (1991b). Elastoplastic finite element analysis of repeated three-dimensional, elliptical rolling contact with rail wheel properties. *Journal of Tribology* 113, pp. 434-441.

Kuroda, T., Ikeuchi, K. & Ikeda, H. (2006). Flash butt resistance welding for duplex stainless steels. *Vacuum* 80 (11-12), pp. 1331-1335.

References

Lai, Q., Abrahams, R., Yan, W., Qiu, C., Mutton, P., Paradowska, A., Soodi, M. & Wu, X. (2018). Effects of preheating and carbon dilution on material characteristics of laser-cladded hypereutectoid rail steels. *Materials Science and Engineering: A* 712, 548-563.

Lai, Q., Abrahams, R., Yan, W., Qiu, C., Mutton, P., Paradowska, A., Soodi, M. & Wu, X. (2019). Influences of depositing materials, processing parameters and heating conditions on material characteristics of laser-cladded hypereutectoid rails. *Journal of Materials Processing Technology* 263, pp. 1-20.

Lee, C. H., Van Do, V. N. & Chang, K. H. (2014). Analysis of uniaxial ratcheting behaviour and cyclic mean stress relaxation of a duplex stainless steel. *International Journal of Plasticity* 62, pp. 17-33.

Lewis, R., Christoforou, P., Wang, W. J., Beagles, A., Burstow, M. & Lewis, S. R. (2019). Investigation of the influence of rail hardness on the wear of rail and wheel materials under dry conditions (ICRI wear mapping project). *Wear* 430, pp. 383-392.

Lewis, R., Evans, G. & Buckley-Johnstone, L. E. (2014). Assessment of railway curve lubricant performance using a twin-disc tester. *Wear* 314 (1-2), pp. 205-212.

Lewis, R., & Dwyer-Joyce, R. S. (2004). Wear mechanisms and transitions in railway wheel steels. In: *Proceedings of the Institution of Mechanical Engineers, Part J: Journal of Engineering Tribology* 218 (6), pp. 467-478.

Lewis, R. & Dwyer-Joyce, R. S. (2006). Wear at the wheel/rail interface when sanding is used to increase adhesion. In: *Proceedings of the Institution of Mechanical Engineers, Part F: Journal of Rail and Rapid Transit* 220 (1), pp. 29-41.

Lewis, R. & Dwyer-Joyce, R. S. (2009). Effect of contaminants on wear, fatigue and traction. In: *Wheel–rail interface handbook*, edited by Lewis, R. & Olofsson, U., pp. 437-455, Woodhead Publishing, Cambridge, UK, ISBN 978-1-84569-110-3.

Lewis, S. R., Lewis, R. & Fletcher, D. I. (2015). Assessment of laser cladding as an option for repairing/enhancing rails. *Wear* 330, pp. 581-591.

Lewis, R., Magel, E., Wang, W. J., Olofsson, U., Lewis, S., Slatter, T. & Beagles, A. (2017). Towards a standard approach for the wear testing of wheel and rail materials.

In: *Proceedings of the Institution of Mechanical Engineers, Part F: Journal of Rail and Rapid Transit* 231 (7), pp. 760-774.

Lewis, R. & Olofsson, U. (2004). Mapping rail wear regimes and transitions. *Wear* 257 (7-8), pp. 721-729.

Lewis, R. & Olofsson, U. (2009). Basic tribology of the wheel–rail contact. In: *Wheel–rail interface handbook*, edited by Lewis, R. & Olofsson, U., pp. 34-57, Woodhead Publishing, Cambridge, UK, ISBN 978-1-84569-110-3.

Lewis, S. R., Lewis, R., Olofsson, U., Eadie, D. T., Cotter, J. & Lu, X. (2013). Effect of humidity, temperature and railhead contamination on the performance of friction modifiers: Pin-on-disk study. In: *Proceedings of the Institution of Mechanical Engineers, Part F: Journal of Rail and Rapid Transit* 227 (2), pp. 115-127.

Li, W., Xiao, G., Wen, Z., Xiao, X. & Jin, X. (2011). Plastic deformation of curved rail at rail weld caused by train–track dynamic interaction. *Wear* 271 (1-2), pp. 311-318.

Li, Z. (2009). Squats on railway rails. In: *Wheel–rail interface handbook*, edited by Lewis, R. & Olofsson, U., pp. 409-436, Woodhead Publishing, Cambridge, UK, ISBN 978-1-84569-110-3.

Li, Z., Zhao, X., Esveld, C., Dollevoet, R. & Molodova, M. (2008a). An investigation into the causes of squats—Correlation analysis and numerical modelling. *Wear* 265 (9-10), pp. 1349-1355.

Li, Z., Zhao, X., Dollevoet, R. & Molodova, M. (2008b). Differential wear and plastic deformation as causes of squat at track local stiffness change combined with other track short defects. *Vehicle System Dynamics* 46 (S1), pp. 237-246.

Li, Z., Zhao, X., Esveld, C. & Dollevoet, R. (2006). Causes of squats: correlation analysis and numerical modeling. In: *Proceedings of the 7th International Conference on Contact Mechanics and Wear of Rail/Wheel Systems (CM2006)*, pp. 439-446, Brisbane, Queensland, Australia.

Lim, C. B., Kim, K. S. & Seong, J. B. (2009). Ratcheting and fatigue behaviour of a copper alloy under uniaxial cyclic loading with mean stress. *International Journal of*

Fatigue 31 (3), pp. 501-507.

Linder, C. (1997). Verschleiss von Eisenbahnradern mit Unrundheiten. Dissertation ETH Zurich Nr. 12342.

Lyu, Y., Zhu, Y. & Olofsson, U. (2015). Wear between wheel and rail: A pin-on-disc study of environmental conditions and iron oxides. *Wear* 328, pp. 277-285.

Lu, L., Wang, X., Gao, Z. & Jiang, Y. (2011). Influence of the contact pressure on rolling contact fatigue initiation of 1070 steel. *Procedia Engineering* 10, pp. 3000-3005.

Lu, P., Xu, Z., Jiang, K., Ma, F. & Shu, Y. (2017). Influence of flash butt welding parameters on microstructure and mechanical properties of HSLA 590CL welded joints in wheel rims. *Journal of Materials Research* 32 (4), pp. 831-842.

Lundén, R. & Paulsson, B. (2009). Introduction to wheel–rail interface research. In: *Wheel–rail interface handbook*, edited by Lewis, R. & Olofsson, U., pp. 3-33, Woodhead Publishing, Cambridge, UK, ISBN 978-1-84569-110-3.

Luo, H., Kang, G., Kan, Q. & Huang, Y. (2017). Experimental investigation on the heterogeneous ratcheting of SUS301L stainless steel butt weld joint during uniaxial cyclic loading. *International Journal of Fatigue* 105, pp. 169-179.

Luo, H., Kang, G., Kan, Q. & Ma, C. (2020). Experimental study on the whole-life heterogeneous ratcheting and ratcheting-fatigue interaction of SUS301L stainless steel butt-welded joint. *Fatigue & Fracture of Engineering Materials & Structures* 43 (1), pp. 36-50.

Ma, L., He, C. G., Zhao, X. J., Guo, J., Zhu, Y., Wang, W. J., Liu, Q. Y. & Jin, X. S. (2016). Study on wear and rolling contact fatigue behaviours of wheel/rail materials under different slip ratio conditions. *Wear* 366, pp. 13-26.

Ma, L., Shi, L. B., Guo, J., Liu, Q. Y. & Wang, W. J. (2018). On the wear and damage characteristics of rail material under low temperature environment condition. *Wear* 394, pp. 149-158.

Ma, N., Cai, Z., Huang, H., Deng, D., Murakawa, H. & Pan, J. (2015). Investigation of

welding residual stress in flash-butt joint of U71Mn rail steel by numerical simulation and experiment. *Materials & Design* 88, pp. 1296-1309.

Magel, E. E. (2017). A survey of wheel/rail friction (No. DOT/FRA/ORD-17/21). Office of Research, Development and Technology, Federal Railroad Administration, United States.

Mansouri, H. & Monshi, A. (2004). Microstructure and residual stress variations in weld zone of flash-butt welded railroads. *Science and Technology of Welding and Joining* 9 (3), pp. 237-245.

Marich, S. (2009). Managing the wheel–rail interface: the Australian experience. In: *Wheel–rail interface handbook*, edited by Lewis, R. & Olofsson, U., pp. 759–791, Woodhead Publishing, Cambridge, UK, ISBN 978-1-84569-110-3.

Martua, L., Ng, A. K. & Sun, G. (2018). Prediction of rail rolling contact fatigue crack initiation life via three-dimensional finite element analysis. In: *Proceedings of the International Conference on Intelligent Rail Transportation (ICIRT)*, pp. 1-5, IEEE.

McDowell, D. L. (1995). Stress state dependence of cyclic ratcheting behaviour of two rail steels. *International Journal of Plasticity* 11 (4), pp. 397-421.

Meymand, S. Z., Keylin, A. & Ahmadian, M. (2016). A survey of wheel–rail contact models for rail vehicles. *Vehicle System Dynamics* 54 (3), pp. 386-428.

Micenko, P. & Li, H. (2013). Double dip hardness profiles in rail weld heat-affected zone: literature and research review report. *Brisbane: CRC for Rail Innovation*.

Mizuno, M., Mima, Y., Abdel-Karim, M. & Ohno, N. (2000). Uniaxial ratcheting of 316FR steel at room temperature—Part I: experiments. *Journal of Engineering Materials and Technology* 122 (1), pp. 29-34.

Molodova, M., Li, Z., Núñez, A. & Dollevoet, R. (2014). Validation of a finite element model for axle box acceleration at squats in the high frequency range. *Computers & Structures* 141, pp. 84-93.

Mroz, Z. (1967). On the description of anisotropic work hardening. *Journal of the*

Mechanics and Physics of Solids 15 (3), pp. 163-175.

Mutton, P., Cookson, J. & Chiu, W. (2011). Fatigue behaviour of flash butt welds in high strength, eutectoid and hypereutectoid rail steels under high axle loads. In: *Proceedings of the 9th International Heavy Haul Association Conference*, pp. 1-8, Calgary, Canada.

Mutton, P., Cookson, J., Qiu, C. & Welsby, D. (2016). Microstructural characterisation of rolling contact fatigue damage in flash butt welds. *Wear* 366, pp. 368-377.

Mutton, P., Jeffs. T. (1992). Towards improving the performance of wail welds. In: *Proceedings of the 9th International Rail Track Conference*, Perth, Australia.

Mutton, P., Tan, M., Bartle, P. & Kapoor, A. (2009a). The effect of severe head wear on rolling contact fatigue in heavy haul operations. In: *Proceedings of the 8th International Conference on Contact Mechanics and Wear of Wheel/Rail Systems (CM2009)*, Firenze, Italy.

Mutton, P., Welsby, D. & Alvarez, E. (2009b). Wear and rolling contact fatigue behaviour of heat-treated eutectoid and hypereutectoid rail steel under high axle load conditions. In: *Proceedings of the 8th International Conference on Contact Mechanics and Wear of Wheel/Rail Systems (CM2009)*, Firenze, Italy.

Mutton, P., Welsby, D., Cookson, J. & Qiu, C. (2015). On the behaviour of rail welds under high axle loads. In: *Proceedings of the 10th International Conference on Contact Mechanics and Wear of Wheel/Rail Systems (CM2015)*, Colorado Springs, Colorado, USA.

Nackenhorst, U. (2004). The ALE-formulation of bodies in rolling contact: Theoretical foundations and finite element approach. *Computer Methods in Applied Mechanics and Engineering* 193 (39-41), pp. 4299-4322.

Nakata, T. & Tanigawa, H. (2012). Evaluation of local deformation behaviour accompanying fatigue damage in F82H welded joint specimens by using digital image correlation. *Fusion Engineering and Design* 87 (5-6), pp. 589-593.

Nilsson, R. (2005). On Wear in Rolling/Sliding Contacts. PhD thesis, KTH Royal

Institute of Technology, Stockholm, Sweden.

Ohno, N. (1982). A constitutive model of cyclic plasticity with a nonhardening strain region. *Journal of Applied Mechanics* 49, pp. 721-727.

Ohno, N. & Wang, J. D. (1993a). Kinematic hardening rules with critical state of dynamic recovery, part I: formulation and basic features for ratcheting behaviour. *International Journal of Plasticity* 9 (3), pp. 375-390.

Ohno, N. & Wang, J. D. (1993b). Kinematic hardening rules with critical state of dynamic recovery, Part II: application to experiments of ratchetting behaviour. *International Journal of Plasticity* 9 (3), pp. 391-403.

Ohno, N. & Wang, J. D. (1994). Kinematic hardening rules for simulation of ratcheting behaviour. *European Journal of Mechanics. A. Solids* 13 (4), pp. 519-531.

Olivares, R. O., Garcia, C. I., DeArdo, A., Kalay, S. & Hernández, F. R. (2011). Advanced metallurgical alloy design and thermomechanical processing for rails steels for North American heavy haul use. *Wear* 271 (1-2), pp. 364-373.

Olofsson, U. (2009). Adhesion and friction modification. In: *Wheel–rail interface handbook*, edited by Lewis, R. & Olofsson, U., pp. 510-527, Woodhead Publishing, Cambridge, UK, ISBN 978-1-84569-110-3.

Olofsson, U. & Telliskivi, T. (2003). Wear, plastic deformation and friction of two rail steels—a full-scale test and a laboratory study. *Wear* 254 (1-2), pp. 80-93.

Ozakgul, K., Piroglu, F. & Caglayan, O. (2015). An experimental investigation on flash butt welded rails. *Engineering Failure Analysis* 57, pp. 21-30.

Özdemir, Y. & Voltr, P. (2017). Analysis of wheel–rail contact under partial slip and low speed conditions. *Mechanics* 23 (1), pp. 5-10.

Pan, R., Ren, R., Chen, C. & Zhao, X. (2017). The microstructure analysis of white etching layer on treads of rails. *Engineering Failure Analysis* 82, pp. 39-46.

PANDROL. Retrieved from https://www.pandrol.com/product/aluminothermic-

welding-kit/.

Pang, T. & Dhanasekar, M. (2006). Dynamic finite element analysis of the wheel–rail interaction adjacent to the insulated rail joints. In: *Proceedings of the 7th international conference on contact mechanics and wear of rail/wheel systems (CM2006)* 2, pp. 509-516, Brisbane, Queensland, Australia.

Papadopoulos, I. V., Davoli, P., Gorla, C., Filippini, M. & Bernasconi, A. (1997). A comparative study of multiaxial high-cycle fatigue criteria for metals. *International Journal of Fatigue*, 19 (3), pp. 219-235.

Parker, R. (2002). The influence of composition on the microstructural response and mechanical properties of heat-affected zones of welds in pearlitic rail steels. Final Year Project Report, Department of Materials Engineering, Monash University.

Pascal, J. P. & Sauvage, G. (1992). New method for reducing the multi-contact wheel/rail problem to one equivalent contact patch. *Vehicle System Dynamics* 20 (sup1), pp. 475-489.

Pavlina, E. J. & Van Tyne, C. J. (2008). Correlation of yield strength and tensile strength with hardness for steels. *Journal of Materials Engineering and Performance* 17 (6), pp. 888-893.

Peters, W. H. & Ranson, W. F. (1982). Digital imaging techniques in experimental stress analysis. *Optical Engineering* 21 (3), 213427.

Pickering, F. B. (1992). Structure–property relationships in steels/high strength low alloy steels. In: *Materials Science & Technology: A Comprehensive Treatment*, edited by Cahn, R. W., Haasen, P. & Kramer. E. J., 2 (7), pp. 41-44, VCH Wiley, Weinheim, Germany.

Piotrowski, J. & Chollet, H. (2005). Wheel–rail contact models for vehicle system dynamics including multi-point contact. *Vehicle System Dynamics* 43 (6-7), pp. 455-483.

Piotrowski, J. & Kik, W. (2008). A simplified model of wheel/rail contact mechanics for non-Hertzian problems and its application in rail vehicle dynamic simulations.

Vehicle System Dynamics 46 (1-2), pp. 27-48.

Pointner, P. (2008). High strength rail steels—The importance of material properties in contact mechanics problems. *Wear* 265 (9-10), pp. 1373-1379.

Polach, O. (1999). A fast wheel–rail forces calculation computer code. *Vehicle System Dynamics* 33 (sup1), pp. 728-739.

Ponter, A. R. S., Hearle, A. D. & Johnson, K. L. (1985). Application of the kinematical shakedown theorem to rolling and sliding point contacts. *Journal of the Mechanics and Physics of Solids* 33 (4), pp. 339-362.

Porcaro, R. R., Faria, G. L., Godefroid, L. B., Apolonio, G. R., Cândido, L. C. & Pinto, E. S. (2019). Microstructure and mechanical properties of a flash butt welded pearlitic rail. *Journal of Materials Processing Technology* 270, pp. 20-27.

Portier, L., Calloch, S., Marquis, D. & Geyer, P. (2000). Ratcheting under tension–torsion loadings: experiments and modelling. *International Journal of Plasticity* 16 (3-4), pp. 303-335.

Pun, C. L., Kan, Q., Mutton, P. J., Kang, G. Z. & Yan, W. Y. (2014a). On constitutive models for ratcheting of a high strength rail steel. In: *Advanced Materials Research* 891, pp. 1146-1151, Trans Tech Publications Ltd.

Pun, C. L., Kan, Q., Mutton, PF. J., Kang, G. & Yan, W. (2014b). Ratcheting behaviour of high strength rail steels under biaxial compression–torsion loadings: experiment and simulation. *International Journal of Fatigue* 66, pp. 138-154.

Pun, C. L., Kan, Q., Mutton, P. J., Kang, G. & Yan, W. (2015a). An efficient computational approach to evaluate the ratcheting performance of rail steels under cyclic rolling contact in service. *International Journal of Mechanical Sciences* 101, pp. 214-226.

Pun, C. L., Kim, C. S., Mutton, P. J. & Yan, W. (2015b). Microstructural characterisation of high strength rail steels. In: *Proceedings of the 10th International Conference on Contact Mechanics and Wear of Wheel/Rail Systems (CM2015)*, Colorado Springs, Colorado, USA.

Pun, C. L., Welsby, D., Mutton, P. & Yan, W. (2017). Rolling contact fatigue life predictions for rails and welds in heavy haul. In: *Proceedings of the 12th International Heavy Haul Association Conference*, edited by Grabe, P. J. & Fröhling, R.D., pp. 56-62, Cape Town, South Africa.

Ranjha, S. A., Ding, K., Mutton, P. J. & Kapoor, A. (2012). Finite element modelling of the rail gauge corner and underhead radius stresses under heavy axle load conditions. In: *Proceedings of the Institution of Mechanical Engineers, Part F: Journal of Rail and Rapid Transit* 226 (3), pp. 318-330.

Ringsberg, J. W. (2001). Life prediction of rolling contact fatigue crack initiation. *International Journal of fatigue* 23 (7), pp. 575-586.

Ringsberg, J. W., Bjarnehed, H., Johansson, A. & Josefson, B. L. (2000a). Rolling contact fatigue of rails—finite element modelling of residual stresses, strains and crack initiation. In: *Proceedings of the Institution of Mechanical Engineers, Part F: Journal of Rail and Rapid Transit* 214 (1), pp. 7-19.

Ringsberg, J. W., Loo-Morrey, M., Josefson, B. L., Kapoor, A. & Beynon, J. H. (2000b). Prediction of fatigue crack initiation for rolling contact fatigue. *International Journal of fatigue* 22 (3), pp. 205-215.

Ringsber, J. W. & Josefson, B. L. (2001). Finite element analyses of rolling contact fatigue crack initiation in railheads. In: *Proceedings of the Institution of Mechanical Engineers, Part F: Journal of Rail and Rapid Transit* 215 (4), pp. 243-259.

Roy, T., Lai, Q., Abrahams, R., Mutton, P., Paradowska, A., Soodi, M. & Yan, W. (2018). Effect of deposition material and heat treatment on wear and rolling contact fatigue of laser cladded rails. *Wear* 412, pp. 69-81.

Ruggles, M. B. & Krempl, E. (1990). The interaction of cyclic hardening and ratcheting for AISI type 304 stainless steel at room temperature—I. Experiments. *Journal of the Mechanics and Physics of Solids* 38 (4), pp. 575-585.

Saita, K., Karimine, K., Ueda, M., Iwano, K., Yamamoto, T. & Hiroguchi, K. (2013). Trends in rail welding technologies and our future approach. *Nippon Steel & Sumitomo*

Metal Technical Report 105, pp. 84-92.

Saita, K., Ueda, M., Miyazaki, T. & Yamamoto, T. (2017). Developing technologies to improve the reliability of flash-butt welds. In: *Proceedings of the 12th International Heavy Haul Association Conference*, edited by Grabe, P. J. & Fröhling, R.D., pp. 208-215, Cape Town, South Africa.

Satoh, Y. & Iwafuchi, K. (2008). Effect of rail grinding on rolling contact fatigue in railway rail used in conventional line in Japan. *Wear* 265 (9-10), pp. 1342-1348.

Satyadevi, A., Sivakumar, S. M. & Bhattacharya, S. S. (2007). A new failure criterion for materials exhibiting ratcheting during very low cycle fatigue. *Materials Science and Engineering: A* 452, pp. 380-385.

Sichani, M. & Bezin, Y. (2018). Differential wear modelling–Effect of weld-induced material inhomogeneity on rail surface quality. *Wear* 406, pp. 43-52.

Sichani, M., Enblom, R. & Berg, M. (2014). A novel method to model wheel–rail normal contact in vehicle dynamics simulation. *Vehicle System Dynamics* 52 (12), pp. 1752-1764.

Sichani, M., Enblom, R. & Berg, M. (2016). An alternative to FASTSIM for tangential solution of the wheel–rail contact. *Vehicle System Dynamics* 54 (6), pp. 748-764.

Shur, E. A., Bychkova, N. Y. & Trushevsky, S. M. (2005). Physical metallurgy aspects of rolling contact fatigue of rail steels. *Wear* 258 (7-8), pp. 1165-1171.

Skyttebol, A., Josefson, B. L. & Ringsberg, J. W. (2005). Fatigue crack growth in a welded rail under the influence of residual stresses. *Engineering Fracture Mechanics* 72 (2), pp. 271-285.

Sladkowski, A. & Sitarz, M. (2005). Analysis of wheel–rail interaction using FE software. *Wear* 258 (7-8), pp. 1217-1223.

Smith, K.N., Watson, P. & Topper, T.H. (1970). A stress-strain function for the fatigue of metals. *Journal of Materials* 5, pp. 767-778.

References

Spiryagin, M., Polach, O. & Cole, C. (2013). Creep force modelling for rail traction vehicles based on the Fastsim algorithm. *Vehicle System Dynamics* 51 (11), pp. 1765-1783.

Spiryagin, M., Sajjad, M., Nielsen, D., Sun, Y. Q., Raman, D. & Chattopadhyay, G. (2014). Research methodology for evaluation of top-of-rail friction management in Australian heavy haul networks. In: *Proceedings of the Institution of Mechanical Engineers, Part F: Journal of Rail and Rapid Transit* 228 (6), pp. 631-641.

Srivastava, J. P., Kiran, M. R., Sarkar, P. K. & Ranjan, V. (2017). Numerical investigation of ratchetting behaviour in rail steel under cyclic rolling-sliding Contact. *Procedia Engineering* 173, pp. 1130-1137.

Sroba, P., Oldknow, K., Dashko, R. & Roney, M. (2005). Canadian Pacific Railway 100% effective friction management strategy. In: *Proceedings of the 8th International Heavy Haul Conference*, pp. 93-102, Rio de Janeiro, Brazil.

Stanford, J., Magel, E. & Scroba, P. (2001). Transitioning from corrective to preventive rail grinding on the BNSF railroad. In: *Proceedings of the 7th International Heavy Haul Conference*, pp. 493-501, Brisbane, Australia.

Steenbergen, M. J. M.M. (2006). Modelling of wheels and rail discontinuities in dynamic wheel–rail contact analysis. *Vehicle System Dynamics* 44 (10), 763-787.

Steenbergen, M. J. M.M. (2008). Quantification of dynamic wheel–rail contact forces at short rail irregularities and application to measured rail welds. *Journal of Sound and Vibration* 312 (4-5), 606-629.

Steenbergen, M.J.M.M. (2015). Squat formation and rolling contact fatigue in curved rail track. *Engineering Fracture Mechanics* 143, pp. 80-96.

Steenbergen, M.J.M.M. (2016). Rolling contact fatigue in relation to rail grinding. *Wear* 356, pp. 110-121.

Steenbergen, M. J. M. M. & Esveld, C. (2006). Relation between the geometry of rail welds and the dynamic wheel–rail response: numerical simulations for measured welds. In: *Proceedings of the Institution of Mechanical Engineers, Part F: Journal of Rail and*

Rapid Transit 220 (4), pp. 409-423.

Steenbergen, M.J.M.M. & Van Bezooijen, R.W. (2009). Rail welds. In: *Wheel–rail interface handbook*, edited by Lewis, R. & Olofsson, U., pp. 377-408, Woodhead Publishing, Cambridge, UK, ISBN 978-1-84569-110-3.

Stephens, R.I., Fatemi, A., Stephens, R.R. & Fuchs H.O. (2001). Metal fatigue in engineering, Second ed., John Wiley and Sons, New York, USA.

Stock, R., Eadie, D. T., Elvidge, D. & Oldknow, K. (2011). Influencing rolling contact fatigue through top of rail friction modifier application–A full scale wheel–rail test rig study. *Wear* 271 (1-2), pp. 134-142.

Stock, R. & Pippan, R. (2011). RCF and wear in theory and practice—the influence of rail grade on wear and RCF. *Wear* 271 (1-2), pp. 125-133.

Su, X. & Clayton, P. (1997). Ratcheting strain experiments with a pearlitic steel under rolling/sliding contact. *Wear* 205 (1-2), pp. 137–143.

Sunwoo, H., Fine, M. E., Meshii, M. & Stone, D. H. (1982). Cyclic deformation of pearlitic eutectoid rail steel. *Metallurgical Transactions A* 13 (11), pp. 2035-2047.

Szablewski, D., Kalay, S. & LoPresti, J. (2011). Development and evaluation of high-performance rail steels for heavy haul operations. In: *Proceedings of the 9th International Heavy Haul Association Conference*, pp. 19-22, Calgary, Canada.

Szablewski, D. & LoPresti, J. (2014). Performance of Improved Rail Steels Under Heavy-axle-loads at FAST. *Railway Track and Structures* 110 (6), pp. 12-14.

Taleb, L. & Cailletaud, G. (2010). An updated version of the multi-mechanism model for cyclic plasticity. *International Journal of Plasticity* 26 (6), pp. 859-874.

Tanaka, E. (1994). A nonproportionality parameter and a cyclic viscoplastic constitutive model taking into account amplitude dependences and memory effects of isotropic hardening. *European Journal of Mechanics. A. Solids* 13 (2), pp. 155-173.

Tao, G., Wen, Z., Zhao, X. & Jin, X. (2016). Effects of wheel–rail contact modelling

on wheel wear simulation. *Wear* 366, pp. 146-156.

Tawfik, D., Mutton, P. J. & Chiu, W. K. (2005). The effects of short-term post-weld heat treatments on residual stresses in flash butt welds. In: *Proceedings of the 6th International Heavy Haul Association Conference*, pp. 653-658, Cape Town, South Africa.

Tawfik, D., Kirstein, O., Mutton, P. J. & Chiu, W. K. (2006). Verification of residual stresses in flash-butt-weld rails using neutron diffraction. *Physica B: Condensed Matter* 385, pp. 894-896.

Tawfik, D., Mutton, P. J. & Chiu, W. K. (2008). Experimental and numerical investigations: Alleviating tensile residual stresses in flash butt welds by localised rapid post-weld heat treatment. *Journal of Materials Processing Technology* 196 (1-3), pp. 279-291.

Telliskivi, T. & Olofsson, U. (2004). Wheel–rail wear simulation. *Wear* 257 (11), pp. 1145-1153.

Tokaji, K., Horie, T. & Enomoto, Y. (2006). Effects of microstructure and carbide spheroidisation on fatigue behaviour in high V-Cr-Ni cast irons. *International Journal of Fatigue* 28 (3), pp. 281-288.

Tomeoka, M., Kabe, N., Tanimoto, M., Miyauchi, E. & Nakata, M. (2002). Friction control between wheel and rail by means of on-board lubrication. *Wear* 253 (1-2), pp. 124-129.

Tyfour, W. R., Beynon, J. H. & Kapoor, A. (1995). The steady state wear behaviour of pearlitic rail steel under dry rolling-sliding contact conditions. *Wear* 180 (1-2), pp. 79-89.

Tyfour, W. R., Beynon, J. H. & Kapoor, A. (1996). Deterioration of rolling contact fatigue life of pearlitic rail steel due to dry-wet rolling-sliding line contact. *Wear* 197 (1-2), pp. 255-265.

Uchino, K., Ueda, M., Kutaragi, K. & Babazono, K. (1997). Development of hypereutectoid steel rail for heavy haul railways. In*: Proceedings of the 4th*

References

International Symposium on 'Rail Steels' as part of the 39th International Symposium on 'Mechanical Working and Steel Processing', pp. 1047-1056, Indianapolis, IN, USA, Iron & Steel Society, Warrender, PA, USA & Association of American Railroads, Washington DC, USA.

Ueda, M., Iwano, K. & Yamamoto, T. (2011). Rail Performance and Recent Developments of Rail. In: *Proceedings of the 9th International Heavy Haul Association Conference*, Calgary, Canada.

Ueda, M. & Matsuda, K. (2020). Effects of carbon content and hardness on rolling contact fatigue resistance in heavily loaded pearlitic rail steels. *Wear* 444, 203120.

Ueda, M., Matsushita, K., Iwano, K., Kobayashi, A., Miyazaki, T. Y. T., Takahashi, J. & Kobayashi, Y. (2013). Development of Long Life Rail for Overseas Freight Railways. *Nippon Steel Technical Report* 395, pp. 64-72.

Vermeulen, P. J. & Johnson, K. L. (1964). Contact of non-spherical elastic bodies transmitting tangential forces. *Journal of Applied Mechanics* 31, pp. 339-346.

Vo, K. D., Tieu, A. K., Zhu, H. T. & Kosasih, P. B. (2014). A 3D dynamic model to investigate wheel–rail contact under high and low adhesion. *International Journal of Mechanical Sciences* 85, pp. 63-75.

Vo, K. D., Zhu, H. T., Tieu, A. K. & Kosasih, P. B. (2015). FE method to predict damage formation on curved track for various worn status of wheel/rail profiles. *Wear* 322, pp. 61-75.

Voyiadjis, G. Z. & Basuroychowdhury, I. N. (1998). A plasticity model for multiaxial cyclic loading and ratcheting. *Acta Mechanica* 126 (1-4), pp. 19-35.

Wang, W. J., Lewis, R., Beagles, A., He, C. G. & Liu, Q. Y. (2017a). The role of slip ratio in rolling contact fatigue of rail materials under wet conditions. *Wear* 376, pp. 1892-1900.

Wang, W. J., Lewis, R., Evans, M. D. & Liu, Q. Y. (2017b). Influence of different application of lubricants on wear and pre-existing rolling contact fatigue cracks of rail materials. *Tribology Letters* 65 (2), pp. 1-15.

Wang, W. J., Lewis, R., Yang, B., Guo, L. C., Liu, Q. Y. & Zhu, M. H. (2016). Wear and damage transitions of wheel and rail materials under various contact conditions. *Wear* 362, pp. 146-152.

Wang, Q. & Liu, X. (2017). Non-saturated cyclic softening and uniaxial ratcheting of a high strength steel: Experiments and viscoplastic constitutive modelling. *Mechanics of Materials* 113, pp. 112-125.

Webster, P. J., Mills, G., Wang, X. D., Kang, W. P. & Holden, T. M. (1997). Residual stresses in aluminothermic welded rails. *The Journal of Strain Analysis for Engineering Design* 32 (6), pp. 389-400.

Wei, Z., Li, Z., Qian, Z., Chen, R. & Dollevoet, R. (2016). 3D FE modelling and validation of frictional contact with partial slip in compression-shift-rolling evolution. *International Journal of Rail Transportation* 4 (1), pp. 20-36.

Weingrill, L., Krutzler, J. & Enzinger, N. (2017). Temperature field evolution during flash butt welding of railway rails. In: *Materials Science Forum* 879, pp. 2088-2093, Trans Tech Publications Ltd.

Welsby, D. R., Pun, C. L. J., Mutton, P. J. & Yan, W. (2014). Rail performance and management of rolling contact fatigue under heavy axle load conditions. In: *Proceedings of the 2nd International Conference on Railway Technology: Research, Development and Maintenance*, Civil-Comp Press, Stirlingshire, Scotland.

Wen, Z., Jin, X. & Jiang, Y. (2005). Elastic-plastic finite element analysis of non-steady state partial slip wheel–rail rolling contact. *Journal of Tribology* 127, pp. 713-721.

Wen, Z., Wu, L., Li, W., Jin, X. & Zhu, M. (2011). Three-dimensional elastic-plastic stress analysis of wheel–rail rolling contact. *Wear* 271 (1-2), pp. 426-436.

Wen, Z., Xiao, G., Xiao, X., Jin, X. & Zhu, M. (2009). Dynamic vehicle–track interaction and plastic deformation of rail at rail welds. *Engineering Failure Analysis* 16 (4), pp. 1221-1237.

Wessels, L., Oswald, S., Welsby, D. & Mutton, P. (2015). Managing the transition from

rail wear to rolling contact fatigue in a heavy haul environment. In: *Proceedings of the 11th International Heavy Haul Association Conference*, Perth, Australia.

Wetscher, F., Stock, R. & Pippan, R. (2007). Changes in the mechanical properties of a pearlitic steel due to large shear deformation. *Materials Science and Engineering: A* 445, pp. 237-243.

Wimmer, W. E., Connell, D. A. & Boos, M. J. (2002). Joint elimination through mobile flash butt welding on Union Pacific Railroad. In: *Proceedings of Innotrans*, Berlin, Germany, 24-27 September.

Wöhnhart, A. & Wenty, R. (2002). Mobile flash-butt rail welding: three decades of experience. *Rail Engineering International* 3, pp. 11-16.

Wriggers, P. (2006). Constitutive equations for contact interfaces. In: *Computational contact mechanics*, pp. 69–108, Springer, Berlin, Heidelberg, ISBN 978-3-540-32608-3.

Wu, J., Petrov, R. H., Kölling, S., Koenraad, P., Malet, L., Godet, S. & Sietsma, J. (2018). Micro and nanoscale characterization of complex multilayer-structured white etching layer in rails. *Metals* 8 (10), pp. 749-766.

Wu, S. R. & Gu, L. (2012). Introduction to the explicit finite element method for nonlinear transient dynamics. John Wiley & Sons Inc. Somerset, United States.

Xi, C., Sun, D., Xuan, Z., Wang, J. & Song, G. (2016). Microstructures and mechanical properties of flash butt welded high strength steel joints. *Materials & Design* 96, pp. 506-514.

Xiong, Y., Yu, Q. & Jiang, Y. (2014). An experimental study of cyclic plastic deformation of extruded ZK60 magnesium alloy under uniaxial loading at room temperature. *International Journal of Plasticity* 53, pp. 107-124.

Xu, B. & Jiang, Y. (2002). Elastic-plastic finite element analysis of partial slip rolling contact. *Journal of Tribology* 124 (1), pp. 20-26.

Yaguchi, M. & Takahashi, Y. (2005). Ratcheting of viscoplastic material with cyclic

softening, part 1: experiments on modified 9Cr-1Mo steel. *International Journal of Plasticity* 21 (1), pp. 43-65.

Yan, S. H., Zhu, Z. Y., Ma, C. P., Su, L., Li, D., Chen, H. & Meng, L. C. (2011). Investigation on the Residual Stress Redistribution under Cyclic Loading. In: *Advanced Materials Research* 337, pp. 588-593. Trans. Tech. Publications Ltd.

Yan, W., Busso, E. P. & O'Dowd, N. P. (2000). A micromechanics investigation of sliding wear in coated components. In: *Proceedings of the Royal Society of London. Series A: Mathematical, Physical and Engineering Sciences* 456 (2002), pp. 2387-2407.

Yan, W. & Fischer, F. D. (2000). Applicability of the Hertz contact theory to rail-wheel contact problems. *Archive of Applied Mechanics* 70 (4), pp. 255-268.

Yang, Z., Deng, X. & Li, Z. (2019). Numerical modelling of dynamic frictional rolling contact with an explicit finite element method. *Tribology International* 129, pp. 214-231.

Yang, Z., Boogaard, A., Wei, Z., Liu, J., Dollevoet, R. & Li, Z. (2018). Numerical study of wheel–rail impact contact solutions at an insulated rail joint. *International Journal of Mechanical Sciences* 138, pp. 310-322.

Yang, Z., Deng, X. & Li, Z. (2019). Numerical modelling of dynamic frictional rolling contact with an explicit finite element method. *Tribology International* 129, pp. 214-231.

Yang, Z., Li, Z. & Dollevoet, R. (2016). Modelling of non-steady-state transition from single-point to two-point rolling contact. *Tribology International* 101, pp. 152-163.

Yu, D., Chen, G., Yu, W., Li, D. & Chen, X. (2012). Viscoplastic constitutive modelling on Ohno–Wang kinematic hardening rule for uniaxial ratcheting behaviour of Z2CND18.12N steel. *International Journal of Plasticity* 28 (1), pp. 88-101.

Yu, W., Liu, H., Jia, W., Fan, M., Shi, J., Xue, F. & Chen, X. (2019). Investigation of heterogeneous ratcheting of a GTAW welded joint for primary coolant piping. *Materials Testing* 61 (10), pp. 947-952.

References

Yu, X., Feng, L., Qin, S., Zhang, Y. & He, Y. (2015). Fracture analysis of U71Mn rail flash-butt welding joint. *Case Studies in Engineering Failure Analysis* 4, pp. 20-25.

Zaayman, L. (2007). Continuous welded rail using the mobile flash butt welding machine. *Civil Engineering Siviele Ingenieurswese* 2007 (v15i5), pp. 62-65.

Zerbst, U., Lundén, R., Edel, K. O. & Smith, R. A. (2009). Introduction to the damage tolerance behaviour of railway rails–a review. *Engineering fracture mechanics* 76 (17), pp. 2563-2601.

Zerbst, U., Mädler, K. & Hintze, H. (2005). Fracture mechanics in railway applications—an overview. *Engineering fracture mechanics* 72 (2), pp. 163-194.

Zhang, H., Hu, X. Y., Lin, F. T. & Zhou, X. J. (2014). Research on Finite Element Model of Wheel–rail Contact. In: *Applied Mechanics and Materials* 644, pp. 7-10, Trans Tech Publications Ltd.

Zhang, J., Sun, S. & Jin, X. (2009). Numerical simulation of two-point contact between wheel and rail. *Acta Mechanica Solida Sinica* 22 (4), pp. 352-359.

Zhang, J. & Jiang, Y. (2005). An experimental study of inhomogeneous cyclic plastic deformation of 1045 steel under multiaxial cyclic loading. *International Journal of Plasticity* 21 (11), pp. 2174-2190.

Zhang, Q., Li, L., Ding, W., Song, H. T. & Gao, Z. K. (2017). Investigation on process and welded joint mechanical properties of bainitic steel rail flash butt welding. In: *Key Engineering Materials* 723, pp. 406-411, Trans Tech Publications Ltd.

Zhao, X., Fan, Y., Liu, Y., Wang, H. & Dong, P. (2015). Evaluation of fatigue fracture mechanism in a flash butt welding joint of a U75V type steel for railroad applications. *Engineering Failure Analysis* 55, pp. 26-38.

Zhao, X. & Li, Z. (2011). The solution of frictional wheel–rail rolling contact with a 3D transient finite element model: Validation and error analysis. *Wear* 271 (1-2), pp. 444-452.

Zhao, X. & Li, Z. (2015). A three-dimensional finite element solution of frictional

wheel–rail rolling contact in elasto-plasticity. In: *Proceedings of the Institution of Mechanical Engineers, Part J: Journal of Engineering Tribology* 229 (1), pp. 86-100.

Zhao, X. & Li, Z. (2016). A solution of transient rolling contact with velocity dependent friction by the explicit finite element method. *Engineering Computations* 33 (4), pp. 1033-1050.

Zhao, X., Li, Z. & Dollevoet, R. (2013). The vertical and the longitudinal dynamic responses of the vehicle‐track system to squat-type short wavelength irregularity. *Vehicle System Dynamics* 51 (12), pp. 1918-1937.

Zhao, X., Li, Z., Esveld, C. & Dollevoet, R. (2007). The dynamic stress state of the wheel–rail contact. In: *Proceedings of the 2nd IASME/WSEAS International Conference on Continuum Mechanics*, pp. 127-133, Portoroz, Slovenia.

Zhong, W., Hu, J. J., Li, Z. B., Liu, Q. Y. & Zhou, Z. R. (2011a). A study of rolling contact fatigue crack growth in U75V and U71Mn rails. *Wear* 271 (1-2), pp. 388-392.

Zhong, W., Hu, J. J., Shen, P., Wang, C. Y. & Lius, Q. Y. (2011b). Experimental investigation between rolling contact fatigue and wear of high-speed and heavy-haul railway and selection of rail material. *Wear* 271 (9-10), pp. 2485-2493.

Zhou, Y., Wang, S., Wang, T., Xu, Y. & Li, Z. (2014). Field and laboratory investigation of the relationship between rail head check and wear in a heavy-haul railway. *Wear* 315 (1-2), pp. 68-77.

Zhu, Y., Chen, X., Wang, W. J. & Yang, H. (2015). A study on iron oxides and surface roughness in dry and wet wheel–rail contacts. *Wear* 328, pp. 241-248.

Zhu, Y., Olofsson, U. & Nilsson, R. (2014). A field test study of leaf contamination on railhead surfaces. In: *Proceedings of the Institution of Mechanical Engineers, Part F: Journal of Rail and Rapid Transit* 228 (1), pp. 71-84.

Zhu, Y., Sundh, J. & Olofsson, U. (2013). A tribological view of wheel–rail wear maps. *International Journal of Railway Technology* 2 (10), pp. 888-901.

References

Zhu, Y., Wang, W., Lewis, R., Yan, W., Lewis, S. R. & Ding, H. (2019). A review on wear between railway wheels and rails under environmental conditions. *Journal of Tribology* 141 (120801), pp. 1-13.

Ziemian, C. W., Sharma, M. M. & Whaley, D. E. (2012). Effects of flashing and upset sequences on microstructure, hardness, and tensile properties of welded structural steel joints. *Materials & Design* 33, pp. 175-184.

Appendix

Mesh Convergence Check

As demonstrated in the Chapters 5 and 6, the mesh at the contact region between the wheel and the rail FE models were refined to capture the high stress or strain and its gradient. In order to ensure that the numerical results were not influenced by the mesh and provided reasonable accuracy, a mesh convergence check was carried out before running the simulations. The corresponding detail is briefly illustrated in the following context.

A. Quasi-Static Wheel–Rail Weld Contact Simulations

Five different mesh sizes were considered in the fine mesh region and the entire rail model was assigned with a cyclic plasticity constitutive model for the PR or a single subzone of the weld material in each quasi-static simulation. Since 12 types of materials were defined in the cyclic plasticity constitutive model presented in Chapter 4, including ten for the subzones in the SZ, one for the BL section and one for the PR, 60 simulations in total were performed for the mesh convergence check. It should be noted that the mesh size in the fine mesh region of the wheel model was identical with that in the rail model. Fig. A presents the relationship between the maximum normal contact pressure and the mesh size for the PR and selected subzones of the weld region. The results clearly show that the maximum normal contact pressure for each rail material becomes converged when the mesh size is reduced to 1 mm. Therefore, 1 mm mesh size was used within the fine mesh region of the FE models without increasing the computational time significantly.

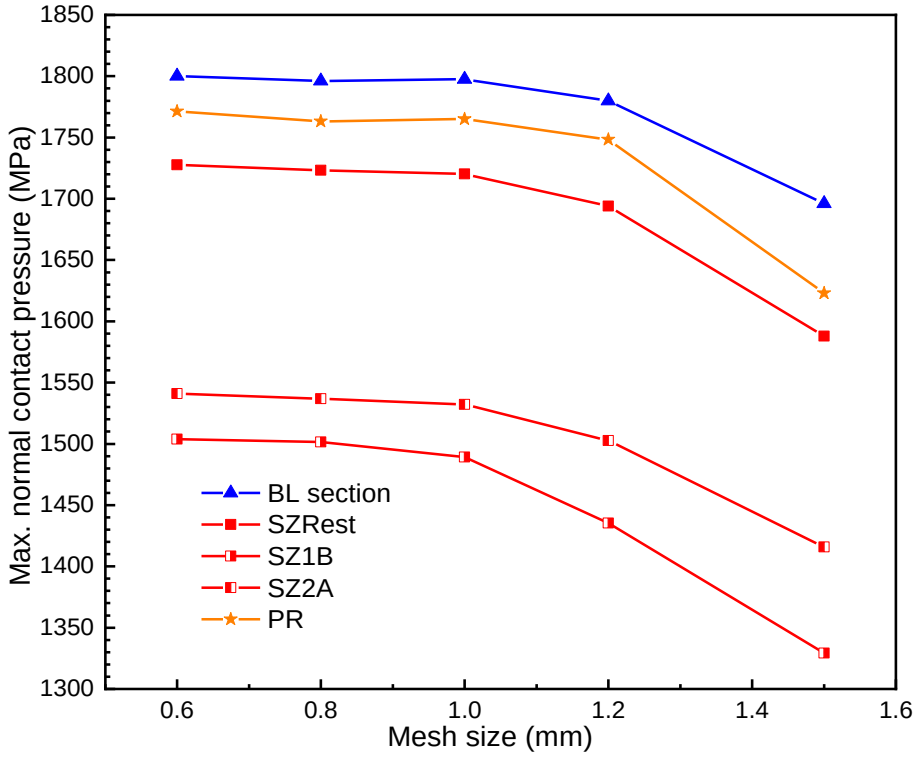

Figure A: The relationship between the maximum normal contact pressure and the mesh size for the PR and selected subzones of the weld region.

B. Cyclic Loading Simulation on Rail Weld

To ensure that 1 mm mesh size is fine enough to obtain the results of ratcheting with acceptable accuracy, a mesh convergence check was carried out by translating the normal contact pressure and longitudinal tangential traction distributions determined from the quasi-static simulations (see Chapter 5.3) for one loading cycle on the rail weld model with 0.5 mm mesh size. The obtained maximum ratcheting strain distribution $\varepsilon_{r,max}$ within the rail weld and the PR is compared with the 1st loading cycle of the maximum ratcheting strain distribution $\varepsilon_{r,max}$ determined from the rail model with 1 mm mesh (Fig. 5-19), which is demonstrated in Fig. B. It can be identified that the difference for the maximum ratcheting strain in most of the target sections by both rail models is less than 5% after the 1st loading cycle. This information indicates that 1 mm mesh size has the capability to capture the gradients of the ratcheting results within the PR and the weld region with reasonale accuracy.

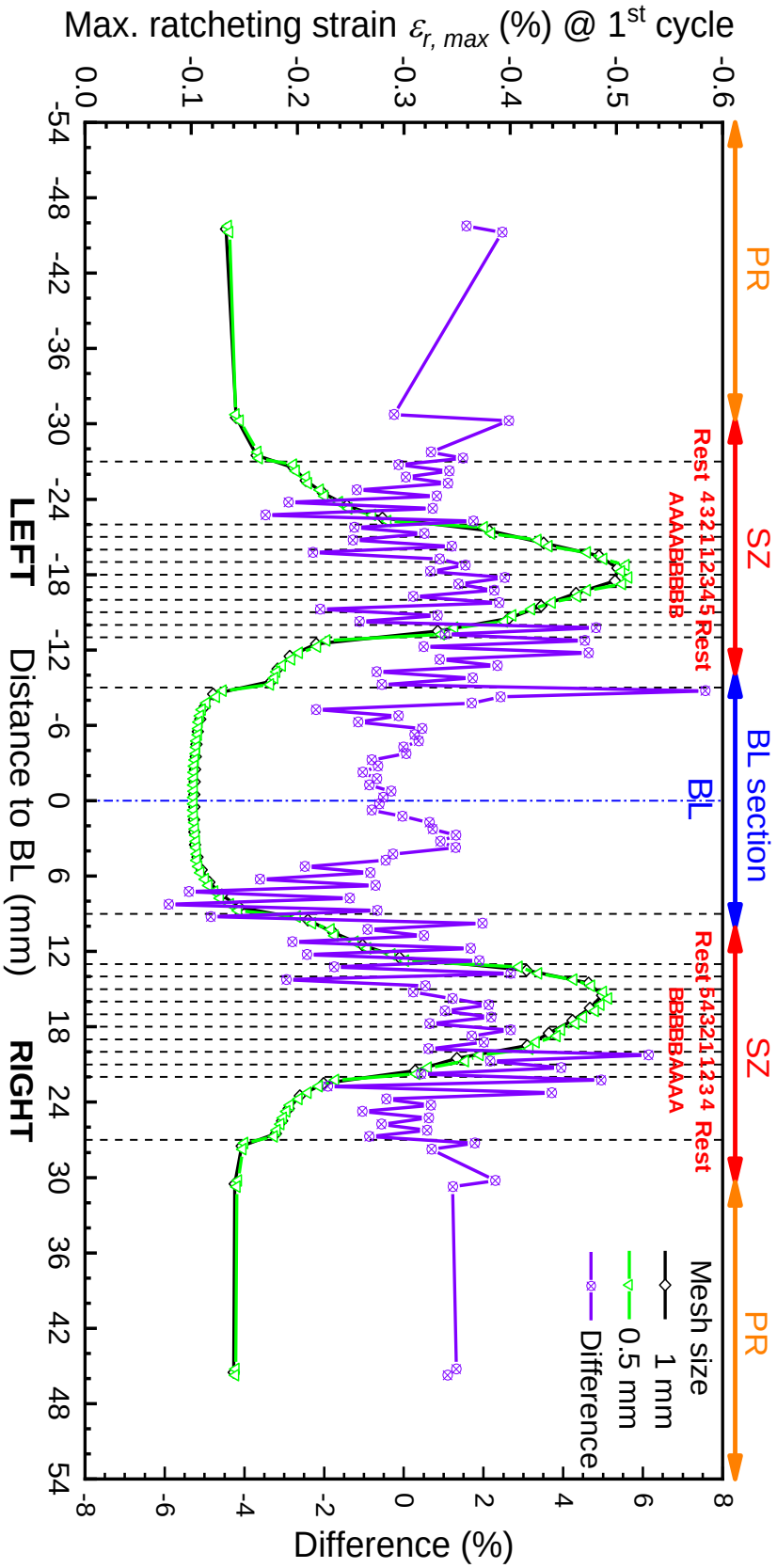

Figure B: Comparison of the difference for the maximum ratcheting strain distribution $\varepsilon_{r,max}$ at the 1st loading cycle. within the PR and the weld region by the rail models with different fine mesh sizes.

C. Quasi-Static Wheel–High Rail Contact Simulations

Similar to the procedure employed in the mesh convergence check for the quasi-static wheel–rail weld contact simulations, five different mesh sizes were considered in the fine mesh region of the wheel–high rail contact model to examine the influence of the mesh density on the normal contact pressure distrbution. Fig. C demonstrates the relationship between the maximum normal contact pressure and the mesh size for LAHT steel under the same loading condition presented in Fig. 6-3. The results reveal that the maxmium normal contact pressure at the top contact patch becomes converged when the mesh size is decreased to 0.8 mm, while the convergence of the maxmium normal contact pressure at the low contact is achieved as the mesh size is reduced to 0.8 mm. Therefore, 0.8 mm mesh size was employed within the fine mesh region of the numerical models.

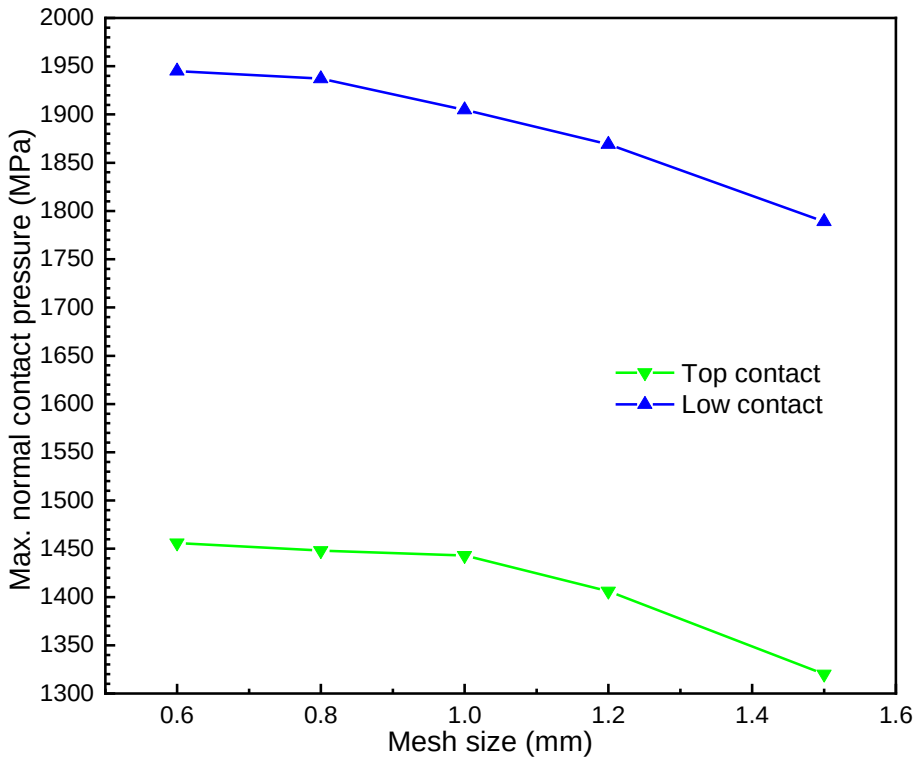

Figure C: The relationship between the maximum normal contact pressure and the mesh size for LAHT steel under the same loading condition presented in Fig. 6-3.